

Abstract

Search for Neutrinoless Double Beta Decay and Detector Physics Measurements with the Final EXO-200 Dataset

Qing Xia

2020

Liquid xenon (LXe) is employed in a number of current and future detectors for rare event searches. This work presents the latest results from the EXO-200 experiment, which searched for neutrinoless double beta decay ($0\nu\beta\beta$) in ^{136}Xe between 2011 and 2018. With upgraded hardware, increased exposure and analysis improvements, the detector resolution, sensitivity and final data limit were also improved over time.

Taking advantage of a single-phase, large detector with good purity and well-calibrated energy response, measurements of the absolute scintillation and ionization yields generated by MeV energy gamma sources over a range of electric fields was performed in EXO-200 and are presented in this thesis. These measurements are useful for simulating the performance of future $0\nu\beta\beta$ detectors employing LXe, such as nEXO, which is a next generation $0\nu\beta\beta$ experiment using ^{136}Xe aiming to reach a half-life sensitivity $\sim 10^{28}$ years. The development of high-bandwidth digital cable prototypes with sufficiently low radioactivity for use in nEXO is described in the end.

**Search for Neutrinoless Double Beta Decay and Detector
Physics Measurements with the Final EXO-200 Dataset**

A Dissertation
Presented to the Faculty of the Graduate School
of
Yale University
in Candidacy for the Degree of
Doctor of Philosophy

by
Qing Xia

Dissertation Director: David Moore

May 2020

Copyright ©
by Qing Xia
All rights reserved.

Acknowledgments

First and foremost, I would like to thank my PhD advisor Prof. David Moore for his continuous support to all aspects of my academic life, from laying out good physics projects to providing down-to-earth advice for carrying them out, from teaching me basic coding techniques to helping me with research grant and fellowship applications, etc.. Very rarely could one find an advisor like him who is always present to have insightful discussions with you when something goes wrong with the experiment, and I feel particularly lucky to be his student. I also thank my thesis committee members — Professors Bonnie Fleming, Karsten Heeger and Witold Skiba for helpful discussion on this work and their career advice in general.

Special thanks to my colleagues and mentors from the EXO/nEXO collaboration: Prof. M. Dolinski for kindly serving as the outside reader for this dissertation; M. Jewell, G. Li, M. Weber and Prof. C. Licciard for their patient explanations of the EXO-200 code, without whom the analysis shown in this thesis would never be done; Professors L. Yang and R. Devoe for their help with the calibrations required for the data analysis presented in this work; A. Jamil and Z. Li for their useful tips on using relevant softwares and instruments; E. Hansen, S. Feyzbakhsh and O. Njoya for telling me aspects about LXe I didn't know before; T. Ziegler and Prof. I. Ostrovskiy for introducing me cutting edge deep learning. B. Mong and J. Davis for showing me how the EXO-200 detector works at WIPP; J. Brodsky for helpful discussions associated with the detector simulation; Professors C. Hall, W. Fairbank, R. Neilson, A. Odian for their feedback on my research; Prof. G. Gratta for his appreciation of my work and support for my career development; and many other co-workers who made the success of our experiment possible.

My general experience working in the physics department at Yale has been great thanks to the wonderful operating and support staff both at the Sloan Physics Lab and the Wright Lab — A. Currie, D. Johnson, F. Lopez, V. Misenti, K. Tighe, L.

Vinston and many others. I also thank the postdocs G. Afek and F. Monteiro who helped me troubleshoot instrumental issues, T. Langford who offered useful advice on computing, and D. Speller who taught me about cryogenic physics.

I am grateful to the company and support from all my friends during the PhD program — Aris, Arpit, Chong, Christian, David, Jérémie, Jingjing, Josh, Kaixuan, Lin, Mark, Mengwen, Michael, Naim, Newton, Ridge, Wenqiang, Olivier, Paul, Supraja, Tong, Tyler, Yueyi, Yukun, and Ziqing. I am especially thankful to Judith, with whom I share common interest in physics and public policy. She is truly a precious friend who was able to point out negative sides in my personality in very artistic ways and made me a better person.

To my parents — my father who introduced me to math and physics, and my mother who kept reminding me that science alone cannot solve all the problems, and to all the sorrows and joys they brought me. I am emotionally attached to my country, China, whose culture taught me the importance of diligence and perseverance. I will do whatever little I can to make it a more open and just society one day.

I am greatly indebted to Dr. Z.X. Yang, whose unconventional perspectives on science and humanity once changed my world view so dramatically as a teenager. Throughout all the years, the strength inspired by his relentless pursuit for truth, justice, compassion and beauty has been my mainstay.

Last but not least, I'd like to express my gratitude to America, whose social system that protects the weak and the voiceless under the rule of law had given me hope to carry on during many years before arriving to this land. Despite all the problems America is facing now, I remain optimistic and grateful to the environment it has provided, which made possible what I have achieved today.

*“Both now and for always, I intend to hold fast to my belief in the hidden strength
of the human spirit.”*

— Andrei Sakharov

Contents

1	Introduction	1
2	Motivations behind Neutrinoless Double-Beta Decay Searches	5
2.1	Neutrino Oscillation and Neutrino Mass	6
2.1.1	The $SU(2) \times U(1)$ Model for Weak Interactions	6
2.1.2	Parameterization for Neutrino Mixing Matrix	8
2.1.3	Measurements of Neutrino Masses and Mixing	11
2.2	Theories for the Origin of Neutrino Mass	15
2.2.1	Dirac and Majorana Neutrino Mass	15
2.2.2	Type-I Seesaw Mechanism	17
2.2.3	Left-right Symmetric Model	18
2.3	Physics of Neutrinoless Double-Beta Decay	20
2.3.1	Best probe on the nature of neutrinos	20
2.3.2	Lepton Number Violation	23
2.3.3	Derivation of $0\nu\beta\beta$ Decay Rate	24
2.3.4	Constraint on the Effective Majorana Mass	26
2.4	Nuclear Matrix Elements for $-\nu\beta\beta$	28
2.4.1	Hadronic Current Operators for $0\nu\beta\beta$	28
2.4.2	Principles of Different Nuclear Structure Approaches	30
2.4.3	Uncertainties on the Nuclear Matrix Element Calculation	33

2.5	Connections of Majorana Neutrinos to Leptogenesis and Baryogenesis	34
3	Overview of the EXO-200 Detector	38
3.1	The EXO-200 Time Projection Chamber	38
3.1.1	Why Liquid Xenon?	40
3.1.2	Charge Detection Channel	42
3.1.3	Light Detection Channel	44
3.2	Cryogenic System in EXO-200	46
3.3	Xenon Purifier	47
3.4	Cosmic Ray Veto System	49
3.5	Interconnection and Electronics	51
3.5.1	Detector Cabling	51
3.5.2	Front-end Electronics	51
3.5.3	Trigger Electronics Module and Data Acquisition	52
3.6	Detector Upgrade	54
4	EXO-200 Analysis Workflow	55
4.1	Event Reconstruction	55
4.1.1	Signal Finding	56
4.1.2	Parameter Estimation of Signals	59
4.1.3	Clustering Algorithm	62
4.1.4	Reconstruction Efficiency	67
4.2	Data Quality	68
4.3	Monte Carlo Simulations	70
4.3.1	Simulated Geometry	71
4.3.2	Simulated Signals	72
4.3.3	Monte Carlo Productions	72
4.4	Energy Calibration and Resolution Measurement	73

4.4.1	Gain Calibrations	74
4.4.2	Electron Lifetime Measurement	75
4.4.3	EXO-200 Lightmap	76
4.4.4	Denoising Algorithm	77
4.4.5	Energy Resolution	80
4.4.6	Denoising performance	84
4.4.7	Detector Uniformity and Stability	86
4.4.8	2D Energy Calibration	87
5	Analysis Results from the ^{136}Xe $0\nu\beta\beta$ Search	90
5.1	Statement of the Author's Contribution	90
5.2	Data Selection	90
5.3	Fit to the Low-background Data	92
5.3.1	Fit Model	92
5.3.2	Background Model	94
5.3.3	Energy scale parameters	96
5.4	Summary of Systematic Errors	96
5.4.1	Signal detection efficiency	96
5.4.2	Single-site Event Fractions	97
5.4.3	Spectral Shape Error	98
5.4.4	Background Model Error	99
5.5	Detector Sensitivity and Data Limit	100
5.5.1	Sensitivity to $0\nu\beta\beta$ Decay Half-life of ^{136}Xe	100
5.5.2	Lower Limit on $0\nu\beta\beta$ Decay Half-life of ^{136}Xe	100
6	W-value Measurement in LXe	103
6.1	Statement of the Author's Contribution	103
6.2	Recombination Model and the W-value	103

6.3	Previous measurements	105
6.4	Measurement of scintillation and ionization yield using ^{228}Th , ^{226}Ra and ^{60}Co sources in EXO-200	108
6.5	Charge and light channel calibrations	109
6.5.1	Measurement of charge and light yields versus field	116
6.6	Comparison between experimental data and the NEST simulation	120
7	Semi-empirical Resolution Model for EXO-200	126
7.1	Statement of the Author’s Contribution	126
7.2	Energy resolution model	126
7.3	Optimal energy resolution predicted by the model	131
7.4	Measurement of the recombination efficiency ϵ_r	136
8	High-bandwidth Digital Data Transmission for nEXO	140
8.1	Introduction of the nEXO detector	140
8.2	Background budget and the choice of interconnection cables	143
8.3	Characterization of the Prototype High-speed Cables for nEXO	147
8.4	Summary	156
9	Conclusions and Future Work	158
	Appendices	161
A	APD Gain Non-uniformity	162
B	Reconstruction of the Scintillation Energy with the DNN	166
B.1	Training data preparation	167
B.1.1	Construction of Datasets with Photopeak Events	167
B.1.2	Construction of Augmented Datasets	169
B.2	DNN Architecture	172

B.3	Evaluation of the Trained DNN	174
B.3.1	Test of the DNN Model Trained on Photopeak Events Only	175
B.3.2	Test of the DNN Model Trained on the Augmented Dataset	176
B.4	Next Steps	178
Bibliography		200

List of Figures

1.1	Standard model of elementary particles: the 12 fundamental fermions and 5 fundamental bosons. Brown loops indicate which bosons (red) couple to which fermions (purple and green). Figure courtesy of Ref. [1]	2
2.1	Pattern of neutrino masses for the normal and inverted hierarchies is shown as mass squared. Flavor composition of the mass eigenstates as the function of the unknown CP phase is indicated. $\Delta m_{atm}^2 \sim \Delta m_{31}^2 \sim \Delta m_{32}^2 $ and $\Delta m_{sol}^2 \sim \Delta m_{21}^2$ stands for the atmospheric and the solar mass-squared splitting, respectively [2].	14
2.2	Feynman diagrams for (a) type-I seesaw mechanism and (b) type-II seesaw mechanisms.	20
2.3	(a) Feynman diagram for ordinary $2\nu\beta\beta$ decay. (b) Feynman diagram for $0\nu\beta\beta$ decay.	21
2.4	(a) Schematic picture of mass parabola for isobaric nuclei with atomic mass $A = 136$. M is the ground state mass for nuclei with different proton number Z . (b) Spectra for the sum of the kinetic energies of the two emitted electrons from $2\nu\beta\beta$ and $0\nu\beta\beta$ decay. The Q value of double beta decays for ^{136}Xe is 2458 keV. The rate of $0\nu\beta\beta$ decay is exaggerated in the figure as it must be much smaller relative to $2\nu\beta\beta$	21
2.5	Diagram showing how a $0\nu\beta\beta$ decay process induces a Majorana neutrino mass term, regardless of the details of how $0\nu\beta\beta$ occurs [3].	22

2.6	Allowed region of $m_{\beta\beta}$ versus m_{min} for the inverted hierarchy (IH) and the normal hierarchy (NH). The calculation is performed by randomly sampling from the distributions of the measured neutrino mixing angles and squared mass differences, as well as a flat distribution of the Majorana phases in the $[0, 2\pi]$ range [4].	27
2.7	Effective Majorana mass $ m_{\nu+N}^{\beta\beta} $ as a function of the lightest neutrino mass in the LRSM [5].	27
2.8	$0\nu\beta\beta$ nuclear matrix elements $M_{0\nu}$ and corresponding half-lives (scaled by $ \langle m_{\beta\beta} \rangle ^2$) calculated from different nuclear models. All the results are obtained with unquenched axial coupling constant g_A [2].	31
2.9	Tree level and one-loop diagrams of heavy neutrino decays that violate CP and lead to leptogenesis	36
3.1	(a) Schematic drawings of the major components of the EXO-200 TPC. (b) The U-V-Z and X-Y-Z coordinate systems in the EXO-200 detector. The hexagonal active Xe region and fiducial Xe region, as well as the circular projection of the Teflon reflector are also shown [6].	39
3.2	One of the two EXO-200 TPC chambers. The interior surface of the APD endplate (2) was coated with aluminum and MgF_2 . Teflon reflectors (1) are installed inside the field cage (3). Both charge and light signals are transmitted to the front-end electronics through flexible cables (4).	40
3.3	The ionization U- and V-wires are visible in front of the APDs. The spring folding scheme at one end of each wire triplet is shown.	42

3.4	(1) A spring-loaded copper receptacle plated with platinum. (2) The PTFE block that contained the receptacle. (3) A special copper adapter connecting the TPC body to the copper conduit (4) that guided the HV cable (5) Platinum plated leaf spring connecting the HV feed to the cathode ring [7].	44
3.5	(a) Large area APDs produced by Advanced Photonix (API) [8]. The active surface of the APD is surrounded by gold-plated ring-wafer anode (left). The cathode is also gold-plated (right), and a bias high voltage is applied across the APD to amplify photoelectric signals. The ruler indicates the size in cm and inches [9]. (b) A copper endplate fully filled with APDs. APDs are ganged into a group of 5 or 7 by platinum plated phosphor bronze springs. The springs electrically connect the cathodes of APDs and copper traces on flexible cables. Acrylic washers provide electrical isolation between the springs and the anchoring screws which go through the endplate [7].	45
3.6	(a) Design of the EXO-200 installation at WIPP. (b) The TPC vessel being inserted into the cryostat.	47
3.7	48
3.8	The calibration source guide tube wrapped around the LXe vessel. Major locations of the calibration source are denoted as S2 = (0.0, 0.0, -29.5 cm), S5 = (25.5 cm, 0.0, 0.0), S8 = (0.0, 0.0, 29.5 cm), and S11 = (0.0, 25.5 cm, 0.0).	48
3.9	Left: The assembled xenon pump in EXO-200. Right: The piston inside the pump, made from a stainless steel canister containing a permanent cylindrical magnet [10].	48

3.10 (a) Layout of the underground facility at WIPP. The location of the EXO-200 detector is marked as the red star. (b) Geant4 simulation of a cosmic muon track (red) along with its spallation products generated in the TPC. Photon (cyan) and neutron (green) tracks in the muon shower are shown [11]. 50

3.11 (a) Acrylic blocks used to mate short flexible cables with long ones. The “V-shaped” block (black) was used for mating cables connected to the ionization wires, and the “T-shaped” block was used for APD channels. The number of channel connections made on each block is indicated. (b) Rectangular copper tubes between the TPC vessel and the cryostat through which the long flexible cables travel to the FEE. The path of cables connected to U- and V-wires are indicated in blue and red, respectively. Green indicates the path of cables connected to APDs [7]. (c) Feedthroughs for cable transitions. (1) Flange that makes the seal from LXe to vacuum. The feedthrough is made from an acrylic cup filled with epoxy. (2) Temporary bracket holding the flange before the TPC’s installation into the cryostat. (3) Flange that makes the seal from the cryostat vacuum to atmosphere. (4) PTFE strain relief inside the cryostat. 52

3.12 Schematic readout electronics systems for the TPC. Bias voltages applied on the V-, U-wires, APDs and the cathode are indicated in the figure. 53

4.1 (a) Raw waveform on a U-wire channel. (b) Filtered waveform. The red line is the calculated threshold from the peak search algorithm [12]. 58

4.2 Identifying multiple signals that occurred nearby one another in time through waveform unshaping. The figures are extracted from [12]. . . 59

4.3	Fits to waveforms on different readout channels. Figures are extracted from [12].	61
4.4	An induction-tagged U-Wire signal which contained a mixture a collection and an induction signal. It can be seen that the mixed signal was better modelled using a linear combination of an induction and a collection (green) waveform template, rather than either an induction (blue) or a collection (red) template individually. The figure is extracted from [13].	63
4.5	The cumulative livetime versus day for physics data. For a run to be considered golden the muon veto efficiency needs to be >90%. The flat region between Phase I and Phase II is due to WIPP incidents from 2014 to 2016.	71
4.6	(a) Spatial part of the channel-by-channel light map used in the denoising algorithm during Phase II. The figure shows the response of one APD channel (with channel number 182) as a function of the X and Y coordinate of events with a specific Z coordinate. The values indicated by the color scale are in the unit of an uncalibrated scintillation count. (b) Relative gain variation over time for the APD channel in (a). . . .	78
4.7	Rotated resolution at Q value versus rotation angle in the three-step scanning.	80
4.8	(a) Rotation angle versus week number during Phase I (b) Rotation angle versus week number during Phase II	81
4.9	Calibration and resolution parameters versus week number during Phase I	81
4.10	Calibration and resolution parameters versus week number during Phase II	82

4.11	Resolution versus time for Phase I and Phase II. Phase II resolution was much improved and became more stable after electronic upgrade. For both Phases, the induction correction to charge energy contributed to a relative 4% improvement, and the denoising of light signals contributed to another relative 5% improvement.	83
4.12	Fitting to the average energy spectra of the Phase I $^{60}\text{Co}+^{228}\text{Th}$ data from (a) cathode runs only (b) both cathode and anode runs. The first row is the spectra for SS events, and the second row is for MS events. Residuals of the fitted energy range are indicated in the bottom pad for each plot.	84
4.13	Fitting to the average energy spectra of the Phase II $^{60}\text{Co}+^{228}\text{Th}$ data from (a) cathode runs only (b) both cathode and anode runs. The first row is the spectra for SS events, and the second row is for MS events. Residuals of the fitted energy range are indicated in the bottom pad for each plot.	85
4.14	For Phase I, the induction correction to charge energy contributed to an overall relative 4% improvement, and the redenoising of light signals after August 2013 contributed to another relative 5% improvement. For Phase II, the overall energy resolution was 5% relatively lower after denoising light signals.	85
4.15	Measured peak position of the Tl-208 peak for Phase I and Phase II (a)(c), and energy resolution (b)(d) in equally sized segments of the detector volume before denoising.	86
4.16	Measured peak position of the Tl-208 peak for Phase I and Phase II (a)(c), and energy resolution (b)(d) in equally sized segments of the detector volume after denoising.	87

4.17	(a) The 2D energy spectrum of ^{228}Th source events. The “orthogonal distance” between the calibrated 2D energy and the rotated axis (black dashed line) is indicated in the plot. (b) The calibrated energy spectrum and the measured resolution for the scintillation, ionization and rotated channel, respectively. Both figures were made using ^{228}Th source calibration data taken during the first week of Phase II.	88
5.1	Blinded low-background data SS events and events removed by the diagonal cut for 3 selected choices.	92
5.2	Comparison between MC (lines) and data (circles) for SS fractions in Phase II using calibration sources positioned near the cathode. The figure is extracted from [14].	97
5.3	(a) Comparison between measured (circles) and MC simulated (lines) energy spectral shapes for three calibration sources (^{228}Th , ^{226}Ra and ^{60}Co) positioned near the cathode. (b) Comparison between data (dots) and MC (solid/dashed lines) for the DNN $0\nu\beta\beta$ discriminator and standoff distance distributions from the ^{226}Ra calibration source and the $2\nu\beta\beta$ spectrum. The red region indicates the expected distributions for $0\nu\beta\beta$ events from MC simulations. All figures are extracted from [14].	98
5.4	Improvements in the EXO-200 detector sensitivity and data limit over time.	101

5.5	Best-fit results for the low background data SS energy spectrum in Phase I (top left) and Phase II (bottom left). The inset shows a zoomed in view of the energy spectrum around the ROI. Best-fit results for the DNN $0\nu\beta\beta$ discriminator distributions of SS and MS events with energy between 2395 keV and 2530 keV (top right). Best-fit results for MS energy spectra (bottom right). The best-fit residuals typically follow normal distributions, with small deviations taken into account in the spectral shape systematic errors. All figures are extracted from [14]	102
6.1	Scintillation and ionization energy deposit produced from particle interaction in LXe.	104
6.2	Schematic diagram of the external calibrator used for the external charge-injection calibration of the U-wire preamplifiers. The external calibrator is used to apply a calibrated amount of charge to the input of the pre-amplifier through C_{in} . The U-wire capacitance, C_U , and stray capacitance from the wiring, C_s , are disconnected during the calibration. The FEC contains the charge sensitive preamplifier with $C_f = 1$ pF, $R_f = 60$ M Ω , and open-loop gain $\gtrsim 10^5$	110
6.3	(a) Measured pulse amplitudes at each voltage step in the external charge-injection calibration. For a fixed voltage, ~ 200 data points were taken. (b) A linear fit to the average pulse amplitudes (ADC counts) versus electron counts, where the electron count is calculated by multiplying the voltage and the nominal capacitance shown in (a).	112
6.4	Comparison between the U-wire gain measured from the external charge-injection calibration at the start of Phase I and the end of Phase II. The difference between them could be attributed to the time variation in the gains or systematic errors in the Phase I calibration, which was not designed to reach the same accuracy as the Phase II calibration. .	112

6.5 (a)-(e) MC-based fit to the anti-correlated number of electrons and photons at the 2615 keV γ peak from the ^{228}Th source data taken in October 2018 under various electric fields. Only bins with more than 10 events are included in the fit. The χ^2/NDF fit statistic is indicated in each plot. The outermost contour contains 68% of peak events on average for the best fit parameters. (f) Combination of the individual fits to the ^{228}Th photopeak under various fields. The magnitude of the slope of each ellipses' major axis is equal to the tangent of the rotation angle. The shaded regions indicate the statistical uncertainty in the best fit value for the rotation angles. 116

6.6 Data and best fit to the 1764 keV γ peak from the ^{226}Ra source, following the same procedure as Figure 6.5. 118

6.7 Data and best fit to 1332 keV and 1173 keV γ peaks from the ^{60}Co source, following the same procedure as Figure 6.5. 118

6.8 Total number of photons vs. number of electrons at electric fields ranging from 50 V/cm to 567 V/cm. The errors indicate statistical fluctuations from the fits shown in Figs. 6.5–6.7, while the shaded bands represent correlated uncertainties on the photon detection efficiency and APD/wire gain measurements. The photon detection efficiency is measured by requiring each line to have a slope of -1 . Residuals between the data and the linear fit, i.e., $((\text{data}-\text{fit})/\text{fit})$ are indicated in the bottom panel along with the statistical errors. 120

6.9 Comparison of the measured charge yields (a) and light yields (b) at various electric fields with the NEST γ and β models. For the ^{228}Th source, measurements from both the Phase I and Phase II data sets are shown, while the other sources only have data available only from Phase II. 121

6.10 (a) Light versus charge response for events when no calibration source is present. Data within the continuous band are predominantly $2\nu\beta\beta$ events from ^{136}Xe . The small peak at the end of the spectrum arises from residual backgrounds in the detector and is excluded from the fits. (b) Charge and light response generated by γ -rays from the ^{228}Th source. (c) Average light versus charge response for γ (orange circles) and $\beta\beta$ (blue squares) events at a range of energies (>500 keV) and an electric field of 567 V/cm. The difference between measurements and the linear fit to the combined dataset (indicated by the red line) in the energy range considered is within 5%. The red bands show the 1σ systematic errors on the response ratio, which are dominated by the uncertainty on ϵ_p . The solid blue and dashed green lines show a comparison with the NEST predictions. 123

7.1 (a) Electronic noise on a single U-wire channel in TPC1 (blue) and TPC2 (green). For a given U-wire channel, the noise is measured through fitting the waveform amplitude before any signal pulse appears in the relevant data runs. (b) Summed electronic noise for all APDs in TPC1 (blue), TPC2 (green) and TPC1 plus TPC2 (red). 132

7.2 Measured recombination fluctuations versus incident γ -ray energy under different electric fields. All points are taken at the energies corresponding to the photopeaks of the calibration sources, but a small plotting offset is added in energy to improve visibility of their errors. The dashed line is a linear extrapolation from the LUX measurements performed at fields varying from 43 to 491 V/cm using β decay signals [15]. 133

7.3	(a) APD excess noise factors measured using the laser calibration data under two different gains for all available APD channels.(b) Comparison between the average APD excess noise factors measured in EXO-200 (blue and green) and previous measurements (black) from [16].	134
7.4	Comparison of measured light and charge energy resolution at 2615 keV under different electric fields with predictions from the resolution model.	135
7.5	Comparison between measured rotated energy resolution at 2615 keV under different electric fields and predictions from the resolution model. Data taken during Phase II has better resolution than Phase I due to the reduced APD noise after the electronics upgrade.	136
7.6	Change in the χ^2 relative to the best fit point (star) obtained by fitting the predicted energy resolution and the expected change in the light and charge yields versus electric field for various values of the photon detection efficiency, ϵ_p , and intrinsic recombination efficiency, ϵ_r , to the observed data.	138
8.1	Schematic design of the nEXO detector, showing the LXe TPC housed in a vacuum insulated cryostat filled with HFE refrigerant fluid which acts as the innermost γ ray shield. The huge water tank provides a thicker shield and also functions as an active cosmic-ray veto detector based on Cherenkov light . The figure is extracted from [17], which assumes that the detector will be located in the Cryopit at SNOLAB with an overburden of 6010 m water equivalent [18].	141
8.2	Design of the anode region in nEXO extracted from [17]. Shown in the figure are the charge collection tiles, SiPM staves behind the field cage, and sapphire tensioned rods.	142

8.3 Energy resolution as a function of the scintillation light detection efficiency at a 400 V/cm drift field. The simulations are performed for charge-channel electronic noise in the case of both room temperature electronics (red) and cold electronics (green). The curve for the Phase-II EXO-200 detector is also shown. Figure courtesy of Ref. [17]. . . . 144

8.4 Background contributions (SS events only) to the ROI by detector component (a) and material (b) in the inner 2000 kg of the nEXO detector. The arrows indicate 90% C.L. upper limits while the circles indicate measured values with 1σ uncertainties. The cables are expected to be the second largest contributors to backgrounds. Figures are extracted from [19]. 145

8.5 (a) Projected sensitivity and discovery potential of the nEXO experiment over time calculated based on the estimated background model. (b) 90% C.L. exclusion sensitivity reach to the effective Majorana mass $\langle m_{\beta\beta} \rangle$ as a function of the lightest neutrino mass for normal (left) and inverted (right) neutrino mass hierarchy. The width of the horizontal bands derive from the uncertainty in nuclear matrix elements. The width of the inner dashed bands result from the unknown Majorana phases. The outer solid lines incorporate the 90% CL errors of the 3-flavor neutrino fit of Ref. [20]. Both figures are extracted from Ref. [17] 146

8.6 Design of the nEXO interconnection system consisting of an ASIC, Kapton cables and a LVDS receiver. 147

8.7 (a) The prototype cables designed at SLAC and tested at Yale. The close-up picture on the right shows the details of the coupled microstrip lines on the Kapton substrate. (b) Coupled transmission lines under microscope. 148

8.8	A cross-section view of a pair of coupled microstrip lines. Figure courtesy of [21]	148
8.9	(a) TDR setup in the Wright Lab at Yale. The system consists of a PicoScope that is connected to a PCB through coaxial cables. The Kapton cables under test are soldered to the PCB. (b) Demonstration of the working principle of the TDR setup.	149
8.10	TDR measurements of the cable's impedance at room temperature (a) and liquid nitrogen temperature (b). The start and end of the copper trace are indicated in the plot.	150
8.11	Schematic picture of the lumped-element circuit model for coupled transmission lines driven by a differential signal. R , L , C , G are series resistance (Ω/m), series inductance (H/m), shunt capacitance (F/m) and shunt conductance (S/m), respectively.	151
8.12	COMSOL simulations of the impedance versus time curve for a single copper trace in the differential pair under room temperature (a) and liquid nitrogen temperature (b).	152
8.13	(a) Wire bonds formed at BNL. Shown are copper traces on a PCB with silver finish, connected through aluminum wire bonds with $25\ \mu\text{m}$ in diameter. (b) 3D geometry of the wire bond observed with the laser microscope at BNL.	153
8.14	The impedance versus time curve for wire bonds of various lengths measured from the TDR. The baseline (blue) in the plot indicates the impedance of a continuous copper trace. As the length of the wire bond increases, its effective impedance also grows.	153

8.15 (a) A new set of cables designed to have characteristic impedance of $\sim 50 \Omega$ and manufactured by Qflex [22] using copper Kapton laminates from Taiflex [23]. (b) TDR measurement performed on one of the new cable channels. 154

8.16 Geometry of the cable in the COMSOL simulation. As the dielectric constants of LXe, the epoxy feedthrough and the cryostat vacuum vary, the copper traces are tapered in the simulation (demonstrated by the close-ups in the figure) to minimize impedance mismatch and optimize signal transmission. 155

8.17 COMSOL simulations of the impedance versus time curve as the cable goes through epoxy. It shows that a $\sim 2 \Omega$ of impedance mismatch exists (left) if the cable geometries in the three media shown in Figure 8.16 are identical. This mismatch can be eliminated after the cable is tapered (right). 155

A.1 PE counts on each APD from a scintillation cluster right above it at $z = 182$ mm for TPC1 (left) and $z = -182$ mm for TPC2 (right) measured using the lightmap before solid angle correction. Five APD channels were disconnected due to hardware problems during EXO-200 operations and are removed from the figure. 163

A.2 PE counts on each APD from a scintillation cluster right above it at $z = 182$ mm for TPC1 (left) and $z = -182$ mm for TPC2 (right) measured using the light map after solid angle correction. The gain non-uniformity is calculated using the PE counts on the selected channels. 163

A.3 PE counts on each APD from a scintillation cluster right above it at $z = 50$ mm for TPC1 (left) and $z = -50$ mm for TPC2 (right) measured using the lightmap before solid angle correction. 164

B.1	(a) An input to the DNN (left panel), made from APD waveforms generated by a photopeak event with energy 2615 keV from the ^{228}Th source. The vertical axis indicates the APD channel number and the horizontal axis represents the time in μs . The middle panel shows the baseline-subtracted waveforms of each APD channel and the right panel is the sum waveform over all channels. (b) Waveform images generated by a photopeak event with energy 1173 keV from the ^{60}Co source.	169
B.2	Selection of events at the full-absorption peaks from the four calibration sources by applying a 2D cut in their charge versus light energy spectra.	170
B.3	Energy distribution of the training set (a) and a validation set (b) that only contain photopeak events from calibration sources.	170
B.4	(a) Example of the fit pulse (red) to a measured waveform (black) from an APD channel generated by a ^{228}Th photopeak event with energy 2615 keV. (b) The red line represents the waveform generated on the same APD channel for an event with energy 2800 keV by scaling the fitted pulse in (a) and adding a simulated noise trace. The black line is the original measured waveform.	171
B.5	(a) An input image to the DNN for an event with energy 2800 keV in the augmented dataset (left panel), made by scaling the measured APD waveforms generated by a 2615 keV event from the ^{228}Th source (b). The vertical axis indicates the APD channel number and the horizontal axis represents the time in μs . The middle panel shows the baseline-subtracted waveforms of each APD channel and the right panel is the sum waveform over all channels.	172

B.6	Event energy and position distribution of the augmented training set. The energy distribution of is designed to be uniform by scaling data from photopeak events, while the spatial distribution is flattened but not perfectly uniform due to the limited amount of photopeak events from various source locations.	173
B.7	Architecture of the DNN for the scintillation energy reconstruction. It consists of four convolutional layers followed by three fully connected layers and a final output layer with dimension 1. Figure adapted from Ref. [24]	173
B.8	Training and validation loss versus training epochs. Both the training and validation sets are made from photopeak events only.	175
B.9	Evaluation of the trained DNN model on an independent set of test data (a) and a ^{228}Th source run with all events near its 2615 keV peak (b). The true scintillation energy spectrum determined by the conventional EXO-200 reconstruction and the predicted spectrum by the DNN are represented by the green and blue distributions, respectively.	176
B.10	Training and validation loss versus training epochs. Both the training and validation sets are augmented datasets made from scaling the energy and waveforms of the photopeak events.	177
B.11	Evaluation of the trained DNN model on an independent set of test data with uniform energy distribution (a) and a ^{228}Th source run with energy beyond 500 keV (b). The true scintillation energy spectrum determined by the conventional EXO-200 reconstruction and the predicted spectrum by the DNN are represented by the green and blue distributions, respectively.	177

List of Tables

4.1	Shaping times for two integration and three differentiation stages for different channels.	57
5.1	Comparison between best-fit results for background events and the total number of events from data in the ROI ($Q \pm 2\sigma$)	101
6.1	Summary of the previous measurements of W and W_i described in the text, along with the year of measurement and particle type. Most data were taken with γ and conversion e^- sources, for which the relevant decay energy is listed. Ref. [25] used an electron beam with total energy listed below, and an energy per e^- of 1–40 keV. Refs. [26] and [27] provide averages of subsets of previous measurements.	108
7.1	Measured values for quantities independent of the drift field in the resolution model and their estimated errors	131
7.2	Quantities depending on the drift field measured using 2615 keV γ s from the ^{228}Th source. Systematic and statistical errors are included.	131
8.1	Concentration of radioactive components in different types of cables	145
8.2	Parameters of the newly designed set of cables, the cross section view of the cable is shown in Figure 8.8	154

Chapter 1

Introduction

The goal of particle physics is to find order amid the seemingly chaotic universe by studying the basic constituents of matter and giving a precise description of the interaction mechanism between them. Before the 1970s, it was known that there exist four types of fundamental interactions: the gravitational and electromagnetic interactions, whose effects can be experienced in everyday life; the strong interaction, which holds ordinary matter together; and the weak interaction, which is responsible for radioactive decays of atoms. In the late 1940s, quantum electrodynamics (QED) successfully described electromagnetic interactions mathematically and explained how electrically charged particles interact with each other through exchanging photons [28–34]. The establishment of QED inspired subsequent quantum field theories to account for strong and weak forces, yet such attempts in the 1950s turned out to be unsatisfactory. Unlike QED which is a normalizable perturbation theory, the then well-known Fermi’s four-fermion theory of weak interactions was discovered to have unremovable infinities, while the Yukawa theory of strong interactions was non-perturbative and thus could not be used to do practical calculations [35]. It was not until 1970s that the modern form of a self-consistent “Standard Model” for fundamental particles was fully developed [36]. The particle content of the Standard

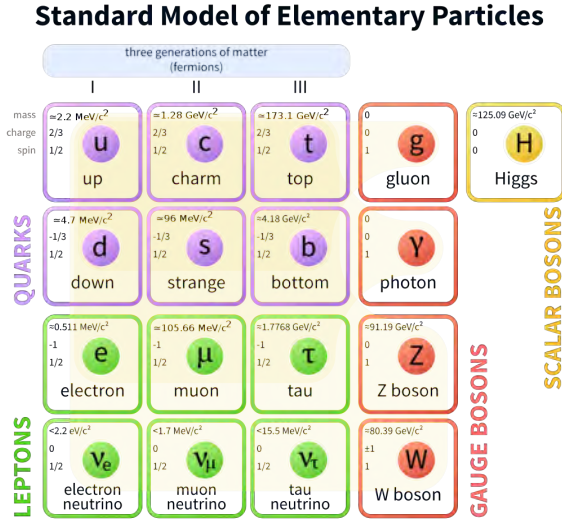


Figure 1.1: Standard model of elementary particles: the 12 fundamental fermions and 5 fundamental bosons. Brown loops indicate which bosons (red) couple to which fermions (purple and green). Figure courtesy of Ref. [1]

Model is shown in Figure 1.1. There are three generations of fermions, with each generation having two types of leptons and two types of quarks, and five fundamental bosons. The description of electromagnetic, strong and weak interactions in the Standard Model were based on gauge symmetries [37]. It predicted the existence of the W and the Z boson, which are intermediate particles for weak interactions, as well as gluons, which are responsible for strong interactions. The quark model was able to make sense of the growing number of hadrons discovered starting in the 1950s [38] and predicted the existence of the Ω^- baryon, which was found in an experiment at Brookhaven National Laboratory [39]. The first evidence for quarks came from deep inelastic scattering experiments at SLAC [40, 41], and the evidence for gluons was found in three-jet events at PETRA [42]. The W and the Z boson were discovered in 1983 and their mass ratio was found to be consistent with the Standard Model prediction [43–45]. Moreover, the Standard Model predicted the existence of the Higgs boson, a particle required in the theory to generate mass terms, which was found experimentally in 2012 at the Large Hadron Collider [46, 47].

Despite the extensive success of the Standard Model, there are a number of crucial questions that it cannot explain, one of them is related to neutrinos – a type of leptons shown in Figure 1.1 that are generated through weak interactions such as nuclear beta decays. Although neutrinos interact weakly with other particles, they were detected in 1956 through the inverse beta decay process using a detector made from large water tanks [48]. However, up till now, we still have not fully understood their properties. For one thing, we are not sure if neutrinos are their own antiparticles, neither do we know how neutrinos acquire masses or what their absolute masses are.

The EXO-200 experiment was aimed at studying some of the unknown properties of neutrinos through searching for a hypothetical decay mode called “neutrinoless double-beta decay” of ^{136}Xe . If this decay mode exists, it would provide clues to the neutrino mass generation mechanism, and would be smoking gun for physics beyond Standard Model. Through minimizing the level of radioactivity of materials used for constructing the detector, as well as maximally shielding radiation from external sources, EXO-200 was designed to be a “low background” experiment that was sensitive to extremely rare neutrinoless double-beta decay signals if they occur with a half-life of $\sim 10^{25}$ years.

This thesis presents the search for ^{136}Xe neutrinoless double-beta decay, using the complete dataset taken from the EXO-200 detector between September 2011 and December 2018. Due to increased exposure, hardware upgrades and analysis improvements over the course of the EXO-200 run, the signal detection efficiency, energy resolution and detector sensitivity were also improved over time. In addition, an independent measurement of absolute scintillation and ionization yields in liquid xenon generated by γ interactions from various radioactive calibration sources was performed. These data are used to model the energy resolution of the EXO-200 detector and are useful for predicting the performance of future neutrinoless double beta decay detectors such as nEXO [19], which is a next generation experiment using

^{136}Xe aiming to reach a half-life sensitivity $\sim 10^{28}$ years. A brief introduction to the nEXO experiment can be found at the end of the thesis.

The structure of the thesis is as follows: Chapter 2 states the theoretical motivations for the neutrinoless double-beta decay searches. Chapter 3 gives an overview of the EXO-200 detector design and operation. Chapter 4 introduces the procedure for data analysis used in EXO-200 including event reconstruction, energy calibration and signal simulations, etc.. The final analysis result including a lower limit on the half-life of neutrinoless double-beta decay of ^{136}Xe is discussed in Chapter 5. Chapter 6 describes the measurement of absolute scintillation and ionization yields generated by MeV energy γ sources over a range of electric fields, from which the W -value in liquid xenon is derived. Based on these measurements, an empirical model is built in Chapter 7, which can successfully model the energy resolution of the detector. Finally, an introduction to nEXO, a future tonne-scale liquid xenon detector, and the development of its ultra-low radioactivity, high-speed cabling are presented in Chapter 8.

Chapter 2

Motivations behind Neutrinoless Double-Beta Decay Searches

The search for neutrinoless double-beta decay ($0\nu\beta\beta$) is aiming to address two fundamental questions in particle physics: first, is the neutrino its own anti-particle, i.e., a Majorana particle? Second, why is the mass of the neutrino much smaller than the other known massive elementary particles? The question of whether neutrinos and antineutrinos could only be distinguished by chirality did not attract considerable attention until neutrino oscillation experiments showed that neutrinos are massive [49, 50], and the introduction of a Majorana mass term in grand unified theories or other extensions to the Standard Model (SM) proved to be able to explain the smallness of neutrino mass in a particularly natural way [51]. Section 2.1 gives a historical review of the discovery of neutrino oscillations which led to the conclusion that neutrinos are massive. Several theoretical mass-generation mechanisms for neutrinos which include right-handed neutrinos with Majorana masses are introduced in Section 2.2. Section 2.3 describes the physics of two-neutrino double-beta decay which has already been observed and the hypothetical process of $0\nu\beta\beta$. The section also contains the calculation of the Feynman diagram for $0\nu\beta\beta$. The contribution of

the hadronic currents to the $0\nu\beta\beta$ decay rate and its calculation with various nuclear structure models is described in Section 2.4. Finally, a discussion on the important possible connection between Majorana neutrinos and the matter-antimatter asymmetry that we observe today is included in Section 2.5.

2.1 Neutrino Oscillation and Neutrino Mass

2.1.1 The $SU(2) \times U(1)$ Model for Weak Interactions

Neutrinos were long believed to be massless because the mass term for all other fermions in the Standard Model requires the mixing between their left- and right-handed components, yet a right-handed neutrino has never been observed in experiments. However, the discovery of neutrino oscillations near the end of the 1990s finally convinced physicists that neutrinos must have mass [49]. The weak interaction between the e, ν, τ and their neutrinos in the Standard Model is described by a $SU(2) \times U(1)$ gauge theory. To ensure gauge symmetry, any derivative term in the Lagrangian is required to be “covariant”, i.e., it has the form of

$$D^\mu = \partial + igW_a^\mu T_a + ig'X^\mu S \quad (2.1)$$

where g is a weak coupling constant, T_a ($a=1,2,3$) and S are generators of $SU(2)$ and $U(1)$, respectively. There are three vector gauge fields W_a^μ associated with the $SU(2)$ group, and one gauge vector field X_μ associated with the $U(1)$ group. We define T_a and S 's action on the lepton doublet

$$\psi_L = \begin{pmatrix} \nu_{eL} \\ e_L \end{pmatrix} \quad (2.2)$$

as $T_a \psi_L = \frac{\tau_a}{2} \psi_L$ (τ_a are the Pauli matrices) and $S \psi_L = -\frac{1}{2} \psi_L$, then a charge-current interaction can be extracted from the kinetic term for the lepton field $i \bar{\psi}_L \not{D} \psi_L$:

$$- \frac{g}{\sqrt{2}} (\bar{\nu}_{eL} \not{W}_+ + e_L^- + \bar{e}_L^- \not{W}_- \nu_{eL}) \quad (2.3)$$

in which the charged vector fields $W_\pm^\mu = \frac{W_1^\mu \mp i W_2^\mu}{\sqrt{2}}$ and $\not{W}_\pm = \gamma_\mu W_\pm^\mu$ is the Feynman slash notation (with γ^μ 's the Dirac matrices). The derivation above also applies to the doublet $\begin{pmatrix} \nu_{\mu L} \\ \mu_L^- \end{pmatrix}$ and $\begin{pmatrix} \nu_{\tau L} \\ \tau_L^- \end{pmatrix}$.

ν_{eL} ($\nu_{L, \tau L}$) in Eq. 2.3 is the ‘‘flavor’’ eigenstate of the neutrino that participate in weak interactions, while e_L (ν_L, τ_L) is both the flavor and mass eigenstate of the charged lepton. This is because if we write down the lepton doublets in a completely arbitrary way $\psi_{jL} = \begin{pmatrix} \nu_j \\ l_j^- \end{pmatrix}_L$ (where $j=1,2,3$ and labels the fields in an arbitrary way) and l_{jR} , then the most general $SU(2) \times U(1)$ invariant Yukawa coupling responsible for the charged-lepton field is

$$- f_{jk} \bar{l}_{jR}^- \phi^\dagger \psi_{kL} + h.c. \quad (2.4)$$

where f_{jk} is a completely arbitrary complex matrix and the Higgs field ϕ transforms under $SU(2) \times U(1)$ as $T_a \phi = \frac{\tau_a}{2} \phi$ and $S \phi = \frac{1}{2} \phi$. After ϕ takes its vacuum expectation value (VEV), the Yukawa coupling term becomes the charged-lepton mass $-M_{jk}^l \bar{l}_{jR}^- l_{kL}^-$ ($M_{jk}^l = f_{jk} \frac{v}{\sqrt{2}}$). We can redefine l_R^- and ψ_L^- so that the mass matrix M^l is real, diagonal, and positive. In this way, the l_L^- and l_R^- can be taken to be mass and flavor eigenstate fields at the same time. However, now if we write down a similar Yukawa coupling term responsible for the neutrino mass

$$- h_{jk} \bar{\nu}_{jR} \tilde{\phi}^\dagger \psi_{kL} + h.c. \quad (2.5)$$

in which $\tilde{\phi} = i \tau_2 \phi^*$ to ensure gauge symmetry [52], then we will find that the neutrino

mass matrix M^ν in $-M_{jk}^\nu \bar{\nu}_{jR} \nu_{kL}$ ($M_{jk}^\nu = h_{jk} \frac{v}{\sqrt{2}}$ after the Higgs field gets its VEV) cannot be diagonalized any more because we have already fixed the ψ_L field. Theoretically there is still freedom to redefine $\bar{\nu}_R$ such that the mass term for neutrinos can be written as:

$$- M_{jl}^\nu U_{lk}^\dagger \bar{\nu}_{jR} \nu_{kL} + h.c. \quad (2.6)$$

where $M^\nu = \begin{pmatrix} m_1 & 0 & 0 \\ 0 & m_2 & 0 \\ 0 & 0 & m_3 \end{pmatrix}$ and U^\dagger is a unitary matrix. This way the ν_{jR} are now mass eigenstates, but the ν_{kL} are related to mass eigenstates by the unitary matrix U^\dagger :

$$\begin{pmatrix} \nu_1 \\ \nu_2 \\ \nu_3 \end{pmatrix}_L = U^\dagger \nu_L \quad (2.7)$$

We note, however, that in principle there is nothing to prevent us from diagonalizing Eq.2.5 first. It is completely out of convention that we choose to the definition described above such that the charge lepton fields, instead of neutrinos, are both mass and flavor eigenstates.

2.1.2 Parameterization for Neutrino Mixing Matrix

Although it is still unclear whether neutrino mass originates from the Yukawa term mentioned above, we can express neutrinos' flavor eigenstates ν_e, ν_μ, ν_τ in terms of their mass eigenstates ν_1, ν_2, ν_3 through a unitary operator without loss of generality:

$$\begin{pmatrix} \nu_e \\ \nu_\mu \\ \nu_\tau \end{pmatrix} = \mathbf{U} \begin{pmatrix} \nu_1 \\ \nu_2 \\ \nu_3 \end{pmatrix} = \begin{pmatrix} U_{e1} & U_{e2} & U_{e3} \\ U_{\mu1} & U_{\mu2} & U_{\mu3} \\ U_{\tau1} & U_{\tau2} & U_{\tau3} \end{pmatrix} \begin{pmatrix} \nu_1 \\ \nu_2 \\ \nu_3 \end{pmatrix} \quad (2.8)$$

In general, a unitary $N \times N$ matrix depends on N^2 independent real parameters. These parameters can be divided into $\frac{N(N-1)}{2}$ mixing angles and $\frac{N(N+1)}{2}$ phases, but not all the phases are physically observable. Because the mixing matrix enters only in the weak charged-current interaction in Eq. 2.3, and all other terms (e.g. mass terms of charged leptons) in the Lagrangian are invariant under a global phase shift of the charged lepton fields, $N = 3$ phases of the mixing matrix can be removed. Therefore, the number of physical parameters in the mixing matrix is $\frac{N(N-1)}{2} = 3$ mixing angles, and $\frac{N(N+1)}{2} - N = 3$ physical phases. If neutrinos are Dirac fermions, $N-1 = 2$ of the phases can be further removed by rephasing neutrino fields, but if neutrinos are Majorana then all three phases should be kept in the mixing matrix. A conventional way for parameterizing the neutrino mixing matrix U is the following:

$$\begin{aligned}
\mathbf{U} &= \begin{pmatrix} 1 & 0 & 0 \\ 0 & c_{23} & s_{23} \\ 0 & -s_{23} & c_{23} \end{pmatrix} \begin{pmatrix} c_{13} & 0 & s_{13}e^{-i\delta} \\ 0 & 1 & 0 \\ -s_{13}e^{i\delta} & 0 & c_{13} \end{pmatrix} \begin{pmatrix} c_{12} & s_{12} & 0 \\ -s_{12} & c_{12} & 0 \\ 0 & 0 & 1 \end{pmatrix} \begin{pmatrix} e^{i\alpha_1/2} & 0 & 0 \\ 0 & e^{i\alpha_2/2} & 0 \\ 0 & 0 & 1 \end{pmatrix} \\
&= \begin{pmatrix} c_{12}c_{13} & & s_{12}c_{13} & s_{13}e^{-i\delta} \\ -s_{12}c_{23} - c_{12}s_{23}s_{13}e^{i\delta} & c_{12}c_{23} - s_{12}s_{23}s_{13}e^{i\delta} & s_{23}c_{13} & \\ s_{12}s_{23} - c_{12}c_{23}s_{13}e^{i\delta} & -c_{12}s_{23} - s_{12}c_{23}s_{13}e^{i\delta} & c_{23}c_{13} & \end{pmatrix} \begin{pmatrix} e^{i\alpha_1/2} & 0 & 0 \\ 0 & e^{i\alpha_2/2} & 0 \\ 0 & 0 & 1 \end{pmatrix}
\end{aligned}$$

in which $c_{ij} = \cos \theta_{ij}$ and $s_{ij} = \sin \theta_{ij}$, and α_1, α_2 are Majorana phases that would vanish if neutrinos are Dirac. Because a massive neutrino state evolves as a plane wave: $|\nu_k(t)\rangle = e^{-iE_k t} |\nu_k\rangle$, a pure flavor state which is a superposition of mass states at $t = 0$ will become a superposition of different flavor states at $t > 0$. The transition amplitude between different flavors is $A_{\nu_\alpha \rightarrow \nu_\beta}(t) = \sum_k U_{\alpha k}^* U_{\beta k} e^{-iE_k t}$, and hence the

transition probability can be written as

$$\begin{aligned}
P_{\nu_\alpha \rightarrow \nu_\beta}(t) &= |A_{\nu_\alpha \rightarrow \nu_\beta}(t)|^2 = \sum_{k,j} U_{\alpha k}^* U_{\beta k} U_{\alpha j} U_{\beta j}^* e^{-i(E_k - E_j)t} \\
&\approx \sum_{k,j} U_{\alpha k}^* U_{\beta k} U_{\alpha j} U_{\beta j}^* e^{-i \frac{\Delta m_{kj}^2 L}{2E}} \quad (2.9)
\end{aligned}$$

In the derivation above, we assumed that neutrinos travel almost at the speed of light and used the approximation that $t \approx L$, the distance between the source and the detector of neutrinos. For ultra-relativistic neutrinos, we also have $E_k \approx E + \frac{m_k^2}{2E}$ where E is the neutrino energy neglecting the mass contribution. Hence $E_k - E_j \approx \frac{\Delta m_{kj}^2}{2E}$ in which $\Delta m_{kj}^2 = m_k^2 - m_j^2$. Given the unitarity condition of \mathbf{U} , Eq. 2.9 can also be written as

$$\begin{aligned}
P_{\nu_\alpha \rightarrow \nu_\beta}(L, E) &= \delta_{\alpha\beta} - 4 \sum_{k>j} \text{Re}[U_{\alpha k}^* U_{\beta k} U_{\alpha j} U_{\beta j}^*] \sin^2\left(\frac{\Delta m_{kj}^2 L}{4E}\right) \\
&\quad + 2 \sum_{k>j} \text{Im}[U_{\alpha k}^* U_{\beta k} U_{\alpha j} U_{\beta j}^*] \sin\left(\frac{\Delta m_{kj}^2 L}{2E}\right) \quad (2.10)
\end{aligned}$$

Since $U_{\alpha k}^* U_{\beta k} U_{\alpha j} U_{\beta j}^*$ is independent of the Majorana phases, we cannot measure Majorana phases in neutrino oscillation experiments, but all the other mixing parameters can be measured – the amplitude of neutrino oscillation is connected to the mixing angles θ_{12} , θ_{23} and θ_{13} , and the oscillation frequency is related to the difference of squared neutrino masses Δm_{kj}^2 .

2.1.3 Measurements of Neutrino Masses and Mixing

For example, the survival probability of electron neutrinos (antineutrinos) after they travel a certain distance in vacuum is:

$$\begin{aligned}
 P(\nu_e \rightarrow \nu_e) &= P(\bar{\nu}_e \rightarrow \bar{\nu}_e) = 1 - \cos^4 \theta_{13} \sin^2 2\theta_{12} \sin^2 \frac{\Delta m_{21}^2 L}{4E} \\
 &\quad - \sin^2 2\theta_{13} \left(\cos^2 \theta_{12} \sin^2 \frac{\Delta m_{31}^2 L}{4E} + \sin^2 \theta_{12} \sin^2 \frac{\Delta m_{32}^2 L}{4E} \right) \quad (2.11)
 \end{aligned}$$

In the late 1960s, the Homestake experiment [53] observed a deficit in the flux of solar neutrinos with respect to the prediction from the Standard Solar Model. The deficit persisted for 30 years [54] and is known as the solar neutrino problem. In 2001, the SNO experiment detected solar neutrinos using a ~ 1 tonne Cherenkov detector and confirmed that electron neutrinos from the sun oscillate into the muon and tau neutrinos. The oscillation takes place inside the sun through a matter-induced resonance known as MSW effect [55, 56]. Because θ_{13} had been determined to be very small (due to the failure to observe $\bar{\nu}_e$ disappearance before 2012 at ~ 1 km short-baseline reactor antineutrino experiments), in the long-baseline solar neutrino or reactor antineutrino flux measurement, the Δm_{21}^2 term in Eq. 2.11 dominates, i.e.,

$$P(\nu_e \rightarrow \nu_e) = P(\bar{\nu}_e \rightarrow \bar{\nu}_e) = 1 - \sin^2 2\theta_{12} \sin^2 \frac{\Delta m_{21}^2 L}{4E} \quad (2.12)$$

The KamLAND experiment placed a detector at $L \approx 50$ km baseline distance from the reactor antineutrino source to have an oscillation maximum at around the peak energy (MeV scale) of the event spectrum and measured $\Delta m_{21}^2 = 7.53_{-0.18}^{+0.18} \times 10^{-5} eV^2$ and $\tan^2 \theta_{12} = 0.436_{-0.025}^{+0.029}$ [57].

Unlike the nuclear fusion reactions in the sun which only produces electron neutrinos, cosmic-ray interactions with the atmosphere of the earth can produce two flavors of neutrinos. When cosmic rays collide with atoms and molecules in the atmosphere,

mainly oxygen and nitrogen, they can produce a cascade of particles which create atmospheric neutrinos through the decay chain: $\pi \rightarrow \mu + \nu_\mu$, $\mu \rightarrow e + \nu_e + \nu_\mu$ (and their charge conjugates). Detailed calculations of the neutrino flux have proved that the flux ratio between $(\nu_\mu + \bar{\nu}_\mu)$ and $(\nu_e + \bar{\nu}_e)$ is approximately 2 in the low energy range ($<1\text{GeV}$). However, a few experiments since 1980s [58] observed that the flavor ratio of the neutrino fluxes was smaller than the expected value. In 1998, the Super-K experiment, which was able to tag the electron or muon flavor of the incoming neutrino based upon the relative sharpness or diffuseness of Cherenkov rings [58], found solid evidence for a deficit of atmospheric muon neutrinos which can be explained by $\nu_\mu \leftrightarrow \nu_\tau$ oscillation. The experiment also found asymmetries in the zenith angle distributions of the atmospheric ν_μ , which indicates a flight distance dependence of the ν_μ event rate and thus provides direct evidence of the neutrino oscillation. The Super-K measurement resulted in an estimation of θ_{23} and $|\Delta m_{atm}^2|$ [49], which is an approximation of $|\Delta m_{32}^2|$.

Assuming $\theta_{13} = 0$, The ν_μ survival probability derived from Eq. 2.10 is

$$\begin{aligned}
P(\nu_\mu \rightarrow \nu_\mu) &= 1 - (\cos^4 \theta_{23} \sin^2 2\theta_{12} \sin^2 \frac{\Delta m_{21}^2 L}{4E} + \cos^2 \theta_{12} \sin^2 2\theta_{23} \sin^2 \frac{\Delta m_{32}^2 L}{4E} \\
&+ \sin^2 \theta_{12} \sin^2 2\theta_{23} \sin^2 \frac{\Delta m_{31}^2 L}{4E}) \quad (2.13)
\end{aligned}$$

Muon neutrinos can also be produced in accelerators with a high intensity. For accelerator neutrinos, L and E can be chosen so that $\frac{\Delta m_{31}^2 L[\text{km}]}{4E[\text{GeV}]} \sim \frac{\pi}{2}$. Hence, $\frac{\Delta m_{21}^2 L}{4E} \ll 1$ (because $\Delta m_{21}^2 \ll \Delta m_{32}^2 \approx \Delta m_{31}^2$), and can be treated as a small perturbation. The survival probability for accelerator ν_μ can then be written as:

$$P(\nu_\mu \rightarrow \nu_\mu) = 1 - \sin^2 2\theta_{23} \sin^2 \frac{\Delta m_{32}^2 L}{4E} \quad (2.14)$$

The MINOS experiment used two detectors 734 km apart to detect the energy and flavor content of the neutrinos produced by the Neutrinos at the Main Injector

(NuMI) beamline at Fermilab. It updated the result of θ_{23} and $|\Delta m_{atm}^2|$ by measuring ν_μ and $\bar{\nu}_\mu$ disappearance using both beam and atmospheric data. $|\Delta m_{32}^2| = 2.41_{-0.10}^{+0.09} \times 10^{-3} \text{ eV}^2$ and $\sin^2(2\theta_{23}) = 0.950_{-0.036}^{+0.035}$ [59]. The magnetized MINOS detectors also allow the separation of the charged-current ν_μ and $\bar{\nu}_\mu$ via curvature of the muon track, and thus can separately measure the mixing parameters for neutrinos and antineutrinos. The results showed the muon antineutrino disappearance is in good agreement with the neutrino result, which indicates the conservation of the charge-parity-time reversal (CPT) symmetry.

Additionally, neutrinos generated from beta decay in nuclear reactors provide us with an approach to measure θ_{13} because they come in only one flavor: electron antineutrinos. The survival probability of electron antineutrinos at a short distance of 1-2 km from the reactors is [60]

$$P = 1 - \sin^2 2\theta_{13} \sin^2 \frac{\Delta m_{31}^2 L}{4E} \quad (2.15)$$

where E is the $\bar{\nu}_e$ energy in MeV and L is the distance between the neutrino source and the detector, and we have used the approximation $\frac{\Delta m_{21}^2 L}{4E} \ll 1$ for the short-baseline experiment. The Daya Bay experiment, which used two near detectors and one far detector to measure $\bar{\nu}_e$'s survival rate via the inverse β -decay (IBD) reaction in gadolinium-doped liquid scintillator (Gd-LS), announced a discovery in 2012 that $\theta_{13} \neq 0$ with a significance of 5.2σ . The result is consistent with earlier, less significant results from Double Chooz [61], and was later confirmed by RENO [62]. A more precise measurement by Daya Bay in 2018 [63] gives $\sin^2 2\theta_{13} = 0.0856 \pm 0.0029$.

As current experiments cannot determine the sign of Δm_{31}^2 or Δm_{32}^2 , there are two possible mass hierarchies for neutrinos, which are shown schematically in Figure 2.1. The scenario in which ν_3 is heavier is referred to as the normal mass hierarchy (NH). The other scenario in which ν_3 is lighter is called the inverted mass

hierarchy (IH). Figure 2.1 also summarizes the present knowledge of flavor composition of the mass eigenstates as the function of the unknown CP phase. The neutrino

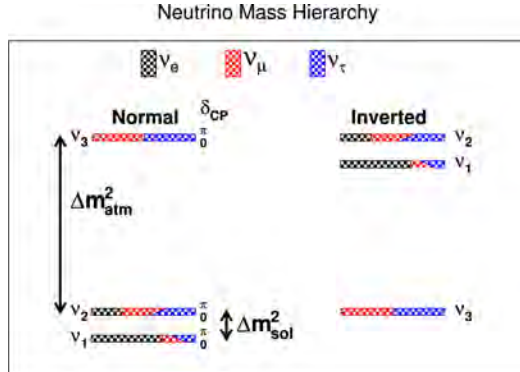


Figure 2.1: Pattern of neutrino masses for the normal and inverted hierarchies is shown as mass squared. Flavor composition of the mass eigenstates as the function of the unknown CP phase is indicated. $\Delta m_{atm}^2 \sim |\Delta m_{31}^2| \sim |\Delta m_{32}^2|$ and $\Delta m_{sol}^2 \sim \Delta m_{21}^2$ stands for the atmospheric and the solar mass-squared splitting, respectively [2].

mass hierarchy question can be addressed by measuring the muon (anti)neutrino disappearance and electron (anti)neutrino appearance data using accelerator-produced muon (anti)neutrino ($\bar{\nu}_\mu$) beams over baselines L of order (100–1000) km, with neutrino energies $E[GeV] \approx L[km] \times |\Delta m_{32}^2[eV^2/c^4]|$ [64]. Due to a small (3%) difference in Δm_{31}^2 and Δm_{23}^2 , the modulation frequency of the neutrino oscillation pattern is slightly different for two different hierarchies. The appearance probability is also affected by the matter effects as the neutrinos travel through the Earth, which enhance either $\nu_\mu \rightarrow \nu_e$, or $\bar{\nu}_\mu \rightarrow \bar{\nu}_e$ depending on the sign of Δm_{32}^2 , i.e., if the mass ordering is normal (inverted), $\nu_\mu \rightarrow \nu_e$ oscillations are enhanced (suppressed) while $\bar{\nu}_\mu \rightarrow \bar{\nu}_e$ oscillations are suppressed (enhanced) [65]. Although the results are not yet conclusive, the most recent analyses from T2K [66] and NOvA [64] both slightly preferred the normal neutrino mass hierarchy. The NOvA result favored the normal mass hierarchy by 1.9σ , and a combined analysis of the two experiments is underway.

The discovery of neutrino oscillation proved, in contradiction to the naive assumption in the Standard Model, that neutrinos are massive. The question following this discovery is how neutrinos gain their mass and why it is much smaller than the mass

of other fermions in the Standard Model. This leads us to the discussion in the next section on whether neutrinos are Dirac or Majorana by nature.

2.2 Theories for the Origin of Neutrino Mass

Neutrino mass is one of the most important subjects of study in neutrino physics. In this section we discuss different mass generation mechanisms for neutrinos. We explain why including a Majorana mass term is particularly appealing for resolving the mystery about the origin of the small neutrino mass.

2.2.1 Dirac and Majorana Neutrino Mass

As mentioned in the previous section, neutrino masses could have been generated from the same Higgs mechanism that gives mass to charged fermions in the Standard Model, through adding a Yukawa coupling term including a Dirac neutrino written as Eq. 2.5. After spontaneous symmetry breaking, Eq. 2.5 gives a Dirac neutrino mass term which can be written as

$$\frac{1}{2}m_D\bar{\nu}_R\nu_L + h.c. \quad (2.16)$$

However, the neutrino mass m_D we have obtained this way is proportional to the Higgs VEV v , just as the masses of charged leptons and quarks. Unless the Yukawa coupling constant in Eq. 2.5 is exceptionally small, there is no explanation for the smallness of the neutrino mass.

Due to the reluctance of artificially assigning neutrinos with tiny Dirac masses, physicists have come up with a number of beyond Standard Model theories that would result in a small neutrino mass more naturally. In 1937, Ettore Majorana

hypothesized that neutral spin-1/2 particles can also be described as Majorana spinors

$$\psi_M = \begin{pmatrix} \chi \\ \epsilon\chi^* \end{pmatrix} \quad (2.17)$$

It is a four component object composed of a single Weyl spinor χ , and $\epsilon = -i\tau_2$ in which τ_2 is the second Pauli matrix) [37]. Unlike a Dirac spinor $\psi_D = \begin{pmatrix} \chi \\ \epsilon\xi^* \end{pmatrix}$ in which ξ is Weyl spinor different from χ , a Majorana spinor is identical to its charge conjugation:

$$\psi_M^c = C\overline{\psi_M}^T = \psi_M \quad (2.18)$$

where the charge conjugation matrix $C = \begin{pmatrix} -\epsilon & 0 \\ 0 & \epsilon \end{pmatrix}$ in the Weyl representation.

A Majorana mass term can then be written in terms of either Majorana spinors ($-\frac{1}{2}m\overline{\psi_M}\psi_M$) or Dirac spinors ($-\frac{1}{2}m((\overline{\psi_L})^c\psi_L + h.c.)$).

In general, physics beyond the Standard Model can be described by a tower of operators O^d of dimension $d > 4$ [67]. These operators consist of the Standard Model fields and are not renormalizable, but they are suppressed by the inverse powers of the new physics scale Λ , and thus can effectively describe physics phenomena at the low energy scale. The generic expression for the beyond Standard Model Lagrangian is:

$$-\mathcal{L} = \mathcal{L}_{SM} + \mathcal{L}_{eff}^{d=5} + \mathcal{L}_{eff}^{d=6} + \dots \quad (2.19)$$

with $\mathcal{L}_{eff}^d \propto \frac{1}{\Lambda^{d-4}}O^d$. Weinberg showed in 1979 [68] that there is only one dimension $d = 5$ operator which can satisfy all gauge symmetries required by the Standard Model: $\mathcal{L}^{(5)} = \frac{C^5}{\Lambda}((\overline{\psi_L})^c\epsilon H)(H^T\epsilon\psi_L) + h.c.$, in which H is the Higgs field and ψ_L is the lepton doublet defined in Eq. 2.2. It gives rise to the Majorana neutrino mass term after the Higgs gets its VEV: $\mathcal{L}^{(M)} = \frac{C^5}{\Lambda}\frac{v^2}{2}(\overline{\nu_L})^c\nu_L + h.c. = \frac{m_L}{2}[(\overline{\nu_L})^c\nu_L + h.c.]$, where the superscript c represents the charge conjugation of the field. As one can observe

from the expression above, the feature of left- and right-handed spinor mixing present in the Dirac mass term no longer exists in the Majorana mass term. In addition, if the Higgs VEV is much smaller than the new physics scale, i.e., $v \ll \Lambda$, then $m_L \approx 0$.

2.2.2 Type-I Seesaw Mechanism

On the other hand, we can write down a Majorana mass term for the right-handed chiral field: $\frac{m_R}{2}[(\nu_R)^c \nu_R + h.c.]$. Since ν_R is a singlet under the gauge transformations in the Standard Model, the Majorana mass m_R is not protected by those gauge symmetries and can be very large. If we define $f = \frac{1}{\sqrt{2}}[\nu_L + (\nu_L)^c]$ and $F = \frac{1}{\sqrt{2}}[\nu_R + (\nu_R)^c]$, the most general mass term, which is the sum of the Dirac mass Eq. 2.16 and the Majorana mass term, can be written in the matrix form:

$$\mathcal{L}_M = (\bar{F}, \bar{f}) \begin{pmatrix} m_R & m_D \\ m_D & m_L \end{pmatrix} \begin{pmatrix} F \\ f \end{pmatrix} \quad (2.20)$$

Notice that $F^c = F$ and $f^c = f$, hence both of them are Majorana spinors. Consider the case of $m_D \ll m_R$ and $m_L = 0$, the eigenvalues of the mass matrix would be $m_1 \approx \frac{m_D^2}{m_R} \ll m_D$ and $m_2 \approx m_R$. This is called type-I seesaw mechanism, which provides a very plausible explanation of the smallness of neutrino masses. The Dirac mass m_D is expected to be the characteristic mass of the charged fermions in the Standard model, and the assumption $m_L = 0$ is natural, since a Majorana mass term for the left-handed chiral field f is forbidden by the symmetries of the Standard Model. On the contrary, the Majorana mass term for the right-handed chiral field F is not restricted by the symmetries of the Standard Model. It is possible that m_R is generated by new physics beyond the Standard Model and the right-handed chiral neutrino field belongs to a nontrivial multiplet of the symmetries of the high-energy theory. In this case, the mass m_R is associated with the breaking scale of the symmetries of this new high-energy theory, which may be at the grand unification

scale that is on the order of $10^{14} - 10^{16}$ GeV [69–71]. Hence this mechanism may give a light-neutrino mass suppressed by a factor of $m_D/m_R \approx 10^{-14} - 10^{-12}$ compared to the typical Dirac fermion mass.

2.2.3 Left-right Symmetric Model

It is also possible that the left-handed Majorana mass m_L is small but non-zero, i.e., $|m_L| \gg \frac{m_D^2}{m_R}$. The mass generation under this case is called type-II seesaw mechanism. For example, in the minimal left-right symmetric model (LRSM) [51, 72, 73], physics at higher energy is described by the gauge group $SU(2)_L \times SU(2)_R \times U(1)_{B-L}$. In this model left and right-handed fermions are doublets of $SU(2)_{L,R}$

$$\psi_L = \begin{pmatrix} \nu_{eL} \\ e_L \end{pmatrix}, \quad \psi_R = \begin{pmatrix} N_{eR} \\ e_R \end{pmatrix} \quad (2.21)$$

and they both couple to their corresponding charged gauge bosons with the same gauge couplings constant $g_L = g_R = g$:

$$- \frac{g}{\sqrt{2}} (\overline{\nu_{eL}} \mathcal{W}_L e_L + \overline{N_{eR}} \mathcal{W}_R e_R) + h.c. \quad (2.22)$$

The Higgs sector in the LRSM consists of a bi-doublet ϕ and two triplets of $SU(2)_{L,R}$,

$$\phi = \begin{pmatrix} \phi_1^0 & \phi_1^+ \\ \phi_2^- & \phi_2^0 \end{pmatrix}, \quad \Delta_{L,R} = \begin{pmatrix} \frac{1}{\sqrt{2}}\delta^+ & \delta^{++} \\ \delta^0 & -\frac{1}{\sqrt{2}}\delta^+ \end{pmatrix}_{L,R} \quad (2.23)$$

The transformation rules are

$$\begin{aligned} SU(2)_L \times SU(2)_R : \quad \phi &\rightarrow U_L \phi U_R^\dagger, \quad \Delta_L \rightarrow U_L \Delta_L U_L^\dagger, \quad \Delta_R \rightarrow U_R \Delta_R U_R^\dagger \\ U(1)_{B-L} : \quad \phi &\rightarrow \phi, \quad \Delta_L \rightarrow e^{i\theta_{B-L}} \Delta_L, \quad \Delta_R \rightarrow e^{i\theta_{B-L}} \Delta_R \end{aligned} \quad (2.24)$$

where U_L and U_R are group elements of $SU(2)_L$ and $SU(2)_R$, respectively, and $e^{i\theta_{B-L}} \in U(1)_{B-L}$.

The gauge-invariant Yukawa couplings can be written as:

$$h_1 \bar{\psi}_L \phi \psi_R + h_2 \bar{\psi}_L \tilde{\phi} \psi_R + h_3 (\overline{(\psi_L)^c} i \tau_2 \Delta_L \psi_L + \overline{(\psi_R)^c} i \tau_2 \Delta_R \psi_R) \quad (2.25)$$

in which $\tilde{\phi} = \tau_2 \phi^* \tau_2$ transforms in the same way as ϕ in Eq. 2.24. It can be shown that the vacuum expectation values of the Higgs multiplets take the following forms [74]:

$$\langle \phi \rangle = \begin{pmatrix} v & 0 \\ 0 & v' \end{pmatrix}, \quad \langle \Delta_L \rangle = \begin{pmatrix} 0 & 0 \\ v_L & 0 \end{pmatrix}, \quad \langle \Delta_R \rangle = \begin{pmatrix} 0 & 0 \\ v_R & 0 \end{pmatrix} \quad (2.26)$$

with $v' \ll v$ in order to suppress $W_L - W_R$ mixing [75].

In the first stage, the left-right symmetry breaks at a high-energy scale $v_R \gg v$ and reduces to the $SU(2)_L \times U(1)$ group of the Standard Model. The right-handed Majorana neutrino picks up a mass m_R of order $h_3 \langle \Delta_R \rangle = h_3 v_R$. After the $SU(2)$ symmetry breaking at the SM electroweak scale v , the triplet Δ_L acquires its VEV $\langle \Delta_L \rangle = \lambda v^2 / v_R$ due to the presence of the term $\lambda \Delta_L \Delta_R^\dagger \phi \phi$ in the potential [74]. Hence, we get $m_L = h_3 v_L = h_3 \lambda v^2 / v_R$ after two stages of spontaneous symmetry breaking. The Feynman diagrams for both type-I and type-II seesaw mechanisms are shown in Figure 2.2 [51].

There are other categories of neutrino mass generation mechanisms such as type-III seesaw [76–78], radiative seesaw [79–81], and inverse seesaw [82–84], which are beyond the scope of this thesis.

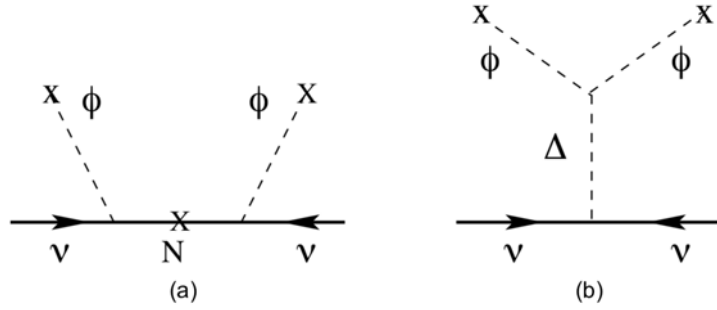


Figure 2.2: Feynman diagrams for (a) type-I seesaw mechanism and (b) type-II seesaw mechanisms.

2.3 Physics of Neutrinoless Double-Beta Decay

2.3.1 Best probe on the nature of neutrinos

Neutrinoless double-beta decay ($0\nu\beta\beta$) experiments are considered as the best probe on the Dirac/Majorana nature of neutrinos, but so far there has been no convincing experimental evidence of such a decay mode. In order to introduce $0\nu\beta\beta$, let us first consider the Standard Model allowed two-neutrino double-beta decay ($2\nu\beta\beta$), which was first proposed by Goeppert-Mayer in 1935 [85]. The $2\nu\beta\beta$ process is a transition among isobaric isotopes that changes the proton number Z of a nucleus by two:

$$(A, Z) \rightarrow (A, Z + 2) + 2e^- + 2\bar{\nu}_e$$

In other words, a $2\nu\beta\beta$ process consists of the simultaneous β decay of two neutrons in the same nucleus. The Feynman diagram demonstrating this process is shown in Figure 2.3a.

For a specific atomic number (i.e., $A = 136$), the masses around the stable isotope can be approximated by a parabola shown in Figure 2.4a. Because of the extra stability associated with pairs of like nucleons, the mass parabola is split into two: nuclei with even number of protons and even number of neutrons (even-even nuclei)

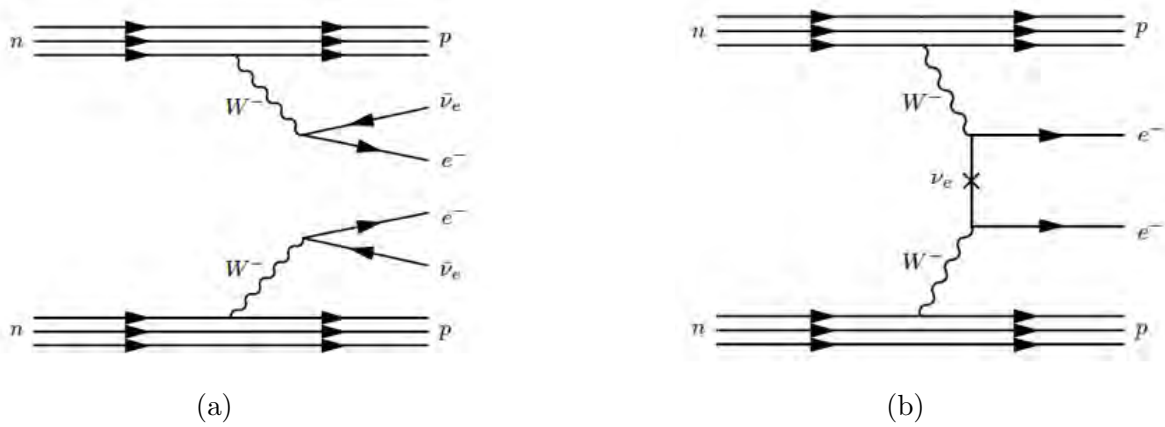


Figure 2.3: (a) Feynman diagram for ordinary $2\nu\beta\beta$ decay. (b) Feynman diagram for $0\nu\beta\beta$ decay.

lie on the lower parabola, while odd-odd nuclei lie on the upper parabola. In order for $2\nu\beta\beta$ to happen, the final nucleus must have a larger binding energy than the original nucleus. For even-even nuclei such as ^{136}Xe , the isobar one atomic number higher has a smaller (absolute) binding energy, hence the single beta decay mode is energetically forbidden. However, its isobar with atomic number two higher have a larger (absolute) binding energy, thus allowing double beta decay to occur.

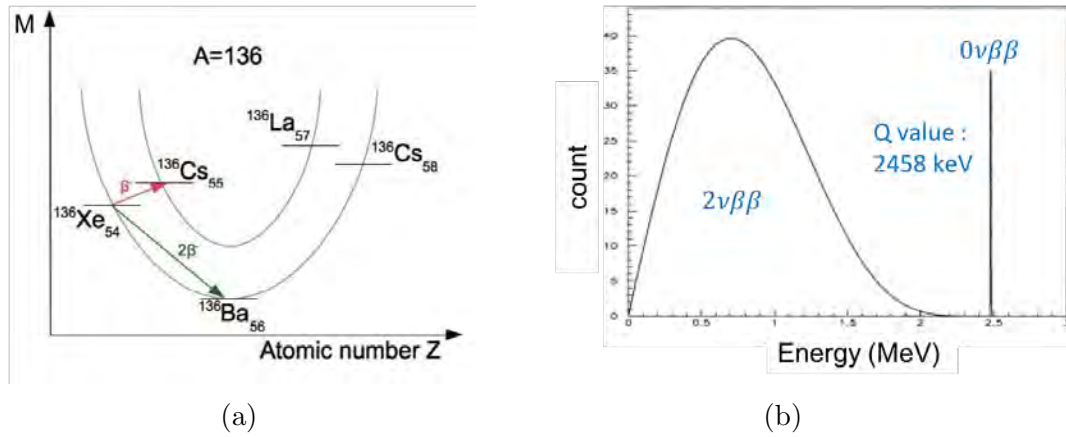


Figure 2.4: (a) Schematic picture of mass parabola for isobaric nuclei with atomic mass $A = 136$. M is the ground state mass for nuclei with different proton number Z . (b) Spectra for the sum of the kinetic energies of the two emitted electrons from $2\nu\beta\beta$ and $0\nu\beta\beta$ decay. The Q value of double beta decays for ^{136}Xe is 2458 keV. The rate of $0\nu\beta\beta$ decay is exaggerated in the figure as it must be much smaller relative to $2\nu\beta\beta$

If neutrinos are Majorana particles, then it is possible for neutrinoless double beta decay to occur in certain nuclei:

$$(A, Z) \rightarrow (A, Z + 2) + 2e^-$$

where neutrinos annihilates in the mediating virtual process, as shown in the Figure 2.3b.

On the other hand, the observation of neutrinoless double beta decay can lead generally to the conclusion that there exist Majorana neutrinos. We can see this by embedding the $0\nu\beta\beta$ into a higher-order process, as shown in Figure 2.5. Regardless of the details of mediating particles involved in the mechanism, the existence of $0\nu\beta\beta$ would necessarily generate a Majorana neutrino mass term.

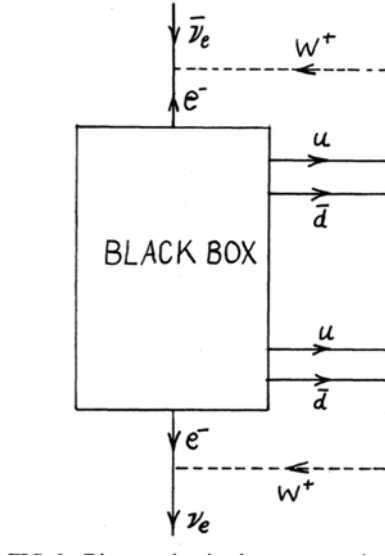


Figure 2.5: Diagram showing how a $0\nu\beta\beta$ decay process induces a Majorana neutrino mass term, regardless of the details of how $0\nu\beta\beta$ occurs [3].

Figure 2.4b shows the energy spectra of the sum of the kinetic energies of the two emitted electrons in two different modes: $2\nu\beta\beta$ and $0\nu\beta\beta$ decay. For the neutrinoless mode one expects a sharp peak at the Q value (total decay energy released during the nuclear decay); and for the two-neutrino mode the energy spectrum for

electrons is continuous because the total decay energy is shared between electrons and antineutrinos.

2.3.2 Lepton Number Violation

Besides the $SU(2) \times U(1)$ symmetry mentioned in Section 2.1.1, the Standard Model also has an accidental symmetry associated with the lepton number. The lepton number is a quantum number used to denote which particles are leptons and which particles are not. Each lepton has a lepton number of 1 and each antilepton has a lepton number of -1. Other particles have a lepton number of 0. In all Standard Model particle reactions, the lepton number is conserved. There have been a number of searches for lepton number violation, which would be unequivocal evidence for physics beyond the Standard Model. For instance, the measured upper limit on the branching ratio of muon-positron conversion ($\mu^- + (Z, A) \rightarrow e^+ + (Z - 2, A)$) is 1.7×10^{-12} [86], and the branching ratio for $K^+ \rightarrow \pi^- \mu^+ \mu^+$ was measured to be smaller than 10^{-10} [87]. Both processes above can be studied using accelerators and will violate the lepton number by two units if they occur.

As shown in Figure 2.3b, the $0\nu\beta\beta$ process will also change the lepton number by two units, resulting from the creation of two leptons with no balancing anti-leptons, a possible manifestation of Grand Unified Theories like $SU(5)$ [88] and $SO(10)$ [89] [90]. $0\nu\beta\beta$ experiments have their particular merit in searching for lepton number violation as compared to accelerator experiments. This is because many moles of target material in $0\nu\beta\beta$ detectors can be studied for a long time, and a single mole of the material contains an Avogadro number (6×10^{23}) of atoms, which is much larger than typical beams (e.g., Fermilab produces $\sim 10^{20}$ protons on target each year [91]).

2.3.3 Derivation of $0\nu\beta\beta$ Decay Rate

For the double beta decay process mediated by the tree-level Majorana interaction shown in Figure 2.3b, the relevant effective interaction term that contributes to the decay rate is a product of leptonic and hadronic current densities at two space-time positions x and y :

$$\left(\frac{G_F}{\sqrt{2}}\right)^2 l_{\mu\nu}(x, y) J^{\mu\nu}(x, y) = \left(\frac{G_F}{\sqrt{2}}\right)^2 [\bar{e}(x)\gamma_\mu(1 - \gamma_5)\nu_e(y)J_L^\mu(x)][\bar{e}(y)\gamma_\nu(1 - \gamma_5)\nu_e(y)J_L^\nu(y)] + h.c.$$

where J_L^μ is the left-handed charge-changing hadronic current density. Because $0\nu\beta\beta$ is a second order process of the weak interaction Lagrangian above, the contribution from the leptonic part to the decay amplitude contains two electrons, while the two neutrino fields can be contracted if they are Majorana fermions:

$$\begin{aligned} \langle 0 | l_{\mu\nu}(x, y) | p_1, p_2 \rangle &= \langle 0 | \sum_{i,k} \bar{e}(x)\gamma_\mu(1 - \gamma_5)U_{ek}\nu_k(x)\bar{e}(y)\gamma_\nu(1 - \gamma_5)U_{ei}\nu_i(y) | p_1, p_2 \rangle \\ &= \langle 0 | - \sum_k \bar{e}(x)\gamma_\mu(1 - \gamma_5)U_{ek}\nu_k(x)\overline{\nu_k^c}(y)\gamma_\nu(1 + \gamma_5)U_{ek}e^c(y) | p_1, p_2 \rangle \\ &= -\frac{i}{4} \int \sum_q \frac{d^4q}{(2\pi)^4} e^{-iq\cdot(x-y)} \bar{u}(p_1)\gamma_\mu(1 - \gamma_5)e^{-i(p_1\cdot x + p_2\cdot y)} \\ &\quad \times \frac{\not{q} + m_k}{q^2 - m_k^2} \gamma_\nu(1 + \gamma_5)u^c(p_2)U_{ek}^2 \end{aligned} \quad (2.27)$$

where we have written the electron flavor neutrino in terms of the Majorana mass eigenstates ν_k ($k = 1, 2, 3$) using the neutrino mixing matrix element U_{ek} . p_1 and p_2 are the four-momenta of the outgoing electrons, and $u(p_i)$ ($u^c(p_i)$) represents a four-component Dirac spinor (its charge conjugation) of the electron. q is the four-momentum of the inter-mediating virtual neutrino, and the \not{q} term in Eq. 2.27 vanishes because it is sandwiched by two currents that are both left-handed. Since neutrino

mass m_k is very small and can be neglected in the denominator, the decay amplitude becomes proportional to

$$\langle m_{\beta\beta} \rangle = \sum_k m_k U_{ek}^2 \quad (2.28)$$

The hadronic part of the decay amplitude can be written as a matrix element of an ordinary product of hadronic currents between initial and final states of the nucleus:

$$\begin{aligned} \langle f | J^{\mu\nu}(x, y) | i \rangle &= \langle f | J_L^\mu(x) J_L^\nu(y) | i \rangle \\ &= \sum_n \langle f | J_L^\mu(\mathbf{x}) | n \rangle \langle n | J_L^\nu(\mathbf{y}) | i \rangle \times e^{-i(E_n - E_f)x_0} e^{-i(E_i - E_n)y_0} \end{aligned} \quad (2.29)$$

where $|f\rangle$ and $|i\rangle$ represent the initial and final state of the nucleus, and $|n\rangle$'s are a complete set of intermediate nuclear states.

In order to obtain the decay amplitude, we need to multiply the contribution from the leptonic current densities 2.27 by the hadronic current densities 2.29 and then integrate the product over the spacetimes x and y , as well as over the phase space of all possible final states. The decay rate for $0\nu\beta\beta$ generated from the exchange of light Majorana neutrinos calculated this way is:

$$\frac{1}{T_{1/2}^{0\nu}} = G_{0\nu} |M_{0\nu}|^2 |\langle m_{\beta\beta} \rangle|^2 \quad (2.30)$$

where $M_{0\nu}$ is the nuclear matrix element calculated from Eq. 2.29. The calculation can be carried out using various nuclear structure models, which will be discussed in Section 2.4. $G_{0\nu}$ accounts for the phase space of all possible final states of the decay, and is exactly-calculable. Since the mass the nucleus is much larger than the masses of electrons, nearly all momentum will be carried by the two outgoing electrons. The phase space factor for the two electrons with momentum p_i and E_i ($i = 1, 2$) can be approximated by the integral: $\int_0^{p_{max}} d^3p_1 d^3p_2 \delta(p_1 - p_2)$. The expression above is

approximately proportional to $\int_0^{E_{max}} E_1 p_1(Q - E_1) p_1 dE_1$, where Q is the decay energy, and E_{max} is the maximum energy an outgoing electron can have. Since the Q value of $0\nu\beta\beta$ decay is typically much larger than the electron mass, we have $E_{max} \approx Q$. In this way, we come to the conclusion that the decay rate of $0\nu\beta\beta$ is approximately proportional to Q^5 .

2.3.4 Constraint on the Effective Majorana Mass

The effective Majorana electron neutrino mass in Eq. 2.30 is defined in Section 2.3.3 as $\langle m_{\beta\beta} \rangle = \sum_k m_k U_{ek}^2$, where m_k 's are the mass eigenvalues of three light neutrinos in the canonical case. The measurement of the lower limit on $T_{1/2}^{0\nu}$ can be translated into an upper limit of $|\langle m_{\beta\beta} \rangle|$ once we obtain the values of $M_{0\nu}$ and $G_{0\nu}$ from theoretical calculations. In turn, the measurement of $|\langle m_{\beta\beta} \rangle|$ can be translated into a limit on the mass of the lightest neutrino m_{min} , shown in Figure 2.6, where ‘‘IH’’ stands for the inverted hierarchy and ‘‘NH’’ stands for the normal hierarchy. The uncertainty of the relation between $|\langle m_{\beta\beta} \rangle|$ and m_{min} is caused by the unknown Dirac and Majorana phases in the neutrino mixing matrix U , as well as the measurement errors of neutrino mixing angles. The experimental sensitivity to $|\langle m_{\beta\beta} \rangle|$ for detectors of various scales are also indicated in the figure.

In Section 2.2.3, we discussed a left-right symmetric model (LRSM) in which the right-handed counterpart of weak interactions can also contribute to the $0\nu\beta\beta$ process. Thus the total effective Majorana mass can be written as $|\langle m_{\nu+N}^{\beta\beta} \rangle| = (|\langle m_{\nu}^{\beta\beta} \rangle|^2 + |\langle m_N^{\beta\beta} \rangle|^2)^{1/2}$ [5], where N represents the three heavy right-handed neutrinos, and ν stands for the three light left-handed neutrinos. Figure 2.7 illustrates the effective Majorana mass as a function of the lightest neutrino mass after including contributions from both left and right currents. As one can observe, there is no room for a vanishing $0\nu\beta\beta$ transition rate in the LRSM even if the total effective Majorana mass is zero. The predicted $0\nu\beta\beta$ decay rate by the LRSM is overall higher than

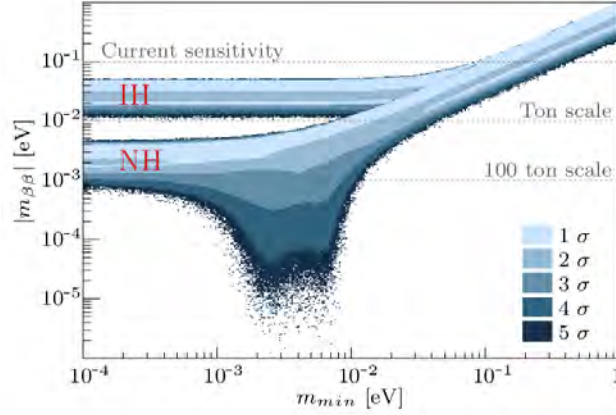


Figure 2.6: Allowed region of $m_{\beta\beta}$ versus m_{min} for the inverted hierarchy (IH) and the normal hierarchy (NH). The calculation is performed by randomly sampling from the distributions of the measured neutrino mixing angles and squared mass differences, as well as a flat distribution of the Majorana phases in the $[0, 2\pi]$ range [4].

the canonical model, and the next-generation experiments are sensitive enough [92] to rule out this LRSM if there is still no evidence for $0\nu\beta\beta$.

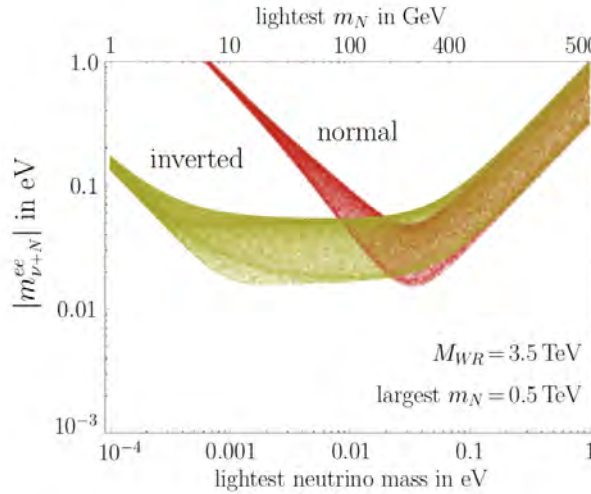


Figure 2.7: Effective Majorana mass $|m_{\nu+N}^{\beta\beta}|$ as a function of the lightest neutrino mass in the LRSM [5].

2.4 Nuclear Matrix Elements for $-\nu\beta\beta$

2.4.1 Hadronic Current Operators for $0\nu\beta\beta$

The prediction the half-life of an isotope which undergoes $0\nu\beta\beta$ decay depends on the calculation of its nuclear matrix element $M_{0\nu}$ in Eq. 2.30. In order to perform the calculation of $M_{0\nu}$, one needs to know the form of hadronic current operators in Eq. 2.29 in the first place. This can be derived from the matrix element for the transition between single nucleons. Using Lorentz covariance, we can write down the most general expression for the hadronic current operator that induces the decay of a neutron into a proton [2]:

$$\begin{aligned} \langle p, \lambda | J_L^\mu(q) | p', \lambda' \rangle = & \bar{u}(p, \lambda) [g_V(q^2)\gamma^\mu - g_A(q^2)\gamma_5\gamma^\mu - ig_M(q^2)\frac{\sigma^{\mu\nu}}{2m_N}q_\nu \\ & + g_P(q^2)\gamma_5q^\mu] \tau^+ u(p', \lambda') \end{aligned} \quad (2.31)$$

Namely, it is a sum of a vector current with the form factor g_V , an axial vector current with the form factor g_A , a term related to the anomalous nucleon magnetic moment g_M , and a pseudo-scalar term with the factor g_P . q is the momentum transfer between the nucleons with momentum p and p' , λ (λ') is the final (initial) spin of the nucleon, and τ^+ is the isospin-raising operator that turns a neutron into a proton. The conservation of the vector current gives $g_V(q^2) = g_V(0) = 1$. $g_M(q^2) \approx 4.7g_V(q^2)$, which is measured from the proton and neutron anomalous magnetic moments [93]), and $g_A(q^2) = g_A(0) \approx 1.27$ is determined from neutron β -decay measurements [94]. In addition, we have the Goldberger-Treiman relation which gives $g_P(q^2) = \frac{2m_N g_A(q^2)}{(q^2 + m_\pi^2)}$, with m_N and m_π the nucleon and pion masses. Given that the nucleon momentum before and after the decay is small, the four-component Dirac spinor $u(p)$ can be

treated non-relativistically [95]:

$$u(p, \lambda) = \begin{pmatrix} \chi_\lambda \\ \frac{\boldsymbol{\sigma} \cdot \mathbf{p}}{2m_N} \chi_\lambda \end{pmatrix} \quad (2.32)$$

where χ_λ is a two-component Pauli spinor, with $\chi_\uparrow = \begin{pmatrix} 1 \\ 0 \end{pmatrix}$, $\chi_\downarrow = \begin{pmatrix} 0 \\ 1 \end{pmatrix}$, and the components of $\boldsymbol{\sigma}$ are Pauli matrices. After some algebra, we can obtain the non-relativistic reduction of Eq. 2.31.

$$\langle p, \lambda | J_L^\mu(q) | p', \lambda' \rangle = \chi_\lambda^\dagger (M_\mu - q_\mu g_P \frac{\boldsymbol{\sigma} \cdot \mathbf{q}}{2m_N}) \tau^+ \chi_\lambda' \quad (2.33)$$

in which

$$\begin{aligned} M_\mu &= (i\mathbf{M}, M_0) \\ \mathbf{M} &= g_A \boldsymbol{\sigma} + (g_V - ig_M) i \boldsymbol{\sigma} \times \frac{\mathbf{q}}{2m_N} - g_V \frac{2\mathbf{p} - \mathbf{q}}{2m_N} \\ M_0 &= g_V - g_A \boldsymbol{\sigma} \cdot \frac{2\mathbf{p} - \mathbf{q}}{2m_N} \end{aligned} \quad (2.34)$$

Most calculations make the assumption the current operator above can also be used to compute the matrix element for a collection of interacting nucleons.

After integrating the product of Eq. 2.27 and Eq. 2.29 over x_0, y_0 and q^0 , then over \mathbf{x} and \mathbf{y} , the term relevant to the computation of $M_{0\nu}$ is $\sum_n \left(\frac{\langle f | J_L^\mu(\mathbf{q}) | n \rangle \langle n | J_L^\nu(-\mathbf{q}) | i \rangle}{|\mathbf{q}|(E_n + |\mathbf{q}| + E_{e2} - E_i)} + \frac{\langle f | J_L^\nu(\mathbf{q}) | n \rangle \langle n | J_L^\mu(-\mathbf{q}) | i \rangle}{|\mathbf{q}|(E_n + |\mathbf{q}| + E_{e1} - E_i)} \right)$, where E_n and E_i are the energy of the initial and final nuclear state, respectively. E_{e1} and E_{e2} are the energy of the two outgoing electrons, while E_n is the energy of the intermediate nuclear state. At this point, since $E_n - E_i$ is generally small compared to $|\mathbf{q}|$, we typically neglect the intermediate state dependent quantity in the denominator of equation and replace E_n with an average value \bar{E} . Thus after integrating over the momentum phase space, the nuclear matrix element $M_{0\nu}$ can be

written as [2]

$$M_{0\nu} = M_{0\nu}^{GT} - \frac{g_V^2}{g_A^2} M_{0\nu}^F + M_{0\nu}^T \quad (2.35)$$

With the non-relativistic reduction of the current operator and approximations made above, the expression for each term in Eq. 2.35 is:

$$\begin{aligned} M_{0\nu}^{GT} &= \frac{2R}{\pi g_A^2} \int_0^\infty |\mathbf{q}| d|\mathbf{q}| \langle f | \sum_{a,b} \frac{j_0(|\mathbf{q}|r_{ab}) h_{GT}(|\mathbf{q}|) \boldsymbol{\sigma}_a \cdot \boldsymbol{\sigma}_b}{|\mathbf{q}| + \bar{E} - (E_i + E_f)/2} \tau_a^+ \tau_b^+ | i \rangle \\ M_{0\nu}^F &= \frac{2R}{\pi g_A^2} \int_0^\infty |\mathbf{q}| d|\mathbf{q}| \langle f | \sum_{a,b} \frac{j_0(|\mathbf{q}|r_{ab}) h_F(|\mathbf{q}|)}{|\mathbf{q}| + \bar{E} - (E_i + E_f)/2} \tau_a^+ \tau_b^+ | i \rangle \\ M_{0\nu}^T &= \frac{2R}{\pi g_A^2} \int_0^\infty |\mathbf{q}| d|\mathbf{q}| \langle f | \sum_{a,b} \frac{j_2(|\mathbf{q}|r_{ab}) h_T(|\mathbf{q}|) (3\boldsymbol{\sigma} \cdot \hat{\mathbf{r}}_{ab} \boldsymbol{\sigma} \cdot \hat{\mathbf{r}}_{ab} - \boldsymbol{\sigma}_a \cdot \boldsymbol{\sigma}_b)}{|\mathbf{q}| + \bar{E} - (E_i + E_f)/2} \tau_a^+ \tau_b^+ | i \rangle \end{aligned} \quad (2.36)$$

where the expressions for h_{GT} , h_F and h_T can be found in Ref. [2]. In Eq. 2.36, j_0 and j_2 are spherical Bessel functions, and $\mathbf{r}_{ab} = \mathbf{x}_a - \mathbf{x}_b$ is the inter-nucleon position vector between the a^{th} and b^{th} nucleon. R is added to the equation to make the matrix element dimensionless.

2.4.2 Principles of Different Nuclear Structure Approaches

The calculation of Eq. 2.36 varies among different nuclear structure approaches. Figure 2.8 shows the $M_{0\nu}$ computed using different nuclear models for a variety of $0\nu\beta\beta$ candidate nuclei. Below we discuss briefly the main features of three approaches used for calculating nuclear matrix elements – the nuclear shell model, the quasiparticle random phase approximation (QRPA), and the energy-density functional (EDF) theory.

The nuclear shell model is a well-established model that has been successful in explaining basic properties of ground-state nuclei. In the shell model, nucleons arrange themselves according to the Pauli exclusion principle into shells that orbit around a

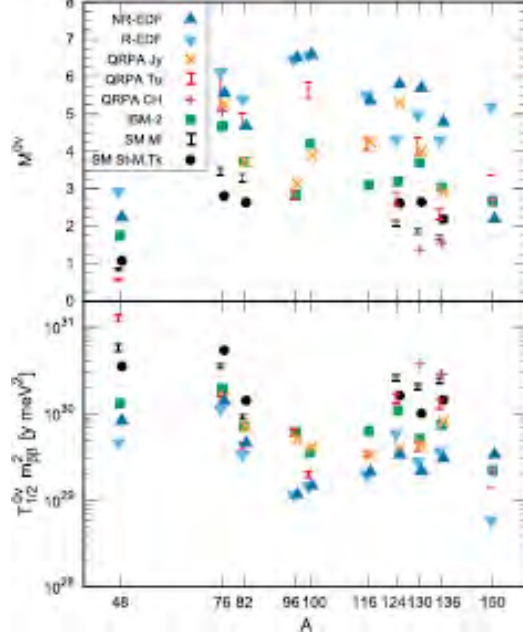


Figure 2.8: $0\nu\beta\beta$ nuclear matrix elements $M_{0\nu}$ and corresponding half-lives (scaled by $|\langle m_{\beta\beta} \rangle|^2$) calculated from different nuclear models. All the results are obtained with unquenched axial coupling constant g_A [2].

central potential. In general, a nuclear state can be described by a Slater determinant, which is a multi-fermionic wave function that satisfies anti-symmetry requirements. For an n -body system with coordinates $\mathbf{r}_1 \dots \mathbf{r}_n$, Slater determinants are written as

$$\psi(\mathbf{r}_1 \dots \mathbf{r}_n) = \begin{vmatrix} \phi_i(\mathbf{r}_1) & \phi_j(\mathbf{r}_1) & \dots & \phi_l(\mathbf{r}_1) \\ \phi_i(\mathbf{r}_2) & \phi_j(\mathbf{r}_2) & \dots & \phi_l(\mathbf{r}_2) \\ \vdots & \vdots & \vdots & \vdots \\ \phi_i(\mathbf{r}_n) & \phi_j(\mathbf{r}_n) & \dots & \phi_l(\mathbf{r}_n) \end{vmatrix} \quad (2.37)$$

where ϕ 's are orthogonal wave functions of the individual particles. They make a convenient basis for the diagonalization of the inter-nucleon Hamiltonian H , and the Slater determinant with the lowest expectation value $\langle H \rangle$ is called the Hartree-Fock ground state. The characteristic feature of the shell model is that only “active” (valence) nucleons near the Fermi level are relevant to low-energy nuclear properties. Therefore, we can write down Slater determinants using a limited set of single-particle

states instead of solving the wave equation in the full Hilbert space. However, this approach requires an exact diagonalization of the effective nuclear interaction Hamiltonian, and due to the limited computational power, often restricts the shell model's range to a single harmonic oscillator shell in $0\nu\beta\beta$ calculations. This would lead to omission of certain pairing correlations, such as the one induced by the operator $\sigma \cdot \sigma \tau^+ \tau^+$ in Eq. 2.36 that may strongly connect nucleons from different shells. The failure of the shell model to capture certain pairing correlations may have affected calculations of matrix elements for both single and double beta decay processes.

Another approach for computing the nuclear matrix element is QRPA. Unlike shell model calculations which involve many Slater determinants restricted to a few single-particle levels, QRPA involves small oscillations around a single determinant, but can involve many shells. In QRPA, one first finds a set of A (the atomic number) orbitals ϕ_i that can form the best possible Slater determinant ψ_0 and then construct another set of “nearby” non-orthogonal Slater determinants $\psi(z)$, each with A occupied orbitals of the form $\chi_i(z)$:

$$\chi_i(z) = \phi_i(z) + \sum_{j=A+1}^{N_0} z_{ij}^* \phi_j \quad (2.38)$$

where N_0 is the number of orbitals included in the calculation. Then all we need to do is to find the a superposition of the $\psi(z)$ that minimizes the energy in the limit that the z_{ij} are small, which is equivalent to solving the Schrödinger equation for a many-body system. The main advantage of the QRPA in comparison to the shell model is the number of single-particle orbits that can be included in the calculation. In most QRPA calculations, all the orbitals within one or two oscillator shells of the Fermi surface are treated explicitly.

QRPA would break down when deviations from the single Slater determinant have large amplitudes. Those large fluctuations are often associated with nuclear defor-

mation and collective motions of nucleons in many orbitals, which can't be described by a single mean field. In EDF, on the other hand, one can find a set of Slater determinants that minimize an energy functional by constraining one or more “collective operators”, e.g. the quadrupole operator $\langle Q_0 \rangle = \langle \sum_i r_i^2 Y_i^{2,0} \rangle$ (where $Y_i^{2,0}$ are spherical harmonics). We then project the states with different $\langle Q_0 \rangle$ onto ones with well defined angular momentum, particle number, etc., and use them as a basis to diagonalize the Hamiltonian.

2.4.3 Uncertainties on the Nuclear Matrix Element Calculation

As shown in Figure 2.8, for certain nuclei the matrix elements obtained from different models vary by factors of two or three. So far there has not been a solid error quantification of the $0\nu\beta\beta$ matrix element. Statistical errors arising from different choices of parameters within a given model are relatively easy to assess, but there also exist systematic uncertainties caused by the insufficiency of models, which are hard to estimate. For example, a well-known problem arises from the observation that measured single- β and $2\nu\beta\beta$ decay rates for a number of isotopes are universally smaller than theoretical predictions, which is often referred to as the “ g_A problem”. The problem can be “cured” by quenching the axial current coupling constant g_A , i.e., $g_A^{eff} \approx 0.74g_A$. If the true $0\nu\beta\beta$ decay rates, which are proportional to the fourth power of g_A , are smaller than model predictions to the same extent, current $0\nu\beta\beta$ searching experiments will be much less sensitive than expected. Whether this would happen depends on the source of g_A quenching. The average momentum transfer in $0\nu\beta\beta$ is much larger than $2\nu\beta\beta$ due to the exchange of a virtual neutrino, so if the amount of g_A quenching depends on the momentum transfer of the intermediate states, the large quenching needed to correctly predict $2\nu\beta\beta$ decay rates may not be needed for $0\nu\beta\beta$. A recent study resolved the discrepancy between the experimental

measurement and theoretical prediction for the single β -decay rate of ^{100}Sn using a first principle calculation and paved the way for systematic theoretical predictions for $0\nu\beta\beta$ decay rates [96].

In addition to the above mentioned nuclear models, recent progress in first-principle-calculations using chiral effective field theories and non-perturbative methods [97–101] provides a promising approach for computing $M_{0\nu}$ more accurately with controlled theoretical errors.

2.5 Connections of Majorana Neutrinos to Leptogenesis and Baryogenesis

One of the greatest mysteries of modern physics is why the universe appears to be populated almost entirely with matter rather than antimatter. If the universe had been matter-antimatter symmetric at temperatures of $O(1 \text{ GeV})$, it is calculated from the Standard Model physics that the number density of baryons and antibaryons relative to photons would have been on the order of $\frac{n_B}{n_\gamma} = \frac{n_{\bar{B}}}{n_\gamma} = 10^{-18}$ as a result of the annihilation process $B + \bar{B} \rightarrow 2\gamma$ [102]. However, the observed baryon and photon energy density is $\frac{n_B}{n_\gamma} \sim 10^{-10}$ [103], indicating a rather large baryonic asymmetry must have been produced in the early universe.

The physical processes that generate the primordial baryon-antibaryon and lepton-antilepton asymmetry early on in the history of the universe are referred to as baryogenesis and leptogenesis, respectively. In 1967, Andrei Sakharov proposed a set of three necessary conditions for baryogenesis [104] – baryon number B violating interactions, C and CP violation, and a departure from thermal equilibrium. There are several proposed mechanisms for the production of baryonic asymmetry. One of the first mechanisms was based on the out of equilibrium decay of a massive particle such as a super-heavy Grand Unified Theory (GUT) scale gauge or Higgs boson [105, 106].

In 1986, a mechanism is pointed out to generate the baryon asymmetry without resorting to grand unified theories [107]. In this mechanism, the decay process of a heavy Majorana neutrino that violates CP symmetry is the key to leptogenesis and baryogenesis.

In the Standard Model, baryon and lepton number are not conserved due to quantum chiral anomaly. The divergence of the baryon current $J_\mu^B = \frac{1}{3} \sum_{\text{generations}} (\bar{q}_L \gamma_\mu q_L + \bar{u}_R \gamma_\mu u_R + \bar{d}_R \gamma_\mu d_R)$ and the lepton current $J_\mu^L = \sum_{\text{generations}} (\bar{l}_L \gamma_\mu l_L + \bar{e}_R \gamma_\mu e_R)$ is

$$\partial^\mu J_\mu^B = \partial^\mu J_\mu^L = \frac{N_f}{32\pi^2} (-g^2 W_{\mu\nu}^a \tilde{W}^{a\mu\nu} + g'^2 B_{\mu\nu} \tilde{B}^{\mu\nu}) \quad (2.39)$$

where N_f the number of generations, and W_μ^a ($a = 1, 2, 3$) and B_μ are gauge fields associated with the $SU(2) \times U(1)$ group defined in Eq. 2.1. As a result, the change in baryon and lepton number can be related to the topological charge of the gauge field:

$$\Delta B = \Delta L = N_f \Delta N_{cs} \quad (2.40)$$

in which $N_{cs} = \frac{g^3}{96\pi^2} \int d^3x \epsilon_{ijk} \epsilon^{abc} W^{ai} W^{bj} W^{ck}$. In the SM, $\Delta B = \Delta L = \pm 3$ is the smallest possible jump, and it is realized through the nonperturbative ‘‘sphaleron effect’’ which cannot be represented by perturbative Feynman diagrams. In a non-abelian gauge theory there are infinite number of degenerate ground states and a sphaleron is a solution to the SM electroweak field equations that rests at the top of the barrier between different low-energy equilibria. One can make transitions between the gauge vacua with different B and L numbers at a significant rate due to thermal fluctuation when the temperature is higher than the potential barrier, i.e., the sphaleron energy. In order to relate baryon asymmetries to lepton asymmetries, we also need to take the $SU(3)$ Quantum Chromodynamics (QCD) instanton processes, etc., into account besides sphaleron processes. It can be shown that for temperatures $T \gg v$ (VEV of the Higgs field), the connection between the B , $B - L$ and L

asymmetries is [108]:

$$B = c_s(B - L), \quad L = (c_s - 1)(B - L) \quad (2.41)$$

with $c_s = (8N_f + 4)/(22N_f + 13)$.

Assume there is a right-handed Majorana neutrino in addition to the conventional leptons. The relevant Lagrangian for the lepton sector is

$$\mathcal{L} = \bar{l}_{Li} i \not{\partial} l_{Li} + \bar{e}_{Ri} i \not{\partial} e_{Ri} + f_{ij} \bar{e}_{Ri} l_{Lj} H^\dagger + h_{ij} \bar{N}_{Ri} l_{Lj} H - \frac{1}{2} M_{ij} N_{Ri} N_{Rj} + h.c. \quad (2.42)$$

where $i, j = 1, 2, 3$ are the flavor indices. l_L is the lepton doublet, e_R is the singlet, H is the Higgs field, and N_R is the heavy right-handed Majorana neutrino. e_R , l_L and N_R can be defined in such a way that f_{ij} and M_{ij} are diagonal. The Yukawa coupling matrix h_{ij} is generically complex and contains high-energy CP -violating phases, but they are difficult to be connected to the low energy CP violation in the neutrino sector [108].

Figure 2.9 shows the Feynman diagrams for the tree-level, the one-loop vertex and self-energy contributions to the heavy neutrino decay. The CP asymmetry involves the interference between them.

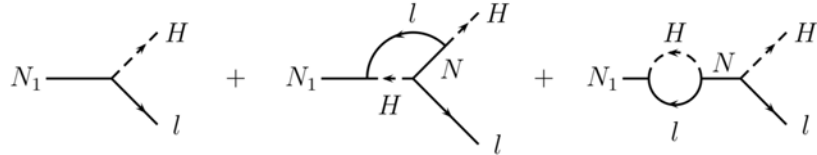


Figure 2.9: Tree level and one-loop diagrams of heavy neutrino decays that violate CP and lead to leptogenesis

The asymmetry between leptons and antileptons produced by the decay of the

right-handed neutrino N_1 (assuming $M_1 \ll M_2, M_3$) is calculated as [108]:

$$\epsilon_1 = \frac{\Gamma_{N_1 l} - \Gamma_{N_1 \bar{l}}}{\Gamma_{N_1 l} + \Gamma_{N_1 \bar{l}}} \approx \frac{3}{16\pi} \frac{1}{(hh^\dagger)_{11}} \sum_{i=2,3} \text{Im}[(hh^\dagger)_{i1}^2] \frac{M_1}{M_i} \quad (2.43)$$

where $\Gamma_{N_1 l}$ and $\Gamma_{N_1 \bar{l}}$ are the rates of N_1 decaying into leptons and antileptons, respectively. Thus the leptogenesis takes place at temperatures $T \sim M_1$, and through sphaleron processes described above Eq. 2.41, this lepton asymmetry can transform into baryon asymmetry.

Chapter 3

Overview of the EXO-200 Detector

The Enriched Xenon Observatory (EXO) Collaboration searched for neutrinoless double beta decay ($0\nu\beta\beta$) in ^{136}Xe using liquid xenon (LXe) as both the source of the decay and the detector medium [109]. The EXO-200 detector was operated at the Waste Isolation Pilot Plant (WIPP) near Carlsbad, New Mexico from 2011–2018. The detector was filled with 175 kg of enriched LXe and particles interacting in LXe can deposit a portion of their energy as scintillation and ionization, which can be detected by incorporating the LXe into a time projection chamber (TPC). EXO-200 was designed to reach a sensitivity on the order of 10^{25} yrs for the half-life of neutrinoless double-beta decay ($T_{1/2}^{0\nu}$) and to serve as the prototype for a multi-ton detector with $T_{1/2}^{0\nu}$ sensitivity $\sim 10^{28}$ yrs [110]. This chapter describes the basic construction of the EXO-200 detector system that enabled the experiment to achieve its physics goal.

3.1 The EXO-200 Time Projection Chamber

Time projection chambers (TPC) are a type of particle detector using a sensitive volume of gas or liquid to perform position and energy reconstructions of particle interactions, and are widely used in neutrino and dark matter search experiments.

The EXO-200 TPC was a cylindrical vessel made of low-background copper, split into two TPCs by a common cathode, each with radius ~ 18 cm and drift length ~ 20 cm. Most regions of the vessel was only 1.37 mm thick, resulting in a total copper mass of <30 kg. A schematic picture of the major components in the EXO-200 TPC is shown in Figure 3.1a. Each end cap of the vessel consisted of two crossed wire grids and an array of large area avalanche photodiodes (APDs). For each interaction, the charge was drifted parallel to the axis of the detector towards the nearest end cap under the action of a uniform electric field, and the scintillation light was collected and measured by the APD arrays. A view into the EXO-200 TPC chamber can be found in Fig 3.2. Details of the material choice as well as the charge and light detectors in the TPC are described in this section.

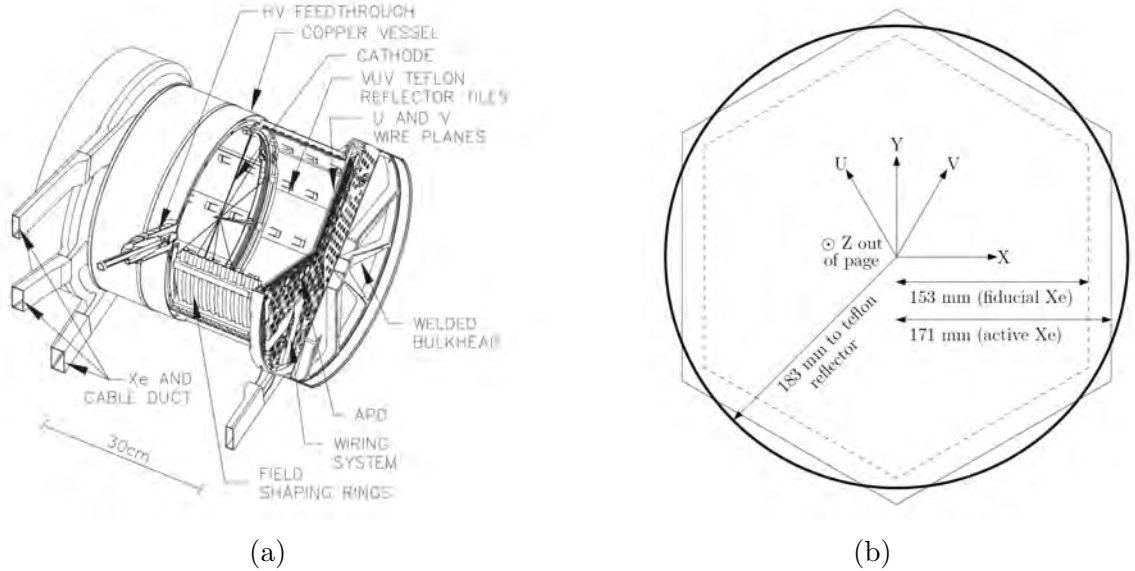


Figure 3.1: (a) Schematic drawings of the major components of the EXO-200 TPC. (b) The U-V-Z and X-Y-Z coordinate systems in the EXO-200 detector. The hexagonal active Xe region and fiducial Xe region, as well as the circular projection of the Teflon reflector are also shown [6].

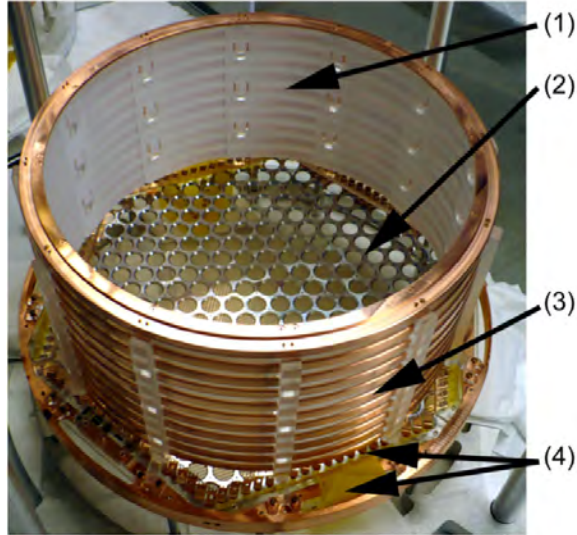


Figure 3.2: One of the two EXO-200 TPC chambers. The interior surface of the APD endplate (2) was coated with aluminum and MgF_2 . Teflon reflectors (1) are installed inside the field cage (3). Both charge and light signals are transmitted to the front-end electronics through flexible cables (4).

3.1.1 Why Liquid Xenon?

The EXO-200 TPC contains LXe enriched to 80.6% in ^{136}Xe , with a density at the operating temperature of 167 K of $3.0305 \pm 0.0077 \text{ g/cm}^3$ [111]. Of the 200 kg of enriched xenon available, 175 kg are in liquid phase, and 110 kg are in the active volume of the detector. The enriched Xe was produced from natural Xe by clean centrifuges and later stored in ten electropolished stainless steel cylinders to guarantee chemical purity. The mass spectrum measurement showed 19.1% of the atoms in the enriched xenon are of the isotope ^{134}Xe , while the concentration of other natural isotopes is negligible [7]. The choice for the $0\nu\beta\beta$ decay source fell on ^{136}Xe in the EXO-200 experiment for the following reasons:

1. ^{136}Xe , with a natural fraction of 8.9%, is the heaviest isotope in natural xenon and is relatively safe and easy to enrich. Xe is in the gas phase at standard temperature and pressure, and therefore is easy to process in centrifuges before being cryopumped into stainless steel containers.

2. There are no long-lived radioactive isotopes of Xe, and because Xe is a noble gas it is easy to be purified from all chemically active contaminants. This is essential for $0\nu\beta\beta$ experiments that have strict low-background requirements. LXe in the EXO-200 detector can also be recycled and purified into future larger-scale detectors.
3. Besides the 2615 keV γ -ray from ^{208}Tl , the Q-value of ^{136}Xe $0\nu\beta\beta$ (2457.8 keV) is larger than the energies of most γ -ray backgrounds, although the 2448 keV γ -ray background from ^{214}Bi could be detrimental to the $0\nu\beta\beta$ search and is included in the background model during physics analysis.
4. The LXe TPC makes use of topological information of each event and has very good signal/background discrimination power. While double beta decay events typically generate localized energy deposition in LXe, most background γ -rays undergo Compton scatterings and can be identified through their multi-site energy deposition in the TPC. A homogeneous, liquid phase TPC may also be the only practical option for building very large detectors [7].
5. Among liquid noble gas elements, LXe has a relatively high stopping power for external radiation due to its large atomic number. It also has a high charge and light yield, so that one can achieve a fair energy resolution after combining the charge and light signals [112].
6. In principle, the barium ion daughter ($^{136}\text{Ba}^{2+}$) produced from the double beta decay of ^{136}Xe can be tagged [113]. Although the techniques for Ba tagging are not part of the design of EXO-200, it would potentially be implemented in the future and significantly reduce background events.

3.1.2 Charge Detection Channel

The drifting charge was measured by induced signals as it first drifted through a shielding, or “V-wire” grid, and then was collected by a second wire grid, known as the “U-wire” grid, both made from photoetched phosphor bronze. The wire grids can be seen in front of the APD plane in Figure 3.3.

We denote the x and y coordinates in Fig 3.1b as those in the plane of the U- and V-wires, while the z coordinate is defined to be along the drift axis of the detector, with the cathode at $z = 0$, and the positive z direction pointing from the anode of the second TPC to that of the first TPC. In each TPC, the V-wire grids were positioned at a separation $\Delta z = 6$ mm in front of the U-wire grids. A copper support ring held acrylic beams which were formed in a hexagonal pattern. U- and V-wires were crossed at an angle of 60° and mounted on different sides of the acrylic beams.

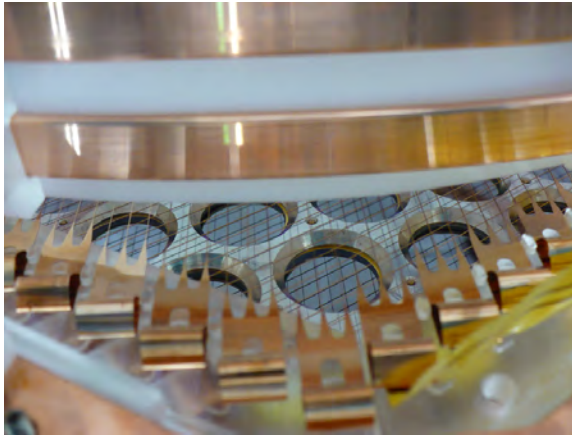


Figure 3.3: The ionization U- and V-wires are visible in front of the APDs. The spring folding scheme at one end of each wire triplet is shown.

Each U- and V-wire grid was segmented into 9 mm wide channels consisting of triplets of wires with 3 mm pitch and read out by charge sensitive preamplifiers. The end of each triplet was folded to form a spring, whose tension was measured to be sufficient to ensure wire stability at the electric fields of interest [7]. The 9 mm channel spacing was determined from an optimization process which showed that too

many electronics channels would increase complexity and materials near the fiducial volume and did not necessarily provide better topological discrimination between signal and background events. This led to each U- and V-wire plane to have 38 read out channels in total. An individual wire had a roughly square cross section with width of $127\pm 40\ \mu\text{m}$, which enabled each wire grid to have an optical transparency of 95.8%.

The V-wire and U-wire grids were separately voltage biased. The average electric field between the U- and V-wire grids is set to be twice the drift field in the bulk of the detector, ensuring all charge to drift through the V-wire plane and be collected on the U-wire plane. Measurements performed during EXO-200 engineering runs, in which the field in the collection region was varied, confirm that this field ratio is sufficient to avoid loss of charge.

In order to drift charge signals to the wire planes efficiently, a special high voltage (HV) feedthrough and a field cage were developed for creating a uniform electric field in bulk of the TPC. As shown in Figure 3.4, a HV cable from the outside of the TPC was inserted into a copper HV delivery conduit welded to the body of the TPC, and the final section of the cable was in touch with a copper receptacle embedded in a PTFE block. A tab that penetrated the PTFE block was connected to the cathode copper ring through a platinum plated leaf spring and thus transferred the HV to the bulk LXe. During the first run of EXO-200 from Sept. 2011 to Feb. 2014 (“Phase I”) the HV system was operated at -8 kV, which resulted in an electric field of 380 V/cm in the drift region. Between May 2016 and Dec. 2018 (“Phase II”), EXO-200 took a second run of data and the system was found to operate stably after ramping up the HV to -12 kV, which corresponded to an electric field of 567 V/cm in the drift region.

The cathode was also made of phosphor bronze and was loaded with a photoetched phosphor bronze grid to provide a uniform electric field in the z-direction. The cath-

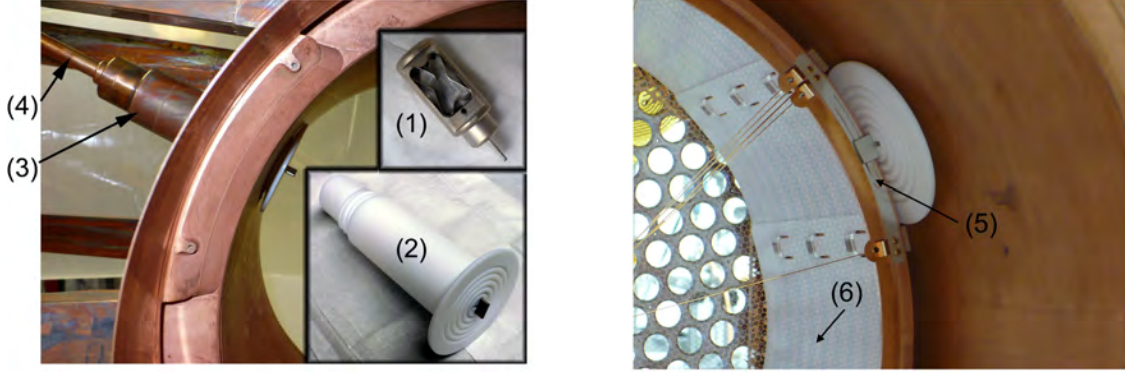


Figure 3.4: (1) A spring-loaded copper receptacle plated with platinum. (2) The PTFE block that contained the receptacle. (3) A special copper adapter connecting the TPC body to the copper conduit (4) that guided the HV cable (5) Platinum plated leaf spring connecting the HV feed to the cathode ring [7].

ode grid had 90% optical transparency and its ring frame was mounted on the last copper ring of the field cage from one of the TPC chambers. The field cage of the other TPC chamber was connected to the cathode using a mated copper ring without any grids. In each field cage the electric field was graded into ten steps from anode to cathode by a set of copper field shaping rings. The field shaping rings are 37.4 cm in outer diameter, and the pitch between them is 1.69 cm. A MAXWELL simulation [114] of this geometry predicted that electrons within a cylinder of radius 0.8 cm smaller than that of the field shaping rings could be fully collected, which resulted in a total active LXe mass of 110 kg.

3.1.3 Light Detection Channel

EXO-200 used 468 APDs in total for detection of light signals. We chose APDs over photomultiplier tubes (PMTs) as light detectors because APDs have much lower radioactivity content [115] and have higher quantum efficiency for detecting 178 nm scintillation light produced in LXe. Each circular APD had a diameter between 19.6 mm and 21.1 mm and an active diameter of 16 mm, which is shown in Figure 3.5a. The device was made by growing the p-type epitaxial layer on n-type

neutron transmutation doped silicon [116]. Both the external contact of the cathode and the ring-shaped anode were gold plated.

The APD arrays were mounted on two specially fabricated support endplates positioned $\Delta z = 6$ mm behind the U-wires. As shown in Fig 3.5b, the APDs were hexagonally packed such that the sensitive area of the endplate on which they were mounted was 48% of the total area. The interior surface of each endplate was covered by vacuum-deposited aluminum and MgF_2 to reflect VUV scintillation photons that did not strike the APD surfaces [111], and the exterior surfaces were coated with gold to improve electrical contact with the anodes of the APDs. A cylindrical Teflon reflector was positioned inside the electric field grading rings at a radius of 183 mm to improve light collection efficiency, shown as (6) in Figure 3.4.

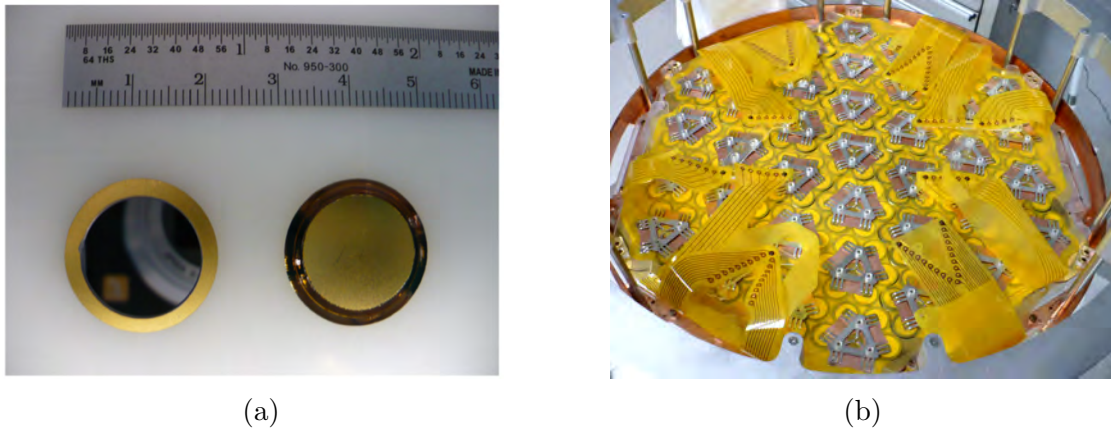


Figure 3.5: (a) Large area APDs produced by Advanced Photonix (API) [8]. The active surface of the APD is surrounded by gold-plated ring-wafer anode (left). The cathode is also gold-plated (right), and a bias high voltage is applied across the APD to amplify photoelectric signals. The ruler indicates the size in cm and inches [9]. (b) A copper endplate fully filled with APDs. APDs are ganged into a group of 5 or 7 by platinum plated phosphor bronze springs. The springs electrically connect the cathodes of APDs and copper traces on flexible cables. Acrylic washers provide electrical isolation between the springs and the anchoring screws which go through the endplate [7].

The APDs were grouped into 74 readout channels (“gangs”) in total, each of which consisted of 5 to 7 individual APDs ganged together in a single readout channel. The APDs within each gang were selected to have matched gains based on testing prior

to installation [9]. The cathodes of all 234 APDs on each endplate are electrically connected together and held at a common voltage around -1400 V. An anode trim voltage, adjustable on groups of six APD channels by up to 100 V, allows all channels to be have a nominal gain near 200 [117]. For each APD plane, one device location was installed with a PTFE diffuser 20 mm in diameter and 0.7 mm in thickness. The diffusers could be illuminated by optical fibers carrying light from an external laser source. During detector operation, the avalanche gain of each APD channel was calibrated *in-situ* using a pulsed 405 nm laser beam that entered the TPC through the diffusers.

Although neighboring APDs within each gang were chosen to have similar gain characteristics, there might still exist gain non-uniformity within an APD channel. Moreover, slight time variations in the gains of an individual APD were possible due to changes in temperature and other systematic effects. While the overall gain was calibrated for each gang as a function of time with the laser calibration mentioned above, gain non-uniformity within the gang could not be calibrated and could lead to additional variation in the light response. This non-uniformity will be studied in detail in Appendix A, and is found to not significantly impact the resolution for events in the detector.

3.2 Cryogenic System in EXO-200

The EXO-200 installation at WIPP is shown in Fig 3.6. The TPC was immersed in 50 cm thick of radio-pure HFE-7000 cryofluid (with chemical formula $\text{CF}_3\text{CF}_2\text{CF}_2\text{OCH}_3$) [118], housed in a double-walled vacuum-insulated cryostat made from the same low-background copper used for the TPC vessel. The cryofluid maintained the low temperature of the TPC and served as a layer of gamma background shielding. Two separate fridges were used during the detector operation. One fridge fed directly into the cryostat and

cooled the HFE via heat exchangers on inner wall of the cryostat, while the other cooled the condenser which liquefied the xenon gas before xenon entered the cryostat. There were two back-up fridges on the side in case of any malfunctions occurred.

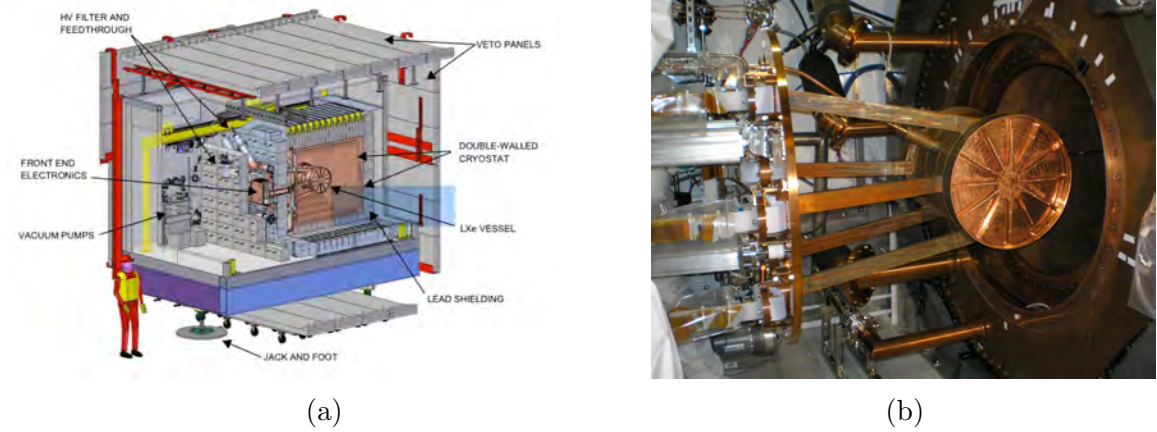


Figure 3.6: (a) Design of the EXO-200 installation at WIPP. (b) The TPC vessel being inserted into the cryostat.

The outer cryostat was surrounded by 25 cm thick lead walls, which served as another layer of external background shielding. The cryostat also featured a copper guide tube which penetrated the lead shield and wrapped around the TPC vessel in the cryofluid volume, as shown in Figure 3.8. During the EXO-200 run, we inserted calibration sources such as ^{228}Th , ^{226}Ra , ^{137}Cs and ^{60}Co of various intensities into the guide tube and placed them near the TPC to understand the detector's response to radiation of known energy.

3.3 Xenon Purifier

Electronegative impurities such as oxygen, nitrogen, and water vapor in LXe could absorb the ionization charge and therefore, the LXe was continuously purified during the EXO-200 operation to ensure that the charge signals could survive the drift length of the TPC. The xenon purification in EXO-200 was achieved in the gas phase using a system consisting of SAES MonoTorr heated zirconium getters [119] and a

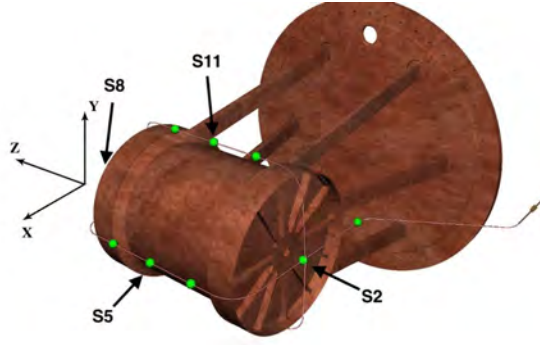


Figure 3.7

Figure 3.8: The calibration source guide tube wrapped around the LXe vessel. Major locations of the calibration source are denoted as $S2 = (0.0, 0.0, -29.5 \text{ cm})$, $S5 = (25.5 \text{ cm}, 0.0, 0.0)$, $S8 = (0.0, 0.0, 29.5 \text{ cm})$, and $S11 = (0.0, 25.5 \text{ cm}, 0.0)$.

magnetically-driven piston pump, located outside of the cryostat.

The Zirconium surface bonds with almost all non-noble gas species and has proved to be an effective absorbent [120]. Components in LXe such as O_2 , H_2O , N_2 and CO_2 bonded to the surface of the zirconium getter could diffuse into the bulk and leave the surface available for additional gettering. The efficiency of the getter improves significantly as its temperature increases due to the decrease in the diffusion time. At a temperature of several hundred degrees Celsius, the zirconium getter was able to reduce the concentration of electronegative impurities in LXe at or below the part-per-billion (ppb) level in one pass [121].

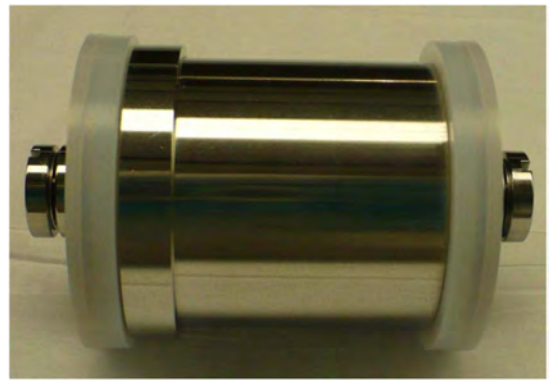


Figure 3.9: Left: The assembled xenon pump in EXO-200. Right: The piston inside the pump, made from a stainless steel canister containing a permanent cylindrical magnet [10].

The piston pump pulled xenon out of the TPC vessel, where a xenon heater was present, and at the same time pushed gaseous xenon into the xenon condenser after it was purified by the hot zirconium getters. Figure 3.9 shows two photos of the xenon pump and the piston inside. The pump itself was made from a thick-walled non-magnetic stainless-steel cylinder, through which xenon gas went across. Inside the cylinder was a piston containing a sealed cylindrical neodymium magnet. A second, ring-shaped neodymium magnet was installed over the stainless-steel cylinder and moved back and forth in the air by a drive mechanism outside of the xenon system. The piston inside the cylinder moved simultaneously with the external ring magnet and was able to pump more than 16 standard liters per minute (SLPM) of xenon gas with 750 torr differential pressure [10]. As will be shown later in Section 4.4.2, the xenon purity level, as indicated by the measurement of the “electron lifetime”, is highly correlated with the xenon flow rate.

3.4 Cosmic Ray Veto System

The entire assembly of the EXO-200 TPC and the cryostat was placed in a class 100 clean room, located at a depth of ~ 650 m in the underground salt mine at WIPP, as shown in Figure 3.10a. Measurements from the EXO-200 detector indicated that the verticle flux of cosmic ray muons at this site was $(4.01 \pm 0.04(\text{stat.})_{-0.05}^{+0.04}(\text{sys.})) \times 10^{-7} \frac{\text{Hz}}{\text{cm}^2\text{sr}}$ [122].

High-energy cosmic ray muons and spallation products (e.g. fast neutrons) generated from their interactions with the surrounding salt could enter the EXO-200 detector and produce radioactive isotopes, potentially creating background sources to the $0\nu\beta\beta$ search. Therefore, we surrounded the clean room on four of its six sides with a cosmic ray veto system made of plastic scintillator panels, as shown in Figure 3.10b. There were twenty-nine 5 cm thick plastic scintillator panels in total, which

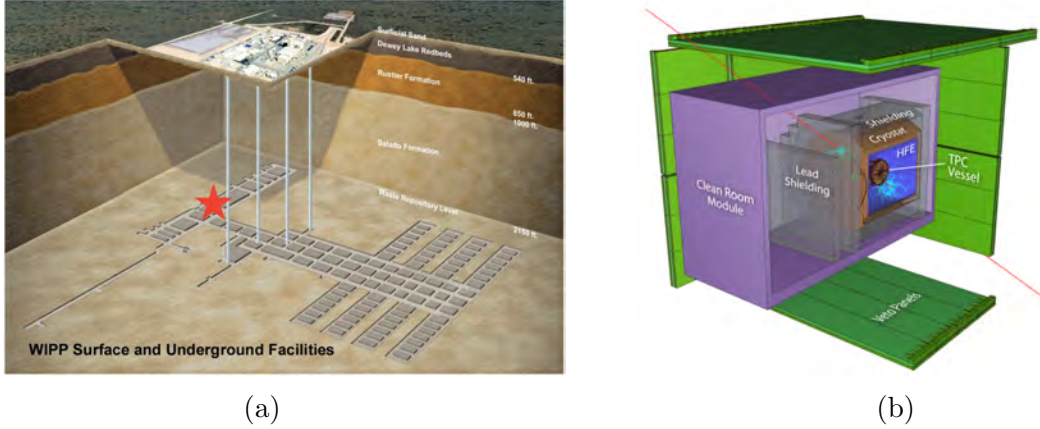


Figure 3.10: (a) Layout of the underground facility at WIPP. The location of the EXO-200 detector is marked as the red star. (b) Geant4 simulation of a cosmic muon track (red) along with its spallation products generated in the TPC. Photon (cyan) and neutron (green) tracks in the muon shower are shown [11].

were obtained from the concluded KARMEN neutrino experiment [123]. The panels were structurally supported by 4 cm of borated polyethylene, which also served as a partial thermal neutron shield for the TPC. Each scintillator panel was observed by eight PMTs which were glued with optical cement to the light guides at the end of the panel. For each cosmic ray event, the PMTs could catch the faint scintillation light produced by cosmic rays hitting the polymerized organic molecule in the plastic scintillator. Coincident light detected by any two PMTs within $1 \mu\text{s}$ would trigger the veto system and be recorded by the Trigger Electronics Module (TEM) which will be described in Section 3.5.3. The efficiency of the veto system for muon transversing the TPC was measured to be $>94\%$ [14].

The cosmic ray veto system allowed rejection of prompt backgrounds associated with muons, such as neutron capture γ s and muon bremsstrahlung. However, there also existed delayed backgrounds produced by muon-activated radionuclide in the detector which could not be vetoed. The most prominent muon-induced background came from the β decay of ^{137}Xe , generated through neutron capture on ^{136}Xe . The ^{137}Xe β decay has a half-life of 3.82 minutes and an endpoint energy of 4173 keV, which was a significant source of background to the $0\nu\beta\beta$ search in LXe. The decay

spectrum of ^{137}Xe was included in the background model for the EXO-200 analysis, which will be discussed in Section 5.3.2.

3.5 Interconnection and Electronics

3.5.1 Detector Cabling

All the U-, V-wires and APDs were connected to the front-end electronics that will be described in Section 3.5.2 by 18 μm thick copper traces on flat, 25 μm polyimide flexible cables. The polyimide flexible copper clad laminate [124] was purchased through Nippon Steel Chemical Co. [125], and proved to have low radioactivity in ^{40}K , ^{232}U and ^{238}Th from the radioassay test [115].

The cable system consisted of two parts: short flexible cables that were directly in contact with the U-, V-wire planes and the APD plane, and long cable strips which brought bias voltages to the TPC and transported signals out via six rectangular copper tubes welded between the cryostat and the two ends of the TPC vessel. The short and long flexible cables were fixed on opposite sides of specially designed acrylic blocks (Figure 3.11a) and electrically connected using phosphor bronze screws. The completed wiring behind one of the APD planes and the path of the cables used for different types of signal transmission can be found in Figure 3.11b.

Figure 3.11c shows the cable feedthroughs made from low out-gassing Master Bond epoxy [126] used for transitioning flexible cables between the LXe volume and the cryostat vacuum, as well as between the vacuum and external atmosphere.

3.5.2 Front-end Electronics

The front-end electronics (FEE) were located outside of the front lead shield wall, about 1 m away from the U-, V-wires and APDs. The principle for processing the

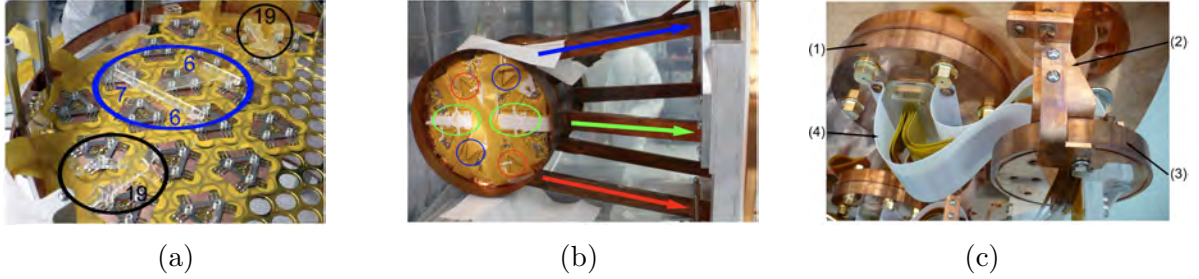


Figure 3.11: (a) Acrylic blocks used to mate short flexible cables with long ones. The “V-shaped” block (black) was used for mating cables connected to the ionization wires, and the “T-shaped” block was used for APD channels. The number of channel connections made on each block is indicated. (b) Rectangular copper tubes between the TPC vessel and the cryostat through which the long flexible cables travel to the FEE. The path of cables connected to U- and V-wires are indicated in blue and red, respectively. Green indicates the path of cables connected to APDs [7]. (c) Feedthroughs for cable transitions. (1) Flange that makes the seal from LXe to vacuum. The feedthrough is made from an acrylic cup filled with epoxy. (2) Temporary bracket holding the flange before the TPC’s installation into the cryostat. (3) Flange that makes the seal from the cryostat vacuum to atmosphere. (4) PTFE strain relief inside the cryostat.

three types of signals through the FEE system was similar. As shown in Figure 3.12, each FEE channel consisted of a charge preamplifier with an open loop gain of $\sim 10^5$ that was connected to two shaper stages, each consisting of an integrator and differentiator. The shaped pulses were then passed into a 12 bit, 1 MS/s analog-to-digital (ADC) converter before being transferred to the trigger module. All the FEE channels were packaged to 18 FEE card, with 3 cards for U-wires, V-wires, and APDs in each TPC, and housed in a shielded electronic box.

3.5.3 Trigger Electronics Module and Data Acquisition

The trigger electronics module (TEM) was responsible determining when to record data from the FEE cards. Upon receiving the data, the TEM would store them in a buffer while passing them to a trigger detection circuit. Once a trigger condition was met, the TEM would record waveform data $1024 \mu s$ before and after the trigger from all detection channels and send them to the hard disk of the data acquisition

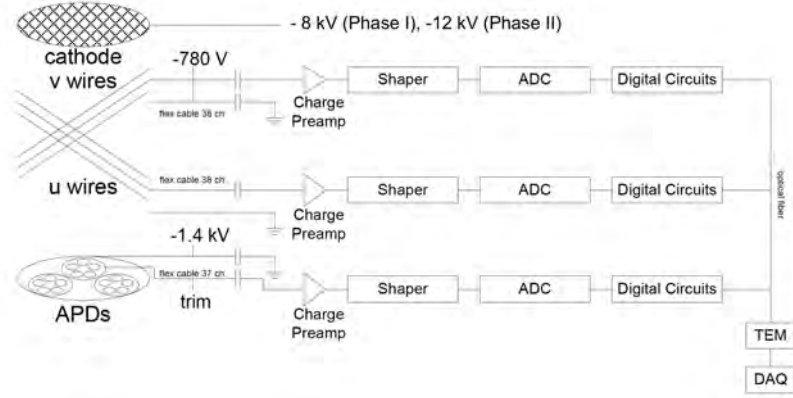


Figure 3.12: Schematic readout electronics systems for the TPC. Bias voltages applied on the V-, U-wires, APDs and the cathode are indicated in the figure.

(DAQ) system. The choice of the ~ 2 ms window was driven by the maximum drift time of an electron in the TPC ($\sim 100 \mu\text{s}$), as well as the required efficiency for capturing common correlated backgrounds, e.g., those from the decay chain $^{214}\text{Bi} \xrightarrow{\beta} ^{214}\text{Po} \xrightarrow{\alpha} ^{210}\text{Pb}$, in which ^{214}Po has a half-life of $164 \mu\text{s}$.

Four different trigger conditions were used during physics data acquisition: first, trigger on any individual U-wire channel that detected signals ~ 100 keV; second, trigger on the individual APD channel that detected signals $\sim 3\text{-}4$ keV; third, trigger on the summed waveform over all APD channels for α events in the LXe (which typically produce ~ 300 k scintillation photons); finally, a trigger that forced TPC channels to be read out every 10 s for detector performance and “lifetime” measurements.

During low-background data taking, i.e., when no calibration source was present, the average trigger rate was measured to be ~ 0.2 Hz. During source calibration runs, on the other hand, the trigger rate was more than 35 Hz. All data acquired were written to a local RAID hard drive array and copied to disks at WIPP. Due to the limited internet bandwidth at WIPP, those disks filled with waveform data were then physically shipped to the data storage facility at SLAC National Accelerator Laboratory where they were copied once again for further data processing and analysis.

3.6 Detector Upgrade

Between Jan. and May 2016, before Phase II started, the detector underwent three upgrades [14, 127]:

1. New front-end electronic boards for APD channels were installed, which significantly reduced APD readout noise.

2. A radon suppression system using charcoal-based adsorption filters was installed to reduce ^{222}Rn , a major background for double beta decay experiments, in the air gap between the cryostat and the lead shield. It was found that the average radon level in the air gap was reduced by a factor of ~ 10 after this system was deployed.

3. The electric field in the drift region of the detector was raised from 380 V/cm to 567 V/cm, which further improved the energy resolution of the detector.

Chapter 4

EXO-200 Analysis Workflow

This chapter describes the procedure of data analysis procedures in EXO-200 from event triggering and reconstructions to Monte Carlo simulations and energy calibrations. The fitting of the experimental data to the simulated background model will be shown in the next chapter.

4.1 Event Reconstruction

The reconstruction of an event was performed following three steps:

1. Signal finding, when signals were identified on the digitized waveform traces for each readout channel;
2. Parameter estimation of signals, when the knowledge from the previous step was used to extract information about the signal such as its arrival time, amplitude, etc., which may be used for event discrimination.
3. “Clustering”, when the signals on each channel were assembled into clusters based on their position and timing information. The clustering algorithm was optimized to group signals arising from the same interaction into a single cluster, from which the total energy and position for each energy deposit in the LXe

can be determined. Events that deposit their energy only in a single cluster were known as “single-site” (SS) events, while those depositing their energy at multiple resolvable locations in the detector were called “multiple-site” (MS) events.

The following sections will describe the different techniques used in these three stages of reconstruction.

4.1.1 Signal Finding

Signals on waveform traces were not always guaranteed to arrive at a given time, hence two methods were used to find signals: applying a matched filter and waveform unshaping. The first was used to pick out the initial set of found signals; the second to further identify signals that occurred close in time.

Matched Filter

The matched filter is the optimal linear filter that can maximize the signal-to-noise ratio [128, 129] by convolving a measured waveform with the time-reversed template signal waveform. In the most general case, suppose we have a measured waveform:

$$x(t) = Ah(t) + n(t) \tag{4.1}$$

where $h(t)$ is the expected pulse shape, A is the amplitude to be estimated, and $n(t)$ is the noise component in the waveform. The best estimator for A can be determined through minimizing the χ^2 defined for the fit of the real waveform to the expected pulse shape:

$$\chi^2 = \int_{-\infty}^{\infty} \frac{|\tilde{x}(f) - A\tilde{h}(f)|}{J(f)} df \tag{4.2}$$

in which $\tilde{x}(f)$ and $\tilde{h}(f)$ are Fourier transforms of the measured waveform and the expected pulse function, i.e., $\tilde{x}(f) = \mathcal{F}[x(t)]$, $\tilde{h}(f) = \mathcal{F}[h(t)]$. The χ^2 in Eq. 4.2

is calculated in frequency domain because different frequency components are independent, whereas in the time domain noise lines that are coherent over the waveform can distort the fit. $J(f)$ is the noise power spectral density given by $J(f) = \lim_{T \rightarrow \infty} \int_{-T}^T R(t) e^{-j\omega t} dt$, where $R(t)$ is the autocorrelation function of the noise waveform $R(t) = \langle n(\tau)n(\tau+t) \rangle = \lim_{T \rightarrow \infty} \frac{1}{2T} \int_{-T}^T n(\tau)n(\tau+t) dt$. Thus by requiring the derivative of Eq. 4.2 with respect to A to be zero, we can find the best estimator for the signal pulse \hat{A} in the measured waveform $\hat{A} = \frac{\int_{-\infty}^{\infty} \frac{\tilde{h}^*(f)\tilde{x}(f)}{J(f)} df}{\int_{-\infty}^{\infty} \frac{|\tilde{h}(f)|^2}{J(f)} df}$

In the practical situation of EXO-200, the matched filter output was not divided by the noise power density spectrum for the U- or V-wires, since there were sometimes multiple signals in the same waveform and weighting by noise could negatively affect signal finding. The expected signal was generated from either a calculated impulse function (in the case of U- and V-wires) or a simple step function (in the case of the APDs) that was passed through a transfer function defined for the detection channel, resulting in the final signal model. The transfer function consisted of two integration and three differentiation stages and the shaping time of each stage is shown in table 4.1.

Channel Type	Integration Time		Differentiation Time		
APDs	$3\mu s$	$3\mu s$	$10\mu s$	$10\mu s$	$300\mu s$
U-wires	$1.5\mu s$	$1.5\mu s$	$40\mu s$	$40\mu s$	$60\mu s$
V-wires[Phase I/II]	$3/1.5\mu s$	$3/1.5\mu s$	$10/40\mu s$	$10/40\mu s$	$60/60\mu s$

Table 4.1: Shaping times for two integration and three differentiation stages for different channels.

The matched filter then took the inverse Fourier transform of the convolution between the Fourier transform of the measured channel waveform $x(t)$ and the complex conjugate of the Fourier transform of the channel transfer function $h(t)$, giving an output waveform

$$y(t) = \mathcal{F}^{-1}[\tilde{x}(f)\tilde{h}^*(f)] \quad (4.3)$$

An algorithm was then performed on the output waveforms to search for peaks that exceeded a certain threshold on each readout channel. The algorithm first calculated the mean absolute deviation (MAD) of the waveform from its baseline, removing all parts of the waveform exceeding 3σ deviation and then recalculated MAD. The threshold was defined as 5 (4) times the final MAD of the signal waveform for the ionization wire (APD) channel. Fig 4.1 shows an example of the matched filter output and the found signal.

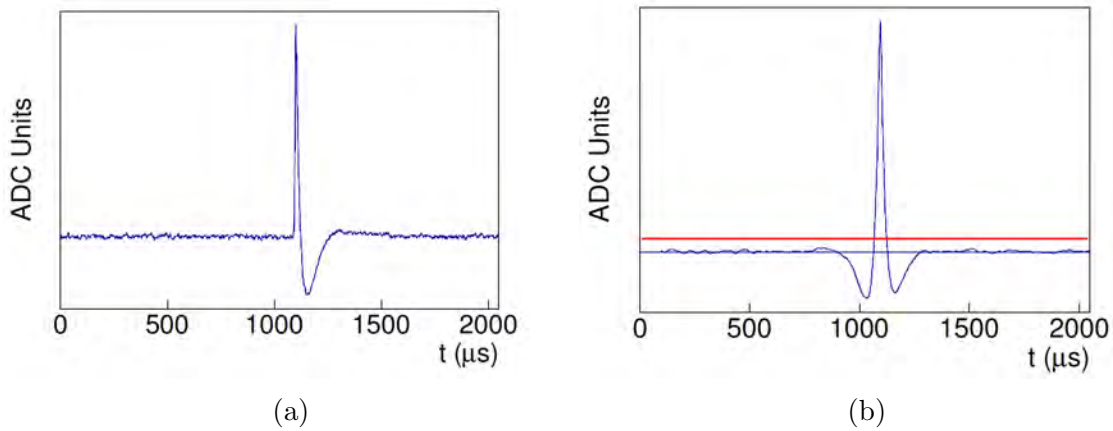
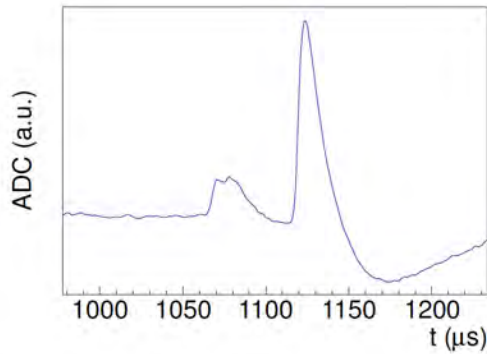


Figure 4.1: (a) Raw waveform on a U-wire channel. (b) Filtered waveform. The red line is the calculated threshold from the peak search algorithm [12].

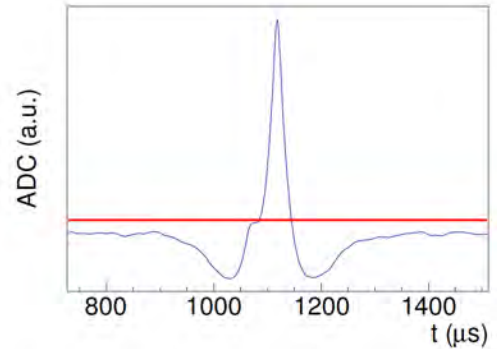
Waveform unshaping

Although the matched filter provided a good approach for determining the presence of a signal on each channel, it could sometimes miss identifying the presence of multiple signals that occurred close in time. For instance, from Figure 4.2a one could tell by eye that two signals were contained in the measured raw U-wire waveform, but one of them was obscured after the matched filter was applied, as shown in Figure 4.2b. To avoid missing any signals, the reconstruction algorithm first used the matched filter to determine if there was a signal present and then used an unshaping algorithm to find if there was more than one signal. The unshaped waveform in Figure 4.2c was then reshaped with a triangular filter, as shown in Figure 4.2d, and any deviation

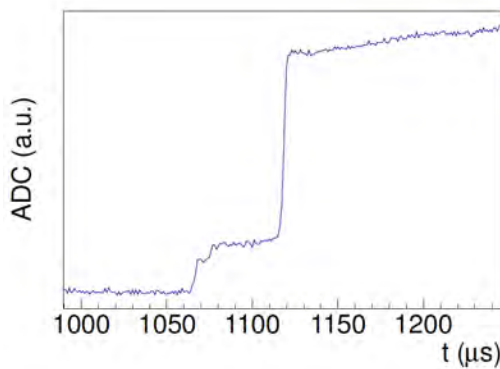
in the reshaped waveform that exceeded 5 times the root mean square (RMS) of the baseline was identified as a signal.



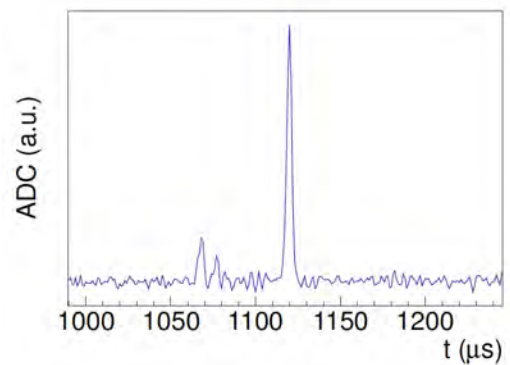
(a) Raw U-wire waveform with two signals arrived close in time.



(b) Filtered waveform from (a) (blue) with measured threshold (red).



(c) Unshaped partial waveform.



(d) Reshaped partial waveform.

Figure 4.2: Identifying multiple signals that occurred nearby one another in time through waveform unshaping. The figures are extracted from [12].

4.1.2 Parameter Estimation of Signals

Once signals on the waveform traces have been found, further algorithms were used to extract the amplitude and timing information of each signal, as well as additional waveform characteristics that could be used for event reconstruction.

Amplitude and Timing Measurement

The amplitudes and arrival time of U-, V-, and APD sum signals were measured by performing a χ^2 fit between the measured waveforms and the expected waveform templates described in 4.1.1:

$$\chi^2 = \sum_{l=0}^{l=L} \frac{[x_l - b - \sum_{i=0}^{i=N} A_i f_{SM}(s_l, t_i)]^2}{\sigma_{noise}^2} \quad (4.4)$$

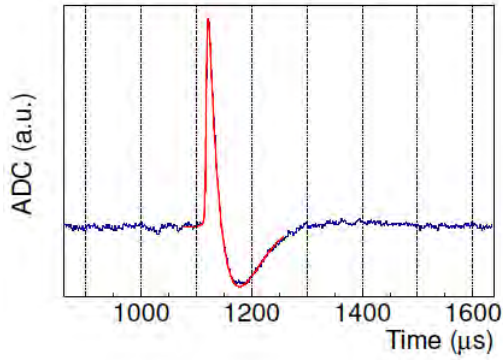
where x_l is the waveform trace at the time point l , L is the length of trace used in the fit. b is the waveform baseline, i is the index of the N signals found on the channel, and f_{SM} is the signal model. A_i and t_i are the amplitude and time of the i th signal, and are the only floating parameters in the fit. When multiple signals were found on the waveform traces, the fit windows would be determined for each signal. Examples of fits to the different types of waveforms are given in Figure 4.3.

The measured signal amplitudes, timing and the value of the minimized χ^2 function were then saved to be used the clustering algorithm described in Section 4.1.3.

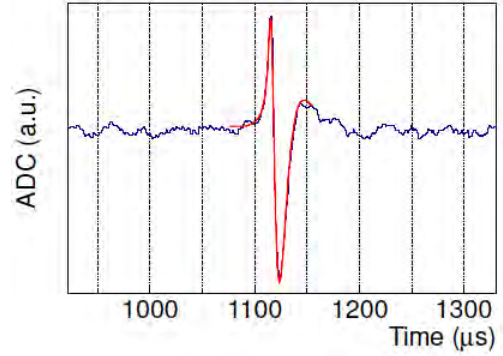
Waveform Characteristics for Collection/Induction Signal discrimination

In addition to the pulse amplitude and timing, several properties of the U-wire waveforms were measured so that induction signals on U-wires could be identified and removed from event energy reconstruction. These included:

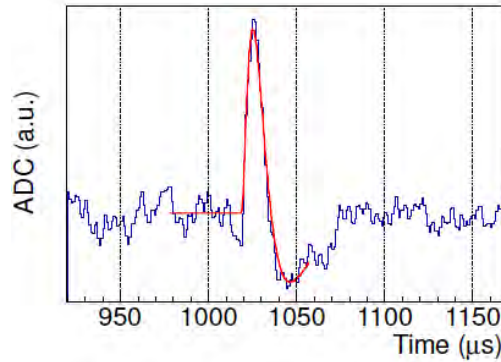
- Pulse timing. The induction signal had a very different pulse shape than the collection signal. To be more specific, the pulse rise time and maximum-to-minimum time were shorter for U-wire induction signals than collection signals.
- Pulse integral. After U-wire waveform unshaping, the integral of the induction pulse would be zero since no charge was deposited on the channel by the event,



(a) Fit to a collection signal waveform on a U-wire channel.



(b) Fit to an induction signal waveform on a V-wire channel.



(c) Fit to the waveform of an APD sum signal.

Figure 4.3: Fits to waveforms on different readout channels. Figures are extracted from [12].

while the integral of the collection pulse would be a non-zero value that was proportional to the deposited charge.

- Fit χ^2 value. Since there were many differences in pulse shape between induction and collection signals, fits to induction pulses with a collection waveform template would give much larger χ^2 value than fits using an induction waveform template. Thus the fit χ^2 could be used to discriminate between induction and collection signals.
- Nearest neighbor energy. An induction signal on the U-wire would only be visible if its neighboring collection signals were $\gtrsim 1$ MeV. Therefore, through

calculating the total energy detected by the nearest neighboring channel, we could identify whether the signal identified on each U-wire was truly an induction signal.

The above properties were used in early results to remove induction signals, but during the final analysis it was observed in Monte Carlo that there was a tail right before the 2615 keV peak in the reconstructed ^{228}Th energy spectrum, indicating that the reconstruction algorithm described above was missing energy collected for certain events. Many of those events were discovered to have a tagged U-wire induction signal with energy ~ 50 keV. Since it was assumed in the algorithm above that all U-wire signals were either completely induction or completely collection signals, some energy was missed when a signal was tagged as induction but was in fact a mixture of both collection and induction. In order to recover the missing energy, the above algorithm was improved by adding a step that fitted all induction-tagged signals with a waveform template that was a linear combination of the collection and an induction signal. An example of such a fit is shown in Figure 4.4 where it can be found that the signal was better modelled when using a template which was a mixture of induction and collection than using either template individually. Another step was added to determine whether to include the recovered energy in the total energy of the reconstructed event. This included searching for a neighboring cluster and evaluating whether the induction-tagged U-wire signal occurred close in time to the cluster, and adding an energy cut so that only the energy of real collection signals were added back.

4.1.3 Clustering Algorithm

After obtaining the time and amplitude of signals on U-, V-, and APD channels, signals with correlated characteristics are grouped into a 3D “cluster”. The clustering algorithm consisted of the following steps:

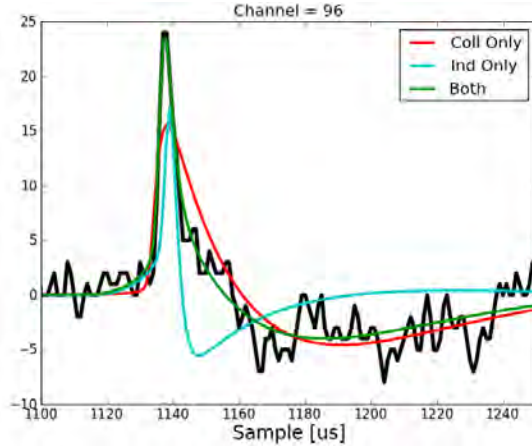


Figure 4.4: An induction-tagged U-Wire signal which contained a mixture a collection and an induction signal. It can be seen that the mixed signal was better modelled using a linear combination of an induction and a collection (green) waveform template, rather than either an induction (blue) or a collection (red) template individually. The figure is extracted from [13].

- Bundling signals of the same type together (U-wire channels with other U-wire channels, etc.) based on their timing information.
- Reconstructing 3D clusters. Grouping together U- and V-wire bundles to generate charge clusters and deciding the Z positions of the charge clusters through associating them with APD bundles (“scintillation clusters”).

Signal Bundling

For U-wire signals, the bundling process was as follows: start with the largest energy signal and add it to an empty bundle, add all signals to the bundle if they were close to this bundle in space and time (i.e., at most one channel away from at least one signal in the bundle and $\leq 3.5 \mu\text{s}$ away in time from the bundle, where the time was calculated as the energy-weighted average time of all U-wire signals in that bundle). Then repeat the steps above for the unbundled signals.

For V-wire signals, the bundling process was similar to that of U-wire signals, but also took the signal amplitudes into account. In order for a V-wire signal to be added to a bundle, it was required to be at most one channel away from at least one V-wire

signal in that bundle, and less than $4.5 \mu\text{s}$ away from the time of the largest signal in the V-wire bundle minus $2.97 \mu\text{s} \cdot \Delta$, where Δ was the absolute channel number difference between this signal and the largest V-wire signal in that bundle.

For APD signals, the bundling process was performed based on timing – APD signals found within $6 \mu\text{s}$ (determined from the integration time of APD electronics) of one another were bundled together to form a scintillation cluster. The time of the scintillation cluster was defined as the weighted average over the time and energy of the APD signals in this cluster.

3D Clusters Reconstruction

In order to reconstruct final 3D clusters, we first needed to determine the 2D position of each energy deposit through grouping U- and V-wire bundles into charge clusters. The matching of U- and V-signals was achieved by minimizing the “cost” – the negative log of the product of three probability density functions (PDFs) which modeled the relation between U- and V-bundles in terms of their amplitudes, timing and positions. The PDFs used to determine how likely a U- and a V-bundle were correlated were [12]:

- The relationship between the sum of signal amplitudes in the U- and V-bundles:

$$f_{amp}(E_U, E_V, Z) = \begin{cases} \tilde{C} & |Z| > 160 \text{ mm} \\ A e^{-0.5 \frac{\rho_E(E_U) - V_E}{\sigma_E(E_U)}} & |Z| \leq 160 \text{ mm} \end{cases} \quad (4.5)$$

where A is a normalization constant, \tilde{C} is the median cost, and $E_{U,V}$ are the amplitudes of the U- and V-bundles. In Eq. 4.5 the function ρ_E is written as:

$$\rho_E(E_U) = \begin{cases} 0 & E_U < -b_E/m_E \\ E_U m_E + b_E & E_U > -b_E/m_E \end{cases} \quad (4.6)$$

which generates an expected V-bundle amplitude once a U-bundle amplitude is given. The function σ_E has the form:

$$\sigma_E(E_U) = \begin{cases} 20.22 & E_U < 350 \text{ keV} \\ c_E E_U + d_E \sqrt{E_U} & E_U \geq 350 \text{ keV} \end{cases} \quad (4.7)$$

in which the parameters were determined in prior from the measured ^{228}Th calibration data – b_E was determined from a fit to the measured V- vs. U-bundle amplitude for events with only a single U-wire signal, and c_E , d_E were extracted from a fit to the profile of summed V- vs U-wire amplitudes for all events.

In Phase II it was discovered that using the PDF above, there existed a gap between the expected and observed V-wire amplitude for events close to the anode and the effect became worse as $|Z|$ increased. This is because the PDF above was assigned a constant \tilde{C} and ignored the Z dependence of V-bundle amplitudes for events near the anode. Therefore, a Z-dependent factor was added to the PDF later which fixed the problem and further improved the clustering efficiency [13].

- The relation between the timing of U- and V-bundles:

$$f_{time}(t_U, t_V, Z) = B e^{-0.5 \left(\frac{t_U - t_V - \rho_t(Z)}{\sigma_{time}} \right)^2} \quad (4.8)$$

where B is a normalization constant, $t_{U,V}$ are the times of the U- and V-bundles, σ_{time} is a constant and the expression for $\rho(Z)$ was determined from the measured $t_U - t_V$ as a function of the Z position for events that had only one U-wire signal in the ^{228}Th source data.

- The side-to-side diameter of the hexagon spanned by the U- and V-wires was

342 mm. The final PDF included in the cost is one that ensured the resulting (U, V) coordinate was physically allowed:

$$f_{UVpos}(U, V) = \begin{cases} C & U, V \text{ inside the hexagon} \\ C e^{-0.5(\frac{x_{perp}}{\sigma_{UV}})^2} & U, V \text{ outside the hexagon} \end{cases} \quad (4.9)$$

where C is a normalization factor, x_{perp} is the nearest distance to a hexagon side, and $\sigma_{UV} = l/2$ in which $l = 9$ mm is the width of a single wire channel,

If there were different numbers of U- and V-bundles identified, the algorithm would add “dummy” bundles so that the clustering procedure could proceed normally. Every connection containing a dummy bundle was assigned with an average cost such that the sum cost of different configurations only depended on connections between real U- and V-bundles. It is worth emphasizing that the clustering algorithm not only went over all possible combinations of the V- and U-bundles, but also tested the configuration where multiple U-bundles (V-bundles) and a single V-bundle (U-bundle) were grouped together. The final value that was minimized was the ratio between the summed cost of all connections between U- and V-bundles and the total number of connections. In this way, a configuration would not be preferred simply because it involved fewer connections.

In the end, charge clusters would be created for all connections found in the optimized configuration. If the connection were between two real U- and V- bundles, then the 2D position of the cluster could be determined. If a U-bundle (V-bundle) was connected to a dummy V-bundle (U-bundle), then a charge cluster would still be created but with incomplete 2D information. If a U-bundle (V-bundle) was connected to a combined V-bundle (U-bundle), a charge cluster would be created for each constituent of the combined bundle, e.g., if two V-bundles combined together was found to best match a U-bundle, two charge clusters with different V positions but the same U position would be created and the energy of each cluster would be a

fraction of the U-bundle energy.

Note that the product of the PDFs above is dependent on the Z-position of the energy deposit. To obtain the Z-position of a charge cluster, a corresponding scintillation was first found by picking the scintillation cluster closest in time to the charge cluster from all scintillation events that occurred between $3 \mu\text{s}$ after and $3 \mu\text{s}$ plus the maximum drift time ($\sim 116 \mu\text{s}$) before the U-bundle. Thus by combining information from U-, V-wire and APD bundles, we were able to reconstruct final 3D clusters. If no matched scintillation cluster was found, the Z position would be set as undetermined.

4.1.4 Reconstruction Efficiency

From studies of Monte Carlo and real data, the threshold for U-wire reconstruction was found to be much lower than V-wires and APDs. The reconstruction efficiency for U-wires, defined as the ratio between the number of events with a reconstructed U-wire bundle and the total number of events in MC was $\sim 100\%$ at $\lesssim 90 \text{ keV}$. Therefore, we could evaluate V-wire and APD reconstruction efficiency based on identified U-wire signals. Namely, the APD (V-wire) reconstruction efficiency was defined as the fraction of events with one reconstructed U-wire bundle that also had a reconstructed APD (V-wire) bundle. Due to the reduction to APD noise after the electronics upgrade, the reconstruction efficiency for APD signals in Phase II was significantly improved. Studies showed that in order to achieve a 100% APD signal reconstruction efficiency, the required APD energy threshold in Phase I should be 800 keV whereas in Phase II the same threshold was reduced by $\sim 30\%$ to 600 keV.

Moreover, the “2D reconstruction efficiency”, defined as the fraction of U-wire bundle that have a V-wire bundle both reconstructed and associated with the U-bundle, was studied using both MC and data. During Phase II, a slight worsening in 2D reconstruction efficiency was seen in initial analyses compared to Phase I, but was later improved by adding the Z-dependent factor in the amplitude PDF mentioned

in Section 4.1.3.

4.2 Data Quality

Between September 2011 and November 2018, EXO-200 took more than 2500 runs of low-background data (when no calibration source was deployed). The data quality of those runs needed to meet certain standards in order to be considered in the physics analysis. The low-level data quality requirements included:

- The total length of the run was typically required to be larger than 1800 s
- Average rate of the solicited triggers (forced at rate of every 10 s to help characterize noise and triggering efficiency) must be within 0.5% of the expected, optimal value of 0.1 Hz. This is because if physics triggers were being dropped due to pileup with noise triggers then solicited triggers would also be dropped in the data, and their rate would change from 0.1 Hz.
- The live-time of the run calculated from the number of solicited triggers and the length of the run calculated from the beginning and ending time from the DAQ needed to be consistent. The difference between the two quantities should be no larger than 30 s.

In addition, a number of high-level cuts were applied on certain categories of events, as abnormal rates for these events may be indicators of detector malfunctioning. These included:

- Truncated events that had a scintillation trigger within the last 1980 μs of the waveform. Runs that had a truncated event rate of more than 0.5 mHz were excluded from the analysis.
- Noise events which were identified using the noise tagger in the offline analysis software. Runs that had a noise event rate of more than 0.1 Hz were excluded.

Random coincidence between noise and real physics events was negligible in Phase I, but the coincidence rate increased in Phase II due primarily to low frequency microphonic noise, which resulted in a noticeable number of physics events to miss reconstruction. To fix this issue, we checked whether or not a noise-tagged event contained any real U-wire channel signal that had a maximum amplitude exceeding a pre-defined threshold and recovered such a physics event for reconstruction.

- Reconstructable events that had both a scintillation and charge signal associated with them and were not identified as noise, a muon, or a solicited trigger. Reconstructable events were mainly caused by physics events, and should have occurred constantly through time. The ideal rate was between 20 mHz and 70 mHz.
- Non-reconstructable events that had a charge signal but no scintillation associated it and were not identified as noise, muon or solicited triggers. Runs with a non-reconstructable event rate of greater 0.25 Hz were excluded from analysis because a high non-reconstructable rate might affect physics events.

We also cut out data taken during the periods when the underground alarm at WIPP sounded, since the alarm usually triggered large numbers of empty DAQ events. In Phase II, it was observed that the cryostat cooling pulses could trigger large and long bursts of non-reconstructable events, hence an additional cut was applied to remove those data periods based on the record of the cryostat refrigerator cooling valve state.

Given that our system was stable, the rate of different energy events should be relatively constant over time, hence we also set the following cuts on events with certain energies:

- Events with reconstructed ionization energy >0 keV should happen at a rate between 10 mHz and 35 mHz.

- Events with reconstructed ionization energy >300 keV should happen at a rate between 15 mHz and 25 mHz.
- Events with reconstructed ionization energy >1000 keV should happen at a rate between 2 mHz and 5 mHz.
- Events with reconstructed ionization energy >2000 keV should happen at a rate between 0.1 mHz and 3 mHz.

Another critical factor for determining data quality was the efficiency of the muon veto system. The performance of each veto channel was monitored bi-annually via calibrations using a ^{60}Co source placed near each panel. Since the TPC itself was also capable of reconstructing and tagging muon events in LXe, we defined the muon veto efficiency to be the fraction of TPC-tagged muon events that the system vetoed in total and performed run-by-run monitoring of individual veto panel rates and muon veto efficiency. The overall efficiency was required to be greater than 90% in order for a run to be considered as “golden” data. If one or more panels stopped working in a low-background run and they accounted for more than 5% of the averaged TPC-veto panel coincidence event rate, then the run is rejected.

Furthermore, because the electron lifetime could affect the energy resolution of the reconstructed events, i.e., a longer lifetime indicated higher possibility for electrons to reach the wires which could result in better energy resolution, the electron lifetime for a run was required to be >2 ms in order to be considered in the physics analysis.

The combined data quality cuts described above reduced the overall livetime by $\sim 15\%$. The total livetime of the detector is shown in Figure 4.5.

4.3 Monte Carlo Simulations

This section describes Monte Carlo (MC) simulations of the interactions between particles and the EXO-200 detector, which was essential for predicting the performance

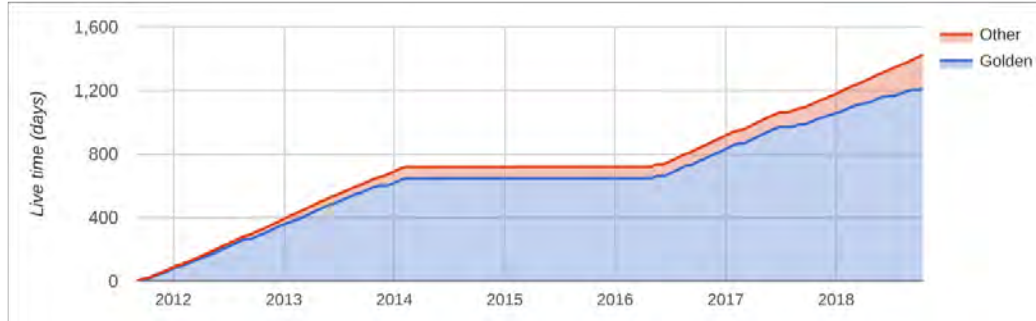


Figure 4.5: The cumulative livetime versus day for physics data. For a run to be considered golden the muon veto efficiency needs to be $>90\%$. The flat region between Phase I and Phase II is due to WIPP incidents from 2014 to 2016.

of the detector as well as extracting physics results from experimental data. The simulation started with implementing EXO-200 detector geometry in the GEANT4 package, which was able to simulate the radioactive decay of a given source. The events were generated by randomly sampling from the probability density function (PDF) describing the decay process in question. The generated PDFs for energy and spatial distribution of double beta decay signals and background sources were later used for physics analysis. The simulated events were also passed through a digitizer which could produce waveforms based on the simulated energy deposits, and the reconstruction of the MC events was identical to that of real data.

4.3.1 Simulated Geometry

The complete 3D geometry of EXO-200 was originally modelled using a computer-aided design (CAD) software. In the MC simulation, the CAD model was coded using GEANT4 shape primitives which embodied details of the internal components of the TPC as well as the surrounding HFE, cryostat and lead shield. Certain parts of some complex components were simplified, e.g., the Teflon reflector was composed of two perfect cylinders in the MC, but was made from a dozen of overlapping Teflon pieces in reality). A check was made by comparing MC simulations with γ source calibration data to ensure that the slight mass difference of materials in the MC and

CAD model only resulted in a very small difference in the attenuation of the γ rays.

4.3.2 Simulated Signals

The GEANT4 simulation first produced charge deposits in the LXe, pixelated in $\sim 100 \mu\text{m}$ voxels, for events with given energies and positions, and then passed them into a digitizer that could simulate signals on the U- and V-wires as the charge clusters drifted towards the anode. The electric field at each time step in the simulated drifting process was extracted from a 3D electric field model in COMSOL [130]. Other input MC parameters, such as the drift velocity of the cluster and the transverse diffusion coefficient which gives the spread of the charge cluster size in LXe [131], were measured from experimental data. The induced pulses on the wires by each pixelated charge cluster were calculated using the Shockley-Ramo theorem [132, 133].

The simulated signals for APD channels were generated using a parameterized light response function, or “lightmap” (see Section 4.4.3), which gave the expected amount of light hitting each APD as a function of event position and time. Effects from the anti-correlation between the light and charge signals (see Section 6.2) were not included in the MC simulation. As the integration time of the APD electronics transfer function was much longer than the APD rise-time, the unshaped APD pulses in MC were assumed to be step functions.

All simulated unshaped pulses on APD, U- and V-wires were then shaped with the corresponding channel transfer function and the final waveforms were generated by adding them with the noise waveforms sampled from real data in Phase I and Phase II separately.

4.3.3 Monte Carlo Productions

The simulated PDF components for both source calibrations and low-background data analysis are listed below:

- Active LXe (^{85}Ar , ^{214}Pb , ^{222}Rn , ^{135}Xe , ^{137}Xe , ^{88}Y , ^{110}mAg)
- Air gap between the cryostat and the lead shield (^{214}Bi)
- TPC vessel (^{60}Co , ^{137}Cs , ^{40}K , ^{54}Mn , ^{232}Th , ^{238}U , ^{88}Y , ^{65}Zn , ^{110}mAg)
- Cathode (surface ^{214}Bi , ^{232}Th)
- HFE fluid (^1H 2200, ^{40}K , ^{232}Th , ^{238}U)
- Inactive LXe (^{222}Rn , ^{137}Xe)
- Inner cryostat (^{60}Co , ^{40}K , ^{232}Th , ^{238}U)
- Outer cryostat (^{40}K , ^{232}Th , ^{238}U)
- Calibration source locations
- $0\nu\beta\beta$, $2\nu\beta\beta$ for ^{136}Xe and $0\nu\beta\beta$ for ^{134}Xe
- Neutron capture (inner cryostat $^{63,65}\text{Cu}$, outer cryostat $^{63,65}\text{Cu}$, TPC vessel $^{63,65}\text{Cu}$, LXe)

4.4 Energy Calibration and Resolution Measurement

In EXO-200 the ionization and scintillation energy of each event were measured after the response of each detection channel to a known energy deposit was well-calibrated. We then linearly combined the ionization and scintillation energy to obtain a “rotated” energy scale, which could result in an optimized energy resolution for the detector. The final calibration of the energy spectrum and the resolution measurement was performed by fitting experimental data to MC simulations.

4.4.1 Gain Calibrations

The absolute U-wire channel gains, defined as the number of electrons detected by the U-wire per ADC count recorded by the DAQ system, were measured through an “external charge-injection calibration”. In this calibration, a known number of electrons were injected into the front-end electronics for the wire grids using a precision pulser and capacitor, and the U-wire gain was calculated from a linear fit to the measured pulse amplitude in ADC counts as versus the amount of injected charge. Due to the need for an external circuit and the requirement for detaching the TPC from the front-end electronics, the external charge-injection calibration for U-wires was only performed twice, one at the start and another at the end of the EXO-200 run.

In order to monitor the stability of the gain, EXO-200 also implemented an “internal charge-injection calibration” using a circuit integrated into the front-end card that injected a certain amount of charge into each channel. Unlike the external charge-injection, the capacitance of the input calibrator in the internal charge-injection calibration was not precisely known, so the gains obtained this way were not absolute. However, the internal charge-injection calibration gave a measurement of the relative change of the wire gain versus time and was also used to monitor the shaping time for the final differentiation stage of the preamplifier.

The V-wires were not directly used in the energy measurement, but we also needed to correct their gain variations because they could affect signal clustering and position reconstructions.

The APD channel gains were monitored using the “laser calibration”, during which all APD channels were illuminated by light from a pulsed 405 nm laser beam that entered the TPC through diffusers positioned at each end of the TPC. The diffusers were illuminated by two optical fibers carrying light from an external laser source.

Since the dynamic range of the DAQ was not sufficiently high to measure the response for both the unity gain (i.e. bias below the avalanche threshold) and full gain APD biases simultaneously, a two-step calibration was used where the laser pulse length was varied. A short laser pulse was measured at full gain and at an intermediate gain and compared to a longer pulse measured at unity gain and the same intermediate gain. Both pulse lengths were short with respect to the times relevant to the front-end electronics. The ratio of the response amplitudes gives the avalanche gain, which was measured during weekly calibrations throughout EXO-200 running. However, for the double-beta decay physics analysis, the gain variations of APDs were absorbed in the lightmap correction described in Section 4.4.3, instead of being explicitly corrected on a channel-by-channel basis.

4.4.2 Electron Lifetime Measurement

Electrons in LXe can capture on electronegative impurities as they drift, which attenuates the charge signal. The number of electrons produced by an incident particle will decay exponentially over time before they reach the anode:

$$N_e(t) = N_0 e^{-\frac{t}{\tau_e}} \quad (4.10)$$

where N_0 is the original number of electrons produced in LXe, and τ_e is the electron lifetime.

To minimize this attenuation, the xenon was continuously circulated through the purifier described in Section 3.3. The electron lifetime of the LXe was monitored several times each week using ^{228}Th source calibration data. In the measurement, each TPC was divided into sixteen drift time bins. Because the charge was being attenuated, the higher drift time a bin corresponded to, the more the full-absorption peak of the ionization spectrum for events within this bin would shift downward. In addi-

tion to the full-absorption Gaussian peak, because some γ rays from ^{228}Th scattered out of the detector without depositing all their energy, the ionization spectrum also contained a Compton shoulder. Therefore, for each bin we fit the ionization spectrum near the peak region using a simple model that was a sum of a Gaussian distribution for the full-absorption events and an error function representing the Compton scattered events. The peak position measured this way as a function of the binned drift time was fitted with an the exponential decay function (derived from Eq. 4.10) to extract the electron lifetime τ_e . The larger value τ_e had, the better the LXe purity was. At the ionization energy reconstruction stage, the measured electron lifetime was used to correct the ionization energy by a factor of $e^{\frac{t}{\tau_e}}$ to compensate for the lost charge signals. In Phase I, we used slightly different purity corrections for TPC1 and TPC2, while in Phase II it was observed that using a single-valued purity correction for the entire TPC resulted in better energy resolution.

4.4.3 EXO-200 Lightmap

The amount of scintillation light collected by the APDs depended on the event location. The time variation of APD gains could also affect the reconstructed scintillation energy. As a result, EXO-200 used a “lightmap”, which characterized the expected scintillation pulse magnitudes from scintillation clusters given their time, position and energy, to correct measured APD signals.

There were two types of lightmaps used in EXO-200, the first one was the so-called “sum-up lightmap”, which described the summed response of all APDs as a function of event position and time, and the other one was a “channel-by-channel lightmap”, which returned the response of each APD channel as a function of event position and time [111, 117]. Both types of lightmaps were constructed using ^{228}Th source calibration data to determine the relative light signals collected for interactions at different locations in the detector.

The sum-up lightmap was made by dividing the detector volume into 1352 spatial voxels (13 radial bins, 8 azimuthal bins, and 13 Z bins). For each bin, the total light response from all APDs on the same plane induced by the ^{228}Th 2615 keV photopeak events was recorded. The final lightmap was normalized such that the mean response was 1. A trilinear interpolation in cylindrical polar coordinates of the lightmap was used to create a continuous correction function, $f(\vec{x})$. To correct for the measured light signal of an SS event, the sum of the two APD plane signals was multiplied by $1/f(\vec{x})$. For the correction of an MS event light signal, a correction factor deduced from taking the appropriate charge-cluster energy-weighted sum was applied instead.

The channel-by-channel lightmap was made by dividing the detector volume into 31360 spatial voxels (28 X bins, 28 Y bins, and 13 Z bins). Compared to the sum-up lightmap, its construction required more data taken from the ^{228}Th source located at various locations around the detector. For each bin, the light response from each APD channel induced by the ^{228}Th full-absorption peak events was recorded. The gain variation was also recorded by measuring the shift of the peak position versus time. The final channel-by-channel lightmap could be written as $L(\vec{x}; t) = R(\vec{x})S(t)$, where $R(\vec{x})$ and $S(t)$ are the spatial and time dependent part, respectively. An example of the channel-by-channel lightmap for one of the APD channels is shown in Figure 4.6.

The sum-up lightmap was originally used for scintillation energy correction, while the channel-by-channel lightmap was used later in a standalone “denoising algorithm” described below, which proved to reduce the effect of correlated APD noise on the scintillation energy resolution and improved the final detector resolution.

4.4.4 Denoising Algorithm

In Phase I, it was observed that APD signals contained rather large noise and the noise were correlated across different APD channels. Therefore, a denoising method

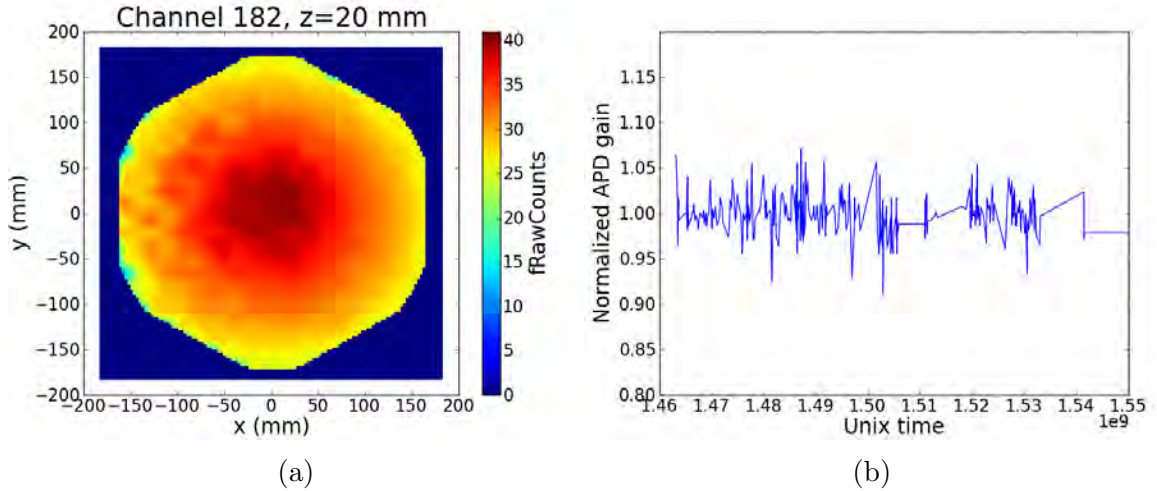


Figure 4.6: (a) Spatial part of the channel-by-channel light map used in the denoising algorithm during Phase II. The figure shows the response of one APD channel (with channel number 182) as a function of the X and Y coordinate of events with a specific Z coordinate. The values indicated by the color scale are in the unit of an uncalibrated scintillation count. (b) Relative gain variation over time for the APD channel in (a).

was developed using three techniques [117]:

1. Weight more heavily the frequency components which contained larger signal-to-noise ratio on a given APD channel.
2. Weight more heavily the channels which had larger expected pulse magnitudes.
3. Make use of correlations between noise on multiple channels to produce a better estimate of the noise component of wave-forms.

Suppose the true energy of a scintillation cluster a has energy E_a , the basic mathematical idea of denoising is to minimize the mean squared error ϵ_a^2 in the energy estimate \hat{E}_a of E_a defined by:

$$\epsilon_a^2 = \langle (\hat{E}_a - E_a)^2 \rangle \quad (4.11)$$

under the constraint of no bias:

$$\langle \hat{E}_a - E_a \rangle = 0 \quad (4.12)$$

The energy estimator \hat{E}_a is a linear combination of the real(\tilde{X}_i^R) and imaginary part(\tilde{X}_i^I) of the Fourier transform of APD waveforms.

$$\hat{E}_a = \sum_{if} A_{ia}[f] \tilde{X}_i^R[f] + B_{ia}[f] \tilde{X}_i^I[f] \quad (4.13)$$

with the APD waveforms $\tilde{X}_i[f] = \sum_a M_{ia} \tilde{Y}_{ia}[f] + \tilde{N}_i[f]$, in which \tilde{N}_i is the Fourier transform of the electronic noise, f represents frequency, and $\tilde{Y}_{ia}[f]$ is the Fourier transform of the template function for the pulse caused by scintillation cluster a on APD channel i . M_{ia} is the unknown magnitude of the pulse whose expectation value can be characterized using the lightmap: $\langle M_{ia} \rangle = L_i(\vec{x}_a, t_a) E_a$.

The denoising code contained an iterative matrix solver that found the optimal parameters $A_{ia}[f]$ and $B_{ia}[f]$ for the estimator (4.13) to minimize ϵ_a^2 . The inputs for the code included the channel-by-channel lightmap, described in Section 4.4.3 and noise correlation files that described how the correlations in APD noise evolve over time.

Applying the denoising method, the energy resolution of the detector was improved by 21% for the Phase I data. The electronics upgrade after Phase I significantly reduced the correlated noise on APDs but the detector resolution was still improved by $\sim 5\%$ in Phase II by implementing the same denoising algorithm. The measured resolution for the ^{208}Tl 2615 keV peak in calibration data before and after denoising for Phase I and Phase II are shown in Figure 4.11.

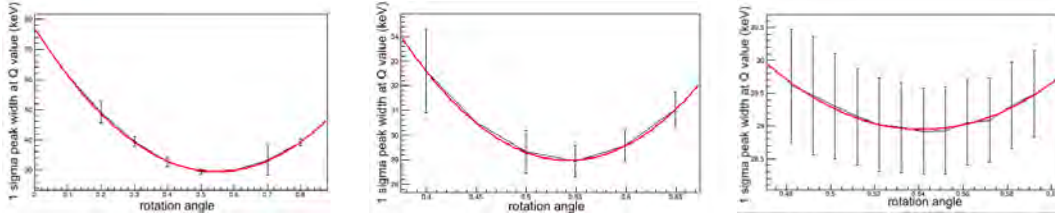


Figure 4.7: Rotated resolution at Q value versus rotation angle in the three-step scanning.

4.4.5 Energy Resolution

EXO-200 estimates the event energy by the following “rotated energy”:

$$E_{rot} = I \cdot \cos(\theta) + S \cdot \sin(\theta) \quad (4.14)$$

where I is the detected charge channel signal, S is the light channel signal and θ is the rotation angle. The data we used for deciding the optimal rotation angle is that from calibration runs with the ^{228}Th source located at S5. Due to the cancellation of recombination fluctuation in the rotated energy, the rotated resolution is improved compared to the individual charge and light channel resolution. θ is defined as the angle at which the energy resolution at Q value is minimized.

Weekly calibration

The energy scale was determined on an approximately weekly basis. The determination of the rotation angle was through a three-step scan of θ . The first step was a coarse scan, and the next two were finer scans near the determined minimum from the previous step. Figure 4.7 shows an example of the rotated resolution versus angle in the three-step scan from week 350. For each angle during the scan, an MC-based model was used to fit the full ^{228}Th energy spectrum for determining the rotated resolution. The MC-based fit model had four tunable parameters, two from the calibration model: $E = E_r \cdot p_{1E} + p_{0E}$, where E_r is the measured energy, and the other two

from the resolution model: $R(E) = \sqrt{E \cdot p_{0R}^2 + p_{1R}^2}$. Figure 4.8a and 4.8b show the optimal rotation angle as a function of time for the whole Phase I and Phase II data, respectively. Figure 4.9 and 4.10 show the calibration and resolution parameters for each week during the two Phases.

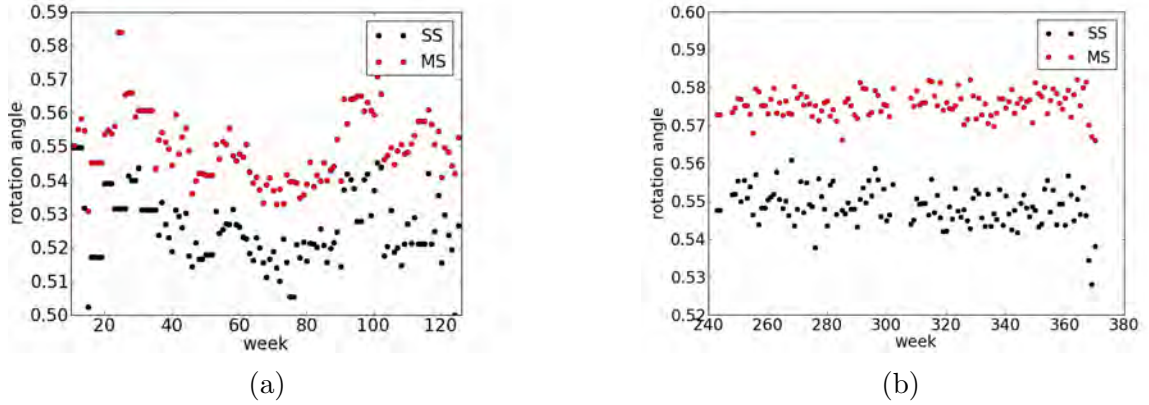


Figure 4.8: (a) Rotation angle versus week number during Phase I (b) Rotation angle versus week number during Phase II

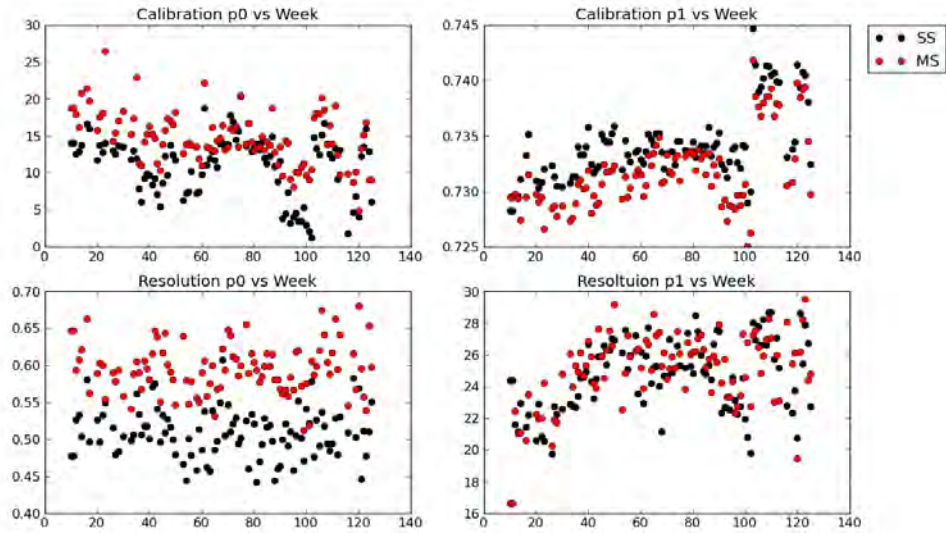


Figure 4.9: Calibration and resolution parameters versus week number during Phase I

After obtaining the resolution parameters we were able to monitor the detector's energy resolution over time. In Figure 4.11 the SS resolution at both the ^{208}Tl peak

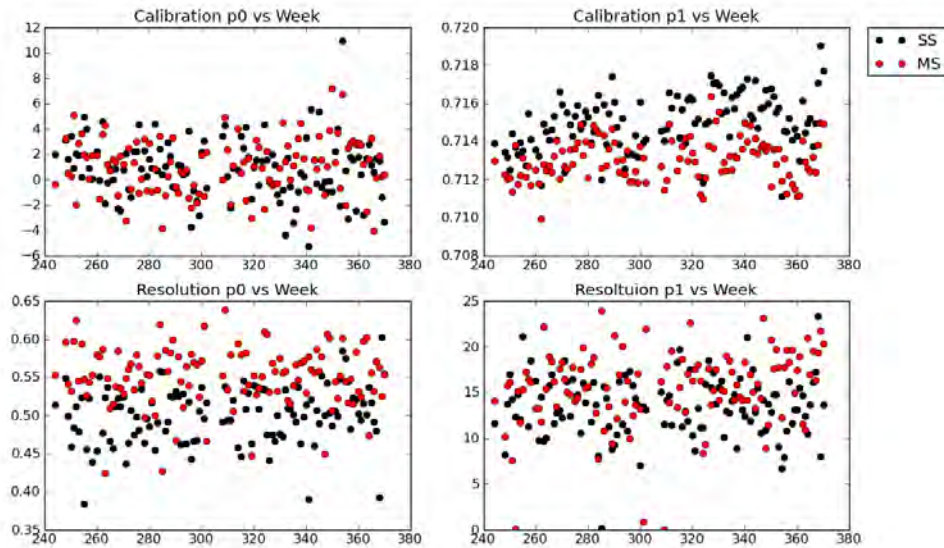


Figure 4.10: alibration and resolution parameters versus week number during Phase II

(2615 keV) and Q value (2458 keV) are shown for both Phase I and Phase II data. The green vertical line indicates the increase in bias voltage from 8 kV in Phase I to 12 kV in Phase II. The energy resolution improved significantly in Phase II compared to Phase I and its time variation also became much smaller. Accounting for the time variation, the averaged weekly resolution at the 2615 keV ^{228}Th peak for Phase I was $1.37\% \pm 0.05\%$, while for Phase II was $1.12\% \pm 0.02\%$. Figure 4.17 shows the calibrated energy spectrum of the scintillation, ionization and rotated channel made from the ^{228}Th source data taken during the first week of Phase II.

Average calibration

The average calibration for both Phase I and Phase II were carried out using three datasets made of calibration source data to account for possible position dependence of the calibration/resolution parameters. The first one was made of cathode runs only, the second was made of anode runs only, and the third was made of both anode and cathode runs. For Phase I, ^{60}Co and ^{228}Th data were used for the average calibration,

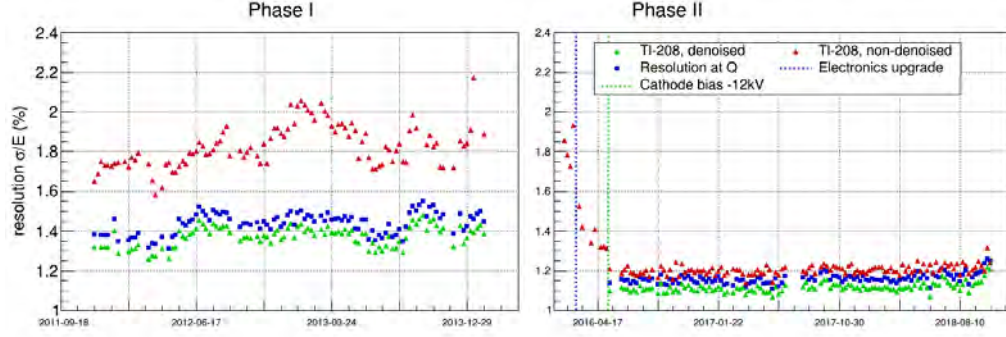


Figure 4.11: Resolution versus time for Phase I and Phase II. Phase II resolution was much improved and became more stable after electronic upgrade. For both Phases, the induction correction to charge energy contributed to a relative 4% improvement, and the denoising of light signals contributed to another relative 5% improvement.

while for Phase II ^{60}Co , ^{226}Ra and ^{228}Th were used. In the cathode-only and anode-only dataset, each source run was weighted by its livetime, and the last one added up the two with equal weights. During the average calibration, the weekly calibration parameters were first applied to the raw data. After adding up all the runs with the given weight, an additional quadratic fit was performed on the summed spectrum to get the average calibration parameters. The fitting plots of the energy spectra for the three types of average calibrations in Phase I and Phase I are shown in Figure 4.12 and 4.13. The average Phase I SS resolution at Q value obtained from each method was 1.39%(cathode data only), 1.21%(anode data only) and 1.35%(both cathode and cathode data) for Phase I.

The average Phase II SS resolution at Q value obtained from each method was 1.15%(cathode data only), 1.14%(anode data only) and 1.15%(both cathode and cathode data).

There was a small offset ($<0.5\%$) between MC and data in Fig.4.12b and Fig.4.13b caused by the fact that the weekly parameters used in the average calibration were measured by ^{228}Th at S5 only. This position-dependence could be reduced by introducing a linear correction to the physics data during the fitting, which will be discussed in Section 5.3.3.

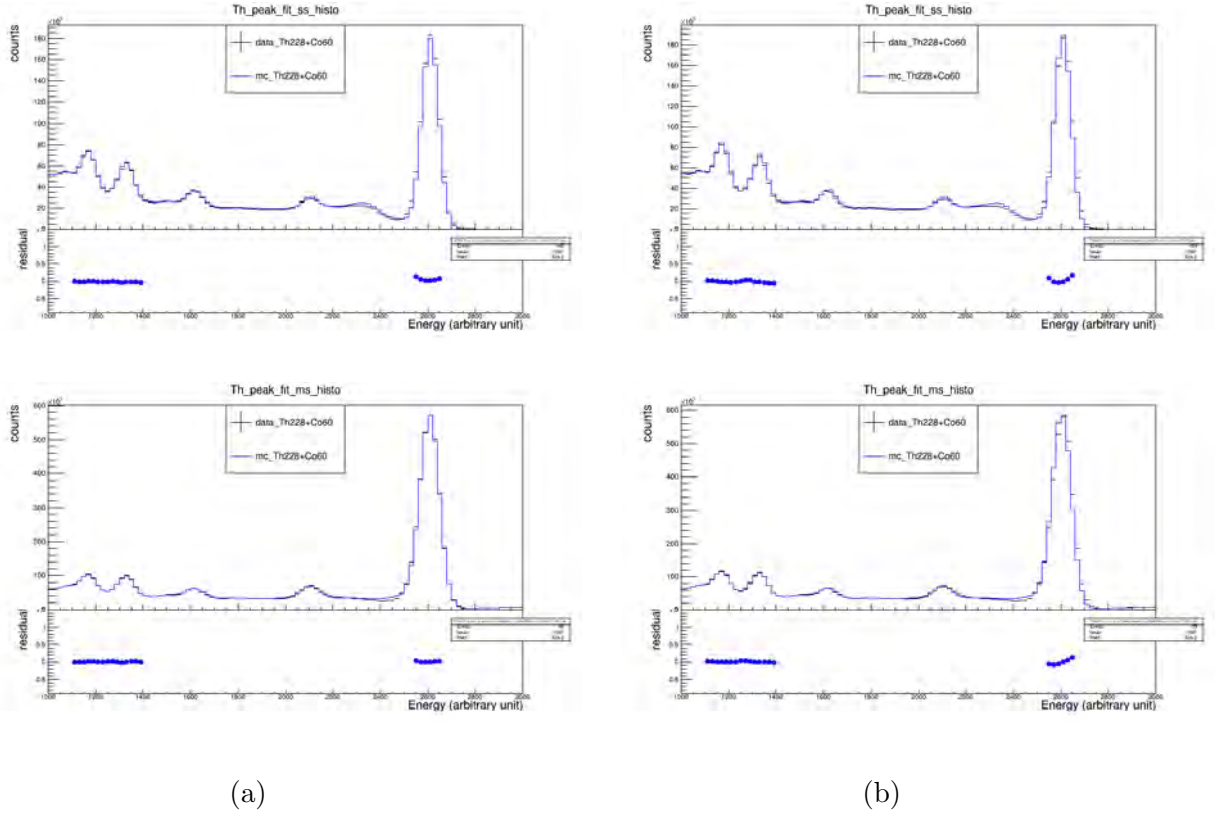


Figure 4.12: Fitting to the average energy spectra of the Phase I $^{60}\text{Co}+^{228}\text{Th}$ data from (a) cathode runs only (b) both cathode and anode runs. The first row is the spectra for SS events, and the second row is for MS events. Residuals of the fitted energy range are indicated in the bottom pad for each plot.

4.4.6 Denoising performance

The denoising algorithm was applied on both Phase I and Phase II data. The energy resolution after denoising versus week is shown in Figure 4.14. Compared to the previous analysis [109], the average denoised energy resolution for Phase I was improved– the induction correction to charge energy contributed to an overall relative 4% improvement, and the redenoising of light signals contributed to another relative 5% improvement for data taken after August 2013. For Phase II, the overall energy resolution was 6% relatively lower than the previous analysis – 4% relatively improvement due to induction correction, and another 5% relatively improvement after denoising light signals.

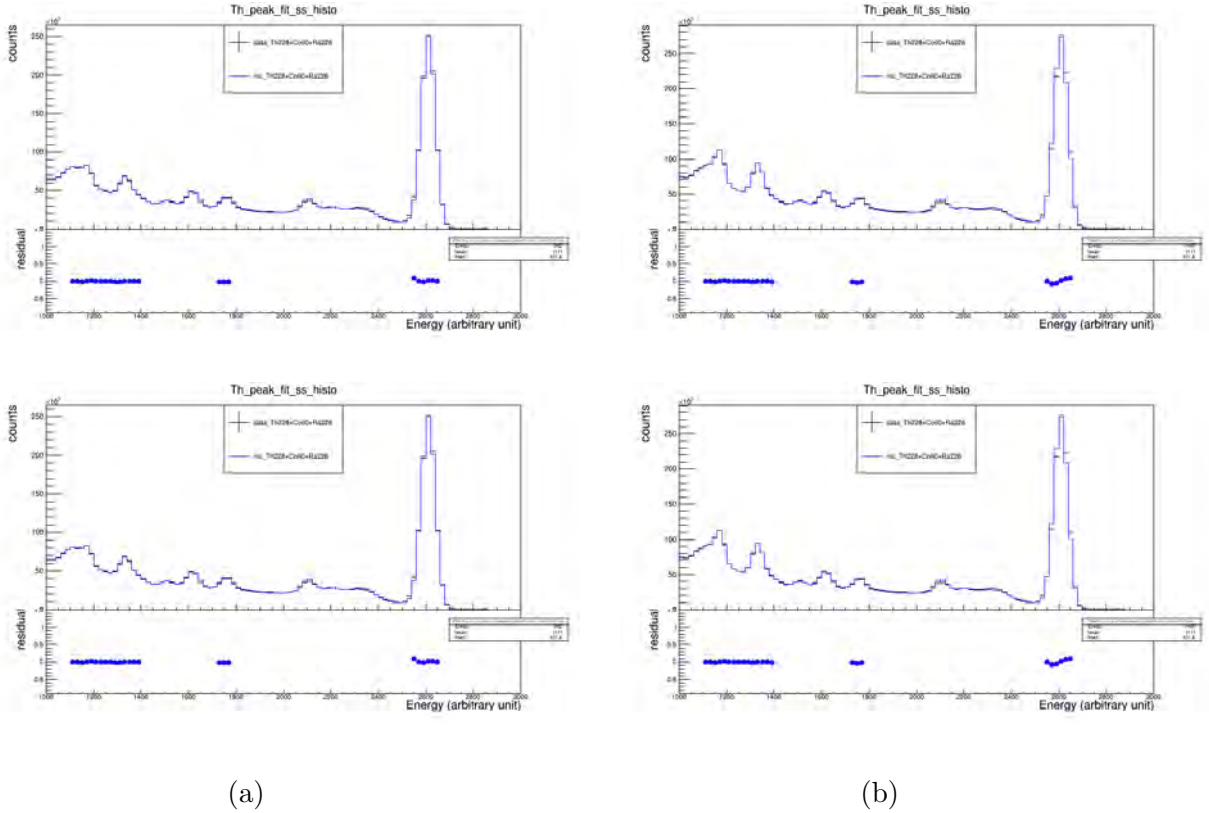


Figure 4.13: Fitting to the average energy spectra of the Phase II $^{60}\text{Co}+^{228}\text{Th}$ data from (a) cathode runs only (b) both cathode and anode runs. The first row is the spectra for SS events, and the second row is for MS events. Residuals of the fitted energy range are indicated in the bottom pad for each plot.

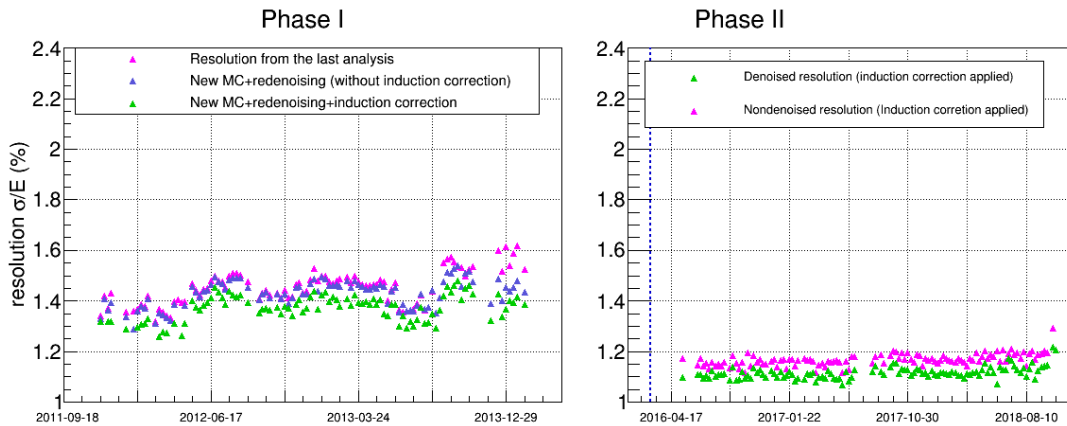


Figure 4.14: For Phase I, the induction correction to charge energy contributed to an overall relative 4% improvement, and the rednoising of light signals after August 2013 contributed to another relative 5% improvement. For Phase II, the overall energy resolution was 5% relatively lower after denoising light signals.

4.4.7 Detector Uniformity and Stability

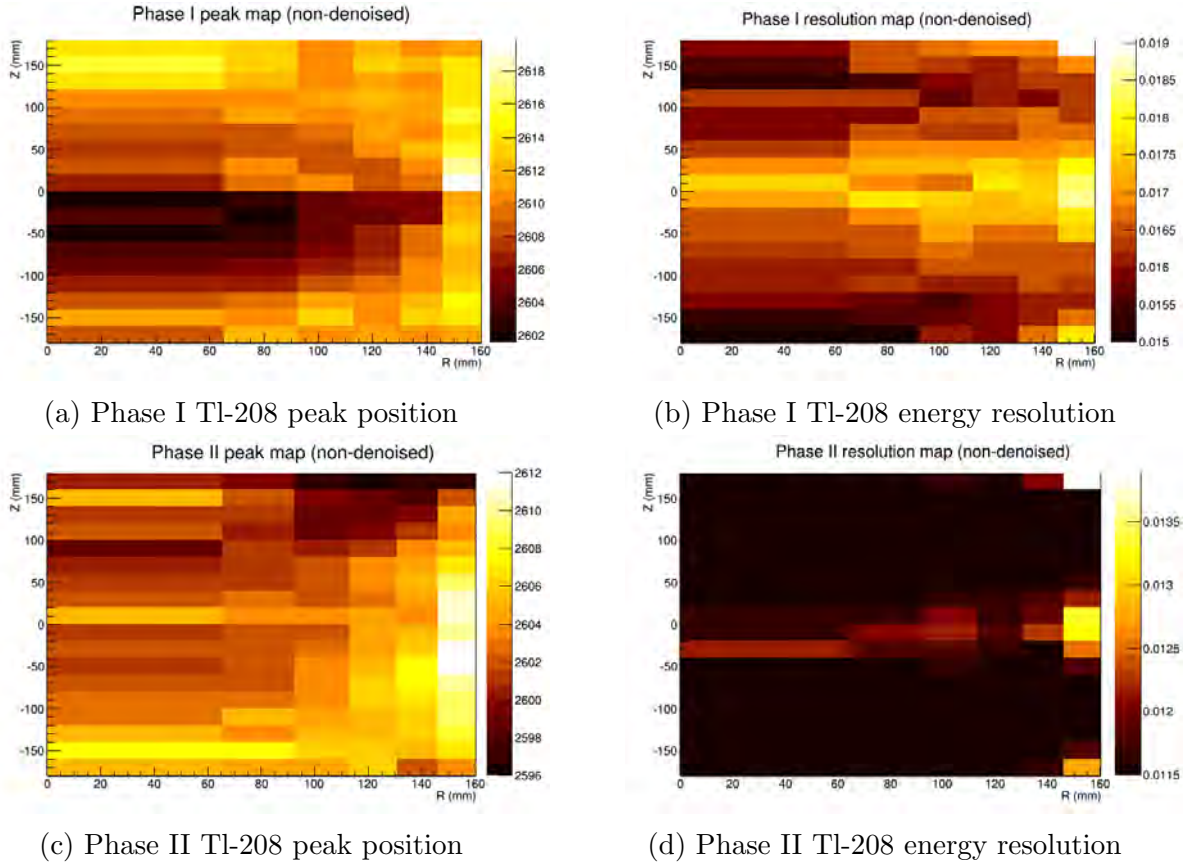


Figure 4.15: Measured peak position of the Tl-208 peak for Phase I and Phase II (a)(c), and energy resolution (b)(d) in equally sized segments of the detector volume before denoising.

It is essential to check the detector uniformity in terms of the energy scale and resolution in order to justify our calibration procedure and to better understand the energy response from different parts of the detector. For these checks, we used calibrated data from ^{228}Th at S5 position collected throughout all weeks in Phase II. The detector was split into 18 equally sized z-slices from $Z=-180$ mm to $Z=180$ mm and 6 R-slices with decreasing dR such that all segments had the same volume. The four plots in Figure 4.15 show the measured peak energy and resolution in each of the segments for Phase I and Phase II, respectively, before denoising. The largest contribution to the Z dependence of the energy peak came from segments at large R.

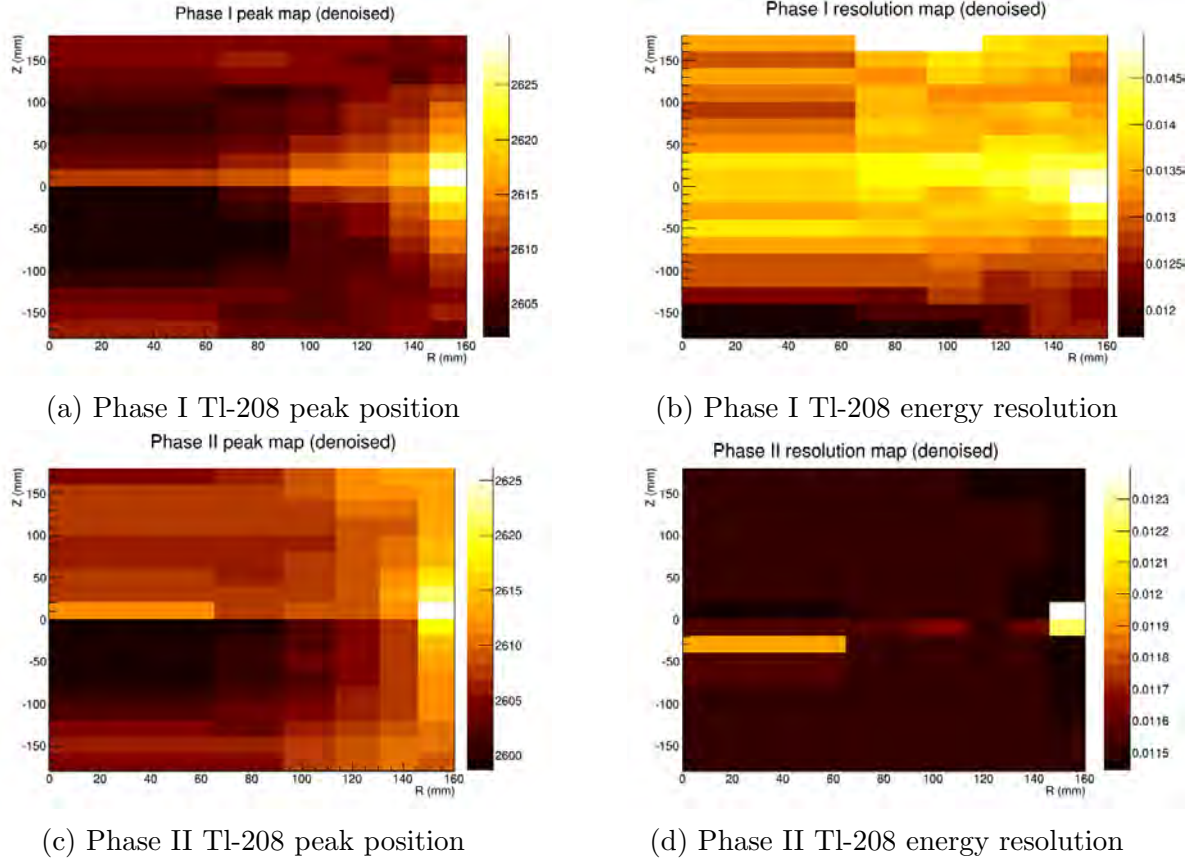


Figure 4.16: Measured peak position of the Tl-208 peak for Phase I and Phase II (a)(c), and energy resolution (b)(d) in equally sized segments of the detector volume after denoising.

The best resolution was achieved at very small R, while the worst resolution occurred near the cathode and anode at large R.

Figure 4.16 shows the measured peak energy and resolution after denoising. The resolution in the region with large R became more uniform after denoising. The spatially averaged resolution after denoising was $1.33\% \pm 0.07\%$ for Phase I and $1.15\% \pm 0.01\%$ for Phase II.

4.4.8 2D Energy Calibration

As will be discussed in Section 5.2, a diagonal cut was applied on the final low-background dataset to remove events with abnormal scintillation-to-ionization ratio.

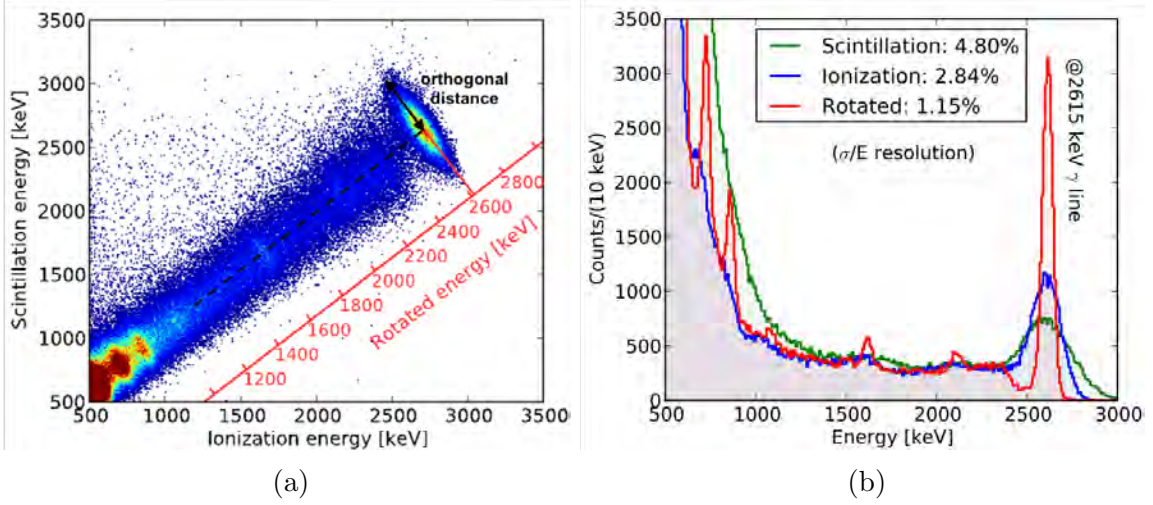


Figure 4.17: (a) The 2D energy spectrum of ^{228}Th source events. The “orthogonal distance” between the calibrated 2D energy and the rotated axis (black dashed line) is indicated in the plot. (b) The calibrated energy spectrum and the measured resolution for the scintillation, ionization and rotated channel, respectively. Both figures were made using ^{228}Th source calibration data taken during the first week of Phase II.

This required a calibration of the orthogonal distance between the calibrated 2D energy and the rotated axis, as shown in Figure 4.17. The 2D energy calibration was performed using a binned 2D Gaussian fit to the characteristic peaks of ^{137}Cs , ^{60}Co and ^{228}Th :

$$f(x, y) = A e^{\frac{-1}{2(1-\rho^2)} \left[\frac{(x-I)^2}{\sigma_I^2} + \frac{(y-S)^2}{\sigma_S^2} - \frac{2\rho(x-I)(y-S)}{\sigma_I\sigma_S} \right]} \quad (4.15)$$

where the x and y coordinates refer to the bin centers for the calibrated ionization and scintillation energy axes, A is an overall amplitude, I and S are the mean ionization and scintillation energy at the photopeak, respectively, ρ is the correlation between ionization and scintillation energy, and σ_I (σ_S) is the standard deviation of the ionization (scintillation) energy. The correlation coefficient ρ is related to the rotation angle, θ_R , defined as $\tan(2\theta_R) = -\frac{2\rho\sigma_S\sigma_I}{\sigma_S^2 - \sigma_I^2}$. The 1-sigma distance along the orthogonal direction of the rotated axis can be derived from the best fit values of σ_I , σ_S and ρ in Eq. 4.15:

$$\sigma_{ort}^2 = \cos^2\theta_{ort}\sigma_I^2 + \sin^2\theta_{ort}\sigma_S^2 + 2\rho\cos\theta_{ort}\sin\theta_{ort}\sigma_I\sigma_S \quad (4.16)$$

in which $\theta_{ort} = \theta_R + 90^\circ$.

The 2D calibration used a linear model to determine energy peak positions for both scintillation and ionization channels: $E = p_0 + p_1 E_{data}$, where E_{data} was the measured energy and E was the true energy. The parameters p_0 and p_1 were found for both channels. The resolution and correlation parameters were determined from non-linear models:

$$\sigma^2 = p_1^2 + p_0^2 E + p_2^2 E^2 \quad (4.17)$$

where the parameters were measured for both channels, and

$$\rho = p_0 e^{-p_1 E/1000} + p_2 \quad (4.18)$$

For each given event with a calibrated 2D energy (E_S, E_I) , the calibrated rotated energy was $E_R = \frac{\cos\theta_R E_I + \sin\theta_R E_S}{\cos\theta_R + \sin\theta_R}$, hence the final orthogonal distance between (E_S, E_I) and the rotated axis in units of sigma was

$$d = \frac{|(E_S, E_I)^2 - (E_R, E_R)^2|}{\cos\theta_R + \sin\theta_R} / \sigma_{ort} \quad (4.19)$$

where σ_{ort} was determined from Eq. 4.16 and the resolution model from Eq. 4.17. The value of d for each event was stored in the file for further use in the analysis.

Chapter 5

Analysis Results from the ^{136}Xe $0\nu\beta\beta$ Search

5.1 Statement of the Author's Contribution

This chapter shows the results published in Ref. [14]. The author of this thesis contributed to the final published results by performing energy calibration and resolution measurement as described in Section 4.4, which was a major component of identifying the mono-energetic peak that would be visible if a significant amount of $0\nu\beta\beta$ events occur. After event reconstruction and energy calibrations, a complete Phase I and Phase II dataset was produced. The following sections describe what data was selected to be used in the final analysis and explain how the fitting model was implemented to extract the lower limit on the $0\nu\beta\beta$ half-life of ^{136}Xe .

5.2 Data Selection

A number of cuts were placed on the calibrated dataset to remove outlier events that may not agree well with the MC background model. These included:

- A fiducial volume (FV) cut was implemented to exclude events in the regions near the detector walls or V-wires where the electric fields might not be uniform. The cut also simplified our background model as external α and β backgrounds were unlikely to penetrate into the fiducial volume. The standard fiducial volume of EXO-200 was defined by the intersection of a hexagonal region with apothem $a < 162$ mm and a cylindrical region of radius $r < 173$ mm. Along the drift axis, only events with $10 \text{ mm} < |z| < 182 \text{ mm}$ were used.
- A TPC coincidence cut which required that only events not within 0.1 s of any other event in the low-background data could be used. This cut was applied to avoid background events correlated in time. In particular this cut allowed us to remove bismuth-polonium (BiPo) coincidence events, since ^{214}Po decay following the decay from ^{214}Bi has a half-life of 0.16 ms.
- A “diagonal cut” was applied to low-background data based on the orthogonal distance between the calibrated 2D energy and the rotated axis described in Section 4.4.8. This cut enabled the rejection of α decay backgrounds and the removal of poorly reconstructed γ and β decay events with an abnormal scintillation to ionization ratio. To ensure that the diagonal cut’s impact on the search sensitivity was negligible, it was required that events within $2.5\text{-}\sigma_{ort}$ of the mean distribution should be kept, which retained $>99\%$ detection efficiency of $0\nu\beta\beta$ events [13]. Figure 5.1 shows the remaining events after this diagonal cut was implemented.
- In earlier $0\nu\beta\beta$ analyses [109, 134], a “3D cut” was applied which required that all events must have a fully reconstructed 3D position inside the fiducial volume. In the most recent analysis however, a relaxed 3D cut that required only 60% of the charge deposits to have full 3D position reconstruction was used. This “partial 3D cut” was able to recover almost all potential $0\nu\beta\beta$ MS events with

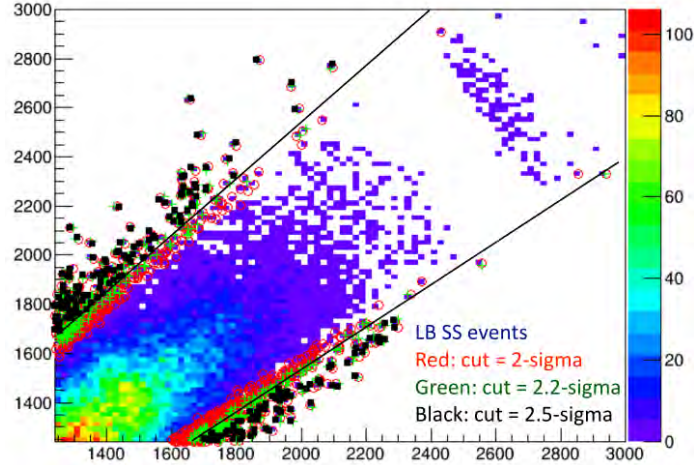


Figure 5.1: Blinded low-background data SS events and events removed by the diagonal cut for 3 selected choices.

only partial 2D reconstruction in the X-Y plane due to small, separated energy deposits from bremsstrahlung [14]. MC studies also showed that although the relaxed 3D cut might introduce $2\nu\beta\beta$ events outside of FV into the analysis and generate systematic errors to fiducial mass, their amount was estimated to be very small. As a matter of fact, the effect was sub-dominant to the $\sim 3\%$ FV uncertainty dominated by position resolution and only added 0.4% uncertainty to the original FV systematics [13].

5.3 Fit to the Low-background Data

To find out whether there was evidence for a significant excess of events in the region of interest (ROI), i.e., within energy region $Q \pm 2\sigma$ (where Q is the decay energy of ^{136}Xe), we performed a maximum likelihood fit of the expected spectra from MC simulation to the low-background experimental data.

5.3.1 Fit Model

There were three dimensions included in the fit model:

- Energy spectrum. For each source, a binned energy PDF with perfect resolution was first produced from MC simulation and then smeared by the energy resolution function measured from data. In other words, each bin of the PDF included in the fit model was smeared by a Gaussian function with width equal to the calibrated resolution at that energy.
- Standoff distance, defined as the shortest distance between the event position and the surface material of the detector excluding the cathode. Because double beta decay events were uniformly distributed in the LXe whereas γ events originated from detector materials or distant background sources, their standoff distance PDFs were very different and could be used to distinguish signals from backgrounds
- A deep neural network (DNN) discriminator. In the most recent analysis, a DNN was trained on the simulated waveforms of U-wire signals. The training dataset composed of γ background events with uniform energy distribution between 1000 keV - 3000 keV and $0\nu\beta\beta$ events with a random decay energy in the same energy range. The two types of events had equal weights in the training set and both had uniform spatial distributions in the detector. The DNN model was evaluated on a separate MC dataset where the output DNN $0\nu\beta\beta$ discriminator for each event was between 0 (background-like) and 1 (signal-like). From MC studies, it was found that there existed a correlation between the output discriminator and the true event size. As $0\nu\beta\beta$ events tended to have a smaller spatial size than γ events with similar energies, their DNN discriminator distributions differ from each other.

The final maximum likelihood fit was performed over all bins in energy, standoff distance and the DNN discriminator distributions. The quantity that was minimized

in the fit model was a negative log likelihood function:

$$-\ln L = \sum_i [(\mu_i^{SS} + \mu_i^{MS} - (k_{obs,i}^{SS} \ln \mu_i^{SS} + k_{obs,i}^{MS} \ln \mu_i^{MS}))] + G_{const} \quad (5.1)$$

where $k_{obs,i}^{SS(MS)}$ were the number of SS (MS) events observed in the i^{th} bin, μ_i^{SS} was the expected number of events from the fit model in the i^{th} bin. G_{const} were Gaussian constraints which written in the form:

$$G_{const}(\boldsymbol{\rho}, \boldsymbol{\rho}_0, \boldsymbol{\Sigma}) = 0.5(\boldsymbol{\rho} - \boldsymbol{\rho}_0)^T \boldsymbol{\Sigma}^{-1}(\boldsymbol{\rho} - \boldsymbol{\rho}_0) \quad (5.2)$$

where $\boldsymbol{\rho}$ was the vector of constrained parameters, $\boldsymbol{\rho}_0$ was the set of expected values for those parameters and $\boldsymbol{\Sigma}$ was the covariance matrix between them. The main constraints included in the fit are listed as follow:

- The single-site fractions of all PDF components were constrained using the uncertainties evaluated in Section 5.4.2;
- The overall normalization was constrained to unity using the estimated systematic errors in signal detection efficiency discussed in Section 5.4.1;
- The ^{222}Rn background was constrained to its measured activity (using the 5.5 MeV alpha peak from ^{222}Rn) within 10% of systematic uncertainty;
- The fraction of neutron-capture PDF components was constrained to 20%, based on the neutron-capture backgrounds identified by the prompt de-excitation γ cascade from the excited state of ^{137}Xe .

5.3.2 Background Model

The PDF components included in the fit are listed below [13].

1. $0\nu\beta\beta$: signal

2. LXe decays

- $2\nu\beta\beta$
- ^{137}Xe
- ^{135}Xe

3. ^{232}Th decay chain

- Near component: TPC vessel copper
- Remote component: HFE refrigerant or cryostat

4. ^{238}U decay chain and its daughter decay chains

- Near component: TPC vessel copper
- Remote component: radon in the air gap between the cryostat and the lead shield
- LXe component:
 - ^{222}Rn chain in inactive LXe
 - ^{214}Bi on the cathode surface
 - ^{214}Pb chain only

5. ^{60}Co decay

- Near component: TPC vessel copper
- Remote component: source guide tube

6. Other decays in the TPC vessel

- ^{40}K
- ^{65}Zn

7. Neutron-capture components

- ^1H in HFE
- ^{63}Cu and ^{65}Cu in the outer cryostat, inner cryostat, and TPC vessel
- ^{136}Xe de-excitation γ s

5.3.3 Energy scale parameters

While performing the maximum log likelihood fit, a possible difference between the energy scale from γ calibration sources (E_γ) and from single- or double-beta decays (E_β) was accounted for by a factor (B): $E_\beta = BE_\gamma$. The so-called “ β -scale”, B , was allowed to freely float during the fit and was found to be consistent with unity to the subpercent level in both Phase I and Phase II.

In addition, due to a small offset observed between the energy scale of calibration data taken with the source located near cathode and the one near the anode, another parameter called “ γ -scale” was introduced into the low-background data fitting. The original offset was only subpercent level (see Section 4.4.5) and wouldn’t have affected the $0\nu\beta\beta$ search, but fitting this additional γ -scale parameter in low-background data for γ -like PDFs further reduced the final residual between data and MC.

5.4 Summary of Systematic Errors

Before giving the fitting result, we discuss in this section a number of factors that contributed to the systematic errors of the $0\nu\beta\beta$ analysis.

5.4.1 Signal detection efficiency

The systematics from signal detection efficiency affected the normalization parameter in the fit. These systematic errors mainly came from the data selection cuts described in Section 5.2. In particular, the FV uncertainty was 2.8% and 2.6% for Phase I and Phase II, respectively, and was increased by another $<0.4\%$ after applying the

partial 3D cut. The diagonal cut uncertainty was conservatively estimated to be 0.9%. In addition, after unblinding the dataset, we found that one SS candidate event which was originally with energy in the ROI, was misreconstructed by the denoising algorithm. The impact of this effect on the detection efficiency in Phase II was found to be less than 1.0%. Other small contributions were estimated to be on the level of 0.9% [14].

5.4.2 Single-site Event Fractions

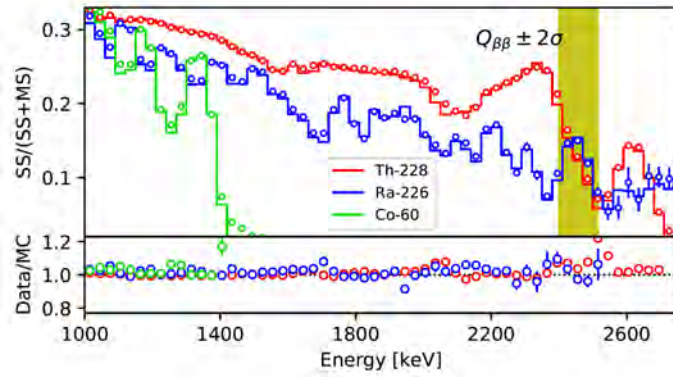
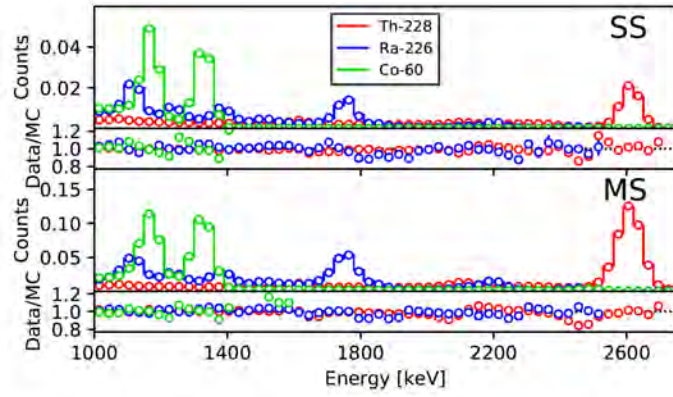


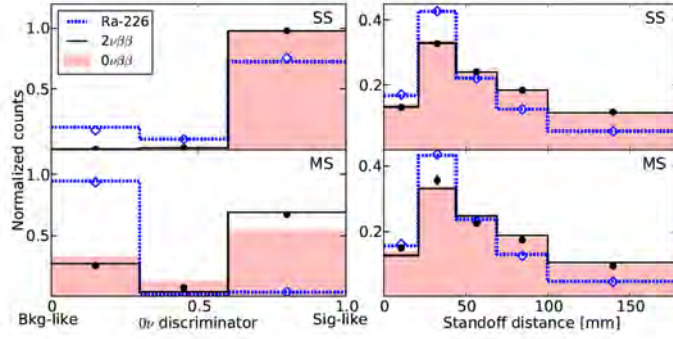
Figure 5.2: Comparison between MC (lines) and data (circles) for SS fractions in Phase II using calibration sources positioned near the cathode. The figure is extracted from [14].

The SS/MS event classification provided a major topological discriminator between signals and backgrounds. In order to estimate the systematic errors related to SS event fractions, i.e., $SS/(SS+MS)$, we compared SS fractions in source calibration data and MC. Figure 5.2 shows the agreement between SS fraction spectra in MC and data for sources placed near the cathode. After accounting for calibration sources at various positions, the systematic errors of SS fractions were measured to be 5.8% (4.6%) for Phase I (Phase II), and were included in the constraint term in Eq. 5.1 of the fit model.

5.4.3 Spectral Shape Error



(a)



(b)

Figure 5.3: (a) Comparison between measured (circles) and MC simulated (lines) energy spectral shapes for three calibration sources (^{228}Th , ^{226}Ra and ^{60}Co) positioned near the cathode. (b) Comparison between data (dots) and MC (solid/dashed lines) for the DNN $0\nu\beta\beta$ discriminator and standoff distance distributions from the ^{226}Ra calibration source and the $2\nu\beta\beta$ spectrum. The red region indicates the expected distributions for $0\nu\beta\beta$ events from MC simulations. All figures are extracted from [14].

Figure 5.3 shows the comparison between data and MC for the spectral shapes of energy, DNN $0\nu\beta\beta$ discriminator and standoff distance distributions of the calibration sources. As one could observe, the MC simulated spectral shapes for energy, DNN $0\nu\beta\beta$ discriminator and standoff distance were slightly “skewed” and did not fully reproduce those in source calibration data. The average bias in the expected number of events in the ROI arising from this spectral shape disagreement between data and MC was evaluated through the following process:

1. Construct an “unskewed” MC model from the best-fit result to the low-background data. For each PDF in the unskewed model, each bin was set to be have the value of the skewed PDF in the same bin multiplied by a correction factor derived from the observed shape deviations between MC simulations and source calibration data. The measured differences between data and MC obtained with the γ calibration sources were used to correct their corresponding γ -like PDFs, while differences in the background-subtracted $2\nu\beta\beta$ distribution were used for correcting β -like PDF components;
2. Generate a toy MC dataset by randomly sampling from the PDFs in the unskewed MC model;
3. Fit ROI signals in the toy MC dataset using the original skewed PDFs.

The process above was repeated many times to find the distribution of the bias in the number of ROI events caused by spectral shape errors. The relative bias were added in quadrature for all contributors (energy, DNN discriminator and standoff distance) and sum to 5.8% (4.4%) in Phase I (Phase II).

5.4.4 Background Model Error

The fit model did not fully considered detailed locations of backgrounds originated from materials far from the TPC vessel, and instead used a few representative locations to simulate ^{238}U , ^{232}Th and ^{60}Co components from such materials. To account for the systematic errors arising from this approximation, alternative PDFs from different locations for these remote components were used in the fit:

- ^{238}U in the air gap / ^{238}U in the inner cryostat
- ^{232}Th in the inner cryostat / ^{232}Th in HFE
- ^{60}Co from the source guide tube / ^{60}Co in the inner cryostat

By switching from the former PDF to the latter for the component ^{238}U , ^{232}Th and ^{60}Co individually, we took into account an extreme deviation from the more realistic case used in the analysis. The resulting relative change in the number of ROI events from the alternative fits were added up in quadrature for all three components and taken as the systematic error of the background model. For Phase I (Phase II), the background model error was evaluated to be 4.0% (4.6%).

5.5 Detector Sensitivity and Data Limit

5.5.1 Sensitivity to $0\nu\beta\beta$ Decay Half-life of ^{136}Xe

Before unblinding the ROI region of the low-background data, the sensitivity of the EXO-200 experiment to $0\nu\beta\beta$ half-life of ^{136}Xe was first studied using ~ 1000 fits to toy MC datasets. The toy datasets were generated from the background model obtained using the best energy-only fit to the blinded low-background data. The $0\nu\beta\beta$ component was profiled between 0 and 50 counts for each fit to cover the 90% confidence level. The final combination of the Phase I and Phase II sensitivity was evaluated to be 5.0×10^{25} yr, and is shown together with the all the previously published EXO-200 results in Figure 5.4. It is worth noting that detailed event topology information was maximally utilized as we included the DNN $0\nu\beta\beta$ discriminator and the standoff distance as fitting dimensions in the analysis, which lead to a 25% improvement relative to the sensitivity using only energy spectra and simple SS/MS discriminators [14].

5.5.2 Lower Limit on $0\nu\beta\beta$ Decay Half-life of ^{136}Xe

After unblinding the dataset, we performed the maximum likelihood fit described in Section 5.3 to Phase I and Phase II separately and the best-fit results for the energy

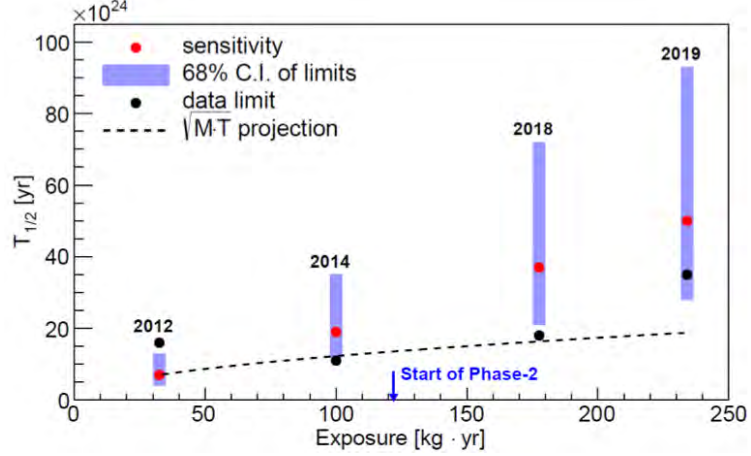


Figure 5.4: Improvements in the EXO-200 detector sensitivity and data limit over time.

(counts)	^{238}U	^{232}Th	^{137}Xe	Total	Data
Phase I	12.6	10.0	8.7	32.3 ± 2.3	39
Phase II	12.0	8.2	9.3	30.9 ± 2.4	26

Table 5.1: Comparison between best-fit results for background events and the total number of events from data in the ROI ($Q \pm 2\sigma$)

spectra and DNN $0\nu\beta\beta$ distributions are shown in Figure 5.5. The results showed no statistically significant evidence for $0\nu\beta\beta$. The background contributions to ROI are shown in Table 5.1. The lower limit on the $0\nu\beta\beta$ half-life of ^{136}Xe was measured to be $T_{1/2} > 1.7 \times 10^{25}$ yr ($T_{1/2} > 4.3 \times 10^{25}$ yr) at 90% CL in Phase I (Phase II), while the combined limit is $T_{1/2} > 3.5 \times 10^{25}$ yr. This corresponds to an upper limit on the effective Majorana neutrino mass of $\langle m_{\beta\beta} \rangle < (93\text{-}286)$ meV, using the nuclear matrix elements of [135–139] and phase space factor from [140].

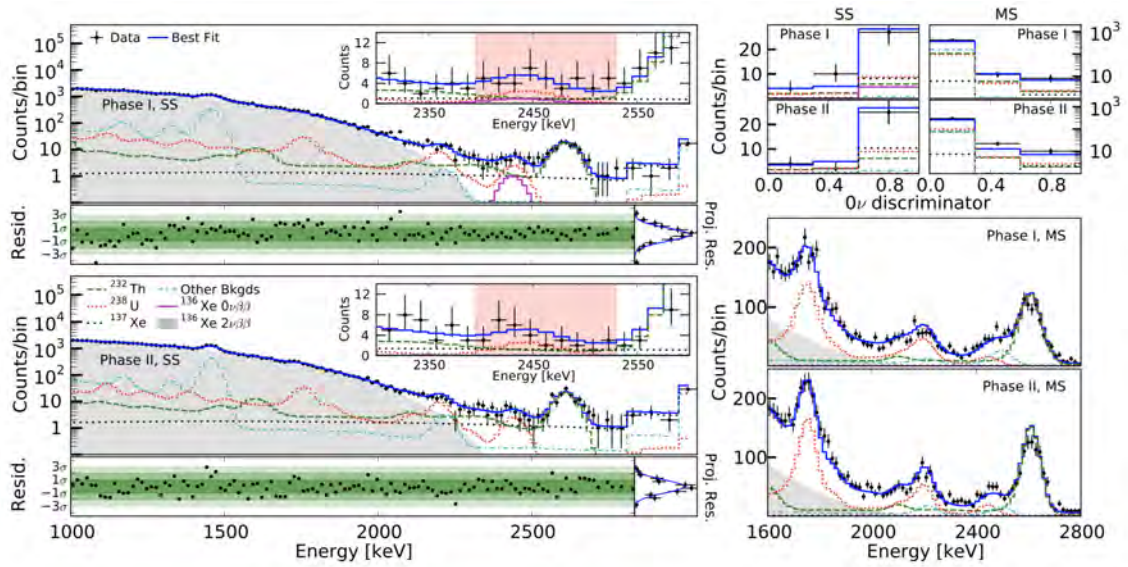


Figure 5.5: Best-fit results for the low background data SS energy spectrum in Phase I (top left) and Phase II (bottom left). The inset shows a zoomed in view of the energy spectrum around the ROI. Best-fit results for the DNN $0\nu\beta\beta$ discriminator distributions of SS and MS events with energy between 2395 keV and 2530 keV (top right). Best-fit results for MS energy spectra (bottom right). The best-fit residuals typically follow normal distributions, with small deviations taken into account in the spectral shape systematic errors. All figures are extracted from [14]

Chapter 6

W-value Measurement in LXe

6.1 Statement of the Author’s Contribution

The following chapter closely follows the text in Ref. [141], of which the author of this thesis is the first author. The author participated in all aspects of this measurement from detector gain calibrations to data analysis. This work is important for understanding the microphysics of particle interactions in LXe, and can guide future simulations of the charge and light production in LXe detectors.

6.2 Recombination Model and the W-value

Particles interacting in LXe can deposit a portion of their energy as scintillation and ionization. As shown in the diagram 6.1, in the ionization process, particles such as γ -ray photons, α particles, or energetic electrons deposit their energy in LXe through different physical mechanisms and produce a number of electron-ion pairs and excited xenon atoms (“excitons”) [142], as well as some loss of energy to undetectable channels (e.g. atomic motion or “heat”). In the scintillation process, two routes are possible: either direct excitation of Xe atoms or electron-ion recombination. Both processes lead to the production of excitons which form excited dimers, Xe_2^* , and then de-excite

with the emission of a ~ 178 nm vacuum ultraviolet (VUV) photon [142]. The relative number of electrons and photons collected from an event is anti-correlated, as first measured in [143], and depends on the electric field applied across the TPC. As the electric field increases, more ionized electrons can be drifted away from the interaction site, reducing the number of photons produced through recombination.

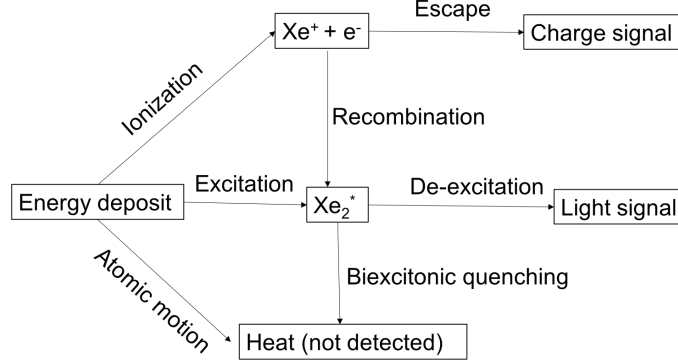


Figure 6.1: Scintillation and ionization energy deposit produced from particle interaction in LXe.

In general, the number of detected electrons and photons depends on the electric field applied to the LXe, since a field-dependent fraction, r , of the initially produced electron-ion pairs can recombine to produce excitons that then emit a photon. For an initial population of n_i electron-ion pairs and n_{ex} excitons, the maximum number of detectable electrons, n_q , at a given field is

$$n_q = (1 - r)n_i \quad (6.1)$$

and the number of detectable photons is

$$n_p = n_{ex} + rn_i \quad (6.2)$$

under the assumption that each recombining electron-ion pair produces an exciton, which in turn produces a photon. This assumption will be relaxed in Section 7.4,

where constraints on the absolute recombination efficiency are studied using EXO-200 experimental data. Under the above assumption, it is possible to define a recombination-independent W -value

$$W = \frac{E}{(n_q + n_p)} \quad (6.3)$$

which corresponds to the energy required to produce a single detectable quantum of either type. Since $n_q + n_p = (1 - r)n_i + n_{ex} + rn_i = (1 + \alpha)n_i$ for $\alpha = n_{ex}/n_i$, this definition of $W = \frac{E}{(1+\alpha)n_i}$ does not depend on electric field.

We note, as pointed out in Ref. [144], that if the efficiencies for an exciton or recombining electron-ion pair to create a detectable photon (ϵ_e or ϵ_r , respectively) differ from unity, a generalized form of Eq. 6.2 should be written as: $n_p = \epsilon_e n_{ex} + \epsilon_r r n_i$. In this case, we can define another photon quanta $N_p = n_p/\epsilon_r$, which denote the number of recombining electron-ion pairs needed to produce the observed scintillation signal if there were no direct exciton production, so that a recombination-independent energy scale can still be defined:

$$W = \frac{E}{(n_q + N_p)} = \frac{E}{(1 + \alpha)n_i} \quad (6.4)$$

with α replaced by the expression $\alpha = \frac{\epsilon_e}{\epsilon_r} \left(\frac{n_{ex}}{n_i} \right)$. In the case of $\epsilon_r = 1$, N_p is equal to n_p and Eq. 6.4 becomes identical to Eq. 6.3

Using these definitions, we can also define the energy required to produce a single electron-ion pair prior to recombination, $W_i = E/n_i$ such that $W = W_i/(1 + \alpha)$.

6.3 Previous measurements

A number of previous detectors have measured the charge and light response of LXe to α -, β -, and γ -induced electron recoils, and neutron-induced nuclear recoils (see,

e.g., [27, 145–157]). In addition, the Noble Element Simulation Technique (NEST) software tool has been developed to provide an empirical model to simulate the charge and light responses for LXe under different electric fields and for the various particle types [26, 158].

Since the sum of total electron and photon quanta is constant prior to detection, if an absolute calibration of the electron count is performed (see Section 6.5.1), the overall light detection efficiency can be calculated from the change in the detected number of electrons and photons as the recombination fraction r is varied with electric field [144, 159]. This allows the light detection efficiency to be absolutely calibrated from the charge signal, which is important since the detection efficiency for charge can be nearly unity for practical detectors, while the overall efficiency for detecting VUV photons is typically only $\sim 10 - 20\%$ [145, 160–163] and can be difficult to model without empirical measurements.

A number of previous measurements of W_i and W exist in the literature for these particle types, with a significant spread in the reported values, as shown in Table 6.1. For example, early measurements for 976 keV conversion electrons from a ^{207}Bi source found $W_i = 15.6 \pm 0.3$ eV [164], while independent measurements using 662 keV ^{137}Cs γ s gave $W_i = 13.6 \pm 0.2$ eV [165]. Later measurements employing an electron beam with energy per electron of 1–40 keV (and total deposited energy between 20 MeV and a few GeV) found $W_i = 9.76 \pm 0.70$ eV [25]. More recent measurements using 122 keV γ -rays found $W_i = 16.5 \pm 0.8$ eV [146]. In Ref. [27] the authors perform a compilation of measurements of W and W_i and find a combined estimate of $W_i = 14.30 \pm 0.14$ eV, consistent with their data obtained from a variety of β and γ sources between $\sim 3 - 700$ keV [27].

Measurements of the recombination independent value, W , have also been reported. In a reanalysis of data taken with ^{207}Bi conversion electrons from Ref. [166], Ref. [149] finds a value of $W = 13.8 \pm 0.9$ eV. This value relies on their previous mea-

surement of W_i [164,166], which is converted to W using the average of their measured value of $\alpha = 0.20$ [149] and their calculated value of $\alpha = 0.06$ [164]. The error bar reported on W indicates the difference between the measured and calculated values for α . Significant non-linearity is seen in the measured sum of the charge and light response, which is ascribed to possible variation in the amplifier response with rise time or loss of electrons due to electronegative impurities [149]. In addition, Ref. [159] finds a value of $W = 13.46 \pm 0.29$ eV, although this value is not included in the combined average in Ref. [26] due to a possible calibration problem [26]. Dahl reported a value of $W = 13.7 \pm 0.2$ using 122 keV γ events in a 30 g detector, which could be operated in single-phase or dual-phase mode [144]. The compilation in Ref. [26] additionally references two other values: $W = 14.0$ eV, appearing only in the preprint version of Ref. [167] and excluded from the average in [26] since it lacks an error estimate; and $W = 14.7 \pm 1.5$ eV [168,169]. The latter value comes from earlier work by a subset of the authors of Ref. [149] and agrees within errors with the later result. Finally, taking the combined estimate of $W_i \sim 14.3$ eV from Ref. [27] and assuming the measured value of $\alpha \sim 0.2$ [149,170] would correspond to $W \sim 11.9$ eV, where only an approximate value is given due to the spread in the values used to form the average and the uncertainty in the difficult to measure parameter, α .

The above summary indicates that there are substantial variations in previous measurements of the absolute calibration of charge and light yields of γ and β events in LXe. The spread in the values of W , either directly measured or derived from W_i , can be as large as 60%. Such differences could arise in part from detector effects such as variations in density, temperature, or xenon purity; differences in the energy deposition process for different particle types or energies; or unknown calibration systematics, as described in Section 6.6. While the relative calibration of charge and light yields versus field is straightforward for many detectors, the absolute measurement of these yields typically requires an accurate calibration of n_q , which can be

W (eV)	W_i (eV)	Particle type	Year	Ref.
-	15.6 ± 0.3	e^- (976 keV)	1975	[164]
-	13.6 ± 0.2	γ (662 keV)	1979	[165]
14.7 ± 1.5	-	e^- (976 keV)	1990	[168, 169]
-	9.76 ± 0.70	e^- (0.02-3 GeV)	1992	[25]
13.8 ± 0.9	-	e^- (976 keV)	2002	[149]
13.46 ± 0.29	-	γ (122 keV)	2007	[159]
13.7 ± 0.2	-	γ (122 keV, 136 keV)	2009	[144]
14.0	-	γ (164 keV)	2010	[167]
13.7 ± 0.4	-	Compilation	2011	[26]
-	16.5 ± 0.8	γ (122 keV)	2011	[146]
-	14.30 ± 0.14	Compilation	2014	[27]

Table 6.1: Summary of the previous measurements of W and W_i described in the text, along with the year of measurement and particle type. Most data were taken with γ and conversion e^- sources, for which the relevant decay energy is listed. Ref. [25] used an electron beam with total energy listed below, and an energy per e^- of 1–40 keV. Refs. [26] and [27] provide averages of subsets of previous measurements.

performed in a single-phase detector through the use of a calibrated charge-sensitive amplifier. Since many modern large-scale LXe TPCs are dual-phase in order to amplify the charge signal prior to collection, absolute measurements of the charge yield are difficult due to the possibility that not all the charge is extracted into the gas phase, even at extremely high applied fields [171, 172].

6.4 Measurement of scintillation and ionization yield using ^{228}Th , ^{226}Ra and ^{60}Co sources in EXO-200

Here we perform an absolutely calibrated measurement of the total yield with a precision of 4.5% using a variety of calibration sources with γ energies between 1.1–2.6 MeV. These measurements take advantage of a single-phase, large detector with good purity and a well-understood position and energy calibration, and the availability of a detailed Monte Carlo (MC) simulation of the detector energy response to

calibration sources.

6.5 Charge and light channel calibrations

In order to measure the scintillation and ionization yield of LXe, we select data for analysis from ^{228}Th , ^{226}Ra , and ^{60}Co source calibrations, with γ signal energies of 2615 keV, 1764 keV, 1332 keV and 1173 keV (the latter are the energies of the two photopeaks of ^{60}Co), respectively, as shown in Figure 5.3a. For each calibration source, data were taken during two dedicated week-long calibrations: in February 2016 (near the end of EXO-200 “Phase I” operations [134]) under electric fields 39 V/cm, 75 V/cm, 186 V/cm and 375 V/cm; and in October, 2018 (near the end of EXO-200 “Phase II” operations [109]) under electric fields 50 V/cm, 100 V/cm, 200 V/cm, 400 V/cm and 567 V/cm. Data were processed using the standard EXO-200 algorithms for event reconstruction and clustering. In all the measurements, only events within the standard EXO-200 fiducial volume defined by the intersection of a hexagonal region with apothem $a < 162$ mm and a cylindrical region of radius $r < 173$ mm are considered. Along the drift axis, only events with $10 \text{ mm} < |z| < 182 \text{ mm}$ are used [109].

Since EXO-200 is a single-phase TPC, electrons are directly collected on the U-wires with high collection efficiency. This allows an accurate determination of the total number of electrons produced in the LXe from an absolute calibration of the response of the charge readout electronics. The recorded waveforms from the charge and light channels in units of ADC counts are converted into electron and photon counts using the following calibrations.

In the external charge-injection calibration mentioned in Section 4.4.1, a known number of electrons from a calibrated capacitor were injected into the front-end electronics for the wire grids or APDs. The pulse magnitude recorded by the data ac-

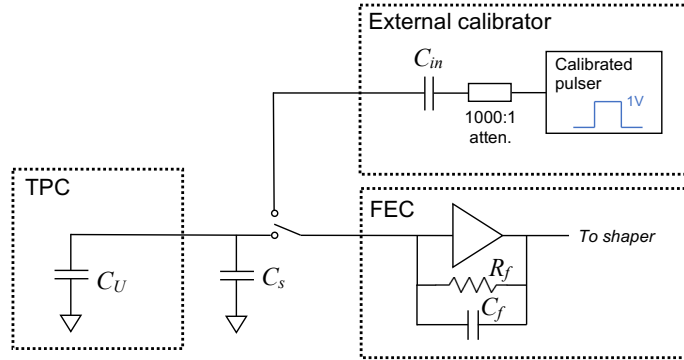


Figure 6.2: Schematic diagram of the external calibrator used for the external charge-injection calibration of the U-wire preamplifiers. The external calibrator is used to apply a calibrated amount of charge to the input of the pre-amplifier through C_{in} . The U-wire capacitance, C_U , and stray capacitance from the wiring, C_s , are disconnected during the calibration. The FEC contains the charge sensitive preamplifier with $C_f = 1$ pF, $R_f = 60$ M Ω , and open-loop gain $\gtrsim 10^5$.

quisition (DAQ) system in units of ADC counts was then determined for a calibrated amount of charge.

Due to the importance of an accurate absolute calibration of the preamplifiers for the results reported here, the external charge-injection calibration for the U-wires was performed twice throughout EXO-200 operations. The calibration required a specialized circuit and the detachment of the TPC from the front-end card (FEC) and therefore difficult to carry out frequently. Absolute charge-injection calibrations were originally performed for all U-wire, V-wire, and APD channels at the start of Phase I operations. To confirm the original calibration of the U-wires, the external calibration was repeated—for the U-wire channels only—using a newly fabricated external calibrator in November 2018 at the end of Phase II running. Both calibrations were found to agree on the average U-wire gain within 4% (see Figure 6.4). The difference between the two calibrations could arise from time variation in the gains over the course of detector operation, or from small systematic errors present in the Phase I calibration, which was not designed to reach the percent level absolute accuracy of the Phase II calibration. The Phase II calibration provided a measurement of the

preamplifier response taken within a week following the calibration runs used here to avoid any systematics from changes in gain or operating characteristics throughout EXO-200 operations.

Figure 6.2 shows a schematic of the circuit used for the Phase II external charge-injection calibration for the U-wires. The test pulse was a step function with amplitude between 0.6–1.4 V and rise time much smaller than the sampling rate of the DAQ. The absolute amplitude accuracy for the pulse generator was measured to be $< 0.5\%$. The voltage step was applied through a calibrated attenuator with measured attenuation of $V_{out}/V_{in} = (1.00 \pm 0.01) \times 10^{-3}$ to the calibration capacitor, C_{in} . This silver mica capacitor was hand-selected from tests of multiple capacitors to closely match the specified nominal value of 20 pF using a precision capacitance bridge (with absolute accuracy of 0.05%). Measurements were performed before and after removing the capacitor leads, and after installing in the external calibrator board to account for any stray capacitance related to the installation. The total effective capacitance of the capacitor and board was found to be $C_{in} = 20 \pm 0.2$ pF, with the effects of stray capacitance once installed measured to be $\lesssim 0.1$ pF.

The voltage step injected through C_{in} provided a calibrated amount of charge ($\sim [75 - 195] \times 10^3 e^-$) at the input to the preamplifier. As shown in Figure 6.3, a linear fit is performed to the measured pulse amplitudes in ADC units versus the injected electron counts.

The external charge-injection calibration was performed by disconnecting the U-wire cables coming from the detector from the FECs containing the charge preamplifiers. When connected, the total detector and wiring capacitance, $C_s + C_U$, was dominated by the stray capacitance of the cables connecting the U-wires to the FECs, $C_s = 60 - 80$ pF [173]. The feedback capacitance, $C_f = 1$ pF and open-loop gain of all preamplifiers $\gtrsim 10^5$ led to a $< 0.1\%$ change in the amplifier response when the TPC and wiring were disconnected.

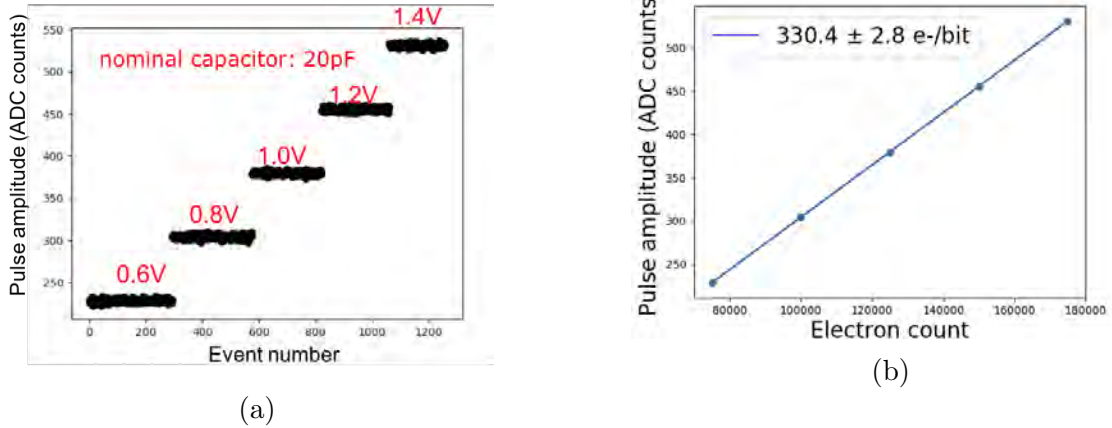


Figure 6.3: (a) Measured pulse amplitudes at each voltage step in the external charge-injection calibration. For a fixed voltage, ~ 200 data points were taken. (b) A linear fit to the average pulse amplitudes (ADC counts) versus electron counts, where the electron count is calculated by multiplying the voltage and the nominal capacitance shown in (a).

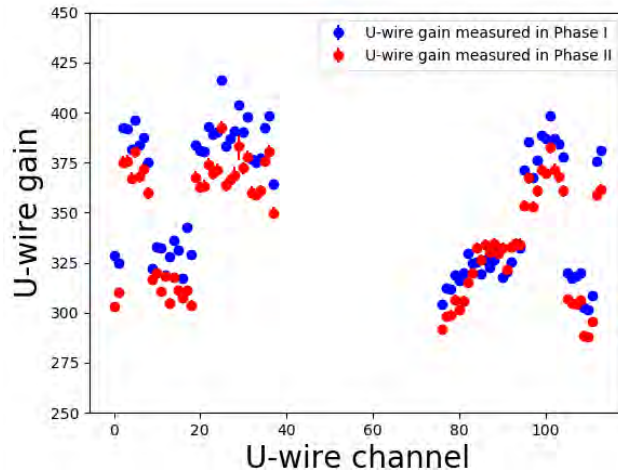


Figure 6.4: Comparison between the U-wire gain measured from the external charge-injection calibration at the start of Phase I and the end of Phase II. The difference between them could be attributed to the time variation in the gains or systematic errors in the Phase I calibration, which was not designed to reach the same accuracy as the Phase II calibration.

Combining all systematic errors in the external calibration hardware described above, the gain uncertainty common to all channels is $\lesssim 1.5\%$. Averaged over all channels, the resulting calibration indicates that each ADC count from a U-wire

signal corresponds to ~ 340 electrons, with a relative variation of 9% across different channels. However, there are additional possible sources of systematic error resulting from possible time variation of these gains during data runs; differences in pulse shape between the charge injection calibration and physics data; and loss of electrons prior to collection by the U-wires.

To account for possible time variation in the gains, an “internal charge-injection” calibration was also performed several times per week during the data-taking period. This calibration used charge injected into the preamplifier directly from the calibration hardware on the FEC. Unlike the external charge injection, the total capacitance of the calibrator was not precisely known, so gains measured from the internal charge injection were used only to perform a relative measurement over time, which was anchored by the absolute value measured from the external charge-injection calibration. The internal calibration performed at the same time as each source calibration run was used to account for any time variation of the U-wire gain for that run. The overall gain fluctuations were measured to be $\lesssim 1\%$ over the entire period of EXO-200 operations and $\lesssim 0.1\%$ over the week-long data taking period in Phase II considered here.

The charge injection calibrations were performed with step function input (with negligible rise time), while real physics signals have a charge pulse rise time varying between 3–6 μs [111]. This difference in rise time could lead to changes in the reconstructed amplitude of the signal after the pulse shaping electronics (i.e. “ballistic deficit”). Simulations show that this effect generates a relative 0.7% systematic error on the reconstructed pulse height for a signal with typical rise time relative to the step function input.

Electrons in LXe can capture on electronegative impurities as they drift, which attenuates the charge signal. To minimize this attenuation, the xenon was continuously circulated through purifiers [173]. The purity of the LXe was monitored several

times each week by dedicated source-calibration data, from which the electron lifetime could be determined. A drift-time dependent correction to the reconstructed charge energy is implemented in the data analysis, following the same procedure as described in 4.4.2. To limit effects of finite purity, only data for which the electron lifetime is >2 ms are used in this analysis. The maximum charge loss for the lowest lifetime data considered here is $< 5\%$ over the full drift length, prior to correction. After correction, the resulting error on the reconstructed charge is estimated to be $< 0.5\%$.

Combining all systematic errors from the internal and external calibrations, electron lifetime calibration, and pulse shape studies, the total systematic uncertainty on the U-wire gain for each channel is 1.8%.

Using this absolute calibration of the charge channels, the APD channels can be calibrated under the assumption of perfect recombination efficiency. For this calibration, it is assumed that every recombined electron-ion pair produces an exciton, which de-excites to emit an additional VUV photon. Under this assumption, the total number of quanta (either electron-ion pairs or photons) produced at a given energy is independent of field [144, 159]. The change in the light and charge signals versus field can then be used to calibrate the total response of the light channels, which results from a product of the APD quantum efficiency, the geometrical collection efficiency, the APD avalanche gain, and the amplifier gain. The advantage of this method is that the total photon count can be determined based only on the previously calibrated change in the number of electrons, and without the need to independently measure each component of the photon detection efficiency. With additional calibration of the APD readout electronics it is possible to also determine the overall photon detection efficiency, ϵ_p , defined as the ratio between the number of photon induced “photo-electrons” (PE) produced in the APDs prior to the avalanche amplification, relative to the total number of photons initially produced in the LXe. The efficiency

for detecting photons is significantly smaller than for charge due to the imperfect quantum efficiency of the APDs and the overall loss of photons as they are absorbed by uninstrumented detector surfaces.

The external charge-injection calibration was also performed for the preamplifiers for each of the APD readout channels at the beginning of EXO-200 Phase I operations. While this calibration is not directly required to obtain the charge yields and W -value from EXO-200 data, along with the APD avalanche gain calibration, it can be used to estimate the photon detection efficiency from the calibrated total light response. The measured response indicates that one ADC count corresponds to ~ 900 electrons at the input to the preamplifier, depending on channel. The relative APD preamplifier gain variation is 11% across different channels and the time variation is $\sim 1.5\%$ over the entire period of EXO-200 operations (excluding differences due to the electronics upgrade between Phase I and II), as measured from the internal charge-injection calibration.

The avalanche gain of each APD could be calibrated accurately using an *in-situ* laser calibration, during which all channels were illuminated by light from a pulsed 405 nm laser beam that entered the TPC through diffusers positioned at each end of the TPC. The diffusers were illuminated by two optical fibers carrying light from an external laser source. Since the dynamic range of the DAQ was not sufficiently high to measure the response for both the unity gain (i.e. bias below the avalanche threshold) and full gain APD biases simultaneously, a two-step calibration was used where the laser pulse length was varied. A short laser pulse was measured at full gain and at an intermediate gain and compared to a longer pulse measured at unity gain and the same intermediate gain. Both pulse lengths were short with respect to the times relevant to the front-end electronics. The ratio of the response amplitudes then gave the avalanche gain, which was measured during weekly calibrations throughout EXO-200 running. The operating APD voltage biases for the data used here result

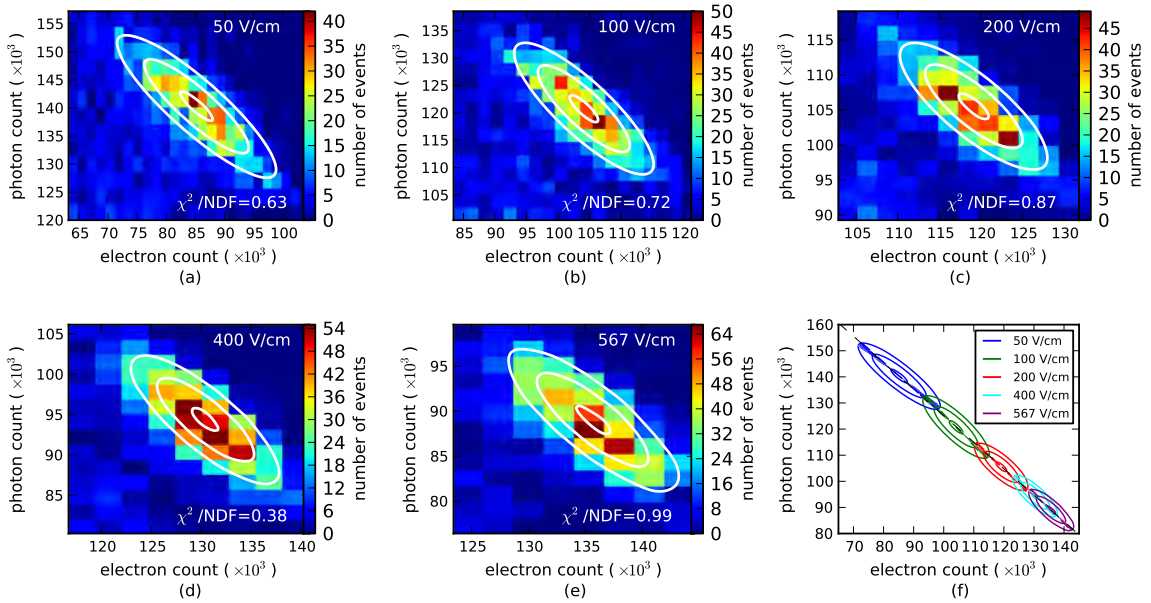


Figure 6.5: (a)-(e) MC-based fit to the anti-correlated number of electrons and photons at the 2615 keV γ peak from the ^{228}Th source data taken in October 2018 under various electric fields. Only bins with more than 10 events are included in the fit. The χ^2/NDF fit statistic is indicated in each plot. The outermost contour contains 68% of peak events on average for the best fit parameters. (f) Combination of the individual fits to the ^{228}Th photopeak under various fields. The magnitude of the slope of each ellipses' major axis is equal to the tangent of the rotation angle. The shaded regions indicate the statistical uncertainty in the best fit value for the rotation angles.

in a mean gain of 200, consistent with the earlier EXO-200 measurement from [174]. Combined with the preamplifier calibration, this corresponds to a conversion between APD pulse height and PEs on the order of 4.5 PEs/ADC.

6.5.1 Measurement of charge and light yields versus field

After obtaining the electron and PE counts in each event near the photopeak using the calibrations described in Section 6.5, we perform a binned 2D Gaussian fit to the data:

$$f(x, y) = Ae^{\frac{-1}{2(1-\rho^2)} \left[\frac{(x-n_q)^2}{\sigma_q^2} + \frac{(y-n_{PE})^2}{\sigma_{PE}^2} - \frac{2\rho(x-n_q)(y-n_{PE})}{\sigma_{PE}\sigma_q} \right]} \quad (6.5)$$

where the x and y coordinates refer to the bin centers for the charge and light axes, respectively, A is an overall amplitude, n_q and n_{PE} are the mean number of electrons and light-induced PEs at the photopeak, respectively, ρ is the correlation between the electron and PE counts, and σ_q (σ_{PE}) is the standard deviation of the electron (PE) counts, which includes both the detector noise and electron-ion recombination fluctuations. To account for the detailed energy spectrum of the calibration events, a simulation based on the EXO-200 detector MC [111] is used to produce the expected event energy distribution for each source. This spectrum is smeared by a 2D Gaussian function for the resolution as in Eq. 6.5 to give the overall fitting function for each source. The best-fit calibration and resolution parameters are then determined through a χ^2 fit to the data. This MC-based fit accounts for events in the Compton shoulders near each photopeak, to minimize any effect of background events on the measurement. Using the best-fit values of electron and PE counts for each of the photopeaks in the calibration sources, the overall photon detection efficiency can be determined by requiring $n_q + (n_{PE}/\epsilon_p)$ to be a constant under different electric fields for each photopeak.

The resulting photon detection efficiency estimated from the least squares fit to all calibration data from sources positioned near the cathode is $\epsilon_p = (8.1 \pm 0.5)\%$, where the uncertainty is dominated by systematic variations between different calibration sources. Using this efficiency, which as described above relies on the assumption that each recombining electron-ion pair produces a photon, the best-fit values of n_{PE} can be scaled to photon counts, n_p .

Figures 6.5–6.7 show the MC-based 2D Gaussian fit to electron-photon count spectra for the ^{228}Th (2615 keV), ^{226}Ra (1764 keV) and ^{60}Co (1332 keV and 1173 keV) sources, respectively. Overall the use of the MC-based fit minimizes systematic errors due to the presence of backgrounds from Compton scattering near the photopeaks. However, the difference between the results of the MC-based fit and a simple 2D

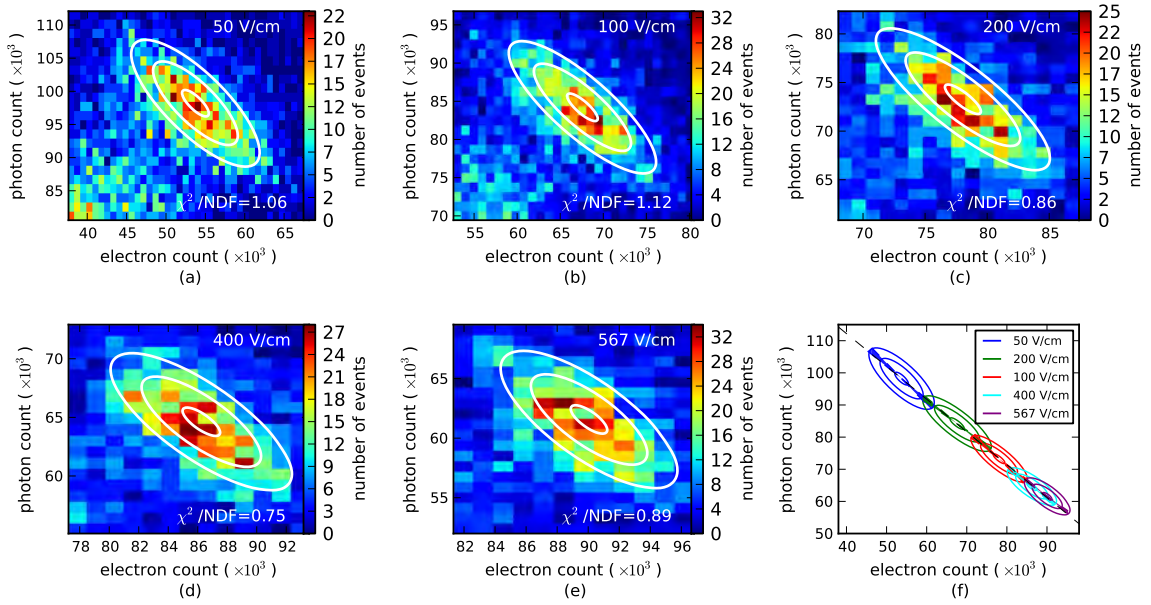


Figure 6.6: Data and best fit to the 1764 keV γ peak from the ^{226}Ra source, following the same procedure as Figure 6.5.

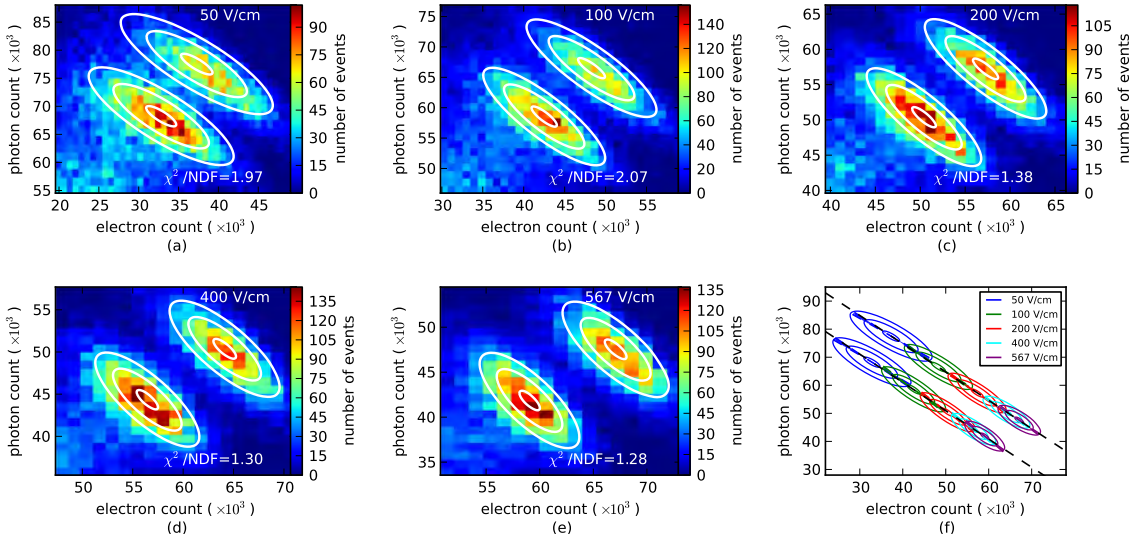


Figure 6.7: Data and best fit to 1332 keV and 1173 keV γ peaks from the ^{60}Co source, following the same procedure as Figure 6.5.

Gaussian fit to each peak including a constant background is small ($\lesssim 5\%$), indicating that background model systematics are not large.

The coefficient ρ can be converted to the rotation angle, θ , defined as $\tan(2\theta) =$

$-\frac{2\rho\sigma_p\sigma_q}{\sigma_p^2-\sigma_q^2}$, indicating the optimal weighting of the charge and light signal to form the “rotated energy” that minimizes the overall resolution, as described in Section 4.4.

Figures 6.5f–6.7f show the total photon count versus electron count and the rotation angle θ under various drift fields measured using the three sources. The rotation angle decreases slightly as the electric field increases, due to the higher signal-to-noise in the charge channel compared to the light channel. In addition, as the drift field increases, the spread of the photon and electron distributions is reduced, leading to improved energy resolution. Figure 6.8 shows the number of electrons and photons at the peak measured from various calibration sources under different electric fields. The estimated errors are dominated by the correlated uncertainties on the photon detection efficiency and APD/U-wire gain measurements. To account for these uncertainties, an overall scale factor within the systematic error on the photon and electron count is indicated by the shaded bands.

From these data we measure a recombination independent W -value of:

$$W = 11.5 \pm 0.5(\text{syst.}) \pm 0.1(\text{stat.}) \text{ eV}$$

The uncertainty on the W -value is dominated by systematic errors in the detector calibrations of the charge and light response. The primary contribution to this systematic error is the 6% uncertainty on the photon detection efficiency measured using the calibration sources at different electric fields. The estimated 1.8% absolute uncertainty on the charge response (described in Section 6.5) provides a subdominant systematic error.

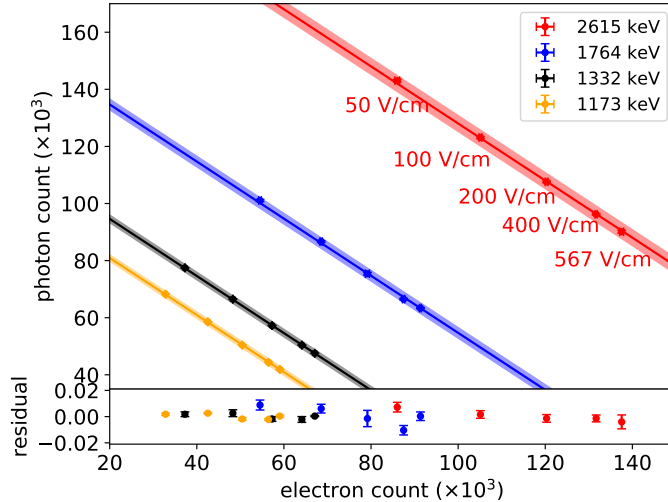


Figure 6.8: Total number of photons vs. number of electrons at electric fields ranging from 50 V/cm to 567 V/cm. The errors indicate statistical fluctuations from the fits shown in Figs. 6.5–6.7, while the shaded bands represent correlated uncertainties on the photon detection efficiency and APD/wire gain measurements. The photon detection efficiency is measured by requiring each line to have a slope of -1 . Residuals between the data and the linear fit, i.e., $((\text{data}-\text{fit})/\text{fit})$ are indicated in the bottom panel along with the statistical errors.

6.6 Comparison between experimental data and the NEST simulation

Figure 6.9 shows the measured charge and light yield, defined as number of electrons, n_q , or photons, n_p , produced per keV of deposited energy for the three calibration sources. The measured yields vary with electric field due to its effect on electron-ion recombination. The measured data are compared to the predictions from the NEST 2.0 simulation package [158], with its γ model (relevant for photoelectric absorption) and β model (relevant for β decays and Compton scattering) predictions shown as the solid and dotted lines, respectively. The NEST predictions are calculated for the density of the enriched Xe used in EXO-200 of 3.03 g/cm^3 as described in Section 3.1.1, and are simulated versus the electric field and energy for each of the photopeaks from the calibration sources.

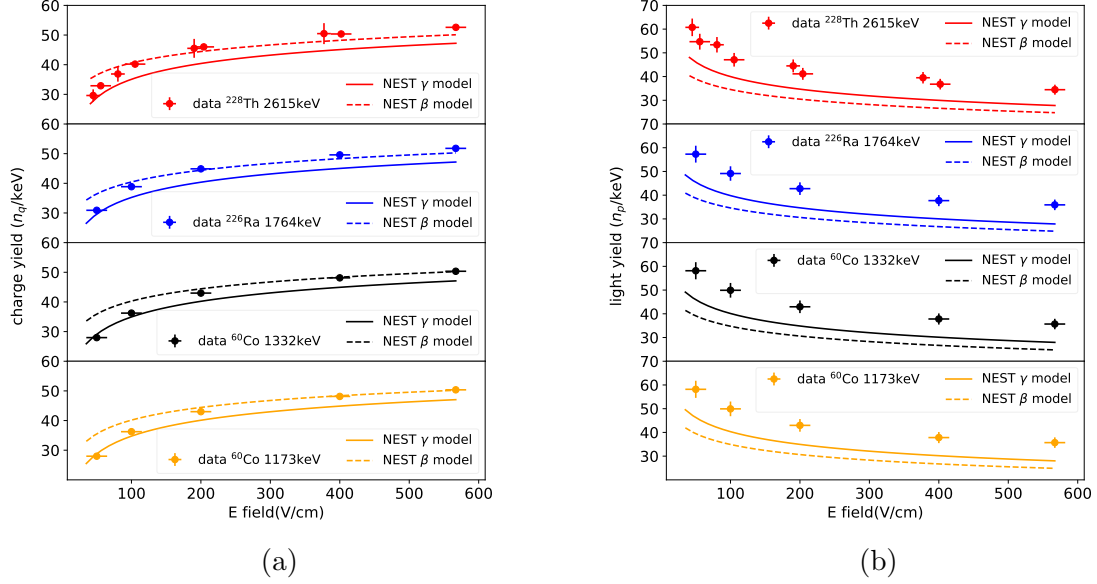


Figure 6.9: Comparison of the measured charge yields (a) and light yields (b) at various electric fields with the NEST γ and β models. For the ^{228}Th source, measurements from both the Phase I and Phase II data sets are shown, while the other sources only have data available only from Phase II.

For the ^{228}Th data, calibrations from both the Phase I and Phase II data sets are shown, while the other sources only have data available for the Phase II calibration. The Phase II data points have smaller errors due to their coincidence in time with the external charge calibration described previously. Relative to this calibration, the Phase I data have larger errors due to hardware modifications performed between the two data sets that introduce additional uncertainty on the absolute gain calibration in Phase I.

The uncertainty on the electric field is determined by a 3D finite element simulation of the TPC geometry. This simulation indicates that there is some position-dependence ($\lesssim 5\%$) in the magnitude of the electric field over the fiducial volume of the detector. In addition, evidence for charge buildup on the PTFE reflector surrounding the TPC is observed in the same datasets used here, at the lowest electric fields. The estimated charge buildup is comparable to that seen in other LXe TPCs employing PTFE [175] and corresponds to a position dependent field distortion of

10–15 V/cm, independent of field. This possible field distortion dominates the systematic error on the electric field in the detector, and is relatively more significant at lower fields.

The EXO-200 detector also allows us to compare the charge and light yield for events with and without a calibration source present, as shown in Figure 6.10. In the absence of a calibration source, events are primarily generated by ^{136}Xe $2\nu\beta\beta$ decays, which can be compared to the γ events from the ^{228}Th source at an operating field of 567 V/cm. The data without the source were acquired during Phase II between July 2016 and October 2018, while the ^{228}Th calibration dataset was taken within 2 days in October 2018. Only events in the fiducial volume within the energy range 500–2615 keV are used in the analysis. For both the $2\nu\beta\beta$ or γ spectrum, data are first binned by rotated energy with non-overlapping bins of width equal to the 1σ resolution at each rotated energy. In addition, a single bin encompassing the entire 2615 keV photopeak from the ^{228}Th source is included. This binning avoids bias in the selected energy of the events due to non-uniformity in the event distribution. After binning in rotated energy, the charge and light yield at each point is determined from the median of the electron and photon counts in each bin and is plotted in Figure 6.10(c). A linear fit to the combined $2\nu\beta\beta$ or γ dataset is indicated by the red line, and the residuals are shown in the bottom panel.

The ratio between the charge and light yield versus energy is found to be nearly constant over the energy range considered, with small deviations ($\lesssim 5\%$) occurring at low energies. In the energy range between 500 keV and 1500 keV, the charge-to-light ratio for events from the ^{228}Th γ events is $\sim 3\%$ smaller than those from $2\nu\beta\beta$ on average, and the difference grows larger for events with lower energy. No significant difference is found between the charge-to-light ratio for the $\beta\beta$ - and γ -induced events in the energy range above 1500 keV. In particular, the charge-to-light ratio for single-cluster events from the 2615 keV photopeak of the ^{228}Th source, which

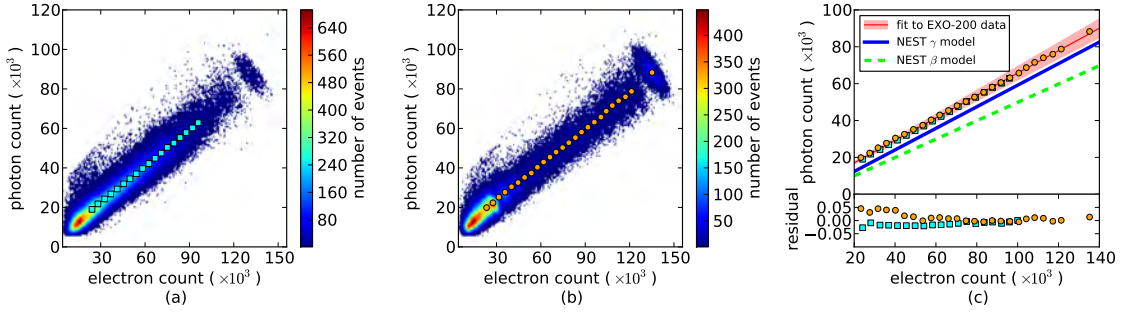


Figure 6.10: (a) Light versus charge response for events when no calibration source is present. Data within the continuous band are predominantly $2\nu\beta\beta$ events from ^{136}Xe . The small peak at the end of the spectrum arises from residual backgrounds in the detector and is excluded from the fits. (b) Charge and light response generated by γ -rays from the ^{228}Th source. (c) Average light versus charge response for γ (orange circles) and $\beta\beta$ (blue squares) events at a range of energies (>500 keV) and an electric field of 567 V/cm. The difference between measurements and the linear fit to the combined dataset (indicated by the red line) in the energy range considered is within 5%. The red bands show the 1σ systematic errors on the response ratio, which are dominated by the uncertainty on ϵ_p . The solid blue and dashed green lines show a comparison with the NEST predictions.

consists of both photoelectric absorption and closely spaced, unresolved Compton scatters, agrees with the corresponding average yield for $2\nu\beta\beta$ events within $\sim 1\%$. The agreement between the charge and light yield for high-energy $\beta\beta$ and γ induced events is consistent with the energy scale measured by fits to the detailed shape of the $2\nu\beta\beta$ spectrum in EXO-200. In these fits, the absolute $\beta\beta$ energy scale is found to be consistent with the calibrations using photopeaks from external γ sources at the sub-percent level [14, 109]. In contrast to these data, NEST predicts a difference between the relative yields for its γ model and β model of $\sim 25\%$ in the charge-to-light ratio in this energy range, as indicated in Figure 6.10(c).

Relative to previous measurements, the data used here were taken at higher energies than most previous data listed in Table 7.1. While the data for the calibration sources considered here are consistent with a single value of W between 1–2.5 MeV (i.e., no energy dependence is observed within this range), these data do not constrain energy dependence in this value below 1 MeV. In addition, the EXO-200 APDs are

sensitive to infrared red (IR) photons with wavelength $\lesssim 1000$ nm, which could provide a difference in overall photon collection efficiency relative to experiments employing photo-multipliers (PMTs). While significant scintillation in the IR is observed in gas Xe [176–179], IR emission in LXe has been measured to be substantially smaller [177]. These previous measurements indicate that effects from additional collection of IR photons are expected to be small, although further work is needed to precisely measure the contribution from IR photons emitted in LXe [178].

The NEST simulation of the charge and light yields has a small density dependence. At the EXO-200 enriched LXe density of 3.03 g/cm^3 , NEST predicts a W -value of 13.3 eV. This value is 3% smaller than the average value from Ref. [26] of 13.7 eV, which corresponds to the value predicted by NEST at a density of 2.9 g/cm^3 . Variations in the value of W_i have been measured versus density in gas and liquid detectors [180]. Additional density dependent effects are also parameterized in NEST for the parameter α and the charge and light yields based on global fits to previous measurements. However, including the higher mass density of the enriched LXe in the NEST simulation does not fully alleviate the differences between the data measured here and predictions. In addition, for γ and β interactions, variations in the yields may be expected to vary with the electron density rather than mass density. Scaling the yields by the electron density instead would produce slightly larger tension between the EXO-200 measurements and the NEST predictions.

In summary, our measurement of $W = 11.5 \pm 0.5(\text{syst.}) \pm 0.1(\text{stat.})$ eV does not agree within errors with the NEST prediction. However, it does lie within the broad range of previous measurements summarized in Section 6.3. The tension between our measurements and the NEST simulation cannot be fully relaxed by rescaling the NEST W -value down to 11.5 eV since the charge-to-light ratio predicted by NEST differs from our measurement. Differences as large as $\sim 8\%$ (6%) in the charge yield and $\sim 24\%$ (41%) in the light yield are seen between the EXO-200 measurements

presented here and NEST's γ model (β model) predictions, which is larger than the estimated systematic errors on these measurements. This is the first simultaneous measurement of absolute light and charge yields over the 1–2.5 MeV energy range, and can be used to improve modeling of this region in future iterations of the NEST software package.

Chapter 7

Semi-empirical Resolution Model for EXO-200

7.1 Statement of the Author’s Contribution

The following chapter also closely follows the text in Ref. [141], of which the author of this thesis is the first author. This work successfully models the energy resolution of the LXe detector in EXO-200 and can inform the design of future detectors. In addition, it sets a constraint on the recombination efficiency, i.e., the fraction of recombined electrons that result in the emission of a detectable photon in LXe.

7.2 Energy resolution model

EXO-200 defines a “rotated” energy scale

$$E \propto \cos(\theta)\langle E_q \rangle + \sin(\theta)\langle E_p \rangle \quad (7.1)$$

where $\langle E_q \rangle$ is the estimated energy deposited as charge and $\langle E_p \rangle$ is the estimated energy deposited as light, for each event. These energy estimates are determined

from the amplitude of signals observed in the summed charge and light channels:

$$\langle E_a \rangle = \frac{A_a}{g_a \epsilon_a} W = n_a W \quad (7.2)$$

where A_a is the amplitude of the signal in ADC counts, ϵ_a is the average efficiency (*i.e.* fraction from 0-1) for measuring a given type of quanta, g_a is the conversion factor between ADC counts and quanta, and W is the average energy to create a single quantum (of either charge or light) for $a = (p, q)$.

The total number of quanta can be estimated by:

$$\langle n \rangle = \frac{\langle E \rangle}{W} \propto \cos(\theta) \langle n_q \rangle + \sin(\theta) \langle n_p \rangle \quad (7.3)$$

We are generally interested in the relative energy resolution, which is given by $\sigma_E/E = \sigma_n/\langle n \rangle$, where σ_n is the standard deviation of $\langle n \rangle$. In terms of quanta, the relative variance can be expressed as:

$$\frac{\sigma_n^2}{\langle n \rangle^2} = \frac{\cos^2(\theta) \sigma_q^2 + \sin^2(\theta) \sigma_p^2 + 2 \sin(\theta) \cos(\theta) \text{Cov}_{q,p} + \sigma_{Xe}^2}{\langle n \rangle^2} \quad (7.4)$$

where $\sigma_{Xe}^2 = f_{Xe} \langle n \rangle$ are the intrinsic fluctuations in the initial total number of quanta. The Fano factor f_{Xe} is calculated to be ~ 0.059 in LXe [142], but is typically subdominant to detector readout noise. Other sources of noise are also dominant in EXO-200, and even assuming a Fano factor as large as $f_{Xe} = 1$ would not lead to a significant change in the predicted resolution. Thus, we exclude this factor in the following estimates.

The variance, σ_q^2 , of our estimate of n_q is:

$$\sigma_q^2 = \sigma_r^2 + n_q \frac{(1 - \epsilon_q)}{\epsilon_q} + \frac{\sigma_{q,noise}^2}{\epsilon_q^2} \quad (7.5)$$

where σ_r^2 is the variation in units of quanta resulting from recombination fluctuations.

The second term represents the binomial fluctuations for non-unity charge collection efficiency, and $\sigma_{q,noise}^2$ is the electronics noise of the charge collection wires in units of electrons. Since the average electron lifetime of the selected data is 3.2 ms, the fraction of electrons absorbed by impurities in the LXe is $\sim 3\%$ and therefore the charge collection efficiency $\epsilon_q = 97\%$. Due to this high collection efficiency, the second term in Eq. 7.5 is negligible compared to the electronics noise and recombination fluctuations.

Similarly, we can write the variance of the estimator of the number of photons as:

$$\sigma_p^2 = \sigma_r^2 + \frac{n_p}{\epsilon_p} [(F_N - 1) + B^2] + \frac{\sigma_{p,noise}^2}{\epsilon_p^2} + n_p^2 \sigma_{NU}^2 \quad (7.6)$$

In addition to the recombination fluctuations, σ_r^2 , and the electronics noise of the APD readout channels, $\sigma_{p,noise}^2$, there are three additional noise terms caused by fluctuations related to the initial number of PE created in the APDs, $n_{PE} = \epsilon_p n_p$. The term $B^2 \cdot n_p \epsilon_p$ describes fluctuations in the number of PEs created by the photons reaching the APDs. The factor B is determined from the binomial fluctuations in the number of detected photons, due to the imperfect collection efficiency, and also includes sub-Poissonian fluctuations arising from the creation of PEs by VUV photons in the Si APDs.

For 5.9 keV X-rays interacting in Si, the PE creation process has been measured in detail [174,181]. These measurements indicate that the average energy to create a PE is 3.72 eV [181] at LXe temperatures, with the fluctuations in n_{PE} well described by a Fano factor of ~ 0.1 . However, at the much lower energy corresponding to 178 nm VUV photons (7.0 eV per photon), the intrinsic PE creation process and the number of PEs (μ_{PE}) created by a single photon in Si is less well-characterized. A direct measurement of PE creation by 7.0 eV photons found a mean of $\mu_{PE} = 3.0$ PE/photon [182] with an 8% uncertainty, which implies a lower creation energy

per PE than for keV-scale X-rays. For ~ 5 eV photons, measurements have found values between 1.3–2.0 PE/photon [183–186], with the higher end of this range being consistent with the measurements in Ref. [182]. Simulations of PE creation by VUV photons are consistent with a mean of $\mu_{PE} = 2\text{--}3$ PE/photon at 7 eV [187, 188], with variance described by a Fano factor, $f_{Si}(7 \text{ eV}) \approx 0.2$ [188].

To determine the overall value of B , which includes fluctuations in both the number of photons detected as well as fluctuations in the PE creation process, a two-step simulation is employed. First, a random number of collected photons is determined from a binomial distribution with n_p trials and probability ϵ_p/μ_{PE} . For each collected photon, a discrete number of PEs is then generated from a distribution with mean μ_{PE} and variance of $f_{Si}\mu_{PE}$. The total number of PEs, n_{PE} , is then determined for each simulated event along with the variance over all trials. Under all electric fields, and for μ_{PE} varying from 2–3, the value of B is 1.8 ± 0.2 , where the error accounts for the uncertainty in μ_{PE} .

Following Ref. [174], there are two additional variance terms relative to the quanta n_{PE} at the input to the APD: $\sigma_{PE}^2 = (F_N - 1)n_{PE} + n_{PE}^2\sigma_{NU}^2$. The first term is related to fluctuations of the APD avalanche gain that are parameterized by the excess noise factor F_N [116, 174]. The second term accounts for non-uniformity or position dependence of the detector response. This non-uniformity can arise both from differences in gains between APD gangs and differences in gains between the APDs within a single gang. The overall variation in gain between different gangs and over time can be calibrated and removed using the source calibration data [117]. While this overall gain variation can be $\gtrsim 10\%$, σ_{NU} , which represents the variation in the total light response is measured to be only $\sim 1\%$ for events from sources near the cathode, where the uniform distribution of photons averages over these gain variations. For the data considered here, the contribution to σ_{NU} due to gain variations between gangs is sub-dominant compared to other terms in the resolution

model, even prior to applying the gang-dependent correction.

In addition to the gain non-uniformity among various APD channels, there may also exist gain non-uniformity within an APD channel. The APDs within each gang were selected to have matched gains based on testing prior to installation [174], but small residual differences remain. Moreover, slight time variations in the gains of an individual APD are possible due to changes in temperature and other systematic effects. While the overall gain is calibrated for each gang as a function of time, gain non-uniformity within the gang cannot be calibrated and could lead to additional variation in the light response. This non-uniformity is studied in detail in Appendix A, and is found to not significantly impact the resolution for events in the fiducial volume of the detector.

Source calibration data can be used to determine the relative number of photons collected for interactions at different locations in the detector. This position-dependent response is used to calculate the “lightmap,” which describes the summed response of all APDs as a function of event position and time [111, 117]. Since the lightmap is constructed empirically from calibration data from the ^{228}Th source, detector regions far from the calibration source can have limited statistics, leading to an uncertainty on the detector response. Such statistical or systematic errors in the lightmap can lead to position-dependent errors in the energy estimate. While it is difficult to simulate the light response of the EXO-200 detector at the percent level accuracy needed to verify the empirical lightmap, as will be shown in Section 7.3, the resolution model can describe the experimental data without including additional sources of position dependent error. The agreement of the measured resolution and model indicate that systematic errors in the lightmap are subdominant compared to other sources contributing to the energy resolution.

Finally, the covariance between the light and charge signals is represented by $\text{Cov}_{q,p}$. Assuming perfect recombination efficiency, i.e. that every recombined electron

Quantity	Value	Syst. err. [%]	Stat. err. [%]
ϵ_p	0.081	6.2	0.6
F_N	2.15	11.9	1.4
$\sigma_{q,noise}(e^-)$	770	4.5	1.5
$\sigma_{p,noise}(\text{PE})$ [Phase I/II]	446/148	3.5	0.5
σ_{NU}	0.012	5.0	5.3

Table 7.1: Measured values for quantities independent of the drift field in the resolution model and their estimated errors

E (V/cm)	field	$n_q(\times 10^3)$ (syst.) (stat.)	$n_p(\times 10^3)$ (syst.) (stat.)	$\sigma_r(\times 10^3)$ (syst.) (stat.)
39		$79 \pm 5.5 \pm 0.1$	$161 \pm 9.7 \pm 0.1$	$8.4 \pm 0.5 \pm 0.3$
50		$86 \pm 1.5 \pm 9.8$	$143 \pm 8.9 \pm 6.6$	$8.3 \pm 0.4 \pm 0.5$
75		$98 \pm 6.9 \pm 0.1$	$141 \pm 8.5 \pm 0.1$	$7.8 \pm 0.5 \pm 0.3$
100		$105 \pm 1.9 \pm 0.7$	$123 \pm 7.6 \pm 0.9$	$7.1 \pm 0.3 \pm 0.4$
186		$121 \pm 8.5 \pm 0.1$	$118 \pm 7.1 \pm 0.1$	$6.1 \pm 0.5 \pm 0.2$
200		$120 \pm 2.2 \pm 0.5$	$107 \pm 6.6 \pm 0.5$	$5.4 \pm 0.3 \pm 0.4$
375		$134 \pm 9.4 \pm 0.1$	$105 \pm 6.3 \pm 0.1$	$5.0 \pm 0.5 \pm 0.2$
400		$132 \pm 2.4 \pm 0.4$	$96 \pm 5.9 \pm 0.5$	$4.9 \pm 0.2 \pm 0.3$
567		$138 \pm 2.5 \pm 0.4$	$90 \pm 5.6 \pm 0.5$	$4.7 \pm 0.2 \pm 0.3$
615		$141 \pm 9.9 \pm 0.1$	$97 \pm 5.8 \pm 0.1$	$3.6 \pm 0.8 \pm 0.3$

Table 7.2: Quantities depending on the drift field measured using 2615 keV γ s from the ^{228}Th source. Systematic and statistical errors are included.

results in the emission of a VUV photon, the recombination fluctuations in the charge and light signals will be identical, as indicated in Eq. 7.5 and 7.6, and the covariance between electron and photon counts will be $\text{Cov}_{q,p} = -\sigma_r^2$. As described below, consistency of this model with the measured resolutions can provide constraints on the assumption of perfect recombination efficiency.

7.3 Optimal energy resolution predicted by the model

The quantities $n_q, n_p, \epsilon_p, \sigma_{q,noise}, \sigma_{p,noise}, \sigma_r$ and F_N in the resolution model are directly measured from experimental data. The measurements of n_q, n_p , and ϵ_p have

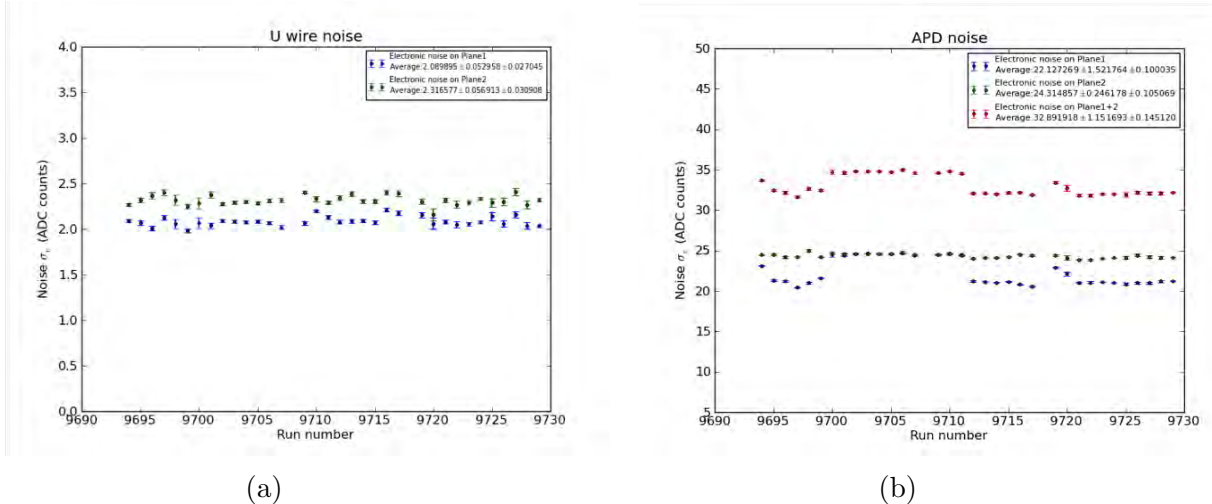


Figure 7.1: (a) Electronic noise on a single U-wire channel in TPC1 (blue) and TPC2 (green). For a given U-wire channel, the noise is measured through fitting the waveform amplitude before any signal pulse appears in the relevant data runs. (b) Summed electronic noise for all APDs in TPC1 (blue), TPC2 (green) and TPC1 plus TPC2 (red).

been described in Section 6.5.1. The total electronics noise for the APD and U-wire channels is measured by fitting the pre-pulse baselines recorded by the DAQ to the same signal model used to reconstruct data. This method ensures that the reconstructed noise is filtered and processed in the same way as the detector signals. The resulting noise measurements, after accounting for the average channel multiplicity (i.e. that multiple charge and light channels typically need to be summed to fully reconstruct all energy) are shown in Table 7.1. The charge channels have similar noise in Phase I and Phase II data, with a mean of $\sigma_{q,noise} = 770 e^-$ (see Figure 7.1a) and $\sim 4.5\%$ variation over different channels. The light channels have significantly smaller noise in Phase II relative to Phase I due to an upgrade to the electronics between the two operating periods described in Section 3.6. The measured noise summed over all APD channels is ~ 450 PEs in Phase I and ~ 150 PEs in Phase II (see Figure 7.1b), corresponding to a reduction by $\sim 3\times$.

The recombination fluctuations, σ_r , listed in Table 7.2 are measured by subtracting the detector noise from the total measured variance in the charge and light pho-

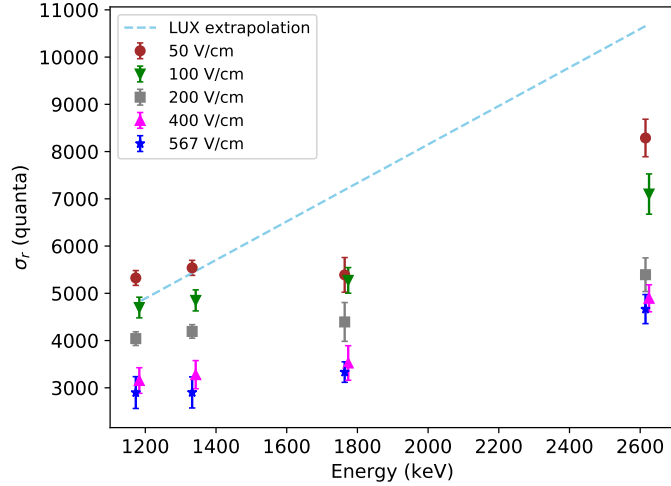


Figure 7.2: Measured recombination fluctuations versus incident γ -ray energy under different electric fields. All points are taken at the energies corresponding to the photopeaks of the calibration sources, but a small plotting offset is added in energy to improve visibility of their errors. The dashed line is a linear extrapolation from the LUX measurements performed at fields varying from 43 to 491 V/cm using β decay signals [15].

topeaks [189]. Figure 7.2 shows the measured recombination fluctuations, σ_r , as a function of energy using data taken during Phase II. While these recombination fluctuations have been found to scale approximately linearly in energy at energies below 1 MeV [15, 110, 145], in the higher energy region measured here, the increase in σ_r with energy is found to be smaller than would be expected from extrapolating the linear dependence observed at lower energy.

The same laser calibration data used to determine the APD avalanche gain (described in Section 6.5) can be used to measure the APD excess noise factor, F_N , due to fluctuations in the avalanche process. The variance of the amplitude of repeated laser pulses (5000 pulses are taken at each gain setting in each calibration) can be written as $\sigma_{laser}^2 = G^2 F_N n_{PE} + n_{PE}^2 \sigma_{NU}^2 + \sigma_{noise}^2$, where G is the APD gain obtained in Section 6.5.1 and n_{PE} is the average number of PEs per pulse. Here σ_{noise} includes all noise terms that do not depend on the avalanche gain, including electronics noise, fluctuations in the laser power between pulses, etc. Since the laser

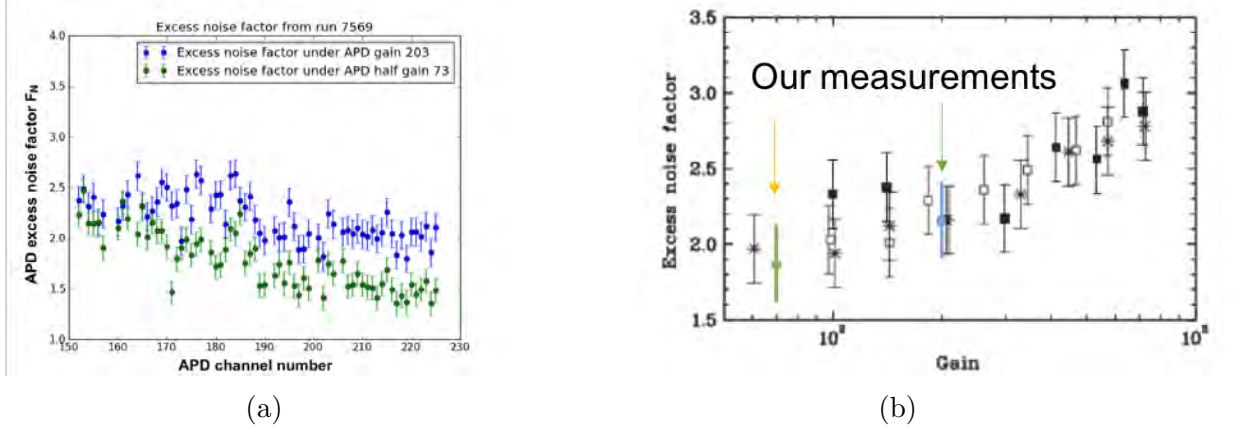


Figure 7.3: (a) APD excess noise factors measured using the laser calibration data under two different gains for all available APD channels. (b) Comparison between the average APD excess noise factors measured in EXO-200 (blue and green) and previous measurements (black) from [16].

light passing through the diffuser in the opposite TPC illuminates each APD channel in a gang approximately uniformly, the non-uniformity term σ_{NU}^2 is negligible. Therefore the excess noise after avalanche can be estimated using the measured variance in the unity gain calibration, $F_N = (\sigma_{laser}^2 - \sigma_{p,noise}^2)/(G^2 n_{PE})$. The measured F_N for different APD channels are shown in Figure 7.3a. The average value of $F_N \sim 2.15$ obtained from EXO-200 data is consistent with previous measurements performed in Ref. [16] for a similar type of APD, as shown in Figure 7.3b.

The values of the resolution model quantities that are independent of the electric field are listed in Table 7.1. The measured electric field dependent quantities are listed in Table 7.2.

Using the measured quantities above, the best resolution predicted by the model can be obtained through minimizing Eq. 7.4 with respect to the rotation angle θ . The comparison between the measured resolution in Phase I and Phase II, and the predictions from the resolution model under various electric fields is shown in Figure 7.5. The resolution values shown here are measured without implementing the de-noising algorithm described in [117] to allow the noise to be directly estimated from the summed charge and APD waveforms.

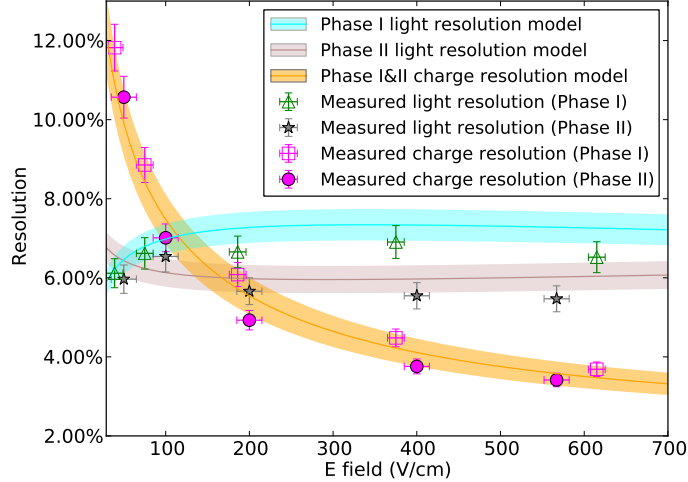


Figure 7.4: Comparison of measured light and charge energy resolution at 2615 keV under different electric fields with predictions from the resolution model.

The resolution for the individual charge and light channels are shown in Figure 7.4. The measured values agree with the prediction from the resolution model within the systematic errors. For data taken during Phase I, the light channel resolution becomes slightly larger as the electric field increases since the APD electronics noise remains constant while the photon yield decreases. In contrast, data taken during Phase II have lower APD electronics noise compared to Phase I, and the light channel resolution improves as the recombination fluctuations are reduced at higher electric fields.

The overall energy resolution is improved after the electronics upgrade, due to the lowered APD noise. In addition, the rotated resolution improves with increasing electric field in both the model and data since more energy is collected by the charge channels, which have relatively lower noise. The model predicts the resolution at -12 kV cathode bias (corresponding to an electric field of 567 V/cm) of $\sigma_E/E = [1.25 \pm 0.08$ (syst.) ± 0.02 (stat.)]%, achieved at the optimal angle in the model of $\theta = 39 \pm 2^\circ$. This value is consistent, within error, with the rotation angle of $43 \pm 3^\circ$ measured in Figure 6.5 under the same field. The model also agrees with the measured Phase II resolution of 1.23% for the non-denoised data [109]. As shown in

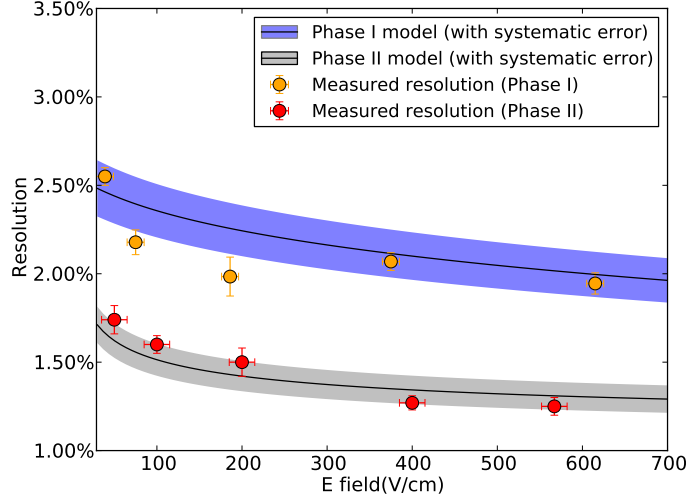


Figure 7.5: Comparison between measured rotated energy resolution at 2615 keV under different electric fields and predictions from the resolution model. Data taken during Phase II has better resolution than Phase I due to the reduced APD noise after the electronics upgrade.

Figure 7.5, the model matches the data for both Phase I and Phase II (before and after the electronics upgrade) and can reproduce the electric field dependence within systematic errors.

In summary, this resolution model is consistent with the observed resolution in EXO-200 and can be used to predict the performance of future LXe detectors once all relevant quantities are measured. Relative to EXO-200, the energy resolution for LXe detectors can be further improved by eliminating the dominant sources of noise above, e.g. electronics noise in the photo-detector readout [19].

7.4 Measurement of the recombination efficiency

$$\epsilon_r$$

In previous sections, it is assumed that every recombined electron generates a VUV photon, such that the recombination fluctuations of the charge channel σ_{rq}^2 and the light channel σ_{rp}^2 are identical. In general, the fluctuation for the light channel is

$\sigma_{rp}^2 = \epsilon_r \sigma_{rq}^2$, where ϵ_r is the recombination efficiency, i.e., the fraction of recombined electrons which produce a VUV photon. The covariance between the charge and light response is then $\text{Cov}_{q,p} = -\epsilon_r \sigma_{rq}^2$. A value of $\epsilon_r = 1$ would correspond to perfect recombination efficiency. If an absolute calibration of the light detection efficiency ϵ_p were available, ϵ_r could be directly measured from the change in the charge and light response at different fields, but since the measurement of ϵ_p above relies on the assumption that $\epsilon_r = 1$, the previous measurements cannot be used directly to determine ϵ_r . However, we can use the agreement of the resolution model with the observed variance in data to test this assumption.

Since both the light channel fluctuations and the covariance term can be written in terms of σ_{rq} , the variance in the total number of quanta for a general value of ϵ_r is:

$$\sigma_n^2 = \cos^2(\theta)\sigma_q^2 + \sin^2(\theta)\sigma_p^2 - 2\epsilon_r \cos(\theta) \sin(\theta)\sigma_{rq}^2 \quad (7.7)$$

where the total charge and light variances are: $\sigma_q^2 = \sigma_{rq}^2 + \sigma_{q,noise}^2$ and $\sigma_p^2 = \epsilon_r^2 \sigma_{rq}^2 + \frac{1}{\epsilon_p^2} [n_{PE}(F_N - 1 + B^2) + \sigma_{p,noise}^2 + n_{PE}^2 \sigma_{NU}^2]$. σ_{rq} in Eq. 7.7 denotes the recombination fluctuations in the electron count and is estimated by subtracting the electronics noise term from the measured total charge variance.

Using the measurements of the various detector parameters described above (and relaxing the assumption of $\epsilon_r = 1$ used to previously estimate ϵ_p), Eq. 7.7 is a function of only two unknown parameters, ϵ_p and ϵ_r , with the optimal rotation angle θ determined by minimizing the rotated resolution for each set of parameters. We construct a χ^2 statistic by comparing the resolution predicted by the model with the experimental data: $\chi^2 = \sum \frac{[X(\epsilon_p, \epsilon_r) - X_{exp}]^2}{\sigma_X^2}$, where the sum is over all measurements performed under various electric fields, $X(\epsilon_p, \epsilon_r)$ is the predicted observable for photon detection efficiency ϵ_p and recombination efficiency ϵ_r , X_{exp} is the measured value from experimental data, and σ_X is the uncertainty of the measured observable. The values, X , used in the fit include the charge resolution, light resolution, rotated res-

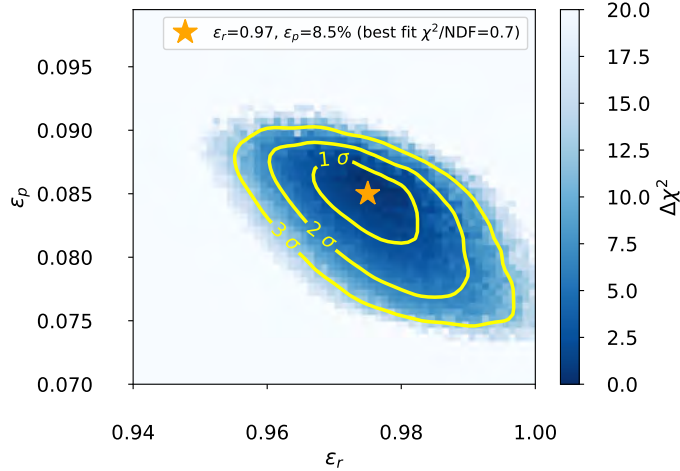


Figure 7.6: Change in the χ^2 relative to the best fit point (star) obtained by fitting the predicted energy resolution and the expected change in the light and charge yields versus electric field for various values of the photon detection efficiency, ϵ_p , and intrinsic recombination efficiency, ϵ_r , to the observed data.

olution, the change in the mean number of electrons, Δn_q , and the decrease in PE counts, Δn_{PE} , as the electric field changes. Since the mean change in the electron and PE counts are related by $\Delta n_{PE} = \Delta n_q \cdot \epsilon_r \cdot \epsilon_p$, a simultaneous fit to these data and the resolution in each channel is used to constrain ϵ_p and ϵ_r . The fit contains nuisance parameters incorporating possible systematic errors on B and the overall calibration of the number of PE/ADC counts, which are profiled over when calculating the χ^2 .

The combined χ^2 fit is performed using the ^{228}Th source calibration data from Phase II as described in Section 6.5, for which there is a single high-statistics photopeak that can be used to measure the data values at each electric field. The results of the χ^2 fit to these data are shown in Figure 7.6. The best fit occurs at $\epsilon_r = 0.97$ and $\epsilon_p = 8.5\%$. While the fit finds a value of ϵ_r very close to 1 as assumed in previous sections, it does prefer a non-unity value for this parameter at 3σ , indicating that the best fit to the resolution in the model occurs if 1–4% of recombining electron-ion pairs do not produce a detectable photon. In addition, relaxing the assumption on ϵ_r does not substantially affect the best-fit value of ϵ_p , and the W value that would be inferred using this best-fit point agrees within systematic errors with that reported in

Section 6.5.1. These results depend on the accuracy of the semi-empirical resolution model described above, and unknown sources of systematic errors or contributions to the overall resolution that are not included in the model could affect the best fit value for ϵ_r and its consistency with unity.

Chapter 8

High-bandwidth Digital Data

Transmission for nEXO

nEXO is the next generation tonne-scale $0\nu\beta\beta$ experiment using ^{136}Xe aiming to achieve a half-life sensitivity of $\sim 10^{28}$ years [19]. nEXO requires substantially more electronics channels compared to EXO-200 due to higher data rates. This chapter gives an introduction to the nEXO detector design and then focuses on the development of high-speed cables with low radio-activity for signal transmission in the nEXO detector.

8.1 Introduction of the nEXO detector

nEXO is aimed to improve its sensitivity to $0\nu\beta\beta$ signals by three orders of magnitude compared to its precursor experiment EXO-200. To achieve that goal, the nEXO TPC is designed to be a single, ~ 1.3 m long cylinder vessel made of low-radioactivity copper with a diameter exceeding 1 m that contains 4038 kg of LXe enriched to 90% in the ^{136}Xe . It is housed in a spherical, vacuum insulated cryostat. The inner cryostat vessel has a diameter of 338 cm and is filled with $\sim 33,000$ kg HFE cryo-fluid. The outer vessel with diameter of 446 cm provides the vacuum insulation

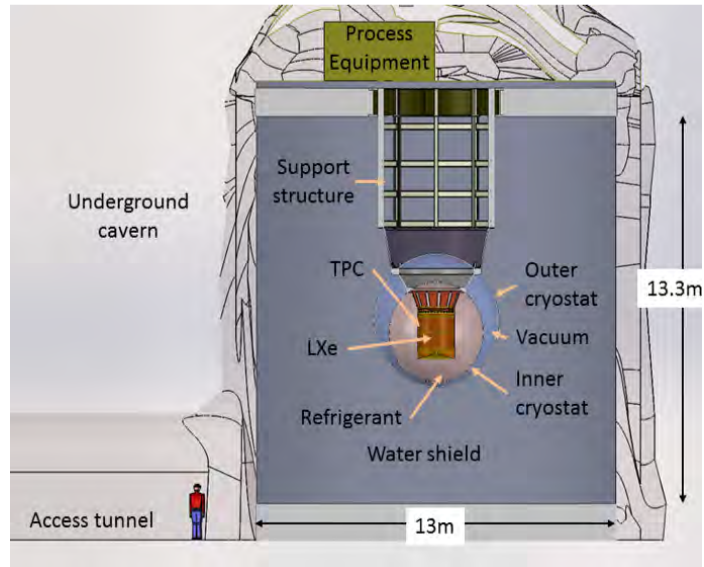


Figure 8.1: Schematic design of the nEXO detector, showing the LXe TPC housed in a vacuum insulated cryostat filled with HFE refrigerant fluid which acts as the innermost γ ray shield. The huge water tank provides a thicker shield and also functions as an active cosmic-ray veto detector based on Cherenkov light. The figure is extracted from [17], which assumes that the detector will be located in the Cryopit at SNOLAB with an overburden of 6010 m water equivalent [18].

required to maintain the inner cryostat at cryogenic temperature and keeps the LXe detector operating at the temperature of 167 K. In addition to creating a thermal bath for LXe, the HFE cryo-fluid also serves as the innermost γ ray shield. The thickness of HFE was chosen to be 76 cm to minimize the total backgrounds from the outer cryostat vessels and the HFE itself. The cryostat is submerged in a huge water tank which acts as a cosmic-ray veto detector. The water also reduces the neutron-induced background and shields against backgrounds originating from the walls of the underground lab. The conceptual design of the detector is shown in Figure 8.1, where we assume the experiment is going to take place in the Cryopit at the Sudbury Neutrino Observatory Laboratory (SNOLAB) near Sudbury, Ontario, Canada. With an overburden of 6010 m water equivalent, SNOLAB is significantly deeper underground than WIPP and can reduce cosmic-ray induced backgrounds.

Similar to EXO-200, a uniform electric field planned to be ~ 400 V/cm will be

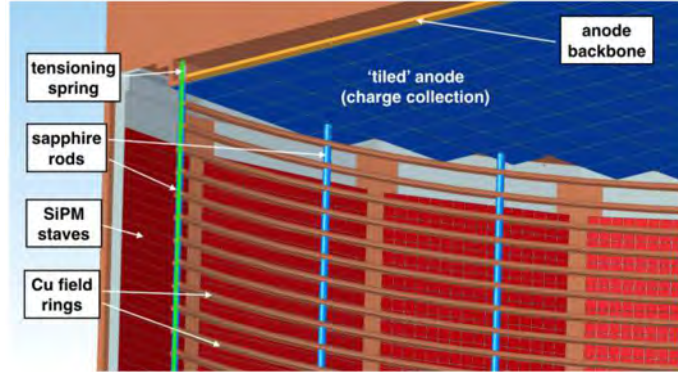


Figure 8.2: Design of the anode region in nEXO extracted from [17]. Shown in the figure are the charge collection tiles, SiPM staves behind the field cage, and sapphire tensioned rods.

generated by field shaping rings in the TPC in nEXO. However, unlike EXO-200 which has its cathode in the center, the cathode of the nEXO is positioned at the bottom of the cylindrical TPC. This design can remove radioactive backgrounds originating from the cathode itself from the TPC center. The field shaping rings are planned to be made of high-purity copper and separated by cylindrical sapphire vertical spacers shown in Figure 8.2. The sapphire rods are held in tension by springs above the anode region.

The ionization signals from particle interactions in nEXO are read out by crossed conductive strips with 3 mm width at the anode, deposited on $10 \times 10 \text{ cm}^2$ dielectric tiles [190]. Simulations have shown that a strip pitch of both 3 mm and 6 mm can both result in rather good background rejection [191], and the final pitch has not yet been fully determined. Compared to the wire readout used in EXO-200, the tile design avoids issues with long crossed wires, which require a large substantial tensioning frame and are vulnerable to ambiguity in reconstructing the position of MS events.

The scintillation signals are detected by UV-sensitive silicon photomultipliers (SiPMs) installed on SiPM staves in the barrel region inside the TPC, behind the field-shaping rings. Because the top and bottom of the cylinder are covered by opaque

charge collection tiles and the cathode, respectively, no SiPMs are installed at either end of the TPC volume. Characterizations of the SiPMs manufactured by Fondazione Bruno Kessler (FBK) [192], including their photon detection efficiency and the impact on the energy resolution of nEXO has been performed in [193]. The properties of an alternative SiPM produced by Hamamatsu was published in [194].

Both scintillation and ionization signals are digitized and transmitted out to the external data acquisition system using high-speed digital cables.

8.2 Background budget and the choice of interconnection cables

The large size of the nEXO TPC enables the shielding of backgrounds and increases the chance of detecting a $0\nu\beta\beta$, but at the same time makes it challenging to build and maintain certain aspects of the performance achieved in smaller detectors. For one thing, unlike EXO-200 where the front-end electronics were positioned outside of the cryostat, in nEXO the electronics are required to be placed very close to the TPC and operated at the cryogenic temperature. The advantage of using these “cold electronics” is that the path each signal has to travel before getting amplified can be shortened such that their noise is much lower than with warm electronics [195]. Figure 8.3 compares the simulated overall energy resolution at the Q-value in the case of room temperature electronics and cold electronics, which shows that using cold electronics can result in a substantial resolution improvement. On the other hand, since a large portion of the cables for transmitting digital data are located very close to the detector center, they are required to have low radioactivity to avoid contamination of the liquid xenon detector, as well as low outgassing of electronegative impurities to maintain the electron-lifetime of the charge signal. However, so far there has been no commercial high bandwidth digital cable which has low enough radioactivity for

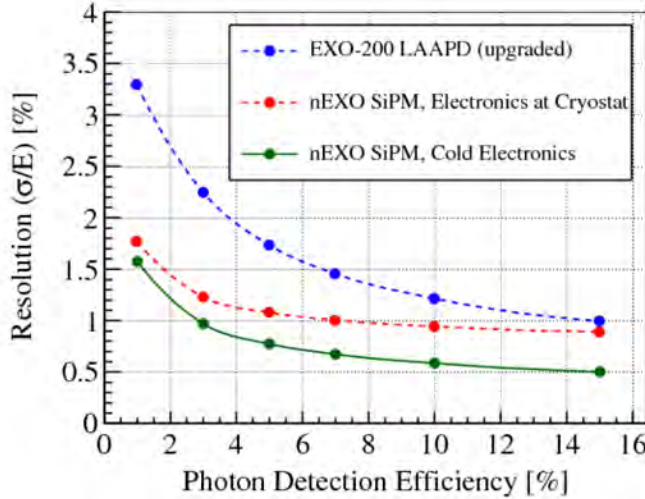


Figure 8.3: Energy resolution as a function of the scintillation light detection efficiency at a 400 V/cm drift field. The simulations are performed for charge-channel electronic noise in the case of both room temperature electronics (red) and cold electronics (green). The curve for the Phase-II EXO-200 detector is also shown. Figure courtesy of Ref. [17].

use.

A few options of transmission cables were considered at the research and development (R&D) stage for the interconnection system – Category 5 (Cat 5) Ethernet cables, Gore[®] cables [196], and flexible flat cables (used in EXO-200, mentioned in Section 3.5.1). The concentration of radioactive components in the three types of cables measured from radioassay are listed in Table 8.1. The Cat 5 Ethernet cable is a twisted pair cable commonly used for computer networks. Its radioactivity in ²³²Th and ⁴⁰K are so high that even if we have only ~ 1 m of such cables near the nEXO TPC, the amount of backgrounds produced in the ROI will surpass the sum of backgrounds from all other sources combined. Gore[®] cables, on the other hand, are made from copper wires and PTFE jackets which are much more radiopure, but their mass density (~ 2.6 g/m per channel) is rather high and will contribute to 75% of backgrounds in the ROI from the cables alone if used in nEXO, given that ~ 250 channels are needed in total. The EXO-200 experiment chose to use Espanex flat cable MC18-25-00CEM (1 mil Kapton, 18 μ m Cu) manufactured by Nippon Steel

Cable type	^{238}U	^{232}Th	^{40}K
Cat 5 Ethernet cable	-400 ± 400 ppt	1750 ± 1000 ppt	± 2500 ppb
Gore [®] cable	-10 ± 30 ppt	-108 ± 80 ppt	-90 ± 140 ppb
Flexible cable used in EXO-200 (Cu/Kapton)	161 ± 3 ppt	25 ± 1.5 ppt	< 210 ppb

Table 8.1: Concentration of radioactive components in different types of cables

Chemical Co. [115]. The flexible flat cables are very light and low-radioactive and are estimated to contribute to only $\sim 10\%$ of the total backgrounds in the ROI once deployed in nEXO. Our choice fell on the flexible flat cables for the following reasons: First, they have largest bandwidth per unit radioactivity compared to twisted pairs of wires such as Ethernet cables and Gore[®] cables; Second, they allow access and connections in the very limited space behind the charge collection plane so that active xenon volume can be maximized; Third, they allow for complicated routing into the cable conduits. On top of that, nEXO can borrow experience from EXO-200 when building the low background vacuum feedthrough (demonstrated in Figure 3.11c) for the flat cables.

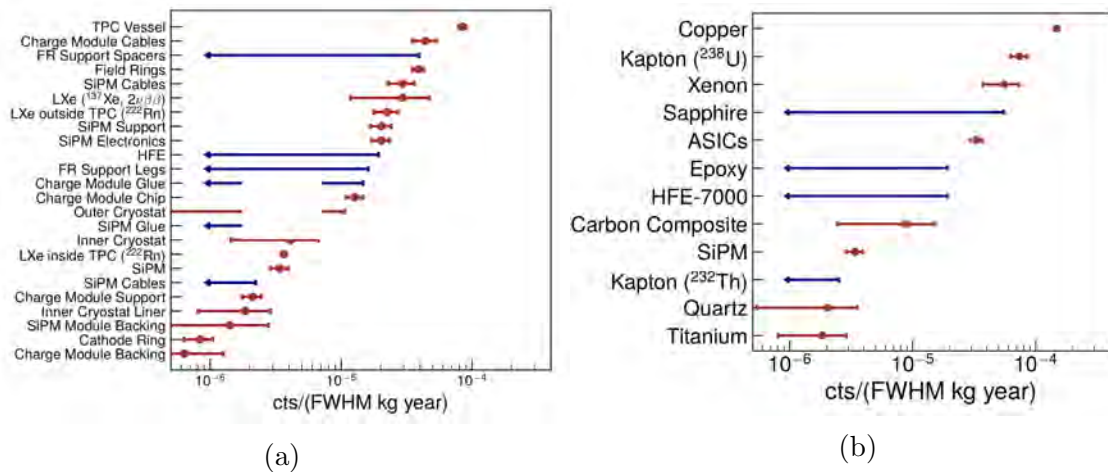


Figure 8.4: Background contributions (SS events only) to the ROI by detector component (a) and material (b) in the inner 2000 kg of the nEXO detector. The arrows indicate 90% C.L. upper limits while the circles indicate measured values with 1σ uncertainties. The cables are expected to be the second largest contributors to backgrounds. Figures are extracted from [19].

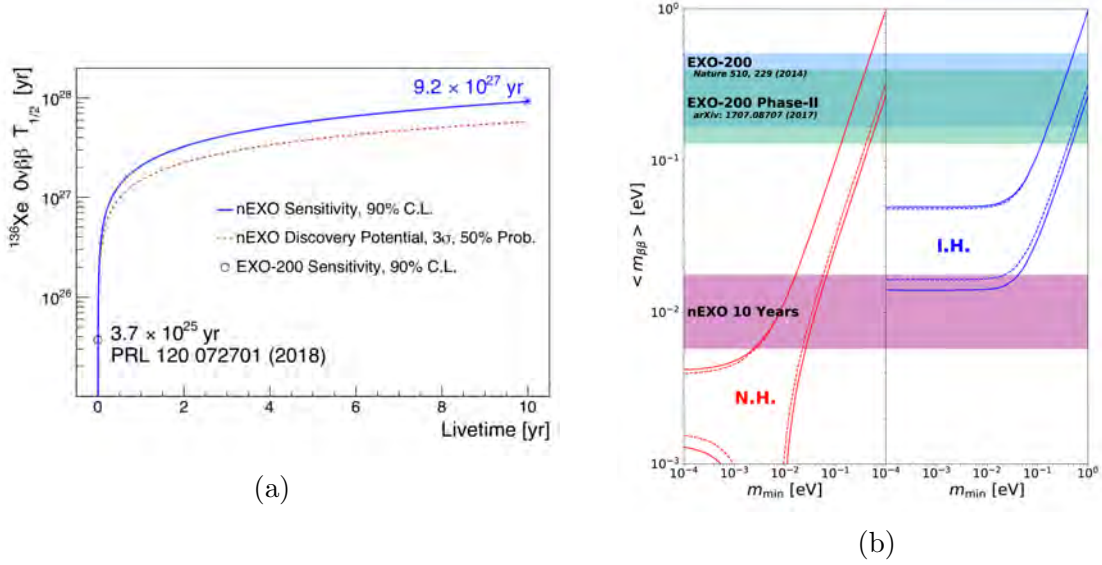


Figure 8.5: (a) Projected sensitivity and discovery potential of the nEXO experiment over time calculated based on the estimated background model. (b) 90% C.L. exclusion sensitivity reach to the effective Majorana mass $\langle m_{\beta\beta} \rangle$ as a function of the lightest neutrino mass for normal (left) and inverted (right) neutrino mass hierarchy. The width of the horizontal bands derive from the uncertainty in nuclear matrix elements. The width of the inner dashed bands result from the unknown Majorana phases. The outer solid lines incorporate the 90% CL errors of the 3-flavor neutrino fit of Ref. [20]. Both figures are extracted from Ref. [17]

Besides the data transmission cables, a careful selection of other materials for building the detector and a detailed evaluation their backgrounds was carried out in order to achieve the projected sensitivity. Figure 8.4 demonstrates the background budget grouped by detector component and material, from which we can observe that the largest contributors to backgrounds in the ROI are radio-impurities in the copper, primarily from the TPC vessel, while cables and field rings are the next largest contributors. Given the measured and estimated background level, the sensitivity of nEXO over time can be calculated, which is shown in Figure 8.5a. Figure 8.5b demonstrates the exclusion sensitivity reach of nEXO to the effective Majorana mass $\langle m_{\beta\beta} \rangle$ as a function of the lightest neutrino mass.

8.3 Characterization of the Prototype High-speed Cables for nEXO

The nEXO readout chain will consist of an Application-specific integrated circuit (ASIC), copper microstrip transmission lines on a Kapton substrate, together with warm and cold feedthroughs for the cables transitioning from the liquid xenon volume to the cryostat insulation vacuum and from the vacuum to the external atmosphere. A schematic picture of the interconnection design is shown in Figure 8.6. For each interconnection channel, the ionization or scintillation signals are digitized by the ASIC and transmitted through the Kapton cables wire bonded to the ASIC substrate, and then be collected by the Low-voltage differential signaling (LVDS) receiver in the end.

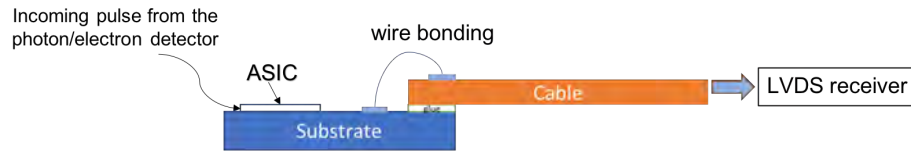


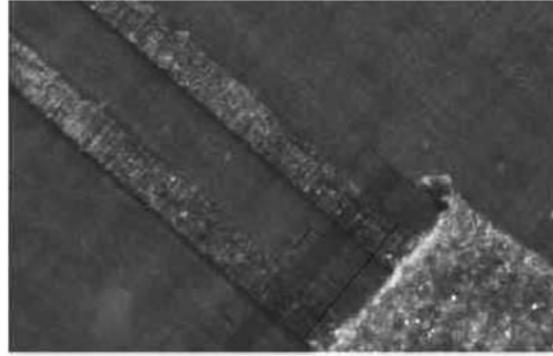
Figure 8.6: Design of the nEXO interconnection system consisting of an ASIC, Kapton cables and a LVDS receiver.

A set of prototype cables designed at SLAC was fabricated and preliminary studies of them were performed in the Wright Lab at Yale. Using microscope and the Time Domain Reflectometry (TDR) described below, we found the manufacturing of the transmission lines to meet nEXO requirements for tolerance and yield. No apparent discontinuities or tapering of the transmission lines were observed (see Figure.8.7b).

In Figure 8.7a there are three channels of transmission cables with different lengths. Each cable channel is a pair of coupled microstrip lines made of copper that can transmit differential signals. A schematic picture of the cross section of the coupled microstrip lines is shown in Figure 8.8. For the design in Figure 8.7, each copper trace has thickness $T = 1$ mil and width $W = 6.5$ mil. The spacing between



(a)



(b)

Figure 8.7: (a) The prototype cables designed at SLAC and tested at Yale. The close-up picture on the right shows the details of the coupled microstrip lines on the Kapton substrate. (b) Coupled transmission lines under microscope.

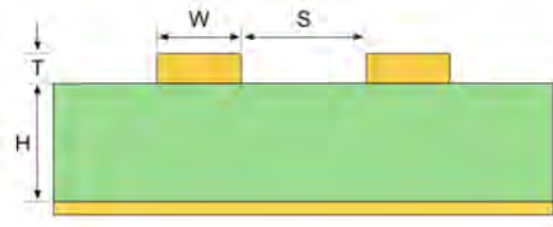


Figure 8.8: A cross-section view of a pair of coupled microstrip lines. Figure courtesy of [21]

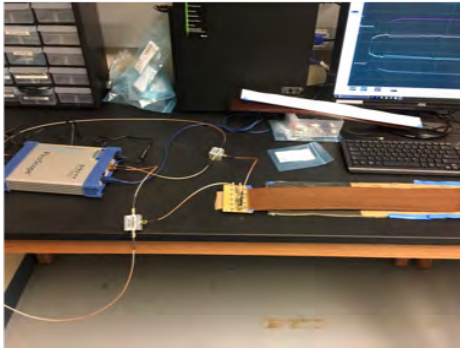
the two traces $S = 11$ mil and the Kapton substrate height $H = 2$ mil.

The TDR setup shown in Figure 8.9a consists of a pulse generator and receiver – PicoScope 9211A, a printed circuit board (PCB) which connects the signal generator to the cables. The PicoScope operates at a bandwidth of 12 GHz and has a rise time of 100 ps to 130 ps. Figure 8.9b demonstrates how a TDR measurement is performed. In a TDR measurement, a differential signal is generated by the PicoScope through the output channel 1 and 2 and split in to halves by the voltage dividers. Half of the pulse is transmitted to the PicoScope receiver directly, while the other half is propagated through the device under test. By analyzing the amplitude of the reflected pulse

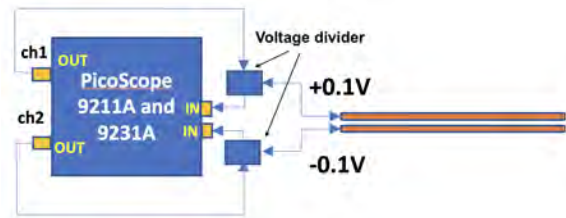
along the device, the nature of its impedance can be studied. If the device under test is of a uniform impedance there will be no reflections, but if there are impedance variations and mismatch, then we will be able to observe some signals reflected back to the PicoScope. The impedance Z of the device can be derived from the expression below:

$$Z = Z_0 \frac{1 + \rho}{1 - \rho} \quad (8.1)$$

where $Z_0 = 50 \Omega$ is the characteristic impedance of the coaxial cable that connects the PicoScope to the device under test, and ρ is the ratio between the reflected signal and the incident signal.



(a)



(b)

Figure 8.9: (a) TDR setup in the Wright Lab at Yale. The system consists of a PicoScope that is connected to a PCB through coaxial cables. The Kapton cables under test are soldered to the PCB. (b) Demonstration of the working principle of the TDR setup.

Each cable under test in Figure 8.9a is soldered to the circuit board, and there is a termination resistor between each differential pair to prevent large voltage reflection. The result from the TDR measurement for one cable channel is shown in Figure 8.10, which indicates each copper trace of the differential pair has a characteristic impedance of 37Ω . This impedance is also known as “odd impedance”, as the two copper traces are driven with opposite polarity signals. The measured odd impedance is in agreement with the theoretically calculated value of 39.2Ω from Ref. [21] for the given cable geometry.

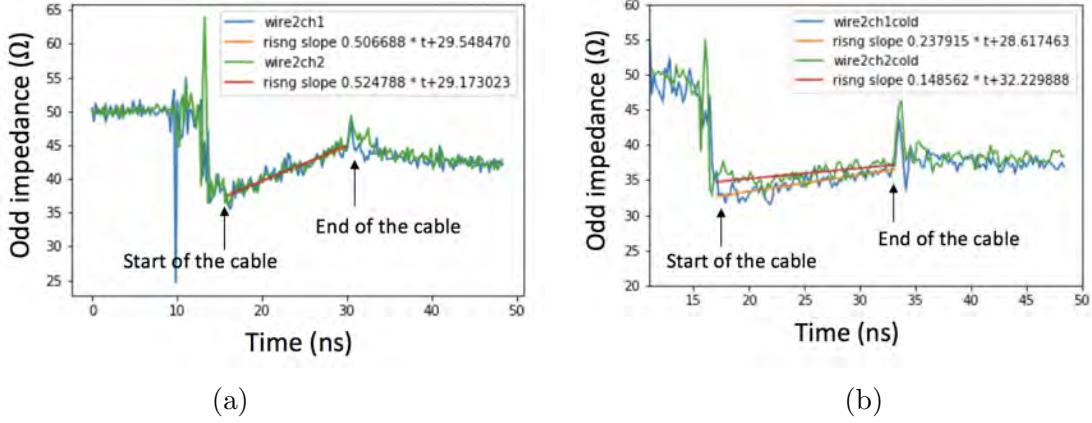


Figure 8.10: TDR measurements of the cable's impedance at room temperature (a) and liquid nitrogen temperature (b). The start and end of the copper trace are indicated in the plot.

The huge spikes in the impedance versus time curve in Figure 8.10 are caused by impedance mismatch at the interconnection point between the copper traces and the coaxial cables.

Based on the telegrapher's equations [197], the expression for the characteristic impedance of a generic transmission line shown in Figure 8.11 is $Z = \sqrt{\frac{R+j\omega L}{G+j\omega C}}$, in which R , L , C , G are series resistance, series inductance, shunt capacitance and shunt conductance, respectively. In the limit $G \rightarrow 0$, Z can be written as $Z = Z_c(1 + \frac{1}{j\omega\tau})$ using a first-order Taylor-series approximation, where $Z_c = \sqrt{\frac{L}{C}}$ and $\tau = \frac{2L}{R}$. In the time domain, this indicates that the impedance of the transmission line in response to a step input has a gradual rising slope:

$$Z(t) = Z_c(1 + \frac{t}{\tau}) \quad (8.2)$$

By similar reasoning, if $R \rightarrow 0$, the shunt conductance G will generate a negative slope with $\tau = -\frac{2C}{G}$. More details of the derivation of Eq. 8.2 can be found in Ref. [198]. In our experimental setup, the resistive loss of the copper $R \approx 4 \Omega/\text{m}$ is measured with a multimeter, the shunt conductance between the two copper traces $G \approx 6 \times 10^{-4} \text{ S}/\text{m}$ is estimated from the loss tangent measurement [199], the inductance of the copper

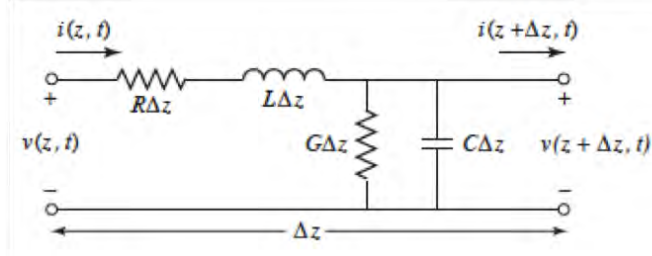


Figure 8.11: Schematic picture of the lumped-element circuit model for coupled transmission lines driven by a differential signal. R , L , C , G are series resistance (Ω/m), series inductance (H/m), shunt capacitance (F/m) and shunt conductance (S/m), respectively.

trace $L \approx 2 \times 10^{-7} \text{ H}/\text{m}$ and the capacitance $C \approx 1 \times 10^{-10} \text{ F}/\text{m}$ are calculated by the COMSOL finite element simulation. Therefore, the slope caused by resistive loss R is $0.4 \text{ } \Omega/\text{ns}$, while by shunt conductance G is $-0.072 \text{ } \Omega/\text{ns}$. Clearly the resistive effect R dominates the total loss, which results in $\tau \approx 100 \text{ ns}$ in Eq. 8.2. Thus the theoretical calculation is roughly consistent with the measured slope ($0.5 \text{ } \Omega/\text{ns}$).

Since the resistive loss of the microstrip transmission lines is smaller at lower temperature, the slope of the impedance versus time curve is observed to be significantly reduced when the TDR measurement is performed at liquid nitrogen temperature ($\sim 77 \text{ K}$), as shown in Figure 8.10b.

COMSOL simulations of impedance versus time curve in Figure 8.12a also indicates a similar slope of $0.49 \text{ } \Omega/\text{ns}$ under the room temperature setting, and is reduced by a factor of ~ 2 when the temperature is lowered to $\sim 77 \text{ K}$, which is consistent with experimental observations.

Given the resistive loss measured and simulated at low-temperature, and assuming perfect impedance matching in the interconnection system so that signal loss only takes places as it transmits through the cable, it can be estimated that a cable lengths up to 5 m is allowed if we want to ensure $>95\%$ of the signal can survive. This could satisfy the need of nEXO, which only requires cables of length less than 2 m .

To characterize the signal transmission through the wire bonds that connect the

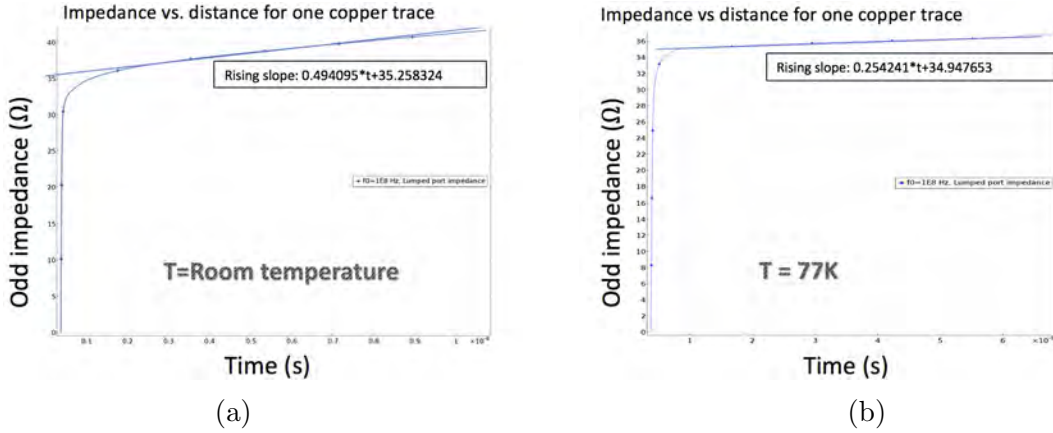


Figure 8.12: COMSOL simulations of the impedance versus time curve for a single copper trace in the differential pair under room temperature (a) and liquid nitrogen temperature (b).

cables to the ASIC substrate shown in Figure 8.6, we first formed some test wire bonds of different lengths between copper traces on two PCB boards using the wire bonding machine at Brookhaven National Laboratory (BNL). As shown in Figure 8.13, the geometry of the wire bond can be visualized and measured accurately under the microscope. Then we performed a TDR measurement on the wire bond connection and the resulting odd impedance versus time curves are shown in Figure 8.14. Because the wire bond’s inductance increases with its length, the effective impedance for the longer wire bond is larger. Based on the measurement results, it is estimated that a ~ 1 mm wire bond or shorter should be good enough to minimize impedance mismatch and enable relatively smooth signal transmission. To make the interconnection more robust and further reduce the total effective impedance, it will also be helpful to form multiple wire bonds on each copper trace in the future.

From the TDR measurement shown in Figure 8.10, one can observe that the cables designed at SLAC have much smaller odd impedance than coaxial cables (50 Ω). Since the LVDS receiver in Figure 8.6 also has an odd impedance of 50 Ω (i.e., 100 Ω total differential impedance), it is required that we redesign a set of cables that have higher characteristic impedance to minimize impedance mismatch. The geometry of

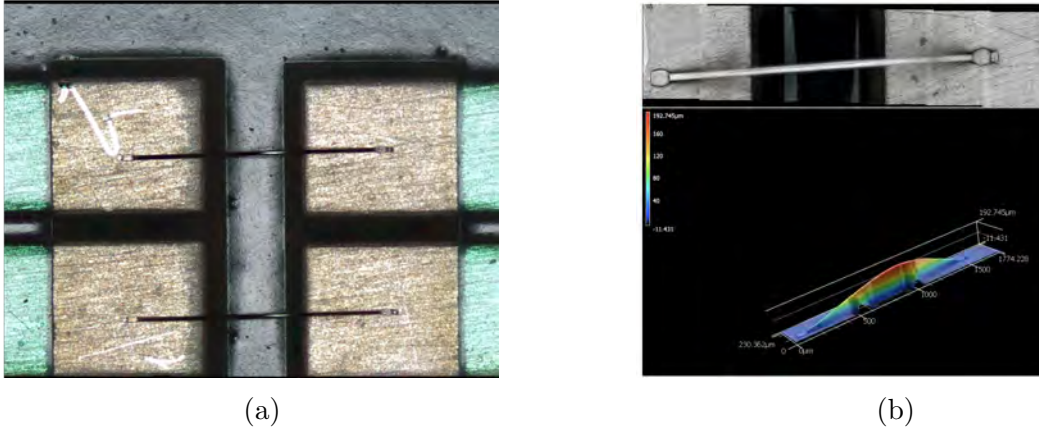


Figure 8.13: (a) Wire bonds formed at BNL. Shown are copper traces on a PCB with silver finish, connected through aluminum wire bonds with $25 \mu\text{m}$ in diameter. (b) 3D geometry of the wire bond observed with the laser microscope at BNL.

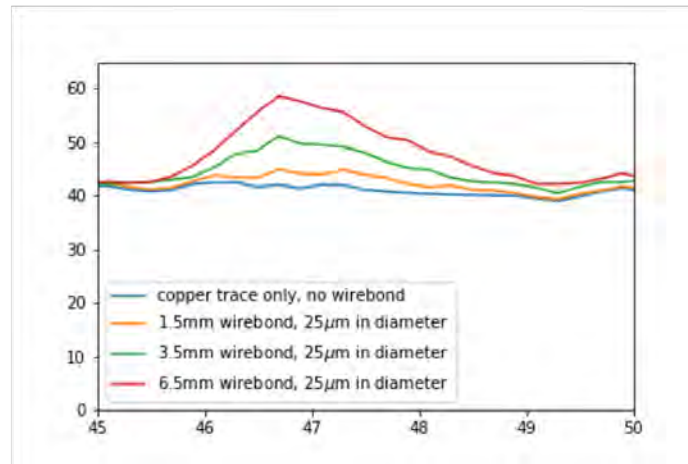


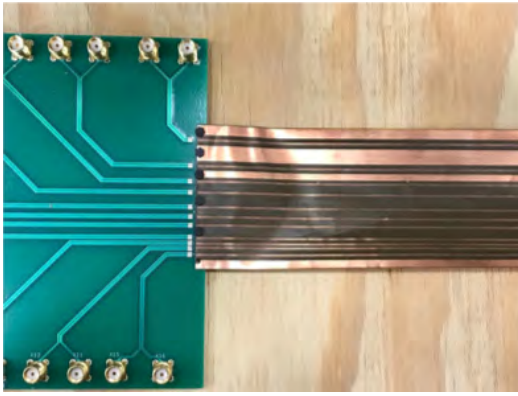
Figure 8.14: The impedance versus time curve for wire bonds of various lengths measured from the TDR. The baseline (blue) in the plot indicates the impedance of a continuous copper trace. As the length of the wire bond increases, its effective impedance also grows.

the new coupled microstrip lines is listed in Table 8.2, and a picture of the new cables manufactured by Qflex [22] using copper Kapton laminates from Taiflex [23] is shown in Figure 8.15a. The TDR measurement result for the new cable is demonstrated in Figure 8.15b, which indicates its characteristic odd impedance is the same as designed ($\sim 50 \Omega$) and will meet the requirements for the LVDS receiver. Moreover, the ICP-MS radioassay analysis performed at Pacific Northwest National Laboratory (PNNL) shows that after proper cleaning, this set of new cable we designed has ~ 10 times

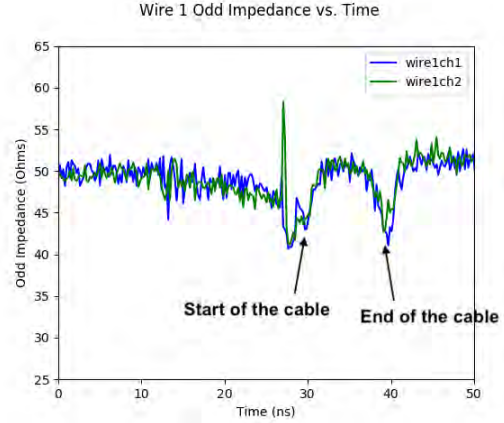
Copper trace length	Trace thickness	Kapton substrate height	Trace width	Trace spacing	Substrate Dielectric
1 m	0.7 mil	2 mil	4.8 mil	11 mil	3.3

Table 8.2: Parameters of the newly designed set of cables, the cross section view of the cable is shown in Figure 8.8

lower radioactivity in ^{232}Th and ^{238}U compared to the cables used in EXO-200 [200].



(a)



(b)

Figure 8.15: (a) A new set of cables designed to have characteristic impedance of $\sim 50 \Omega$ and manufactured by Qflex [22] using copper Kapton laminates from Tai-flex [23]. (b) TDR measurement performed on one of the new cable channels.

Finally, COMSOL simulations are carried out to account for possible impedance mismatch as the cables transition from the LXe volume to the cryostat insulation vacuum through the epoxy feedthrough. As shown in Figure 8.16, since the dielectric constants of LXe ($\epsilon_r \sim 1.9$), epoxy ($\epsilon_r \sim 4$) and the cryostat vacuum ($\epsilon_r \sim 1$) are different, the shunt capacitance between the copper traces varies in these three media, and so does their characteristic impedance. Therefore the copper traces are tapered in the simulation to minimize impedance mismatch at the interfaces between the different materials. In particular, for the fraction of the cable inside the epoxy, where the dielectric constant is relatively large compared to LXe, the increase in capacitance between the copper traces can be counteracted by reducing the width of each copper trace and increasing the spacing between the two traces. For the portion

of cable inside the vacuum, on the other hand, the width of each copper trace needs to be increased while the spacing between them should be decreased. Such a tapering method ensures that the final channel width is almost unchanged, and we can have the same number of cable channels on a given Kapton substrate before and after the cables are tapered.

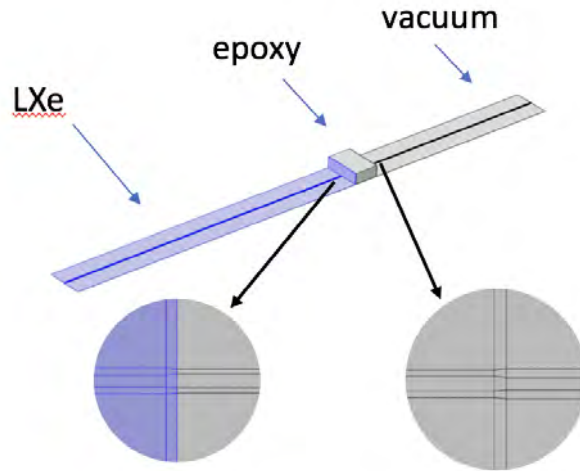


Figure 8.16: Geometry of the cable in the COMSOL simulation. As the dielectric constants of LXe, the epoxy feedthrough and the cryostat vacuum vary, the copper traces are tapered in the simulation (demonstrated by the close-ups in the figure) to minimize impedance mismatch and optimize signal transmission.

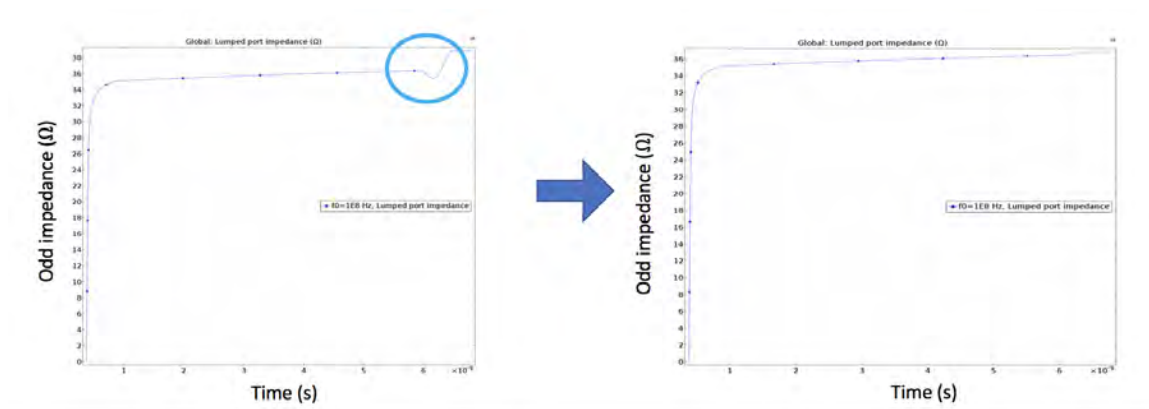


Figure 8.17: COMSOL simulations of the impedance versus time curve as the cable goes through epoxy. It shows that a $\sim 2 \Omega$ of impedance mismatch exists (left) if the cable geometries in the three media shown in Figure 8.16 are identical. This mismatch can be eliminated after the cable is tapered (right).

8.4 Summary

Above we have discussed the necessity of developing high-speed cables with low radioactivity for signal transmission in the nEXO detector. Prototype cables have been designed and manufactured and a number of their key features needed for nEXO have been demonstrated by this work:

- The TDR measurement has proved the signal loss on the differential microstrip lines to be sufficiently low.
- The design of the cable on a thin substrate has met the impedance requirements. The measured and theoretically calculated impedance are consistent with each other.
- The electrical connection between the cable and interface PCB board has low loss.
- We have identified that the cables manufactured using Taiflex copper Kapton laminates have more than an order of magnitude lower background than previously known laminates used in EXO-200.

The next steps for the interconnection development will be continued at BNL. These include:

- Build radiopure cable-to-cable connections to facilitate cable fabrication and detector assembly.
- Replace the current test interface boards made of epoxy with quartz boards that have lower loss, and be able to form wire bonds between them and the flat cables. Alternatives to wire bonds such as bump bonds, conductive epoxy, and fuzz buttons will also be considered.

- Determine the layout of cables in the detector and build prototype feedthroughs.

Finally we will need to demonstrate the full readout chain including the ASIC, cables and feedthrough and optimize the bit-error-rate of the data transmission system.

Chapter 9

Conclusions and Future Work

In this work, we have presented results from an improved search for $0\nu\beta\beta$ of ^{136}Xe . The lower limit on the $0\nu\beta\beta$ half-life of ^{136}Xe measured from the complete EXO-200 dataset is $T_{1/2} > 3.5 \times 10^{25}$ yr at 90% CL, and the combined Phase I and Phase II sensitivities is 5.0×10^{25} yr. It is also worth noting that with a ~ 200 kg detector, EXO-200 has achieved similar sensitivity as the kton-scale liquid scintillator loaded with ~ 400 kg enriched xenon in the KamLAND-Zen experiment [201]. Among all the efforts for analyzing the final data, the author of this thesis was the primary analyzer responsible for various aspects of the energy calibration and resolution measurement. Beyond this work, which improved the energy resolution through correcting the spatial and time variation of the detector's energy response to calibration sources, there is some room for further improvement in the energy resolution. For one thing, the lightmaps that we used in data processing and the denoising algorithm were constructed from ^{228}Th source calibration data, which were subject to systematic and statistical noise. Because the ^{228}Th source could only be positioned at four locations outside the TPC, the available data in the bulk LXe for constructing the lightmap was not as sufficient as those near the anode and cathode. To avoid this issue, it is proposed that for future experiments, we can inject radon into the bulk LXe and

use its characteristic α peaks to construct the lightmap. Alternatively, if we can build a more accurate lightmap through precise simulations of the transportation of photons generated by light signals of given energies in the LXe detector, then the reconstructed scintillation energy resolution is likely to be further improved. As for the charge channel, studies have shown that using a deep neural network (DNN) trained on the raw waveforms collected by the U-wires for energy and position reconstruction could improve the final resolution [24]. In principle, similar DNNs could be applied on the light signals, and several attempts for building a DNN model to reconstruct the light energy are described in Appendix B. Further work is needed to enable the DNN approach to improve both the charge and light energy resolution.

We have also shown an absolute measurement of ionization and scintillation yields and the W-value in LXe using γ -rays from ^{228}Th (2615 keV), ^{226}Ra (1764 keV) and ^{60}Co (1332 keV and 1173 keV) calibration sources at a variety of electric fields. The measurement benefits from the use of a large, single-phase TPC, for which the charge response can be absolutely calibrated. This is the first simultaneous measurement of absolute light and charge yields over the 1–2.5 MeV energy range, and the W-value $W = 11.5 \pm 0.5(\text{syst.}) \pm 0.1(\text{stat.}) \text{ eV}$ derived from it deviates by $\sim 15\%$ from the value currently adopted by NEST. A number of systematic cross-checks have been performed on these measurements, using the detailed understanding of the EXO-200 detector response developed throughout the operation of the experiment. This measurement takes advantage of a large detector with a well-understood energy response, which is based on a comprehensive detector Monte Carlo simulation. These results provide new measurements of the absolute yields of charge and light in LXe at MeV energies, extending previous measurements primarily performed with smaller R&D systems at lower energies. The discrepancy observed between our measured W-value and previous measurements could be attributed to the use of calibration sources of different energies, the emission of IR photons in LXe that PMTs used in previous

experiments were not sensitive to, and the fact that smaller detectors from the past were subject to larger systematic errors. The measurements presented can also guide simulations of the charge and light production in future $0\nu\beta\beta$ and rare event searches employing LXe. Moreover, a semi-empirical model consistent with the energy resolution measured in EXO-200 data at a variety of electric fields is provided, based on direct measurements of the relevant detector parameters, including recombination fluctuations in the number of electrons and photons at various energies. This model can account for the dominant sources of noise in the EXO-200 energy measurement, and places constraints on the recombination efficiency of electron-ion pairs in LXe. For future studies, absolute measurements of ionization and scintillation yields produced by α decays can be carried out using the ^{222}Rn source injected into the LXe at the end of EXO-200 run. The measured data can be used to further improve modeling in the NEST software package. In addition, similar yield measurements for γ sources with energies below 1 MeV need to be performed using LXe detectors similar to or larger than EXO-200 in order to confirm the W-value of LXe at all energies.

The success of the EXO-200 experiment has paved the way to nEXO, the next generation tonne-scale $0\nu\beta\beta$ experiment. In final chapter of the thesis, we have described the development of high-bandwidth digital data transmission cables for the nEXO detector. In the future, we will integrate these cables with the readout ASIC and required vessel feedthroughs to ensure smooth signal transitioning from the liquid xenon volume to the cryostat insulation vacuum and from the vacuum to the external atmosphere. The prototype readout system for nEXO composed of flexible cables and interconnecting circuits will be tested and optimized to minimize the system's bit-error-rate. While the interconnection system will be designed specifically for nEXO, the demonstration of radiopure high-bandwidth cabling and interconnection techniques is relevant for many next-generation rare-event searches with large channel counts and high-speed digital electronics.

Appendices

Appendix A

APD Gain Non-uniformity

Each APD channel consists of ~ 7 individual APDs ganged together in a single readout channel [173], which are biased with a single voltage for the entire gang. The gain non-uniformity among the APDs within a gang may cause variation in the measured photon count for a given photopeak.

We make use of the lightmap described in Section 4.4, which provides an empirical measurement of the PE number created in each APD channel given a scintillation cluster's 3D position, to determine this additional σ_{NU} in Eq. 7.6. The APD plane in TPC1 (TPC2) is located at $z = 204$ mm ($z = -204$ mm). To select energy deposits occurring near the APD plane, but within the fiducial volume of the detector, we select clusters occurring at $z = 182 \pm 1$ mm ($z = -182 \pm 1$ mm), and record the number of PEs collected by the APD closest to each event. For such events, a larger number of photons are collected by the single APD in each readout gang closest to the event position, which allows the estimation of the gain variation among the APDs within the gang. During EXO-200 operations, five APD gangs could not be operated due to hardware problems and were not considered in the measurement.

Figure A.1 shows the response of the closest APD gang to the cluster location as a function of x - y position. Only x - y positions directly above the circular face of an APD

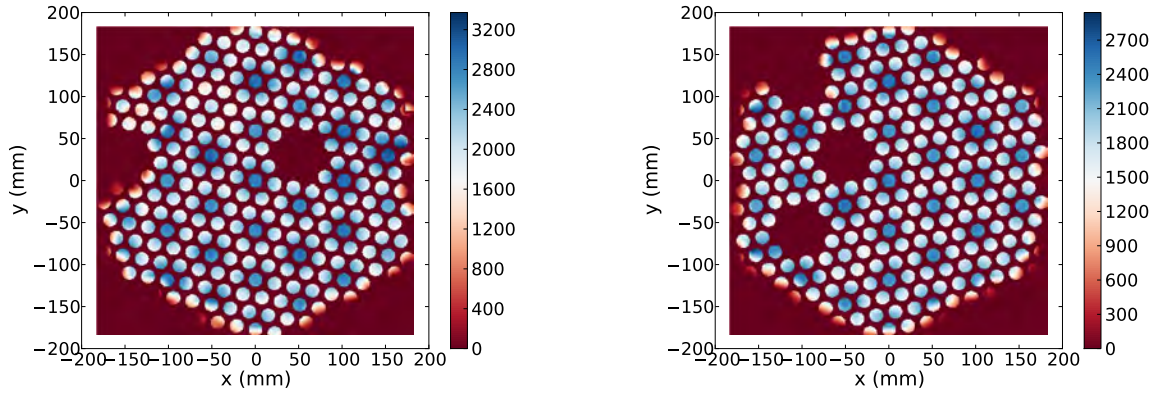


Figure A.1: PE counts on each APD from a scintillation cluster right above it at $z = 182$ mm for TPC1 (left) and $z = -182$ mm for TPC2 (right) measured using the lightmap before solid angle correction. Five APD channels were disconnected due to hardware problems during EXO-200 operations and are removed from the figure.

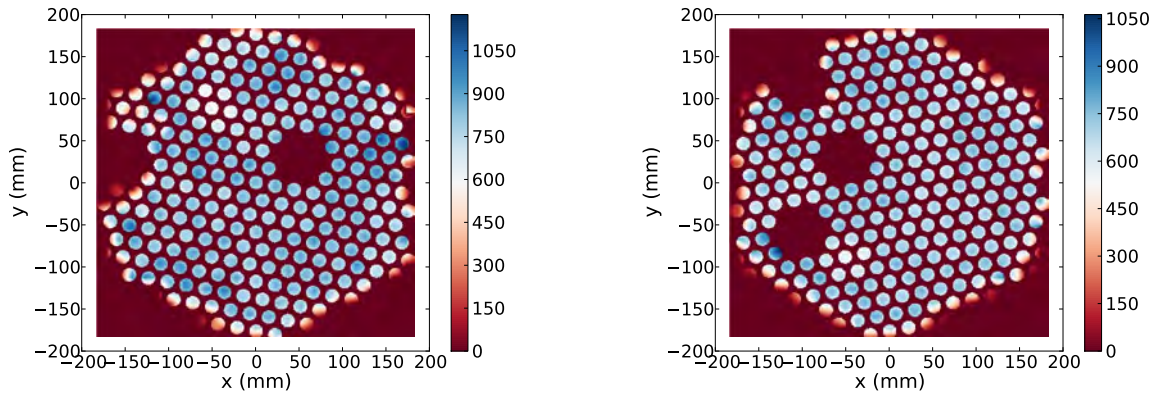


Figure A.2: PE counts on each APD from a scintillation cluster right above it at $z = 182$ mm for TPC1 (left) and $z = -182$ mm for TPC2 (right) measured using the light map after solid angle correction. The gain non-uniformity is calculated using the PE counts on the selected channels.

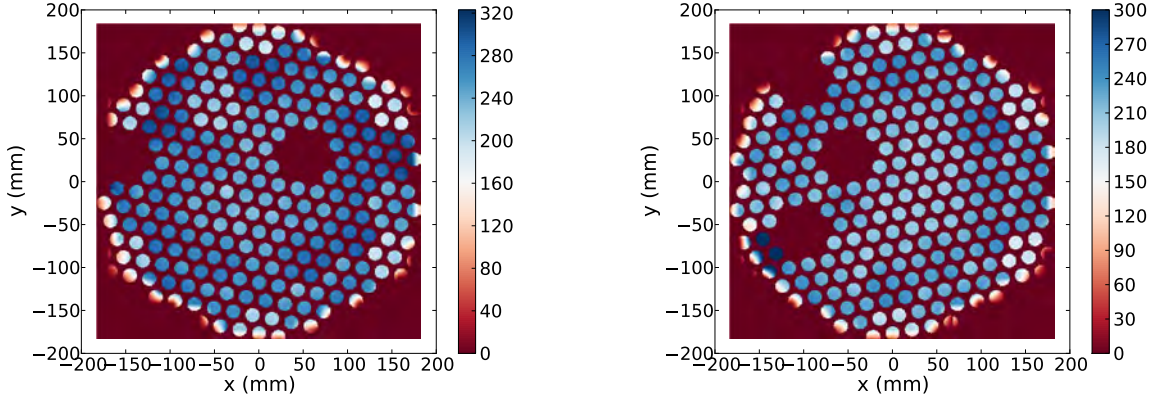


Figure A.3: PE counts on each APD from a scintillation cluster right above it at $z = 50$ mm for TPC1 (left) and $z = -50$ mm for TPC2 (right) measured using the lightmap before solid angle correction.

are considered. As shown in Figure A.1, the center APD of each channel receives a larger number of photons than the surrounding APDs for events directly above each individual APD. This pattern results from the different solid angles subtended by the entire gang closest to a given event and the selection cut that only the response of the closest APD gang is shown. After correction for this solid angle dependence a more homogeneous PE number distribution is seen in Figure A.2. This correction allows more subtle features to be observed such as the larger response for events directly below the center of each individual APD relative to events below an APD edge, and the variation between the average response for APDs within a single gang.

The gain non-uniformity—namely the differences in gain at fixed bias for APDs within the same channel—is measured by first calculating the variation among the total PE number for the 7 component APDs and dividing by the mean number of PEs. This non-uniformity is determined after the solid-angle correction for the amplitude distribution shown in Figure A.2. The average APD gain non-uniformity is measured to be $2.4\% \pm 1.1\%$, in which the error denotes the spread in the non-uniformity values among the measurements on different gangs. Edge channels with APDs outside the fiducial volume are not included in the average.

For events occurring very near the APD plane, the measured gain non-uniformity

can have an impact on the rotated resolution that is non-negligible compared to other terms. However, the non-uniformity has a substantially smaller effect on σ_p^2 when the event is far away from the anode, as can be seen from Figure A.3, where the PE counts on each APD from a scintillation cluster that is ~ 150 mm from the plane are shown. In this case, the uniform distribution of photons across each gang due to the smaller solid angle variation with position and relatively larger amount of reflected light smooths out the effects of gain non-uniformity within each gang. For the source calibrations considered here, the sources were positioned near the cathode, at maximal distance from each APD plane. After accounting for the uniformity of the response on each gang seen in Figure A.3, the σ_{NU} term is estimated to be $< 0.2\%$ and can be neglected from the calculation of σ_p^2 for these results.

Appendix B

Reconstruction of the Scintillation Energy with the DNN

In Section 4.4.4, we described a denoising algorithm that was applied on the EXO-200 data to remove correlated APD noise and significantly improve the energy resolution for the scintillation channel in Phase I. A proposed alternative approach to improve the scintillation energy resolution is through applying deep neural networks (DNN) to the scintillation data. As a matter of fact, a DNN model trained on MC simulated U-wire waveforms has proved to be able to reconstruct the ionization energy from experimental data with better resolution than using the conventional reconstruction method [24], yet no such DNN model has been built for reconstructing the scintillation energy. In the past, attempts have been made to train the DNN on simulated APD waveforms as well. The MC simulation of the light signals is performed by first obtaining the light distribution among APDs for a given event based on the information from the lightmap, and then generating a pulse with simulated noise component added so that it resembles the real APD waveform. It turns out that the DNN model trained on the MC APD waveforms could reconstruct the MC scintillation spectrum with better energy resolution than the traditional method, but did not perform well

in reconstructing real experimental data. One possible reason is that the light map that the MC depends on has systematic differences relative to the data, or too high of a noise level due to limited statistics in certain regions of the detector, and cannot reproduce light signals with high accuracy.

In this section, we describe the effort to develop a data-driven DNN model for reconstructing the scintillation energy, which does not rely on the accuracy of MC. Two approaches were used in training the DNN model, the first approach used raw waveforms from source calibration events with five well-known photopeak energies as inputs for training the network, while in the second approach, an augmented dataset is generated by simultaneously scaling the energy and waveform of the photopeak events from the dataset used in the first method. The architecture of the DNN is identical for both approaches, which will be described below.

B.1 Training data preparation

When training the DNN, the data is divided into three independent sets:

- A training set used to train multiple different DNNs.
- A validation set. The best DNN is selected based on its performance over the validation set.
- A test set used for evaluating the performance of the selected DNN which prevents the DNN from overfitting either the training set or the validation set.

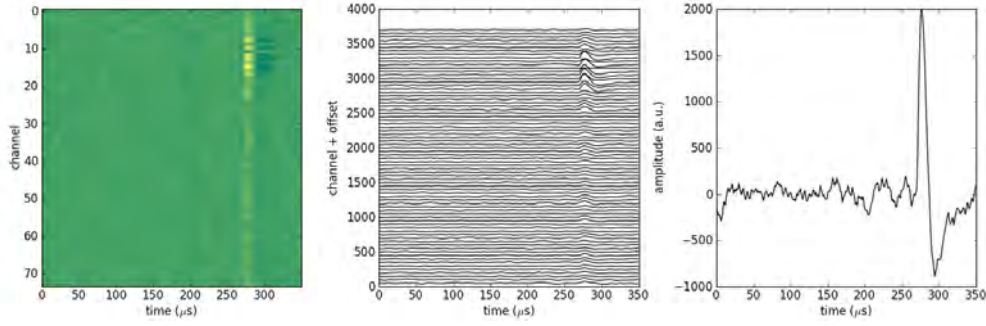
B.1.1 Construction of Datasets with Photopeak Events

In the first trial of this DNN study, a training dataset is made directly from source calibration data. Due to the anti-correlation between the charge and light energy deposits, the scintillation spectrum of the calibration source is smeared, which makes

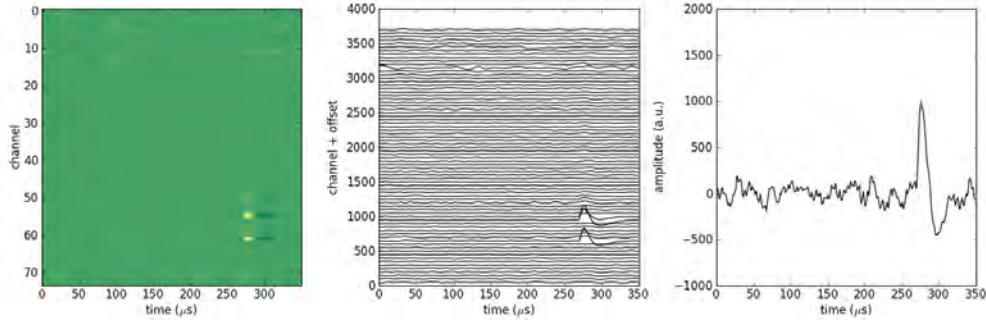
it difficult to know the true scintillation energy of an event. However, in the energy spectra of the four available radioactive sources, there are 5 characteristic photopeaks that are easily recognizable: the 2615 keV peak of ^{228}Th , the 1764 keV peak of ^{226}Ra , the 1332 keV and 1173 keV peak of ^{60}Co , and the 662 keV peak of ^{137}Cs . For each calibration source, we first perform a 2D Gaussian fit to its charge vs. light energy spectrum and then apply a 1σ cut near the best fit center value to select the photopeak events. The true label for each of the selected events is one of the 5 photopeak energies listed above.

The input data for the DNN consists of the raw waveforms of all 74 APD channels with their baseline subtracted. Each waveform contains 350 samples which guarantees that the entire scintillation signal is included in the frame. All APD waveforms from an event are stacked vertically in the order of their assigned channel number to form an image of 350×74 pixels. Examples of input images produced by a scintillation cluster near the cathode with energy ~ 2615 keV, and a scintillation cluster near the anode with energy ~ 2615 keV are shown in Figure B.1. We can qualitatively understand how the energy and position information is encoded in the image: the APDs located near the event location collect most of the scintillation light, and events with larger energy generally produce waveforms with larger amplitudes.

Figure B.2 shows how the photopeak events are selected by setting a 2D cut in the energy spectra of the four different calibration sources. Only SS events are included in the training dataset. In order to minimize bias, data runs from different positions taken during the whole Phase I run are combined to acquire a sufficiently large training set, and a smoothing algorithm is applied to flatten its energy and spatial distributions. Figure B.3 illustrates the energy distribution of all the selected photopeak events in the input dataset. In total, there are ~ 110000 events in the training set and 14000 events in the validation set. In addition, a separate test set is constructed to evaluate the trained model, which is shown in Section B.3.



(a)



(b)

Figure B.1: (a) An input to the DNN (left panel), made from APD waveforms generated by a photopeak event with energy 2615 keV from the ^{228}Th source. The vertical axis indicates the APD channel number and the horizontal axis represents the time in μs . The middle panel shows the baseline-subtracted waveforms of each APD channel and the right panel is the sum waveform over all channels. (b) Waveform images generated by a photopeak event with energy 1173 keV from the ^{60}Co source.

B.1.2 Construction of Augmented Datasets

As will be shown in Section B.3, a training set consisting only of events with energy equal to the five full-absorption peaks cannot provide enough information for the DNN to reconstruct events from the full energy spectrum. Therefore, as a second attempt, we augment the dataset in the previous section with events that have energies other than the photopeaks by scaling the waveform amplitudes of the photopeak events. This is carried out following three steps:

1. For each photopeak event in the dataset described in Section B.1.1, fit its waveform amplitude with the APD signal model, as shown in Figure B.4a.

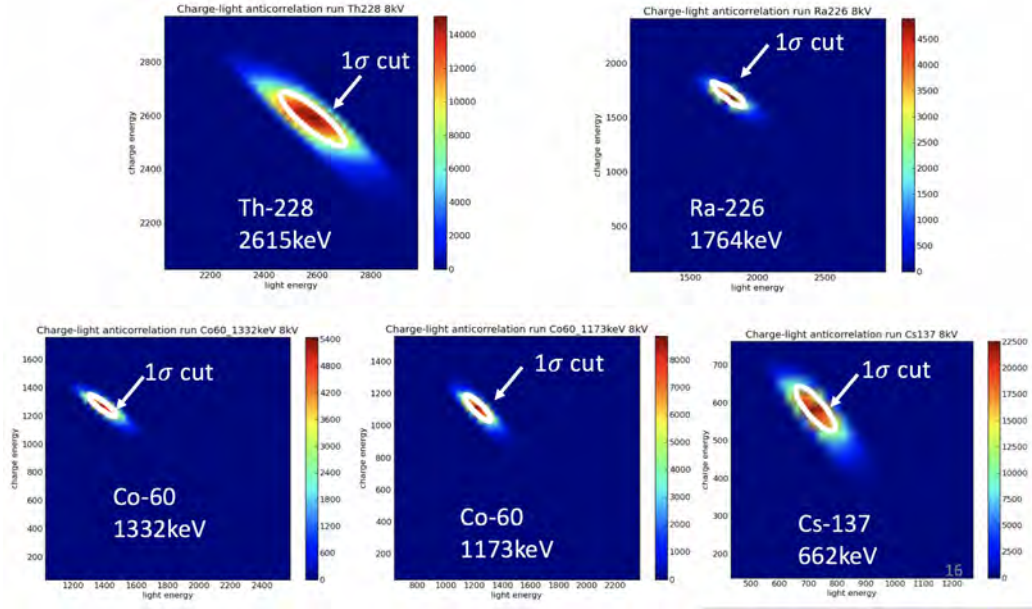


Figure B.2: Selection of events at the full-absorption peaks from the four calibration sources by applying a 2D cut in their charge versus light energy spectra.

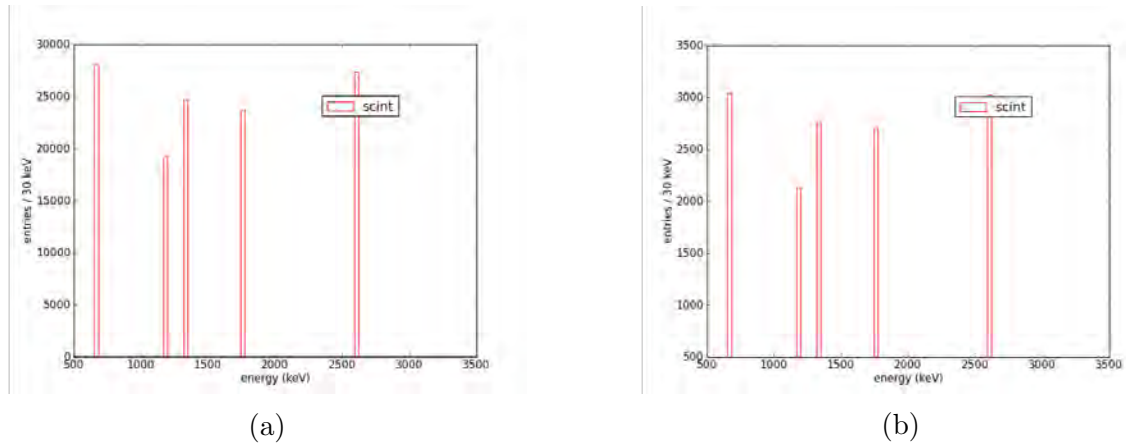


Figure B.3: Energy distribution of the training set (a) and a validation set (b) that only contain photopeak events from calibration sources.

2. Scale the measured pulse amplitude above with the ratio between a given energy we want to add to the dataset and the photopeak energy, then generate a pulse with the scaled amplitude.
3. Add a simulated noise trace to the APD pulse generated above such that the final waveform looks similar to a real waveform, then fill the scaled waveform

data and its energy label into the dataset.

The energy of events in the final augmented dataset ranges from 500 keV to 3000 keV, with an interval of 20 keV. Waveforms for events with energy between 500 keV and 880 keV are scaled from the 662 keV ^{137}Cs source data; events with energy between 900 keV and 1220 keV are scaled from the 1173 keV ^{60}Co data; events with energy between 1240 keV and 1520 keV are scaled from the 1332 keV ^{60}Co data; events with energy between 1540 keV and 2160 keV are scaled from the 1764 keV ^{226}Ra data; events with energy between 2180 keV and 3000 keV are scaled from the 2615 keV ^{228}Th data. The final energy and spatial distribution of the augmented training set is shown in Figure B.6. The size of the validation and test set is $\sim 10\%$ of the training set, and are made separately from the training set.

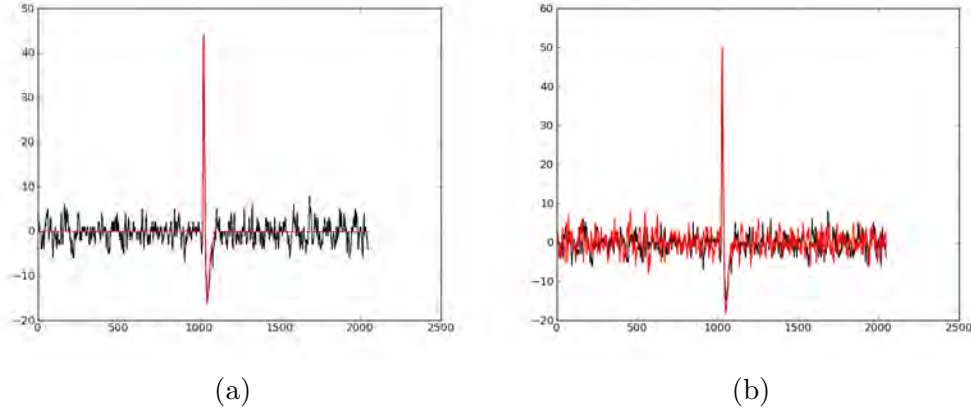
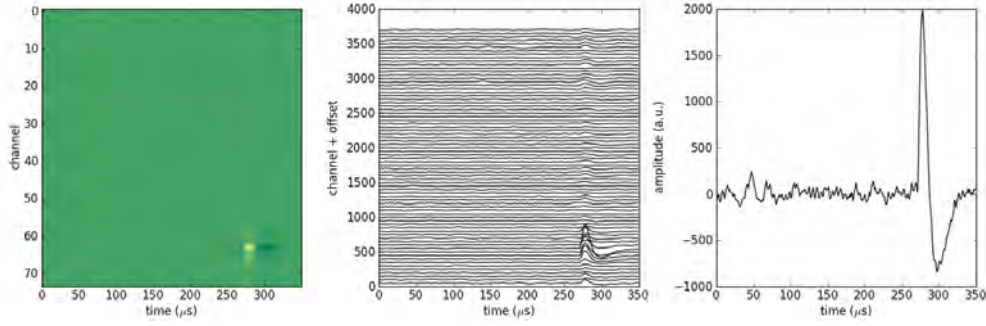
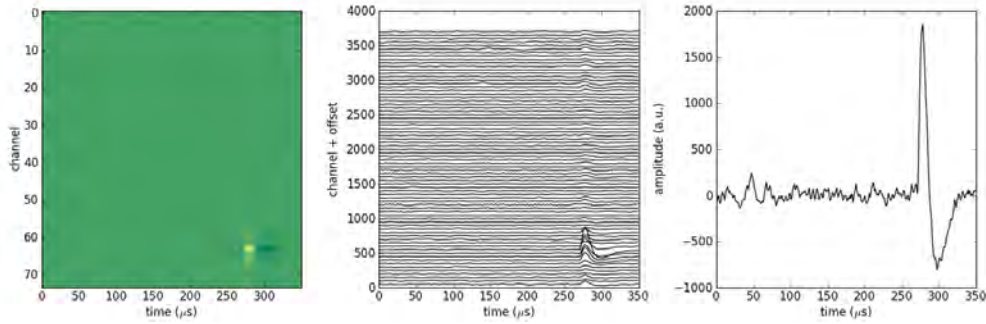


Figure B.4: (a) Example of the fit pulse (red) to a measured waveform (black) from an APD channel generated by a ^{228}Th photopeak event with energy 2615 keV. (b) The red line represents the waveform generated on the same APD channel for an event with energy 2800 keV by scaling the fitted pulse in (a) and adding a simulated noise trace. The black line is the original measured waveform.

All the images in the training and validation sets are then fed into the DNN, and the resulting best trained model is then evaluated on the test set.



(a)



(b)

Figure B.5: (a) An input image to the DNN for an event with energy 2800 keV in the augmented dataset (left panel), made by scaling the measured APD waveforms generated by a 2615 keV event from the ^{228}Th source (b). The vertical axis indicates the APD channel number and the horizontal axis represents the time in μs . The middle panel shows the baseline-subtracted waveforms of each APD channel and the right panel is the sum waveform over all channels.

B.2 DNN Architecture

The architecture of the DNN for this study follows the one presented in Ref. [24] for position reconstructions using scintillation data. An illustration of the structure of the DNN is shown in Figure B.7. The event image fed into the DNN is made from waveforms collected on 74 APD channels, with 350 samples in each waveform (see Figure B.1), and the output layer has only one unit – the scintillation energy. The first convolutional layer has 16 kernels of size 5×5 with a stride of 1 followed by a maximum pooling layer of size 2×3 . The second convolutional layer has 32 kernels of size 5×5 . Its stride size and the size of the following maximum pooling layer are also

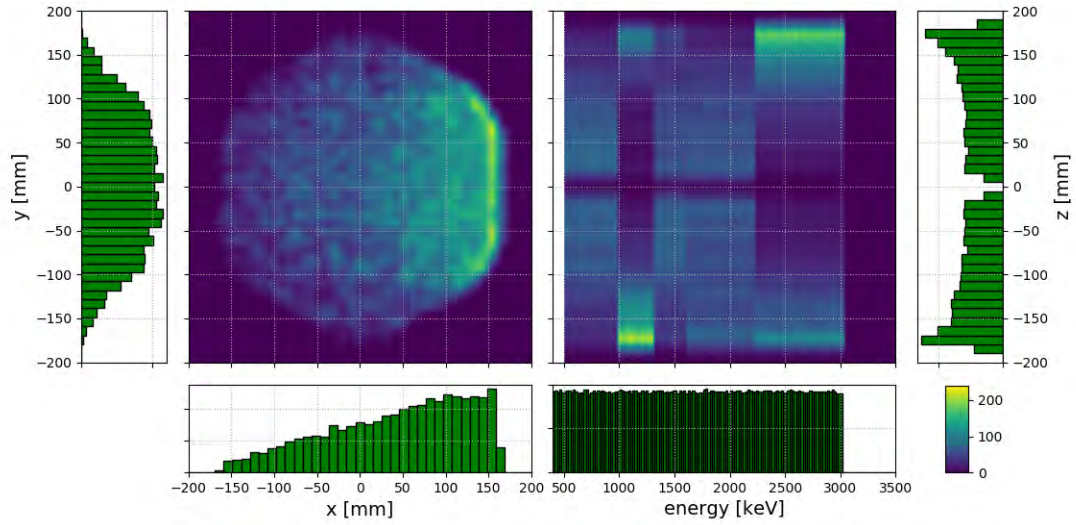


Figure B.6: Event energy and position distribution of the augmented training set. The energy distribution of is designed to be uniform by scaling data from photopeak events, while the spatial distribution is flattened but not perfectly uniform due to the limited amount of photopeak events from various source locations.

identical to the first convolutional layer. In the following two convolutional layers, the number of kernels with the same size is increased to 64 and 128 respectively with max pooling layers of size 2×4 and 3×3 in between. After the last max pooling, the layer is flattened into a one-dimensional array with 2048 units and then transformed into fully connected layers with size 1024, 256 and finally 1 in the output layer.

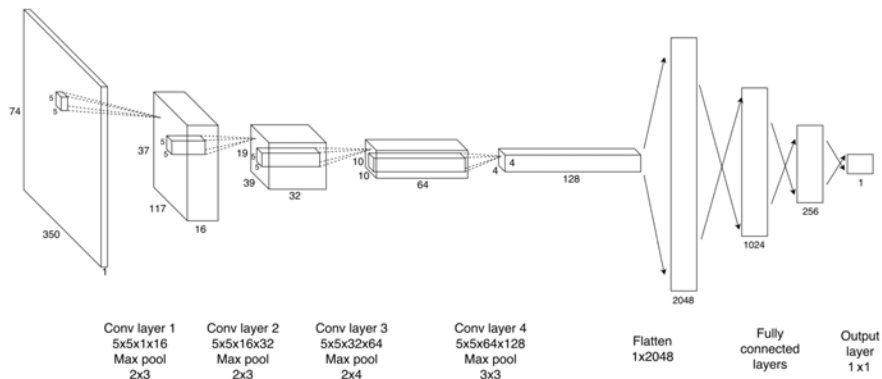


Figure B.7: Architecture of the DNN for the scintillation energy reconstruction. It consists of four convolutional layers followed by three fully connected layers and a final output layer with dimension 1. Figure adapted from Ref. [24]

The training of the DNN involves the minimization the loss function $L = C + \lambda \cdot R$, where C is the mean square deviation of the predicted and true energy, and R is the regularization term. The expression for C is:

$$C = \frac{1}{m} \sum_{j=1}^m (y_j - \hat{y}_j)^2 \quad (\text{B.1})$$

in which m is the size of the mini-batch, y_j and \hat{y}_j are the true energy and the predicted energy of event j , respectively. The regularization parameter λ defines the contribution of the regularization term R to the loss L , and its value is tuned to optimize the training performance on the validation dataset. The regularization term is written as [24]:

$$R = \frac{1}{N} \sum_l^{Lr} \sum_i^{N_l} (w_{[i]}^{[l]})^2 \quad (\text{B.2})$$

where N is the number of weights in the entire network, Lr is the number of layers, N_l the number of weights in the l th layer, and $w_{[i]}^{[l]}$ is the weight vector i of the l th layer. The presence of the regularization term prevents the model from overfitting the input training set. The DNN is set up and trained using the TensorFlow framework [202], where the optimizer we use in the training is the Adaptive Moment Estimation algorithm, also know as Adam [203].

B.3 Evaluation of the Trained DNN

The accuracy of the DNN models trained using the two methods described in Section B.1.2 are evaluated using separate sets of test data. The energy resolution of the ^{228}Th spectrum reconstructed by the DNN model is then compared to that reconstructed by the conventional EXO-200 analysis method.

B.3.1 Test of the DNN Model Trained on Photopeak Events Only

We first evaluate the DNN Model trained on the dataset made of events with five discrete energies only. The value of the loss function as a function of the training epoch is shown in Figure B.8. During each epoch the entire training dataset is passed through the DNN once. After training the network for ~ 7000 epochs, the loss function no longer improves, which can be attributed to the limited amount of events in the training data set, as well as the difficulty of learning light signals that are subject to position-dependent attenuation.

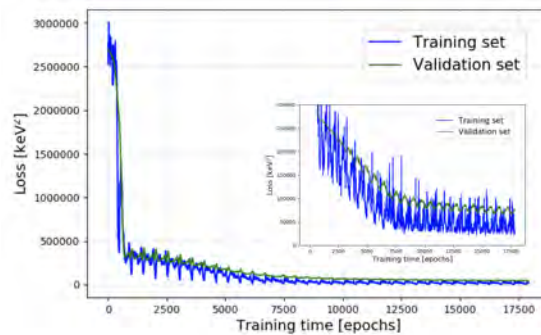


Figure B.8: Training and validation loss versus training epochs. Both the training and validation sets are made from photopeak events only.

Figure B.9 shows the results of evaluating the DNN model on two different test datasets – the first made from events with five photopeak energies, and the second made from a ^{228}Th source run in which only events near the 2615 keV photopeak are used. The green distributions correspond to the true scintillation energy spectrum as determined by the conventional EXO-200 reconstruction method whereas the blue distributions represent the predicted spectrum by the DNN.

We can observe that with events of only five energies present in the training set, the DNN can already predict a scintillation energy spectrum that is roughly in agreement with the one reconstructed by the traditional method. However, due to the limited

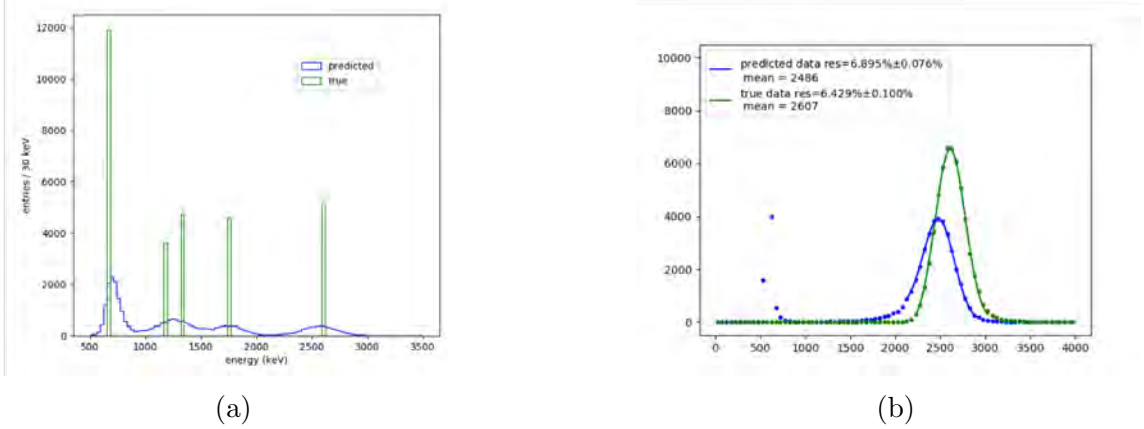


Figure B.9: Evaluation of the trained DNN model on an independent set of test data (a) and a ^{228}Th source run with all events near its 2615 keV peak (b). The true scintillation energy spectrum determined by the conventional EXO-200 reconstruction and the predicted spectrum by the DNN are represented by the green and blue distributions, respectively.

amount of events and energy labels, the energy resolution of the scintillation spectrum reconstructed by the DNN model is 3% worse than the resolution reconstructed by the standard EXO-200 method.

B.3.2 Test of the DNN Model Trained on the Augmented Dataset

We next evaluate the DNN Model trained on the augmented dataset made from events with energy between 500 keV and 3000 keV. The loss function as a function of the training epoch is shown in Figure B.10. After training the network for ~ 7000 epochs, the loss function no longer improves.

Figure B.11 shows the results of evaluating the DNN model on a test set with uniform energy distribution and another independent ^{228}Th source run. The green distributions correspond to the true scintillation energy spectrum as determined by the conventional EXO-200 reconstruction method and the blue distributions represent the predicted spectrum by the DNN.

The result above shows that the energy resolution of the scintillation spectrum

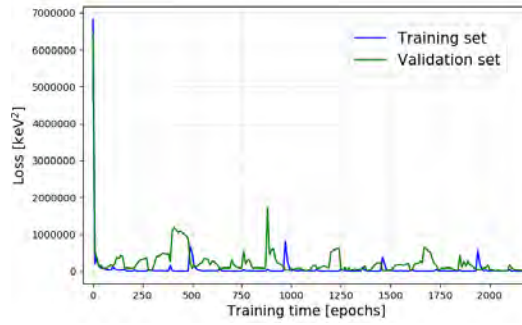


Figure B.10: Training and validation loss versus training epochs. Both the training and validation sets are augmented datasets made from scaling the energy and waveforms of the photopeak events.

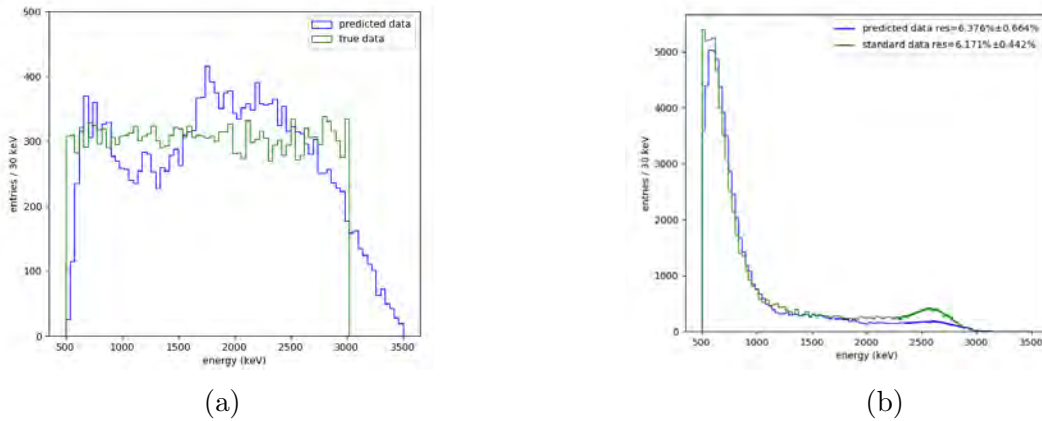


Figure B.11: Evaluation of the trained DNN model on an independent set of test data with uniform energy distribution (a) and a ^{228}Th source run with energy beyond 500 keV (b). The true scintillation energy spectrum determined by the conventional EXO-200 reconstruction and the predicted spectrum by the DNN are represented by the green and blue distributions, respectively.

reconstructed by the DNN model trained on the augmented dataset is still 3% worse than the resolution reconstructed by the standard EXO-200 method, which may be attributed to the limited amount of events and the systematic error of the simulated waveforms in the augmented training and validation sets.

B.4 Next Steps

The above study shows that using data events from a few photopeaks with known energies for building a training set can not provide enough information for the DNN to reconstruct the full scintillation energy spectrum with good resolution, nor is the method of scaling waveforms of these photopeak events able to reproduce real light signals with high accuracy. In addition, we can not generate a training set with perfectly uniform position distribution using the two approaches above due to the limited amount of photopeak events from experimental data. On the other hand, the traditional MC simulation of APD waveforms depends on the lightmap that may have high level of noise or systematic differences from real data and thus is incapable of generating a training set representative enough of real scintillation data either.

A proposed new method for augmenting training sets is through using the generative adversarial network (GAN), which is expected to generate artificial images that look like authentic images. A GAN is based on two networks – a generative and a discriminative network. The discriminator is initially trained on a known dataset, which serves to distinguishes artificial images produced by the generator from real images, whereas the generator produces artificial images from random input and is trained until it can successfully fool the discriminator. If the GAN is able to generate scintillation signals on all APDs with the expected energy and position dependency in EXO-200, it will provide a fast way to generate a great many training events and produce a more representative dataset for use in the DNN-based scintillation energy reconstruction.

Bibliography

- [1] Wikimedia Commons. File:standard model of elementary particles.svg — wiki-media commons, the free media repository, 2019. [Online; accessed 31-January-2020].
- [2] Jonathan Engel and Javier Menéndez. Status and future of nuclear matrix elements for neutrinoless double-beta decay: a review. *Reports on Progress in Physics*, 80(4):046301, Mar 2017.
- [3] J. Schechter and J. W. F. Valle. Neutrinoless double- β decay in $SU(2) \times U(1)$ theories. *Phys. Rev. D*, 25:2951–2954, Jun 1982.
- [4] Giovanni Benato. Effective Majorana Mass and Neutrinoless Double Beta Decay. *Eur. Phys. J.*, C75(11):563, 2015.
- [5] Vladimir Tello, Miha Nemevsek, Fabrizio Nesti, Goran Senjanovic, and Francesco Vissani. Left-Right Symmetry: from LHC to Neutrinoless Double Beta Decay. *Phys. Rev. Lett.*, 106:151801, 2011.
- [6] J. B. Albert et al. Improved measurement of the $2\nu\beta\beta$ half-life of ^{136}Xe with the EXO-200 detector. *Phys. Rev.*, C89(1):015502, 2014.
- [7] M. Auger et al. The EXO-200 detector, part I: Detector design and construction. *JINST*, 7:P05010, 2012.

- [8] API product #SD630-70-75-500 by Advanced Photonix Avenida Acaso, Camarillo, CA 93012, USA.
- [9] R. Neilson et al. Characterization of large area APDs for the EXO-200 detector. *Nucl. Instrum. Meth.*, A608:68–75, 2009.
- [10] F. LePort et al. A Magnetically-driven piston pump for ultra-clean applications. *Rev. Sci. Instrum.*, 82:105114, 2011.
- [11] J.B. Albert et al. Cosmogenic backgrounds to $0\nu\beta\beta$ in EXO-200. *Journal of Cosmology and Astroparticle Physics*, 2016(04):029–029, Apr. 2016.
- [12] Reconstruction group. Reconstruction Document for Run2a Analysis.
- [13] Reconstruction group. Working Document 2019 0ν .
- [14] G. Anton et al. Search for Neutrinoless Double- β Decay with the Complete EXO-200 Dataset. *Phys. Rev. Lett.*, 123(16):161802, 2019.
- [15] D. S. Akerib et al. Improved measurements of the β -decay response of liquid xenon with the lux detector. *Phys. Rev. D*, 100:022002, Jul 2019.
- [16] L. Ludhova et al. Planar laapds: temperature dependence, performance, and application in low-energy x-ray spectroscopy. *Nuclear Instruments and Methods in Physics Research Section A: Accelerators, Spectrometers, Detectors and Associated Equipment*, 540(1):169 – 179, 2005.
- [17] S. Al Kharusi et al. nEXO Pre-Conceptual Design Report. 2018.
- [18] SNOlab User’s Handbook. http://snolab2008.sno.ca/sno/sno_users_handbook_rev02.pdf.
- [19] J. B. Albert et al. Sensitivity and Discovery Potential of nEXO to Neutrinoless Double Beta Decay. *Phys. Rev.*, C97(6):065503, 2018.

- [20] D. V. Forero, M. Tórtola, and J. W. F. Valle. Neutrino oscillations refitted. *Phys. Rev. D*, 90:093006, Nov 2014.
- [21] Edge Coupled Microstrip Impedance. <https://www.eeweb.com/tools/edge-coupled-microstrip-impedance>.
- [22] Q-Flex Inc. <https://www.qflexinc.com/>.
- [23] TAIFLEX Scientific Co., Ltd. http://www.taiflex.com.tw/html/include/include_electron2.php.
- [24] S. Delaquis et al. Deep Neural Networks for Energy and Position Reconstruction in EXO-200. *JINST*, 13(08):P08023, 2018.
- [25] T. Séguinot, G. Passardi, J. Tischhauser, and T. Ypsilantis. Liquid xenon ionization and scintillation studies for a totally active-vector electromagnetic calorimeter. *Nucl. Instrum. Meth. Phys. Res. A*, 323(3):583 – 600, 1992.
- [26] M. Szydagis et al. NEST: A Comprehensive Model for Scintillation Yield in Liquid Xenon. *JINST*, 6:P10002, 2011.
- [27] D. Yu. Akimov et al. Experimental study of ionization yield of liquid xenon for electron recoils in the energy range 2.8 - 80 keV. *JINST*, 9(11):P11014, 2014.
- [28] S. Tomonaga. On a Relativistically Invariant Formulation of the Quantum Theory of Wave Fields*. *Progress of Theoretical Physics*, 1(2):27–42, 08 1946.
- [29] Julian Schwinger. On quantum-electrodynamics and the magnetic moment of the electron. *Phys. Rev.*, 73:416–417, Feb 1948.
- [30] Julian Schwinger. Quantum electrodynamics. i. a covariant formulation. *Phys. Rev.*, 74:1439–1461, Nov 1948.

- [31] R. P. Feynman. Space-time approach to quantum electrodynamics. *Phys. Rev.*, 76:769–789, Sep 1949.
- [32] R. P. Feynman. Mathematical formulation of the quantum theory of electromagnetic interaction. *Phys. Rev.*, 80:440–457, Nov 1950.
- [33] F. J. Dyson. The radiation theories of tomonaga, schwinger, and feynman. *Phys. Rev.*, 75:486–502, Feb 1949.
- [34] F. J. Dyson. The s matrix in quantum electrodynamics. *Phys. Rev.*, 75:1736–1755, Jun 1949.
- [35] Steven Weinberg. The Making of the standard model. *Eur. Phys. J.*, C34:5–13, 2004. [,99(2005)].
- [36] Mary K. Gaillard, Paul D. Grannis, and Frank J. Sciulli. The standard model of particle physics. *Rev. Mod. Phys.*, 71:S96–S111, Mar 1999.
- [37] Scott Willenbrock. Symmetries of the standard model. In *Physics in $D \geq 4$. Proceedings, Theoretical Advanced Study Institute in elementary particle physics, TASI 2004, Boulder, USA, June 6-July 2, 2004*, pages 3–38, 2004.
- [38] Chronology of Milestone Events in Particle Physics. <http://web.ihep.su/owa/dbserv/hw.part1>.
- [39] V. E. Barnes, P. L. Connolly, D. J. Crennell, B. B. Culwick, W. C. Delaney, W. B. Fowler, P. E. Hagerty, E. L. Hart, N. Horwitz, P. V. C. Hough, J. E. Jensen, J. K. Kopp, K. W. Lai, J. Leitner, J. L. Lloyd, G. W. London, T. W. Morris, Y. Oren, R. B. Palmer, A. G. Prodell, D. Radojičić, D. C. Rahm, C. R. Richardson, N. P. Samios, J. R. Sanford, R. P. Shutt, J. R. Smith, D. L. Stonehill, R. C. Strand, A. M. Thorndike, M. S. Webster, W. J. Willis, and

- S. S. Yamamoto. Observation of a hyperon with strangeness minus three. *Phys. Rev. Lett.*, 12:204–206, Feb 1964.
- [40] E. D. Bloom, D. H. Coward, H. DeStaebler, J. Drees, G. Miller, L. W. Mo, R. E. Taylor, M. Breidenbach, J. I. Friedman, G. C. Hartmann, and H. W. Kendall. High-energy inelastic $e - p$ scattering at 6° and 10° . *Phys. Rev. Lett.*, 23:930–934, Oct 1969.
- [41] M. Breidenbach, J. I. Friedman, H. W. Kendall, E. D. Bloom, D. H. Coward, H. DeStaebler, J. Drees, L. W. Mo, and R. E. Taylor. Observed behavior of highly inelastic electron-proton scattering. *Phys. Rev. Lett.*, 23:935–939, Oct 1969.
- [42] D. P. Barber et al. Discovery of three-jet events and a test of quantum chromodynamics at petra. *Phys. Rev. Lett.*, 43:830–833, Sep 1979.
- [43] G. Arnison et al. Experimental observation of isolated large transverse energy electrons with associated missing energy at $s=540$ GeV. *Physics Letters B*, 122(1):103 – 116, 1983.
- [44] G. Arnison et al. Experimental observation of lepton pairs of invariant mass around $95 \text{ GeV}/c^2$ at the CERN SPS collider. *Physics Letters B*, 126(5):398 – 410, 1983.
- [45] G. Arnison et al. Further evidence for charged intermediate vector bosons at the sps collider. *Physics Letters B*, 129(3):273 – 282, 1983.
- [46] G. Aad et al. Observation of a new particle in the search for the standard model higgs boson with the atlas detector at the lhc. *Physics Letters B*, 716(1):1 – 29, 2012.

- [47] S. Chatrchyan et al. Observation of a new boson at a mass of 125 gev with the cms experiment at the lhc. *Physics Letters B*, 716(1):30 – 61, 2012.
- [48] C. L. Cowan, F. Reines, F. B. Harrison, H. W. Kruse, and A. D. McGuire. Detection of the free neutrino: a confirmation. *Science*, 124(3212):103–104, 1956.
- [49] Y. Fukuda et al. Evidence for Oscillation of Atmospheric Neutrinos. *Phys. Rev. Lett.*, 81:1562–1567, Aug 1998.
- [50] Q. R. Ahmad et al. Measurement of the Rate of $\nu_e + d \rightarrow p + p + e^-$ Interactions Produced by 8B Solar Neutrinos at the Sudbury Neutrino Observatory. *Phys. Rev. Lett.*, 87:071301, Jul 2001.
- [51] R. N. Mohapatra and A. Y. Smirnov. Neutrino Mass and New Physics. *Ann. Rev. Nucl. Part. Sci.*, 56:569–628, 2006.
- [52] Howard Georgi. *Weak Interactions and Modern Particle Theory*. Dover Publications, 2009.
- [53] Raymond Davis, Don S. Harmer, and Kenneth C. Hoffman. Search for Neutrinos from the Sun. *Phys. Rev. Lett.*, 20:1205–1209, May 1968.
- [54] Bruce T. Cleveland, Timothy Daily, Jr. Raymond Davis, James R. Distel, Kenneth Lande, C. K. Lee, Paul S. Wildenhain, and Jack Ullman. Measurement of the Solar Electron Neutrino Flux with the Homestake Chlorine Detector. *The Astrophysical Journal*, 496(1):505–526, Mar 1998.
- [55] S. P. Mikheyev and A. Yu. Smirnov. Resonance Amplification of Oscillations in Matter and Spectroscopy of Solar Neutrinos. *Sov. J. Nucl. Phys.*, 42:913–917, 1985.

- [56] L. Wolfenstein. Neutrino oscillations and stellar collapse. *Phys. Rev. D*, 20:2634–2635, Nov 1979.
- [57] A. Gando et al. Reactor on-off antineutrino measurement with KamLAND. *Phys. Rev. D*, 88:033001, Aug 2013.
- [58] W. Anthony Mann. Atmospheric neutrinos and the oscillations bonanza. *Int. J. Mod. Phys.*, A15S1:229–256, 2000.
- [59] P. Adamson et al. Measurement of Neutrino and Antineutrino Oscillations Using Beam and Atmospheric Data in MINOS. *Phys. Rev. Lett.*, 110:251801, Jun 2013.
- [60] F. P. An et al. Observation of electron-antineutrino disappearance at Daya Bay. *Phys. Rev. Lett.*, 108:171803, 2012.
- [61] Y. Abe et al. Indication of Reactor $\bar{\nu}_e$ Disappearance in the Double Chooz Experiment. *Phys. Rev. Lett.*, 108:131801, Mar 2012.
- [62] J. K. Ahn et al. Observation of Reactor Electron Antineutrino Disappearance in the RENO Experiment. *Phys. Rev. Lett.*, 108:191802, 2012.
- [63] D. Adey et al. Measurement of the Electron Antineutrino Oscillation with 1958 Days of Operation at Daya Bay. *Phys. Rev. Lett.*, 121:241805, Dec 2018.
- [64] M. A. Acero et al. First measurement of neutrino oscillation parameters using neutrinos and antineutrinos by nova. *Phys. Rev. Lett.*, 123:151803, Oct 2019.
- [65] K. Abe et al. Measurement of neutrino and antineutrino oscillations by the T2K experiment including a new additional sample of ν_e interactions at the far detector. *Phys. Rev.*, D96(9):092006, 2017. [Erratum: *Phys. Rev.* D98,no.1,019902(2018)].

- [66] K. Abe et al. Search for CP Violation in Neutrino and Antineutrino Oscillations by the T2K Experiment with 2.2×10^{21} Protons on Target. *Phys. Rev. Lett.*, 121(17):171802, 2018.
- [67] Aneesh V. Manohar. Introduction to Effective Field Theories. In *Les Houches summer school: EFT in Particle Physics and cosmology Les Houches, Chamonix Valley, France, July 3-28, 2017*, 2018.
- [68] Steven Weinberg. Baryon- and Lepton-Nonconserving Processes. *Phys. Rev. Lett.*, 43:1566–1570, Nov 1979.
- [69] C. Giunti, C. W. Kim, and U. W. Lee. Running coupling constants and grand unification models. *Mod. Phys. Lett.*, A6:1745–1755, 1991.
- [70] Ugo Amaldi, Wim de Boer, and Hermann Furstenau. Comparison of grand unified theories with electroweak and strong coupling constants measured at LEP. *Phys. Lett.*, B260:447–455, 1991.
- [71] John R. Ellis, S. Kelley, and Dimitri V. Nanopoulos. Probing the desert using gauge coupling unification. *Phys. Lett.*, B260:131–137, 1991.
- [72] Rabindra N. Mohapatra and Goran Senjanović. Neutrino Mass and Spontaneous Parity Nonconservation. *Phys. Rev. Lett.*, 44:912–915, Apr 1980.
- [73] R N Mohapatra. Physics of the neutrino mass. *New Journal of Physics*, 6:82–82, Jul 2004.
- [74] Rabindra N. Mohapatra and Goran Senjanović. Neutrino masses and mixings in gauge models with spontaneous parity violation. *Phys. Rev. D*, 23:165–180, Jan 1981.

- [75] M. A. B. Bég, R. V. Budny, R. Mohapatra, and A. Sirlin. Manifest Left-Right Symmetry and its Experimental Consequences. *Phys. Rev. Lett.*, 38:1252–1255, May 1977.
- [76] S. M. Barr. New Type of Seesaw Mechanism for Neutrino Masses. *Phys. Rev. Lett.*, 92:101601, Mar 2004.
- [77] Carl H. Albright and S. M. Barr. Leptogenesis in the type III seesaw mechanism. *Phys. Rev.*, D69:073010, 2004.
- [78] Roberto Franceschini, Thomas Hambye, and Alessandro Strumia. Type-III seesaw at LHC. *Phys. Rev.*, D78:033002, 2008.
- [79] Ernest Ma. Pathways to Naturally Small Neutrino Masses. *Phys. Rev. Lett.*, 81:1171–1174, Aug 1998.
- [80] Ernest Ma. Naturally Small Seesaw Neutrino Mass with No New Physics Beyond the TeV Scale. *Phys. Rev. Lett.*, 86:2502–2504, Mar 2001.
- [81] Ernest Ma. Verifiable radiative seesaw mechanism of neutrino mass and dark matter. *Phys. Rev. D*, 73:077301, Apr 2006.
- [82] Rabindra N. Mohapatra. Mechanism for understanding small neutrino mass in superstring theories. *Phys. Rev. Lett.*, 56:561–563, Feb 1986.
- [83] R. N. Mohapatra and J. W. F. Valle. Neutrino mass and baryon-number non-conservation in superstring models. *Phys. Rev. D*, 34:1642–1645, Sep 1986.
- [84] A. G. Dias, C. A. de S. Pires, P. S. Rodrigues da Silva, and A. Sempieri. A Simple Realization of the Inverse Seesaw Mechanism. *Phys. Rev.*, D86:035007, 2012.
- [85] M. Goeppert-Mayer. Double Beta-Disintegration. *Phys. Rev.*, 48:512–516, Sep 1935.

- [86] J. Kaulard et al. Improved limit on the branching ratio of $\mu^- \rightarrow e^+$ conversion on titanium. *Physics Letters B*, 422(1):334 – 338, 1998.
- [87] E. Cortina Gil et al. Searches for lepton number violating k^+ decays. *Physics Letters B*, 797:134794, 2019.
- [88] Howard Georgi and S. L. Glashow. Unity of All Elementary-Particle Forces. *Phys. Rev. Lett.*, 32:438–441, Feb 1974.
- [89] H. Georgi. Unified Gauge Theories. *Stud. Nat. Sci.*, 9:329–339, 1975.
- [90] Harald Fritzsch and Peter Minkowski. Unified interactions of leptons and hadrons. *Annals of Physics*, 93(1):193 – 266, 1975.
- [91] Fermilab Steering Group Report. https://www.fnal.gov/directorate/steering/chapter_5.shtml.
- [92] Matteo Agostini, Giovanni Benato, and Jason Detwiler. Discovery probability of next-generation neutrinoless double- β decay experiments. *Phys. Rev.*, D96(5):053001, 2017.
- [93] M. Tanabashi et al. Review of Particle Physics. *Phys. Rev. D*, 98:030001, Aug 2018.
- [94] M. P. Mendenhall et al. Precision measurement of the neutron β -decay asymmetry. *Phys. Rev. C*, 87:032501, Mar 2013.
- [95] J.D. WALECKA. Section 4 - semileptonic weak interactions in nuclei**research sponsored by the air force office of scientific research, office of aerospace research, u.s. air force, under afosr contract no. f44620-71-c-0044. In VERNON W. HUGHES and C.S. WU, editors, *Muon Physics*, pages 113 – 218. Academic Press, 1975.

- [96] P. Gysbers et al. Discrepancy between experimental and theoretical β -decay rates resolved from first principles. *Nature Phys.*, 15(5):428–431, 2019.
- [97] G Hagen, T Papenbrock, M Hjorth-Jensen, and D J Dean. Coupled-cluster computations of atomic nuclei. *Reports on Progress in Physics*, 77(9):096302, Sep 2014.
- [98] H. Hergert, S. K. Bogner, T. D. Morris, A. Schwenk, and K. Tsukiyama. The In-Medium Similarity Renormalization Group: A Novel Ab Initio Method for Nuclei. *Phys. Rept.*, 621:165–222, 2016.
- [99] V. Somà, A. Cipollone, C. Barbieri, P. Navrátil, and T. Duguet. Chiral two- and three-nucleon forces along medium-mass isotope chains. *Phys. Rev. C*, 89:061301, Jun 2014.
- [100] Ulf-G Meißner. The long and winding road from chiral effective Lagrangians to nuclear structure. *Physica Scripta*, 91(3):033005, Feb 2016.
- [101] Dean Lee. Lattice simulations for few- and many-body systems. *Prog. Part. Nucl. Phys.*, 63:117–154, 2009.
- [102] M. S. Turner. Intersection between Elementary Particle Physics and Cosmology Vols 1 and 2: Jerusalem Winter School for Theoretical Physics. 1:99, 1986.
- [103] CJ Copi, DN Schramm, and MS Turner. Big-bang nucleosynthesis and the baryon density of the universe. *Science*, 267(5195):192–199, 1995.
- [104] A. D. Sakharov. Violation of CP Invariance, C asymmetry, and baryon asymmetry of the universe. *Pisma Zh. Eksp. Teor. Fiz.*, 5:32–35, 1967. [Usp. Fiz. Nauk161,no.5,61(1991)].
- [105] Steven Weinberg. Cosmological Production of Baryons. *Phys. Rev. Lett.*, 42:850–853, Mar 1979.

- [106] D. Toussaint, S. B. Treiman, Frank Wilczek, and A. Zee. Matter-antimatter accounting, thermodynamics, and black-hole radiation. *Phys. Rev. D*, 19:1036–1045, Feb 1979.
- [107] M. Fukugita and T. Yanagida. Barygenesis without grand unification. *Physics Letters B*, 174(1):45 – 47, 1986.
- [108] W. Buchmuller, R. D. Peccei, and T. Yanagida. Leptogenesis as the origin of matter. *Ann. Rev. Nucl. Part. Sci.*, 55:311–355, 2005.
- [109] J. B. Albert et al. Search for neutrinoless double-beta decay with the upgraded exo-200 detector. *Phys. Rev. Lett.*, 120:072701, Feb 2018.
- [110] D. S. Akerib et al. Tritium calibration of the LUX dark matter experiment. *Phys. Rev. D*, 93(7):072009, 2016.
- [111] J. B. Albert et al. Improved measurement of the $2\nu\beta\beta$ half-life of ^{136}Xe with the EXO-200 detector. *Phys. Rev. C*, 89(1):015502, 2014.
- [112] E. Aprile and T. Doke. Liquid Xenon Detectors for Particle Physics and Astrophysics. *Rev. Mod. Phys.*, 82:2053–2097, 2010.
- [113] C. Chambers et al. Imaging individual barium atoms in solid xenon for barium tagging in nEXO. *Nature*, 569(7755):203–207, 2019.
- [114] Ansoft. <http://www.ansoft.com/products/em/maxwell/>.
- [115] D. S. Leonard et al. Systematic study of trace radioactive impurities in candidate construction materials for EXO-200. *Nucl. Instrum. Meth.*, A591:490–509, 2008.
- [116] M Moszynski, M Szawlowski, M Kapusta, and M Balcerzyk. Large area avalanche photodiodes in scintillation and x-rays detection. *Nuclear Instru-*

- ments and Methods in Physics Research Section A: Accelerators, Spectrometers, Detectors and Associated Equipment*, 485(3):504 – 521, 2002.
- [117] C. G. Davis et al. An Optimal Energy Estimator to Reduce Correlated Noise for the EXO-200 Light Readout. *JINST*, 11(07):P07015, 2016.
- [118] 3M HFE-7000, <http://www.3m.com>.
- [119] SAES. <http://www.saespuregas.com/>.
- [120] N. Stojilovic, E.T. Bender, and R.D. Ramsier. Surface chemistry of zirconium. *Progress in Surface Science*, 78(3):101 – 184, 2005.
- [121] A. Dobi, D.S. Leonard, C. Hall, L.J. Kaufman, T. Langford, S. Slutsky, and Y.-R. Yen. Study of a zirconium getter for purification of xenon gas. *Nuclear Instruments and Methods in Physics Research Section A: Accelerators, Spectrometers, Detectors and Associated Equipment*, 620(2-3):594–598, Aug 2010.
- [122] Steven Herrin. Double beta decay in xenon-136. measuring the neutrino-emitting mode and searching for majoron-emitting modes. 6 2013.
- [123] H. Gemmeke et al. The High resolution neutrino calorimeter KARMEN. *Nucl. Instrum. Meth.*, A289:490–495, 1990.
- [124] Holders Technology part #MC18-25-00CEM. <http://www.holderstechnology.com/catalog/product.cfm?product=66>.
- [125] Nippon Steel Chemical Co. <http://www.nsccl.co.jp/english/>.
- [126] Master Bond, part #EP29LPSP,. <http://www.masterbond.com/tds/ep29lpsp.html>.
- [127] Liang Yang and. Status and prospects for the EXO-200 and nEXO experiments. *Journal of Physics: Conference Series*, 888:012032, sep 2017.

- [128] Wikipedia contributors. Matched filter — Wikipedia, the free encyclopedia, 2019. [Online; accessed 4-February-2020].
- [129] G. Turin. An introduction to matched filters. *IRE Transactions on Information Theory*, 6(3):311–329, June 1960.
- [130] COMSOL Multiphysics. <http://www.comsol.com>.
- [131] J. B. Albert et al. Measurement of the Drift Velocity and Transverse Diffusion of Electrons in Liquid Xenon with the EXO-200 Detector. *Phys. Rev.*, C95(2):025502, 2017.
- [132] S. Ramo. Currents induced by electron motion. *Proceedings of the IRE*, 27(9):584–585, Sep. 1939.
- [133] W. Shockley. Currents to conductors induced by a moving point charge. *Journal of Applied Physics*, 9(10):635–636, 1938.
- [134] J. B. Albert et al. Search for Majorana neutrinos with the first two years of EXO-200 data. *Nature*, 510:229–234, 2014.
- [135] J. Barea, J. Kotila, and F. Iachello. $0\nu\beta\beta$ and $2\nu\beta\beta$ nuclear matrix elements in the interacting boson model with isospin restoration. *Phys. Rev. C*, 91:034304, Mar 2015.
- [136] Nuria López Vaquero, Tomás R. Rodríguez, and J. Luis Egido. Shape and pairing fluctuation effects on neutrinoless double beta decay nuclear matrix elements. *Phys. Rev. Lett.*, 111:142501, Sep 2013.
- [137] J. Engel, F. Šimkovic, and P. Vogel. Chiral two-body currents and neutrinoless double- β decay in the quasiparticle random-phase approximation. *Phys. Rev. C*, 89:064308, Jun 2014.

- [138] J. Menéndez, A. Poves, E. Caurier, and F. Nowacki. Disassembling the nuclear matrix elements of the neutrinoless $\beta\beta$ decay. *Nuclear Physics A*, 818(3):139 – 151, 2009.
- [139] M. T. Mustonen and J. Engel. Large-scale calculations of the double- β decay of ^{76}Ge , ^{130}Te , ^{136}Xe , and ^{150}Nd in the deformed self-consistent Skyrme quasiparticle random-phase approximation. *Phys. Rev. C*, 87:064302, Jun 2013.
- [140] J. Kotila and F. Iachello. Phase-space factors for double- β decay. *Phys. Rev. C*, 85:034316, Mar 2012.
- [141] G. Anton et al. Measurement of the scintillation and ionization response of liquid xenon at MeV energies in the EXO-200 experiment. 2019. arXiv:1908.04128.
- [142] E. Aprile and T. Doke. Liquid xenon detectors for particle physics and astrophysics. *Rev. Mod. Phys.*, 82:2053–2097, Jul 2010.
- [143] E. Conti et al. Correlated fluctuations between luminescence and ionization in liquid xenon. *Phys. Rev. B*, 68:054201, Aug 2003.
- [144] Carl Eric Dahl. *The physics of background discrimination in liquid xenon, and first results from Xenon10 in the hunt for WIMP dark matter*. PhD thesis, Princeton U., 2009.
- [145] D. S. Akerib et al. Signal yields, energy resolution, and recombination fluctuations in liquid xenon. *Phys. Rev. D*, 95:012008, Jan 2017.
- [146] M. Horn et al. Nuclear recoil scintillation and ionisation yields in liquid xenon from zeplin-iii data. *Phys. Lett. B*, 705(5):471 – 476, 2011.
- [147] M Tanaka et al. Let dependence of scintillation yields in liquid xenon. *Nucl. Instrum. Meth. Phys. Res. A*, 457(3):454 – 463, 2001.

- [148] E. Aprile et al. Simultaneous measurement of ionization and scintillation from nuclear recoils in liquid xenon for a dark matter experiment. *Phys. Rev. Lett.*, 97:081302, Aug 2006.
- [149] Tadayoshi Doke, Akira Hitachi, Jun Kikuchi, Kimiaki Masuda, Hiroyuki Okada, and Eido Shibamura. Absolute scintillation yields in liquid argon and xenon for various particles. *Japn. J. Appl. Phys.*, 41(Part 1, No. 3A):1538–1545, mar 2002.
- [150] A. Manalaysay et al. Spatially uniform calibration of a liquid xenon detector at low energies using $^{83}\text{m}\text{Kr}$. *Rev. Sci. Instrum.*, 81:073303, 2010.
- [151] E. Aprile et al. Measurement of the Scintillation Yield of Low-Energy Electrons in Liquid Xenon. *Phys. Rev. D*, 86:112004, 2012.
- [152] Laura Baudis, Yanina Biondi, Chiara Capelli, Michelle Galloway, Shingo Kazama, Alexander Kish, Payam Pakarha, Francesco Piastra, and Julien Wulf. A Dual-phase Xenon TPC for Scintillation and Ionisation Yield Measurements in Liquid Xenon. *Eur. Phys. J.*, C78(5):351, 2018.
- [153] E. Aprile et al. Signal Yields of keV Electronic Recoils and Their Discrimination from Nuclear Recoils in Liquid Xenon. *Phys. Rev. D*, 97(9):092007, 2018.
- [154] S. Stephenson et al. MiX: A Position Sensitive Dual-Phase Liquid Xenon Detector. *JINST*, 10(10):P10040, 2015.
- [155] E. Aprile et al. Response of the xenon100 dark matter detector to nuclear recoils. *Phys. Rev. D*, 88:012006, Jul 2013.
- [156] E. Aprile, K. L. Giboni, P. Majewski, K. Ni, M. Yamashita, R. Hasty, A. Manzur, and D. N. McKinsey. Scintillation response of liquid xenon to low energy nuclear recoils. *Phys. Rev. D*, 72:072006, Oct 2005.

- [157] G. Plante, E. Aprile, R. Budnik, B. Choi, K.-L. Giboni, L. W. Goetzke, R. F. Lang, K. E. Lim, and A. J. Melgarejo Fernandez. New measurement of the scintillation efficiency of low-energy nuclear recoils in liquid xenon. *Phys. Rev. C*, 84:045805, Oct 2011.
- [158] M. Szydagis et al. Noble element simulation technique v2.0, <https://zenodo.org/record/1314669>, July 2018.
- [159] T. Shutt, Carl E. Dahl, J. Kwong, A. Bolozdynya, and P. Brusov. Performance and Fundamental Processes at Low Energy in a Two-Phase Liquid Xenon Dark Matter Detector. *Nucl. Instrum. Meth.*, A579:451–453, 2007.
- [160] D. S. Akerib et al. Calibration, event reconstruction, data analysis, and limit calculation for the lux dark matter experiment. *Phys. Rev. D*, 97:102008, May 2018.
- [161] E. Aprile et al. The XENON1T Dark Matter Experiment. *Eur. Phys. J.*, C77(12):881, 2017.
- [162] Xiangyi Cui et al. Dark Matter Results From 54-Ton-Day Exposure of PandaX-II Experiment. *Phys. Rev. Lett.*, 119(18):181302, 2017.
- [163] S. Stephenson et al. MiX: A Position Sensitive Dual-Phase Liquid Xenon Detector. *JINST*, 10(10):P10040, 2015.
- [164] T. Takahashi, S. Konno, T. Hamada, M. Miyajima, S. Kubota, A. Nakamoto, A. Hitachi, E. Shibamura, and T. Doke. Average energy expended per ion pair in liquid xenon. *Phys. Rev. A*, 12:1771–1775, Nov 1975.
- [165] I. M. Obodovskii and S. G. Pokachalov. Average energy expended per ion pair in liquid and solid xenon. *Sov. J. Low Temp. Phys.*, 5:393, 1979.

- [166] S. Kubota, A. Nakamoto, T. Takahashi, T. Hamada, E. Shibamura, M. Miyajima, K. Masuda, and T. Doke. Recombination luminescence in liquid argon and in liquid xenon. *Phys. Rev. B*, 17:2762–2765, Mar 1978.
- [167] E. Aprile et al. Design and performance of the XENON10 dark matter experiment. *Astropart. Phys.*, 34:679–698, Apr 2011.
- [168] Tadayoshi Doke, Kimiaki Masuda, and Eido Shibamura. Estimation of absolute photon yields in liquid argon and xenon for relativistic (1 mev) electrons. *Nucl. Instrum. Meth. Phys. Res. A*, 291(3):617 – 620, 1990.
- [169] Tadayoshi Doke. A historical view on the r&d for liquid rare gas detectors. *Nucl. Instrum. Meth. Phys. Res. A*, 327(1):113 – 118, 1993.
- [170] E. Aprile, K. L. Giboni, P. Majewski, K. Ni, and M. Yamashita. Observation of anticorrelation between scintillation and ionization for mev gamma rays in liquid xenon. *Phys. Rev. B*, 76:014115, Jul 2007.
- [171] J. Xu, S. Pereverzev, B. Lenardo, J. Kingston, D. Naim, A. Bernstein, K. Kazkaz, and M. Tripathi. Electron extraction efficiency study for dual-phase xenon dark matter experiments. *Phys. Rev. D*, 99:103024, May 2019.
- [172] B.N.V. Edwards, E. Bernard, E.M. Boulton, N. Destefano, M. Gai, M. Horn, N. Larsen, B. Tennyson, L. Tvrznikova, C. Wahl, and D.N. McKinsey. Extraction efficiency of drifting electrons in a two-phase xenon time projection chamber. *JINST*, 13(01):P01005–P01005, jan 2018.
- [173] M. Auger et al. The EXO-200 detector, part I: Detector design and construction. *JINST*, 7:P05010, 2012.
- [174] R. Neilson et al. Characterization of large area apds for the exo-200 detector. *Nucl. Instrum. Meth. Phys. Res. A*, 608(1):68 – 75, 2009.

- [175] D. S. Akerib et al. 3D Modeling of Electric Fields in the LUX Detector. *JINST*, 12(11):P11022, 2017.
- [176] S. Belogurov, G. Bressi, G. Carugno, E. Conti, D. Iannuzzi, and A. T. Meneguzzo. Infrared scintillation in gases, liquids and crystals. *IEEE Trans. Nucl. Sci.*, 47(6):1791–1797, Dec 2000.
- [177] G. Bressi, G. Carugno, E. Conti, C. Del Noce, and D. Iannuzzi. Infrared scintillation: a comparison between gaseous and liquid xenon. *Nucl. Instrum. Meth. Phys. Res. A*, 461(1):378 – 380, 2001.
- [178] T. Alexander, C.O. Escobar, W.H. Lippincott, and P. Rubinov. Near-infrared scintillation of liquid argon. *JINST*, 11(03):C03010–C03010, mar 2016.
- [179] A. Neumeier, T. Dandl, T. Heindl, A. Himpsl, H. Hagn, M. Hofmann, L. Oberauer, W. Potzel, S. Roth, S. Schönert, J. Wieser, and A. Ulrich. Intense infrared scintillation of liquid Ar-Xe mixtures. *Europhys. Lett.*, 106(3):32001, may 2014.
- [180] Aleksey Bolotnikov and Brian Ramsey. The spectroscopic properties of high-pressure xenon. *Nucl. Instrum. Meth. Phys. Res. A*, 396(3):360 – 370, 1997.
- [181] B.G. Lowe and R.A. Sareen. A measurement of the electron–hole pair creation energy and the fano factor in silicon for 5.9 keV x-rays and their temperature dependence in the range 80–270 K. *Nucl. Instrum. Meth. Phys. Res. A*, 576(2):367 – 370, 2007.
- [182] A. J. Tuzzolino. Quantum efficiency of silicon in the vacuum ultraviolet. *Phys. Rev.*, 134:A205–A213, Apr 1964.
- [183] Victor S. Vavilov. On photo-ionization by fast electrons in germanium and silicon. *J. Phys. Chem. Solids*, 8:223 – 226, 1959.

- [184] M. Wolf, R. Brendel, J. H. Werner, and H. J. Queisser. "solar cell efficiency and carrier multiplication in $\text{si}_{1-x}\text{ge}_x$ alloys". *J. Appl. Phys.*, 83(8):4213–4221, 1998.
- [185] Jet Meitzner, Frederick G. Moore, Brock M. Tillotson, Stephen D. Kevan, and Geraldine L. Richmond. Time-resolved measurement of free carrier absorption, diffusivity, and internal quantum efficiency in silicon. *Appl. Phys. Lett.*, 103(9):092101, 2013.
- [186] Sabine Kolodinski, Jürgen H. Werner, Thomas Wittchen, and Hans J. Queisser. Quantum efficiencies exceeding unity due to impact ionization in silicon solar cells. *Appl. Phys. Lett.*, 63(17):2405–2407, 1993.
- [187] N. Medvedev and B. Rethfeld. Transient dynamics of the electronic subsystem of semiconductors irradiated with an ultrashort vacuum ultraviolet laser pulse. *New J. Phys.*, 12:073037, Jul 2010.
- [188] M. Brigida, C. Favuzzi, P. Fusco, F. Gargano, N. Giglietto, F. Giordano, F. Loparco, B. Marangelli, M.N. Mazziotta, N. Mirizzi, S. Rainò, and P. Spinelli. A new monte carlo code for full simulation of silicon strip detectors. *Nucl. Instrum. Meth. Phys. Res. A*, 533(3):322 – 343, 2004.
- [189] Attila Dobi. *Measurement of the Electron Recoil Band of the LUX Dark Matter Detector With a Tritium Calibration Source*. PhD thesis, Maryland U., College Park, 2014.
- [190] M. Jewell et al. Characterization of an Ionization Readout Tile for nEXO. *JINST*, 13(01):P01006, 2018.
- [191] Z. Li et al. Simulation of charge readout with segmented tiles in nEXO. *JINST*, 14(09):P09020, 2019.

- [192] FondazioneBrunoKessler. <https://www.fbk.eu/en/>.
- [193] A. Jamil et al. Vuv-sensitive silicon photomultipliers for xenon scintillation light detection in nexo. *IEEE Transactions on Nuclear Science*, 65(11):2823–2833, Nov 2018.
- [194] G. Gallina et al. Characterization of the Hamamatsu VUV4 MPPCs for nEXO. *Nucl. Instrum. Meth.*, A940:371–379, 2019.
- [195] Hucheng Chen, Jack Fried, Shanshan Gao, Steve Kettell, Veljko Radeka, Maura Spanu, Elizabeth Worcester, Matthew Worcester, Bo Yu, and Junbin Zhang. Cold electronics readout system for protodune-sp lar-tpc. *Nuclear Instruments and Methods in Physics Research Section A: Accelerators, Spectrometers, Detectors and Associated Equipment*, 936:271 – 273, 2019. Frontier Detectors for Frontier Physics: 14th Pisa Meeting on Advanced Detectors.
- [196] Gore[®] High Data Rate Cables. <https://www.gore.com/products/gore-high-data-rate-cables>.
- [197] Wikipedia contributors. Telegrapher’s equations — Wikipedia, the free encyclopedia, 2019. [Online; accessed 29-January-2020].
- [198] Howard W Johnson and 1926 Graham, Martin. *High-speed signal propagation : advanced black magic*. Upper Saddle River, NJ : Prentice Hall PTR, 2002. Includes bibliographical references and index.
- [199] G. Oliver. Using Flex in High-Speed Applications. Dupont Electronic and Communications. <https://www.dupont.com/content/dam/dupont/products-and-services/electronic-and-electrical-materials/flexible-rigid-flex-circuit-materials/documents/DEC-Using-Flex-in-High-Speed-Applications.pdf>.

- [200] I. Arnquist. PNNL Updates. https://ntpc.ucllnl.org/nEXO/index.php/Radioactivity_and_radon.
- [201] A. Gando et al. Search for Majorana Neutrinos Near the Inverted Mass Hierarchy Region with KamLAND-Zen. *Phys. Rev. Lett.*, 117:082503, Aug 2016.
- [202] Martín Abadi et al. Tensorflow: Large-scale machine learning on heterogeneous distributed systems. *CoRR*, abs/1603.04467, 2016.
- [203] Diederik Kingma and Jimmy Ba. Adam: A method for stochastic optimization. *International Conference on Learning Representations*, 12 2014.